Lehigh University
Lehigh Preserve

Theses and Dissertations

2016

Stabilization of Metastable Oxides via Surface Modification

Daniel Graham Gregory
Lehigh University

Follow this and additional works at: http://preserve.lehigh.edu/etd

Part of the Chemical Engineering Commons

Recommended Citation
Gregory, Daniel Graham, "Stabilization of Metastable Oxides via Surface Modification" (2016). *Theses and Dissertations*. 2614.
http://preserve.lehigh.edu/etd/2614

This Dissertation is brought to you for free and open access by Lehigh Preserve. It has been accepted for inclusion in Theses and Dissertations by an authorized administrator of Lehigh Preserve. For more information, please contact preserve@lehigh.edu.

Stabilization of Metastable Oxides via Surface Modification

by

Daniel G. Gregory

Presented to the Graduate and Research Committee
of Lehigh University
in candidacy for the Degree of
Doctor of Philosophy

in
Chemical Engineering

Lehigh University

May, 2016

Copyright by Daniel G. Gregory
2016

Certificate of Approval

Approved and recommended for acceptance as a dissertation in partial fulfillment of the requirements of the degree of Doctor of Philosophy.

_____
Date

_____
Mark A. Snyder, Ph.D.
Dissertation Advisor

_____
Accepted Date

Committee Members:

_____
Mark A. Snyder, Ph.D.
Committee Chair

_____
Israel E. Wachs, Ph.D.
Committee Member

_____
Christopher J. Kiely, Ph.D.
Committee Member

_____
Hugo S. Caram, Ph.D.
Committee Member

Acknowledgements

I have learned a great deal during my time in graduate school at Lehigh University. I am truly thankful for the education I have received here. I would like to thank my advisor, Professor Mark A. Snyder (a fellow University of Delaware alumni) for his assistance during my graduate studies. Professor Snyder provided me with a great deal of freedom in my research and I was also able to attend many conferences across the country. Because of this I have gained a deep appreciation of the field of Chemical Engineering.

I would like to thank Professor Israel E. Wachs for all of his teachings in the field of Catalysis. Professor Wachs always challenged me in my thinking and opened doors to new areas of research. I am also particularly thankful for his comprehensive review of instrumental characterization; without a thorough understanding of the "tools" available to a researcher, it is difficult to answer even the most basic research questions. Additionally, Professor Wachs provided me with training and access to a variety of characterization techniques which broadened the scope of my research; for this I am truly grateful.

I spent many hours in cold dark rooms in the basement of Whitaker laboratory, squinting at faint green transmission electron microscope images. However without Professor Christopher J. Kiely's assistance, I would have never witnessed individual zirconium atoms aligned within a ZrO_2 lattice in real time. These are the sort of moments you will never forget and I would like to thank Professor Kiely for the opportunity to see individual atoms!

Over the past few years I have had several engaging conversations with Professor Hugo S. Caram on various topics ranging from the thermodynamics of materials to soccer; and

even Sputnik, the Soviet satellite. Professor Caram always made the halls of Iacocca and the weekly seminars an enjoyable occasion.

As an undergraduate student two teachers made a profound impact on me. Professor Annette Shine taught me that: “Good writing is clear thinking made visible”. Professor Douglas Taber inspired me by saying: “There are two types of people in this word: soldiers and generals. You need to decide who you’re going to be”.

Steady progress in my research could not have been made without the support of various members of the Lehigh University community. Many instrumental specialists and fellow researchers have helped me over the years. I would like to thank Dr. Michael E. Ford for his help with various instruments, synthesis procedures, and general discussions on chemistry. I would also like to thank Dr. Robert Keyes (Go Swansea) and Bill Mushock for their help troubleshooting problems with electron microscopes. I would like to acknowledge Li Lu for all the time he spent on the ARM with me; we had a great time and captured some amazing images. I am grateful to Dr. Christopher J. Keturakis for his research insight and for going to the monthly meetings held by The Catalysis Society of Metropolitan New York (NYCS) with me. Additionally, I would like to thank John Caffrey, Barbara Kessler, Tracey Lopez, and Janine Jekels for their help over the years with things ranging from welding to photocopying.

I will always have fond memories of my research group. Cooper (Dr. Shih-Chieh Kung), Bonny (Qianying Guo), and Dr. Zheng Tian were with me throughout my entire time at Lehigh and they will remain life-long friends. Cooper “hey, big-guy” coached me in softball and put me way out in right field. Without a doubt, Bonny was always my best buddy in lab. Additionally, I have shared many long days and nights in the lab with Dr. Minseok Song, Midhun Joy, and Megha Sharma. I wish them all the best in the future.

Over the years I have made routine trips home and worked on Mr. David Wood's farm. I would like to thank him for reminding me that there is a bigger world out there if you actually leave campus; also, as I have been told "there are two ways to put pencils in a pencil box". I would like to thank Leah Spangler for her conversations; long walks on Hellertown's rail trail are always a cure for any passing problem.

Of course, I must thank my family for supporting me in every aspect of graduate school; without them I would have never made it this far.

Table of Contents

List of Tables ..... **x**

List of Figures ..... **xi**

Abstract **1**

Chapter 1. Introduction **3**

1.1 Motivation and Objectives 3

1.1.1 The Pursuit of Stable Catalysts 3

1.1.2 Approach to Catalyst Stabilization 5

1.2 Background 7

1.2.1 Conversion of Metallic Ores to Oxide Precursors 7

1.2.2 Commercial Production of Oxides 8

1.2.3 Soft Chemical Production of Oxides 10

1.2.4 Incipient Wetness, Precipitation, and Co-precipitation 11

1.2.5 Mechanisms of Synthetic Transformation during Preparation of Catalytic Materials 13

1.2.6 Molecular Transport within Catalytic Materials 19

1.2.7 Supported Oxide Surface Functionalities 22

1.2.8 Mechanisms of Catalytic Reconstruction and Deactivation 23

1.2.9 Summary of Background Section 32

1.3 Chapter Outlines 33

1.4 References 39

Chapter 2. Synthesis of Three Dimensionally Ordered Mesoporous (3DOm) Materials **48**

2.1 Abstract 48

2.2 Introduction 49

2.3 Materials and Methods 53

2.4 Results and Discussion 61

2.5 Conclusions 77

2.6 References 78

Chapter 3. Stabilization of Metastable Oxides **83**

3.1 Abstract 83

3.2 Introduction....84
3.3 Materials and Methods....88
3.4 Results and Discussion....91
3.5 Conclusions....108
3.6 References....108
Chapter 4. Interfacial Stabilization of Metastable Oxide Films....113
4.1 Abstract....113
4.2 Introduction....114
4.3 Materials and Methods....118
4.4 Results and Discussion....120
4.5 Conclusions....145
4.6 References....146
Chapter 5. The Influence of Synthesis on the Stabilization of MO_x/ZrO_2^{Cryst} versus MO_x/ZrO_2^{Hyd} Catalysts....151
5.1 Abstract....151
5.2 Introduction....152
5.2.1 Overview of Selected Methods of Catalyst Preparation....153
5.2.2 Dehydrated Catalyst Characterization via *in situ* Raman and IR Spectroscopy....155
5.2.3 Common Terminal Surface Functionalities Observed on Supported Oxides....156
5.2.4 New Routes to Catalyst Synthesis....157
5.2.5 Brief Review of Heterogeneous Acid Catalysis Involving MO_X/ZrO_2^{Hyd} Catalysts....159
5.2.6 Characterization of MO_X/ZrO_2^{Cryst} versus MO_X/ZrO_2^{Hyd} Catalysts....161
5.3 Materials and Methods....161
5.3.1 Catalyst Synthesis....161
5.3.2 Catalyst Characterization....163
5.4 Results and Discussion....166
5.4.1 Thermogravimetric Analysis....166
5.4.2 BET Surface Area Analysis....170
5.4.3 X-Ray Diffraction Characterization....171
5.4.4 Complementary Analysis of Catalytic Reconstruction – TGA, N_2-Ads, XRD, *in situ* Raman, and LEIS....173
5.4.5 Characterization of the Surface Chemistry of Catalytic Oxides....178

5.5 Conclusions....183
5.6 References....184
Chapter 6. Conclusions and Future Outlook....189
6.1 Summary....189
6.2 Chapter Reviews and Future Research Opportunities....189
6.2.1 Synthesis of 3DOm Materials via Templating to Mitigate Transport Limitations....189
6.2.2 Surface Stabilization of Metastable Oxide Powders....190
6.2.3 Interfacial Stabilization of Metastable Oxide Films....192
6.2.4 Influence of Synthesis on the Stabilization of MO_X/ZrO_2^{Cryst} versus MO_X/ZrO_2^{Hyd} Catalysts....193
6.3 Conclusion....194
6.4 References....194
Curriculum Vitae....197

List of Tables

Table 1-1. Common methods of preparing oxides……11

Table 1-2. Compilation of melting points, Tammann, and Hüttig temperatures for various oxides……..25

Table 3-1. Compilation of melting points, Tammann, and Hüttig temperatures for relevant oxides……107

List of Figures

Figure 1-1. Multi-scale depiction of catalytic oxides for industrial applications……..……5

Figure 1-2. The stabilization of metastable oxides via surface modification……..……6

Figure 1-3. Schematic depicting the crystallization of zirconia when utilizing soft chemical processing versus traditional solid-state processing……..……9

Figure 1-4. Alkoxide hydrolysis, condensation, and the precipitation of zirconium hydroxide gels……..……14

Figure 1-5. Chelation can be used to limit the formation of oligomers in solution and delay the onset of hydrolysis and condensation……..……16

Figure 1-6. Syneresis exerts tremendous capillary forces during drying of hydroxide gels……..……17

Figure 1-7. Key processing parameters during synthesis and preparation of a catalytic supported oxide……..……18

Figure 1-8. Depiction of the regimes of porosity as defined by the International Union of Pure and Applied Chemistry (IUPAC) ……..……19

Figure 1-9. Effect of molecular transport limitations on the observed rate of a reaction……..20

Figure 1-10. A depiction of supported oxides under various loadings: isolated monomer species are present below monolayer coverage; polymers and extensive surface coverage is present near monolayer coverage; monolayers and surface crystals are present at loadings which exceed monolayer coverage……..……23

Figure 1-11. Depiction of the spreading of a surface species along the surface of an oxide….24

Figure 1-12. Depiction of bulk-to-surface atomic mobility……..……..25

Figure 1-13. Transmission electron microscope images demonstrating various degrees of ZrO_2 sintering after three hour calcinations at: **(a)** 500˚C; **(b)** 600˚C; **(c)** 900˚C; **(d)** 1000˚C.....26

Figure 1-14. Schematic representation of the variation in surface density and surface functionality due to support sintering when calcining a supported catalyst at: **(a)** low temperatures; **(b)** elevated temperatures; **(c)** extreme temperatures……..27

Figure 1-15. Phase transformation from a metastable oxide structure to a stable oxide crystal structure……..……..28

Figure 1-16. Methods of preventing transformation of a metastable oxide including: **(a)** bulk oxide doping; **(b)** surface modification; **(c)** and confinement of crystallite size……..31

Figure 1-17. Schematic depicting hard templating of a material via colloidal silica templating.....34

Figure 1-18. Model SiO_2/MO_x samples prepared via IWI for stabilization analysis.....35

Figure 1-19. Thin film deposition process.....37

Figure 1-20. Graphic depicting the traditional mono-oxo $O=WO_4$ and $O=MoO_4$ species and a possible structure of the new distorted mono-oxo species.....38

Figure 2-1. Generalized depiction of the 3DOm hard templating methodology utilized for the production of mesoporous materials.....55

Figure 2-2. The controlled hydrolysis and condensation reaction of TEOS during the formation of colloidal SiO_2 nanoparticles.....62

Figure 2-3. Figures demonstrating size control, morphology, and monodispersity of colloidal silica nanoparticles.....63

Figure 2-4. N_2 adsorption characterization of size tunable SiO_2-NP's ranging in diameter from 20-50nm.....63

Figure 2-5. N_2 adsorption characterization of sintered 50nm SiO_2 nanoparticles calcined at temperatures ranging from 500-1000˚C for three hours.....64

Figure 2-6. Characterization of the 3DOm carbon samples: **(a)** TEM image of a composite sample consisting of 50nm SiO_2 NP's and carbon after carbonization under flowing N_2 at 900˚C; **(b)** TEM image of a 3DOm carbon sample after removal of the template; **(c)** Nitrogen adsorption isotherms of 3DOm carbons prepared via coassembly; **(d)** BJH pore size distribution of 3DOm carbons. *Isotherm data and sample preparation was conducted in collaboration with Dr. Zheng Tian*.....65

Figure 2-7. Characterization during preparation of 3DOm TiO_2: **(a)** TEM image of a composite TiO_2/SiO_2 sample; **(b)** XRD comparison of TiO_2/SiO_2 composite samples calcined at 773˚C with an untemplated TiO_2 control powder calcined at 773˚C; **(c)** TEM image of a 3DOm TiO_2 sample after removal of the template; **(d)** N_2 adsorption isotherms and BJH pore size distribution (inset) collected from 3DOm TiO_2 samples. *Isotherm data and sample preparation was conducted in collaboration with Qianying Guo*.....67

Figure 2-8. Dynamic light scattering measurements of ZrO_2 precursor solutions.....68

Figure 2-9. Microsocpy images of various silica and zirconia materials calcined for three hours at 500˚C.....70

Figure 2-10. N_2 adsorption characterization of an untemplated ZrO_2 control sample and a 3DOm ZrO_2 sample prepared via hard templating with a ~30nm SiO_2 colloidal crystal template.....71

Figure 2-11. Unsupported zirconia dried from a $ZrOCl_2$ precursor solution and calcined to 500˚C……72

Figure 2-12. XRD of **(a)** a composite ZrO_2/SiO_2 prepared via incipient wetness with a $ZrOCl_2$ solution and a colloidal SiO_2 template; **(b)** a templated ZrO_2 sample after calcination and etching……73

Figure 2-13. XRD data of **(a)** ZrO_2/SiO_2 composite samples prepared via coassembly of a $ZrOCl_2$ solution and colloidal SiO_2 particles. The samples were calcined to 550˚C to induce crystallization of ZrO_2 and subsequently calcined to higher temperatures ranging from 600-1000˚C; **(b)** ZrO_2/SiO_2 prepared from a physical mixture of $ZrOH_x$ powder and 50nm colloidal SiO_2 powder. The samples were calcined to 550˚C to induce crystallization of the ZrO_2. The samples were then subsequently calcined to higher temperatures ranging from 600-1000˚C……74

Figure 2-14. Compiled XRD data calculating the volume fraction of the tetragonal phase of ZrO_2 in various ZrO_2 and ZrO_2/SiO_2 samples……75

Figure 2-15. ARM of the composite ZrO_2/SiO_2 and TiO_2/SiO_2 samples prepared via IWI reveal the large contact area of the metastable oxide with the SiO_2 template. **(a-b)** ZrO_2/SiO_2 prepared via IWI and calcined at 600˚C. **(c-d)** TiO_2/SiO_2 prepared via IWI and calcined at 773˚C……77

Figure 3-1. XRD characterization of commercial P25 titania and 5-15wt% SiO_2/TiO_2 samples after three hour calcination at temperatures ranging from 500-1000˚C. Panels include: **(a)** XRD characterization of commercial P25 titania; **(b)** XRD characterization of 5wt% SiO_2/TiO_2 samples; **(c)** XRD characterization of 15wt% SiO_2/TiO_2 samples; **(d)** calculated volume percentage of the metastable anatase phase……92

Figure 3-2. ARM images of highlighting the amorphous silica layer in SiO_2/TiO_2 supported samples prepared after three hour calcination. **(a)** 5wt% SiO_2/TiO_2 sample calcined at 1000˚C, inset: image of larger particle; **(b)** 15wt% SiO_2/TiO_2 sample calcined at 1000˚C, inset: image of larger particle; **(c)** 5wt% SiO_2/TiO_2 sample calcined at 500˚C, inset: image of larger particle; **(d)** 15wt% SiO_2/TiO_2 sample calcined at 500˚C, inset: image of larger particle……93

Figure 3-3. EDS mapping demonstrating the surface rich nature of the silicon in the 5wt% SiO_2/TiO_2 sample calcined at 1000˚C for three hours. Images depict: **(a)** ARM image of a crystal; **(b)** titanium K-alpha detection; **(c)** silicon K-alpha detection along the surface of the crystal; **(d)** oxygen K-alpha detection……94

Figure 3-4. XRD characterization of supported SiO_2/TiO_2 samples after prolonged (24 hour) calcination at elevated temperatures: **(a)** extended calcination at 700˚C; **(b)** extended calcination at 1000˚C……95

Figure 3-5. Nitrogen adsorption characterization of commercial titania and supported SiO_2/TiO_2 samples after three hour calcination at 500, 700, and 1000˚C: **(a)** N_2 isotherms of P25 titania, inset: calculated pore volume; **(b)** N_2 isotherms of 5wt% SiO_2/TiO_2 samples, inset:

calculated pore volume; **(c)** N_2 isotherms of 15wt% SiO_2/TiO_2 samples, inset: calculated pore volume; **(d)** comparison of BET surface area of the samples versus calcination temperature……..97

Figure 3-6. XRD characterization of commercial ZrO_2 and 5-15wt% SiO_2/ZrO_2 samples after three hour calcination at temperatures ranging from 500-1000˚C. Panels include: **(a)** XRD characterization of commercial ZrO_2; **(b)** XRD characterization of 5wt% SiO_2/ZrO_2 samples; **(c)** XRD characterization of 15wt% $SiO_2/ZriO_2$ samples; **(d)** calculated volume percentage of the metastable tetragonal phase……..98

Figure 3-7. XRD characterization of supported SiO_2/ZrO_2 samples after prolonged (24 hour) calcination at elevated temperatures: **(a)** extended calcination at 700˚C; **(b)** extended calcination at 1000˚C……..100

Figure 3-8. Nitrogen adsorption characterization of commercial Degussa ZrO_2 and supported SiO_2/ZrO_2 samples after three hour calcination at 500, 700, and 1000˚C: **(a)** N_2 isotherms of commercial ZrO_2, inset: calculated pore volume; **(b)** N_2 isotherms of 5% SiO_2/ZrO_2 samples, inset: pore volume; **(c)** N_2 isotherms of 15% SiO_2/ZrO_2 samples, inset: pore volume; **(d)** comparison of BET surface area of the samples versus calcination temperature……..101

Figure 3-9. XRD characterization of commercial zirconium hydroxide and 5-15wt% SiO_2/ZrO_2 samples after three hour calcination at temperatures ranging from 500-1000˚C. Panels include: **(a)** XRD characterization of ZrO_2 as prepared from a commercial hydroxide; **(b)** XRD characterization of 5wt% SiO_2/ZrO_2 samples; **(c)** XRD characterization of 15wt% $SiO_2/ZriO_2$ samples; **(d)** calculated volume percentage of the metastable tetragonal phase……..102

Figure 3-10. XRD characterization of hydroxide supported SiO_2/ZrO_2 samples after prolonged (24 hour) calcination at elevated temperatures: **(a)** 24 hour calcination at 700˚C; **(b)** 24 hour calcination at 1000˚C……..104

Figure 3-11. Nitrogen adsorption characterization of commercial zirconium hydroxide and supported SiO_2/ZrO_2 samples after three hour calcination at 500, 700, and 1000˚C: **(a)** N_2 isotherms of commercial ZrO_2 prepared from a commercial zirconium hydroxide, inset: calculated pore volume; **(b)** N_2 isotherms of 5wt% SiO_2/ZrO_2 samples, inset: pore volume; **(c)** N_2 isotherms of 15wt% SiO_2/ZrO_2 samples, inset: pore volume; **(d)** comparison of BET surface area of the samples versus calcination temperature……..105

Figure 4-1. Schematic depicting Si-Wafer oxidation, the convective deposition process, and resulting TiO_2 thin films……..121

Figure 4-2. Ellipsometery measurements on silicon wafers: **(a)** silicon oxide thickness after calcination at each temperature; **(b)** silicon oxide thickness after iterative calcinations at 800˚C. Each calcination utilized a 5˚C per minute ramp rate under atmospheric conditions and three hour dwell time……..123

Figure 4-3. SEM images of thin TiO_2 films prepared via convective deposition of 50 µL aliquots of solution and subsequent three hour calcination at 800˚C. Coating rates utilized are as follows: **(a-c)** 0.12 cm/min; **(d-f)** 1.2 cm/min……125

Figure 4-4. SEM images of striations and cracks in TiO_2 films prepared via deposition of 50 µL aliquots of solution and subsequent three hour calcination at 800˚C in air. Coating rates utilized: **(a)** 0.12 cm/min; **(b)** 1.2 cm/min; **(c)** additional view of a 0.12 cm/min film; **(d)** additional view of a 1.2 cm/min film……..127

Figure 4-5. XRD characterization of thin film titania samples prepared via convective deposition at different coating rates. **(a)** X-ray diffractogram; **(b)** Scherrer analysis of crystallite size. The films were prepared with a 50 µL aliquot of precursor solution and calcined at 800˚C for three hours……..128

Figure 4-6. XRD characterization of bulk titania powders and thin TiO_2 films. Films were prepared with a 20 µL aliquot of precursor solution and a coating speed of 1.2 centimeters per minute. Samples were drying and calcined at various temperatures **(a)** XRD of bulk TiO_2 control powder; **(b)** XRD of TiO_2 film diffractograms; **(c)** weighted average of phase composition; **(d)** calculated Scherrer crystallite size……..130

Figure 4-7. XRD and SEM characterization of a TiO_2 film after multiple iterative depositions with 20 µL of precursor solution and intermittent three hour calcinations at 800-1000˚C. **(a)** XRD of the film after intermittent deposition and 800˚C calcination; **(b)** XRD of the thin film after ten depositions and subsequent high temperature calcination 800-1000˚C; **(c)** image of a film after 5 successive depositions; **(d)** SEM image depicting the resulting layers of crystallites……..133

Figure 4-8. SEM images of TiO_2 films prepared via ten iterative deposition steps, cyclical calcination at 800˚C, followed by additional high temperature calcination at a temperature ranging from 800-1000˚C……..134

Figure 4.9. FIB lithography schematic for preparation of TiO_2 coupons……135

Figure 4-10. FIB lithography images during sample preparation. The sample consisted of a thin TiO_2 film prepared via deposition of a 20 µL aliquot of precursor solution at 1.2 cm/min and calcined for three hours at 800˚C. **(a)** preparation of coupon via ion milling; **(b)** the resulting coupon after milling; **(c)** *in situ* lift-out of the coupon; **(d) i**on milling process to thin the wafer; **(e)** the resulting coupon after lift out and milling; **(f)** a magnified image of the resulting coupon……..136

Figure 4-11. ARM characterization and EDS line scan of the thin titania film after FIB lithography: **(a)** representative profile image of the coupon; **(b)** an EDS line can of the corresponding ARM image. The film was prepared via convective deposition of 20 µL of solution at a coating rate of 1.2 centimeters per minute and subsequently calcined at 800˚C for three hours……..137

Figure 4-12. EDS maps of a titania film overlaid on the corresponding ARM image. The film was prepared via convective deposition of 20 µL of solution at a coating rate of 1.2 centimeters per minute and subsequently calcined at 800˚C for three hours……139

Figure 4-13. TEM images of small crystallites within the thick TiO_2 film. The sample was prepared via multiple convective depositions of 20 µL of solution at a coating rate of 1.2 centimeters per minute and intermittent calcination at 800˚C for three hours. A final calcination step was conducted at 950˚C……140

Figure 4-14. TEM images of a large crystallite within the thick TiO_2 film. The sample was prepared via multiple convective depositions of 20 µL of solution at a coating rate of 1.2 centimeters per minute and intermittent three hour calcinations at 800˚C. A final calcination step was conducted at 950˚C to induce phase change……142

Figure 4-15. EDS maps of the thick TiO_2 film overlaid on the corresponding ARM image. The film was prepared via multiple convective depositions of 20 µL of solution at a coating rate of 1.2 centimeters per minute and intermittent three hour calcinations at 800˚C. A final calcination step at 950˚C was conducted to induce phase change……143

Figure 4-16. Schematic depicting particle to particle coherency as a mechanism of phase stabilization……144

Figure 5-1. Spectrum of oxide materials……154

Figure 5-2. Generalized terminal surface species observed on supported oxides……157

Figure 5-3. Schematic depicting the rise of polymeric surface species and NPs due to sintering of a catalyst after calcination at: **(a)** low temperatures; **(b)** elevated temperatures; **(c)** extreme temperatures……161

Figure 5-4. TGA of commercial **(a)** crystalline ZrO_2 and **(b)** amorphous $Zr(OH)_x$ samples after heating in dry air from ambient conditions to 600˚C……168

Figure 5-5. TGA of supported catalyst precursors during calcination in dry air from ambient conditions to 600˚C. Samples include: **(a)** 5% MoO_3/ZrO_2^{cryst}; **(b)** 5% MoO_3/ZrO_2^{Hyd}; **(c)** 5% WO_3/ZrO_2^{cryst}; **(d)** 5% WO_3/ZrO_2^{Hyd}; **(e)** 5% CeO_2/ZrO_2^{Cryst}; **(f)** 5% CeO_2/ZrO_2^{Hyd}……169

Figure 5-6. BET surface areas for **(a)** MO_x/ZrO_2^{cryst} samples and **(b)** MO_x/ZrO_2^{Hyd} as derived from N_2 adsorption isotherms of the supported catalysts after calcination at 5˚C/min to temperatures ranging from 500-1000˚C with three hour dwell times……171

Figure 5-7. XRD of supported oxides prepared using the commercial crystalline ZrO_2 support after calcination at temperatures ranging from 500-1000˚C. Data includes: **(a)** XRD of commercial ZrO_2^{Cryst} samples; **(b)** XRD of 5wt% CeO_2/ZrO_2^{Cryst}; **(c)** XRD of 5wt% $WO_3/ZrO^{Cryst}{}_2$; **(d)** XRD of 5wt% MoO_3/ZrO_2^{Cryst}……172

Figure 5-8. XRD of supported oxides prepared using the commercial hydroxide support after calcination at temperatures ranging from 500-1000˚C. Data includes: **(a)** XRD of commercial hydroxide based ZrO_2^{Hyd} samples; **(b)** XRD of 5wt% CeO_2/ZrO_2^{Hyd}; **(c)** XRD of 5wt% WO_3/ZrO_2^{Hyd}; **(d)** XRD of 5wt% MoO_3/ZrO_2^{Hyd}……173

Figure 5-9. *In Situ* Raman characterization of dehydrated **(a)** 5wt% WO_3/ZrO_2^{Cryst} catalysts and **(b)** 5wt% WO_3/ZrO_2^{Hyd} catalysts after calcination at various temperatures. The samples were heated to 500˚C under flowing 10% O_2 in Ar for dehydration and subsequently cooled to 120˚C for collection of spectra……176

Figure 5-10. Integrated W/Zr count ratio collected during LEIS depth profiling of the **(a)** WO_3/ZrO_2^{Cryst} versus **(b)** WO_3/ZrO_2^{Hyd} catalysts after calcination at temperatures ranging from 500-1000˚C. *LEIS Experiments were performed by Dr. Henry S. Luftman*……177

Figure 5-11. *in situ* IR spectra of dehydrated 5wt% WO_3/ZrO_2^{Cryst} versus WO_3/ZrO_2^{Hyd} catalysts prepared by calcination at 500˚C. Spectra examines the **(a)** mono-oxo region and the **(b)** overtone region……178

Figure 5-12. *in situ* IR spectra of dehydrated 5wt% MoO_3/ZrO_2^{Cryst} versus MoO_3/ZrO_2^{Hyd} catalysts prepared by calcination at 500˚C. Spectra examines the **(a)** mono-oxo region and the **(b)** overtone region. The samples were heated to 500˚C and cooled to 120˚C to collect the spectra……179

Figure 5-13. *in situ* Raman characterization of the surface $O=WO_4$ and $O=MoO_4$ species after dehydration. Data examines the **(a)** $O=WO_4$ vibrations on 5wt% WO_3/ZrO_2^{Cryst} versus WO_3/ZrO_2^{Hyd} catalysts; **(b)** $O=MoO_4$ vibrations on 5wt% MoO_3/ZrO_2^{Cryst} versus MoO_3/ZrO_2^{Hyd} catalysts. The catalysts were prepared via calcination at 500˚C. The catalysts were heated to 500˚C and cooled to 120˚C to collect the spectra under dehydrated conditions……180

Figure 5-14. Graphic depicting the traditional mono-oxo $O=WO_4$ and $O=MoO_4$ terminal surface species and a possible interpretation of the distorted mono-oxo species which are hypothesized to reside within surface defects along the ZrO_2^{Hyd} support……180

Figure 5-15. *in situ* IR spectroscopy during desorption of NH_3 on: **(a-b)** 5wt% MO_X/ ZrO_2^{Cryst} catalysts versus **(c-d)** 5wt% MO_X/ ZrO_2^{Hyd} catalysts. The catalysts were dehydrated prior to NH_3 adsorption……181

Figure 5-16. *in situ* IR characterization of dehydrated WO_3/ZrO_2 catalysts prepared with various calcination temperatures (500, 700, and 1000˚C) during synthesis……183

Abstract

Metal oxides are utilized in diverse applications due to their ability to form single component crystals, multi-component mixed oxide systems, and supported oxide materials. During the preparation of a supported oxide catalyst, low surface energies enable increased atomic surface mobility and permit oxides to spread more readily than metals on the surface of an underlying support. These properties facilitate the synthesis of high surface area catalysts, allow widespread surface coverage, afford the development of monolayers, and offer synergetic catalytic effects between a surface oxide and its support. However, high surface mobility also makes an oxide susceptible to methods of reconfiguration including sintering, pore collapse, phase transformation, and catalytic deactivation at elevated temperatures. Therefore, it remains imperative to develop methods of promoting oxide stability when designing catalysts for operation at high temperatures.

This work provides a conceptual framework for the stabilization of metastable oxides via the incorporation of a second, supported oxide, along the surface of the metastable support. This concept of stabilization via surface modification is first demonstrated in experiments which utilize colloidal silica (SiO_2), in a hard templating approach, to enhance the surface area of zirconia (ZrO_2) and titania (TiO_2). The presence of residual SiO_2 in these templated materials is found to promote stabilization of the metastable phase (i.e. tetragonal ZrO_2 and anatase TiO_2). This method of surface stabilization is then validated as a general phenomenon through a series of studies investigating model supported oxides consisting of SiO_2/ZrO_2, SiO_2/TiO_2, and thin TiO_2 films deposited on silicon wafers. Finally, this technique is

utilized to engineer stabilized catalysts by depositing various surface oxides (e.g. molybdenum oxide, silica, tungsten oxide, and ceria) along crystalline and hydroxide supports.

The selection of an appropriate surface oxide is shown to ballast the underlying support while preserving its surface area and crystal structure at elevated temperatures (T > 500 $^{\circ}$C). This concept can be employed in the synthesis of traditional catalytic materials produced via incipient wetness impregnation (IWI) on either commercial crystalline supports or their hydroxide precursors; in doing so, one can simultaneously stabilize a catalyst and promote unique surface chemistry. A combination of mechanisms is established for oxide stabilization; a surface oxide can act to: increase the cohesive energy of the metastable oxide, limit strain on the supporting oxide, fill surface defects, induce localized surface doping, and generate distorted terminal surface species with unique acidity. The insight provided by this work allows a rational approach for stabilizing supported oxides, limits their high temperature reconstruction, and results in the design of robust catalysts with improved performance.

Chapter 1. Introduction

1.1 Motivation and Objectives

1.1.1 The Pursuit of Stable Catalysts

Modern society has been profoundly impacted by the study of catalysis, the innovative design of catalytic materials, and the application of catalysts for the commercial production of chemicals. A catalyst facilitates a reduction in the activation energy necessary for a given reaction pathway to occur and allows the selective control of molecular product formation. Catalysts are essential for the production of fuels, fertilizers, pharmaceuticals, plastics, and value added chemicals.[1] Additionally, catalysts are employed to reduce pollution in applications such as the selective catalytic reduction (SCR) of nitrogen oxides (NO_x), hydrodesulfurization (HDS) of crude oil, and vehicle emissions control.[2] It is estimated that over 90% of all chemicals are produced in catalytic processes and the resulting profits account for at least 20% of the United States gross domestic product.[3] The impact of catalysis on society compels the continued pursuit of fundamental scientific research on the synthesis, stability, surface chemistry, and performance of catalytic materials.

Many catalytic applications incorporate either bulk, supported,[4] or mixed oxides,[5] as catalysts and catalytic supports.[6] Supported oxides increase the surface area of the catalyst, provide a platform for reaction, and enhance catalytic activity through synergistic interactions between the surface oxide and the underlying support.[7] The characteristically low surface free energies of oxides allow them to be dispersed on a support more readily than metals; this property facilitates rapid atomic surface mobility during synthesis, the ability to form monolayers, and the development of complex terminal surface functionalities. The

combination of multiple oxides can be employed to tailor surface acidity and promote catalytic performance.[8] However, low surface energies and the resulting low temperature surface mobility of oxides also facilitate detrimental mechanisms of catalytic reconstruction such as sintering, pore collapse, phase change, and evolution of terminal surface groups. This becomes problematic as many catalytic processes operate at extreme temperatures (e.g. T > 500˚C) and present stability concerns that should be considered during design of a catalyst. As a consequence, the development of methods for oxide stabilization remains a fundamental pursuit in the field of catalysis.

The underlying thesis of this work is that metastable oxides can be preserved by the addition of a second, supported oxide along the surface of the metastable support; we introduce this mechanism of surface stabilization as a method of preserving crystallinity, structural integrity, surface area, and to produce unique terminal surface functionality. In this endeavor we seek to: understand the structural evolution of supported oxides during synthesis, determine new mechanisms for oxide stabilization, and ultimately improve catalytic performance through a systematic study of supported metal oxides. This knowledge will allow the controlled design of robust supported oxide materials that exhibit tailored stability, improved surface areas, and optimized surface chemistry and in doing so will solve one of today's grand catalytic challenges: the design and controlled synthesis of catalytic structures.[9]

Grand Challenges in Catalysis:

1. **"Understanding mechanisms and dynamics of catalyzed transformations"**
2. **"Design and controlled synthesis of catalytic structures"**

1.1.2 Approach to Catalyst Stabilization

In this thesis, we develop strategies aimed at the construction of supported oxides which exhibit the multi-scale stabilization of catalytic properties including surface area, porosity, crystalline phase, and surface functionality at elevated temperatures (See **Figure 1-1**). These stabilization techniques include the bottom-up synthesis of materials via hard templating with colloidal silica (See Chapter 2), incipient wetness impregnation (IWI) of model supported oxides (See Chapter 3), fundamental studies on the interfacial phenomenon between oxide films (See Chapter 4), and the comparison of mixed oxides prepared via IWI on crystalline supports versus hydroxide precursors (See Chapter 5).

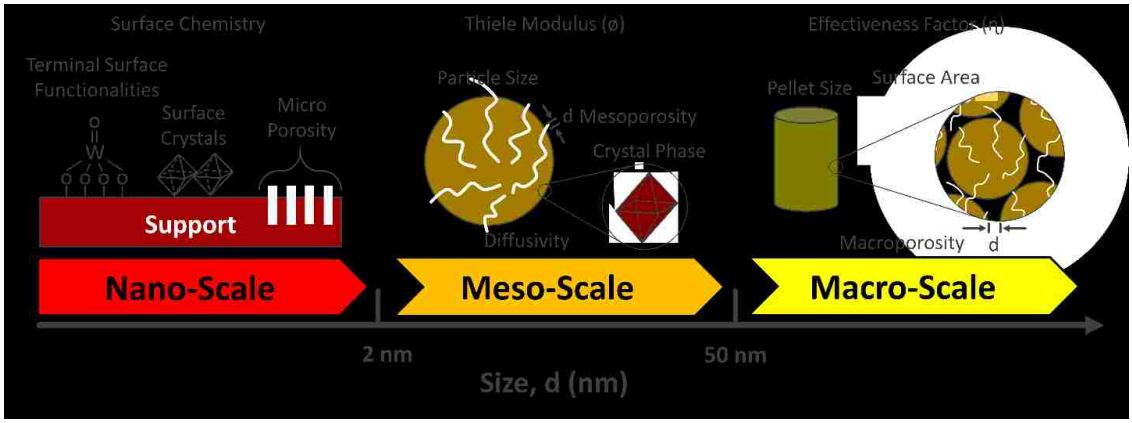

Figure 1-1. Multi-scale depiction of catalytic oxides for industrial applications.

Overview of Stabilization via Surface Modification

The central method of oxide stabilization examined in this work is a method of surface stabilization (See **Figure 1-2**). This technique utilizes a surface oxide to cover the surface of a metastable support and stabilize the surface. The surface oxide acts to increase the cohesive energy of the metastable oxide, limit strain on the supporting oxide, fill surface defects, induce localized surface doping, and can promote the formation of unique surface species. Examples of this method of stabilization have been observed in passing during the preparation of

supported oxide catalysts.[10,11] However, a thorough and systematic examination of this phenomenon has yet to be completed.

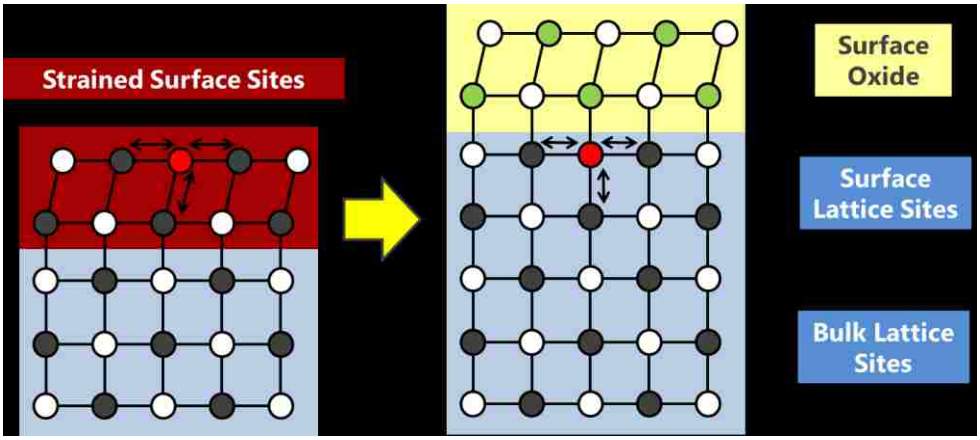

Figure 1-2. The stabilization of metastable oxides via surface modification.

Selection of Oxide Supports

A series of common catalytic supports including titania (TiO_2) and zirconia (ZrO_2) were selected for the systematic evaluation of catalytic stability throughout this thesis. These oxides were selected for their polymorphic crystalline nature and tendency to convert from metastable phases (i.e. anatase TiO_2 and tetragonal ZrO_2) to more stable phases (i.e. rutile TiO_2 and monoclinic ZrO_2) at elevated temperatures (T ~ 500˚C). Additionally, these materials present relatively moderate surface areas (S.A. ~ 50 m^2/g) when prepared via traditional synthetic techniques or when purchased from common commercial sources. The selection of these oxides offers a set of well-established material standards yet allows improvement of material properties including surface area, porosity, crystalline phase, and surface functionality.

Selection of Surface Oxides

A series of surface oxides were selected for stabilization analysis of the underlying supports. Surface oxides included molybdenum oxide (MoO_3), silica (SiO_2), tungsten oxide

(WO_3), and ceria (CeO_2). These materials were selected in part for their common use in the field of catalysis and catalytic performance. The supported oxides were prepared via common preparation techniques including incipient wetness and co-precipitation. Evolution of oxide stability is examined using a range of common characterization techniques after synthesis and calcination at temperatures ranging from 500 - 1000˚C. The work conducted in this thesis is shown to assist in the design of hierarchically porous materials, assist in the prevention of catalytic reconstruction, provide fundamental assessment of stabilization, and facilitate the characterization of new surface sites.

1.2 Background

In order to properly frame the work presented in this thesis, a systematic review of commercial metal oxide production is required. Here we provide a brief overview of the geology, ore refining, oxide chemistry, and industrial production involved during the manufacture of commercial metal oxides. We then provide a review of the common synthetic approaches utilized for the production of supported catalytic oxides. We conclude this background section by highlighting the dynamic physical properties that occur during the synthesis of supported catalytic oxides. For academic purposes we will emphasize the chemistry of silica, zirconia, and titania as these materials encompass the foundation of this thesis. As a result of this summary section, the reader will be presented with a fundamental background of oxide chemistry that will assist in the analysis of the techniques employed for oxide stabilization in the remaining chapters.

1.2.1 Conversion of Metallic Ores to Oxide Precursors

The major zirconium ores found within the earth are baddeleyite and zircon ($ZrSiO_4$), while common titanium ores consist of ilmenite ($FeTiO_3$) and rutile (TiO_2).[12] Ores are typically

processed by heating under chlorine gas to produce a metal chloride (MCl_4) and can be subsequently purified to metals through the Kroll process (See **Equation 1-1 and 1-2**). A range of oxide precursors can be synthesized by refluxing metal chlorides in solution with a desired solvent. Precursor examples include the formation of oxy-chlorides (e.g $ZrOCl_2$), nitrates (e.g. $ZrO(NO_3)_2$), sulfates (e.g. $TiO(SO_4)_2$), metal alkoxides (e.g. $Ti(OR)_4$), and hydroxides (e.g. $Ti(OH)_4$). The refluxing process removes the chlorine ligand and substitutes a solvent molecule in its place (e.g. **Equation 1-3**).[13,14] During this process the titanium and zirconium based molecules undergo a range of reactions consisting of solvent coordination, ligand substitution, ligand bridging, hydrolysis, condensation, gelation, and polymerization. The resulting chemicals offer a series of molecular precursors suitable for the production of commercial oxides.

$$Ore + Chlorine\ Gas \rightarrow TiCl_4 + Impurities \qquad \textbf{Equation 1-1}$$

$$2Mg + TiCl_4 \rightarrow 2MgCl_2 + Ti_{Solid} \quad (Kroll\ Process) \qquad \textbf{Equation 1-2}$$

$$TiCl_4 + 4ROH + 4NH_3 \rightarrow Ti(OR)_4 + 4NH_4Cl \quad (Alkoxide\ Preparation) \qquad \textbf{Equation 1-3}$$

1.2.2 Commercial Production of Oxides

Solid-State Reactions

The conventional methods used for the production of metals and metal oxides utilize solid-state reactions during the high temperature processing of fused solids and powders. During these processes a metal based powder is melted and quenched back to a solid in order to produce a material with a desired composition, phase, and shape. Historically, these techniques originate from the metallurgy field and are closely related to the early production techniques employed for the fabrication of metals.[15]

Solid-state processing allows the tune-ability of a range of macroscopic properties and features but the microscopic structure is ultimately limited by the quenching process. Quenching techniques typically produce highly dense materials with low surface areas, limited homogeneity, and limited phase composition. As an example, zirconia is known to exist in three phases (monoclinic, tetragonal, cubic); however, only the monoclinic phase is able to be quenched without the addition of dopants (See **Figure 1-3**). Thus, solid-state processing is generally undesirable for the production of most catalysts as the resulting fused catalysts do not afford large surface areas or adequate control of surface chemistry.[16,17]

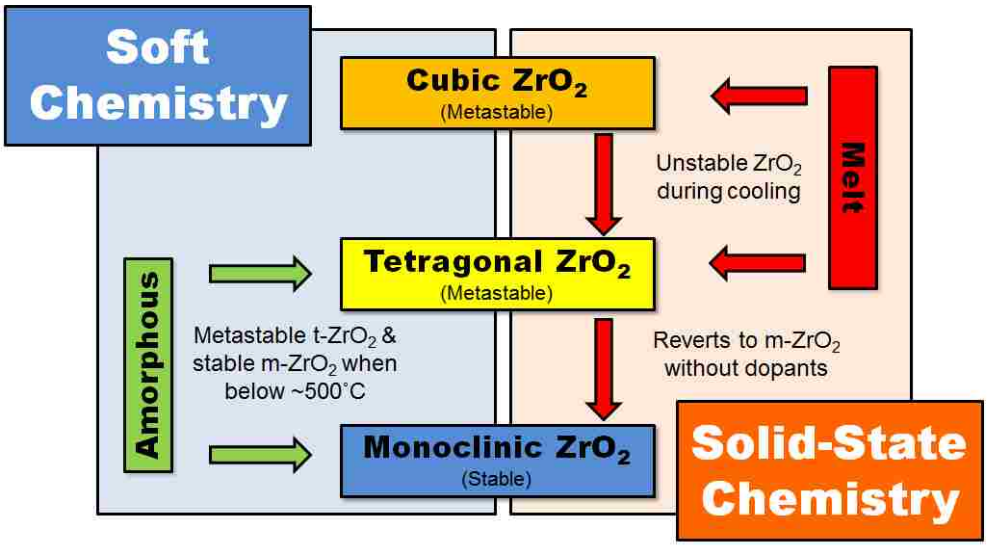

Figure 1-3. Schematic depicting the crystallization of zirconia when utilizing soft chemical processing versus traditional solid-state processing. Soft chemistry techniques can produce metastable t-ZrO_2 when calcined below 500 ˚C while traditional solid-state approaches only produce m-ZrO_2 upon quenching.

Commercial Aerosol Production of Bulk Oxides (Degussa P25, ZrO_2, Al_2O_3, Fumed SiO_2 etc.)

Bulk quantities of commercial oxides are often produced in high temperature industrial scale aerosol operations. These processes include gas-to-particle techniques such as flame hydrolysis and droplet-to-particle based spray pyrolysis operation; the former is used

for applications including paints, abrasives, adsorbents, and catalytic supports while the latter is utilized for applications requiring more dense materials such as ceramics and superconductors.[18] During aerosol processing via flame hydrolysis metal chlorides are vaporized, added to a hydrogen-oxygen gas mixture, pumped through a tubular furnace, and combusted to produce powdered pyrogenic oxides and hydrochloric acid. Cyclone vortex separation is then used to agglomerate the oxide crystallites and separate the acid byproduct.[19] Control of surface area, pore size, and phase composition of the resulting pyrogenic oxide can be achieved by altering the temperature and residence time within the furnace.

Flame hydrolysis affords in the formation of small aggregated crystallites with high surface areas and metastable crystal structures in comparison to traditional methods of high temperature solid-state processing. This technique is utilized for the commercial production of a range of fumed oxides including silica, titania, zirconia, and alumina. These materials are often utilized as model catalytic supports for academic research and are readily convertible to industrial catalytic pellets by the incorporation of a binding agent and processing via tableting or die extrusion. However, flame hydrolysis is not typically employed for the direct production of mixed and supported catalysts as it lacks precise control of surface chemistry; instead, wet chemistry methods including IWI and co-precipitation are utilized to more carefully tailor the surface chemistry and elemental loading of supported catalysts in order to meet the stringent needs of a given industrial application.

1.2.3 Soft Chemical Production of Oxides

Within the last century, researchers have explored a series of wet chemistry based synthetic techniques for the production of catalytic oxides. These techniques are often termed

"chemie douce" or "soft chemical" synthesis.[20] They are utilized to make materials with increased surface area, homogeneity in composition, tunable particle size, and engineered surface chemistry. They include IWI, precipitation, sol-gel synthesis, soft-templating, solvothermal, and hydrothermal synthesis (See **Table 1-1)**.[21] Chemie douce synthesis is now commonly employed for the production of catalysts, zeolites, adsorbents, and porous materials. They generally incorporate mild heating and moderate calcination temperatures (T < 500˚C) which allows the production of metastable crystal structures that are otherwise not attainable with traditional solid-state processes (See **Figure 1-3**). However, when calcined to higher temperatures these metastable phases often revert into more stable but often less desirable phases.

Table 1-1. Common methods of preparing oxides.

Technique	Description
Solid-State Processing	High temperature processing of bulk oxide materials
Aerosol Generation	Flame hydrolysis via pneumatic or ultrasonic atomization within a furnace
Precipitation	Precipitation of oxide precursors from solution
Incipient Wetness	Preparation of supported oxides via incremental precursor addition to a support
Sol-Gel Synthesis	Controlled hydrolysis and condensation of metal alkoxides in solution
Hydrothermal Synthesis	Controlled reaction of solutions at elevated temperature and pressure
CVD	Vapor phase deposition of a material
Emulsion Polymerization	Controlled synthesis of oxides by suspending droplets within a liquid medium

1.2.4 Incipient Wetness, Precipitation, and Co-precipitation

The most common synthetic methods of preparing supported and mixed catalytic oxides include incipient wetness impregnation, precipitation, and co-precipitation.[22] These processes allow control of various parameters including pH, elemental loading, concentration, rate of evaporation, syneresis, and calcination. This facilitates the production of oxides with moderate to high surface areas (S.A. ≥ 40 m^2/g) and adequately disperses catalytically active

components along the surface of the supporting oxide. Additionally, these methods offer reproducible methods of catalyst production from one batch to another.

Preparation via IWI involves a support often consisting of either a commercial oxide or hydroxide and a chemical precursor solution.[23] If the chemical precursor is susceptible to moisture the IWI process is conducted within a glove box under an inert Ar or N_2 atmosphere and the support is first dehydrated in order to drive off surface moisture. The precursor solution is prepared by measuring a volume of solvent equal to the pore volume of the supporting material. Next, a desired quantity of precursor, typically consisting of a metal nitrate (e.g $Ce(NO_3)_3$) or alkoxide (e.g. $Si(OEt)_4$) is added to the solvent. The precursor solution is then slowly added in small aliquots to the dried support and thoroughly mixed between each incremental addition. This procedure is continued until reaching the point of incipient wetness of the support. Capillary forces draw the precursor molecules into the interior of the supporting material and ensure adequate dispersion of the surface component. The amount of precursor used during IWI ultimately governs the resulting loading of the surface oxide. After thorough mixing, the sample is allowed to dry overnight at ambient temperatures, then dried further at ~120˚C to remove physisorbed surface moisture, and subsequently calcined to induce crystallization.[24] Additionally, calcination acts to spread and disperse a surface oxide along the exterior of the supporting oxide.[25] This phenomenon incorporates the same thermodynamic principles observed during the wetting of a solid by a liquid and acts to reduce the surface free energy of the catalyst by titrating the hydroxyl groups found on the surface of the support. As a result of this procedure, a supported oxide catalyst is prepared.

The precipitation and co-precipitation of suspended chemical precursors within a solvent offers a controlled method of producing mixed oxides with tailored chemical

properties.[26] Most transition metals are susceptible to hydrolysis and condensation in the presence of moisture and electronegative elements. During precipitation, a series of oxide precursors are suspended via mixing in a solvent at a controlled pH. Precipitation is then induced by addition of either an acidic (e.g. nitric acid) or basic (e.g. ammonium hydroxide) additive by means of dropwise addition. The chemical precursors nucleate through hydrolysis and condensation reactions resulting in the formation of hydroxide oligomers. Further condensation of the hydroxide results in the formation of large networks which precipitate from solution. Removal of excess solution via drying or decantation results in the formation of a hydroxide gel. Subsequent drying and calcination crystallizes the hydroxide and results in the formation of a mixed oxide catalyst.

1.2.5 Mechanisms of Synthetic Transformation during Preparation of Catalytic Materials

Having reviewed the common techniques utilized for the commercial production of catalytic precursors and supported catalysts we now highlight the chemistry and physical transformations that occur during the synthesis and high temperature reconstruction of a catalyst. Mechanisms of synthetic transformation include the hydrolysis and condensation of chemical precursors in solution, syneresis of hydroxide gels, and finally crystallization. Addition of a supporting oxide via IWI results in the formation of a catalytic structure with a given surface area, pore structure, phase, and surface chemistry. Further heating facilitates undesirable methods of atomic reconstruction including sintering, phase changes, doping, and surface reconfiguration. A review of these concepts will provide the necessary background used in the analysis and discussion of surface driven oxide stabilization as presented in the remaining chapters.

Hydrolysis and Condensation

Transition metals typically possess a partially unfilled *d*-orbital and are thus readily able to expand their coordination number and bond with multiple ligands in solution. This facilitates a complex arrangement of ligands and branched molecules which surround a central transition metal ion.[27] Variation of solution pH initiates rapid hydrolysis and condensation of most transition metal complexes and common catalytic oxide precursors (e.g. $ZrCl_4$, $ZrOCl_2$, $Zr(NO_3)_4$, $Zr(OPr)_4$ etc.).[28] Even under acidic conditions, titanium(IV) and zirconium(IV) aqueous solutions rapidly hydrolyze forming small complexed oligomers and tetramers.[29,30,31,32,33,34,35] Further addition of hydroxide ions results in the immediate precipitation of a gelatinous product (See **Figure 1-4**).[36,37] The resulting hydroxide gel can be collected and calcined for the formation of transition metal catalytic oxides.

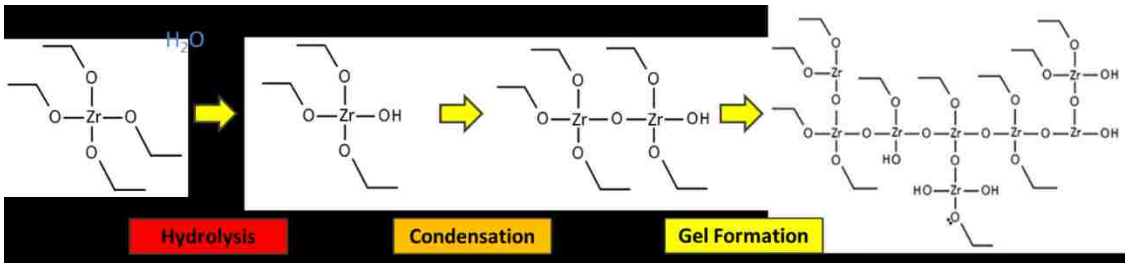

Figure 1-4. Alkoxide hydrolysis, condensation, and the precipitation of zirconium hydroxide gels.

Similarly, many silica based chemical precursors undergo comparable hydrolysis and condensation reactions in solution.[38] However, silicon does not possess as readily accessible valence *d*-orbitals as its transition metal counterparts and typically exhibits lower coordination numbers. The addition of silicon alkoxides such as tetraethyl orthosilicate (TEOS) to water results in the formation of gels, but at much slower rates than that observed in comparable titanium and zirconium alkoxides. As such, silicon alkoxides allow more controlled rates of hydrolysis and condensation and facilitate the synthesis of monodisperse spherical colloids.[39]

In chapter 3 the application of silica nano-colloids will be utilized in a hard templating process to promote the formation of mesoporous TiO_2 and ZrO_2 catalytic supports.

The susceptibility of common transition metal complexes to hydrolysis and condensation has encouraged researchers to employ chelation chemistry as a means of stabilizing oxide precursors in solution.[40] This area of research has culminated in a field known as sol-gel chemistry which seeks to control the formation of both colloids (sol's) and gels during oxide synthesis and drying.[41] Sol-gel chemistry often employs multi-dentate and highly branched ligands to control the rate of formation of solids and gels in solution.[42] These multi-dentate ligands bind to the central transition metal at multiple points within the complex, provide steric hindrance, and ultimately limit the metal's ability to oligomerize (See **Figure 1-5**).[43] Polydentate ligands typically incorporate multiple ketone groups, amines, alcohols, or ethers which can bind to the transition metal. Various chelating groups including acetylacetonate,[44,45] acetic acid,[46] alkanolamines,[47] and diols[48] have been utilized to control the rate of hydrolysis and condensation during the production of metal oxides.[49] *In chapter 4 a series of chelating ligands will be utilized to stabilize TiO_2 precursors in solution for the production of stabilized anatase thin films via convective deposition.*

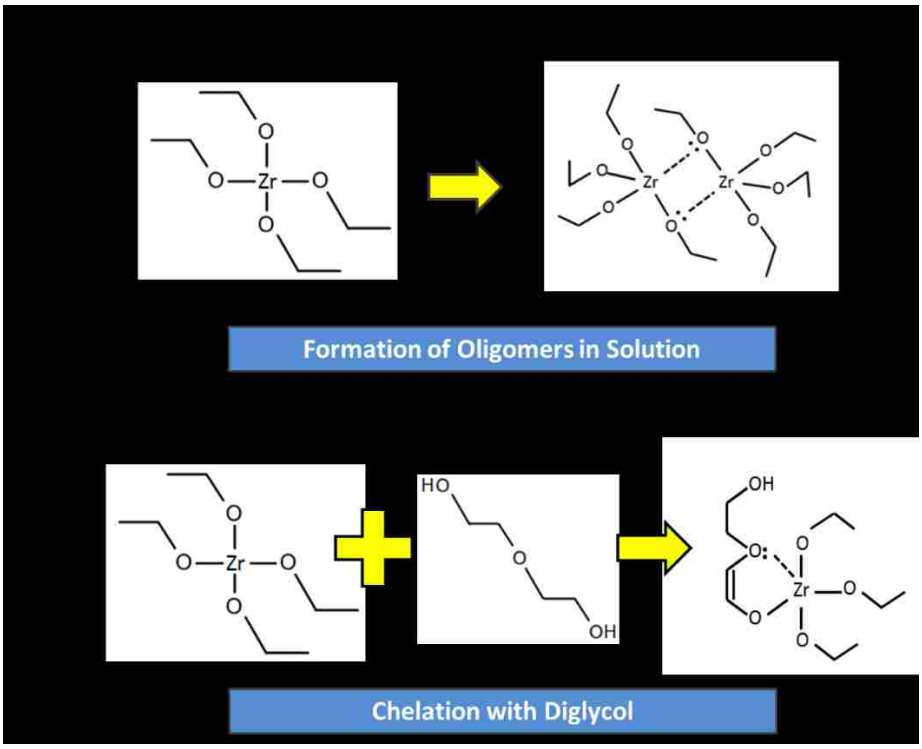

Figure 1-5. Chelation can be used to limit the formation of oligomers in solution and delay the onset of hydrolysis and condensation. Here common chemical structures formed in solution are presented including: **(a)** an oligomerized zirconium alkoxide; **(b)** a chelated alkoxide bound by a multi-dentate ligand comprised of diglycol.

Hydroxide Drying and Syneresis

After the hydroxide is precipitated from solution it is separated from the remaining solvent by either evaporation or decantation. The wet hydroxide gel is then dried and finally calcined to produce a porous oxide. Subsequent drying of the wet hydroxide results in gel dehydration and densification in a process known as syneresis. During syneresis the remaining pore fluid evaporates and generates strong internal capillary forces which collapse the gel upon itself (See **Figure 1-6**). This allows further condensation reactions, increases the density of the hydroxide, and governs the resulting structure of the oxide after calcination.

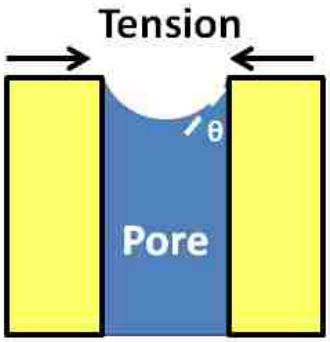

$$P_C = 2\gamma\cos(\theta)/r$$

P_C = CapillaryPressure
γ = SurfaceTension
r = PoreSize
θ = Contact angle

Figure 1-6. Syneresis exerts tremendous capillary forces during drying of hydroxide gels. These forces increase dramatically as the pore size is reduced and collapse the pore structure of the gel.

Syneresis effects such as drying temperature,[50] pore fluid,[51] solvent surface tension,[52] and pH all contribute to variations in gel structure during drying and the onset of calcination.[53] These physical effects have a large impact on the final morphology, phase composition, surface area, and pore volume of the resulting oxide.[54] Additionally, residual chelating groups act to scaffold the hydroxide during syneresis and effectively increase the surface area of the resulting oxide.[55,56] Thus, syneresis parameters offer a wide range of handles for tuning oxide structure and have been used for the formation of ultra-low density oxide based materials including xerogels, cryogels, and aerogels.[57]

Calcination, Crystallization, and Structure

After drying, the gel is calcined to induce oxide crystallinity. Syneresis effects will continue during calcination until the gel has been thoroughly dehydrated and crystallized. The resulting crystalline phase, surface area, pore structure, and elemental composition will be dependent upon the synthetic parameters utilized during each step of the process (See **Figure 1-7**). Subsequent addition of a supported oxide component can be performed via IWI and further calcination on either the oxide support or its hydroxide precursor. *In chapter 5 a systematic analysis will be conducted to compare the structural reconfiguration and resulting*

surface chemistry that occurs during preparation of supported oxides from hydroxide versus crystalline supports.

Figure 1-7. Key processing parameters during synthesis and preparation of a catalytic supported oxide.

After calcination of the hydroxide, the resulting crystalline oxide is typically comprised of small crystallites on the order of about 100 nm in size. These crystallites are aggregated together forming larger primary particles on the order of a few microns. The combination of crystallites and primary particles creates a tortuous network of pores ranging in size from a few nanometers to several microns. Pore size is classified based upon pore diameter and is divided into three regimes. These include micropores which consist of pores less than 2 nm in width, mesopores which range in size from 2-50 nm in diameter, and macropores which consist of pores greater than 50 nm (See **Figure 1-8**).[58]

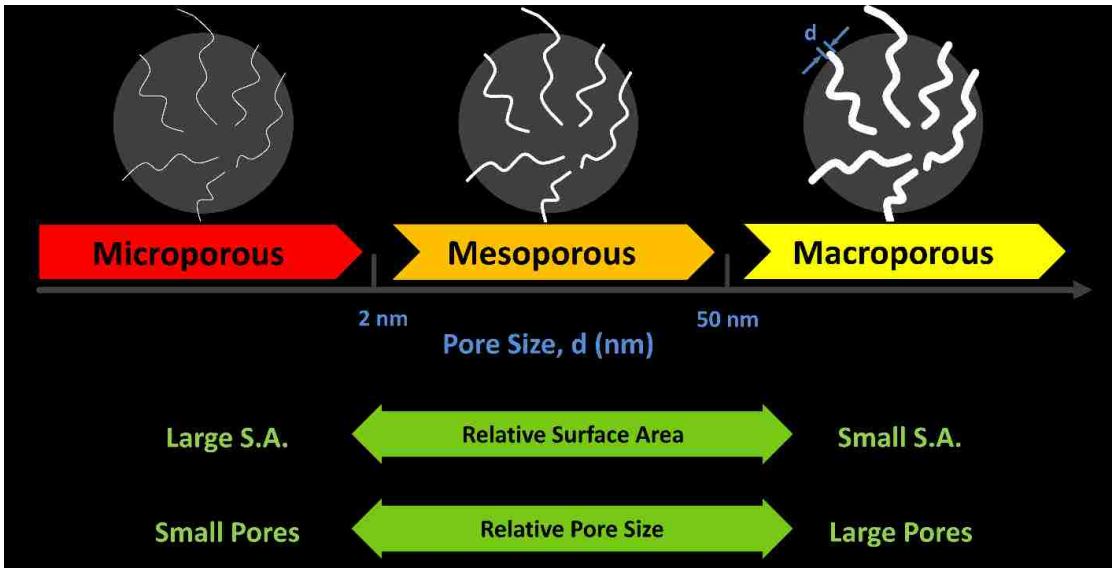

Figure 1-8. Depiction of the regimes of porosity as defined by the International Union of Pure and Applied Chemistry (IUPAC). A relative tradeoff exists between surface area and pore size.

This wide range of porosity enables oxides to exhibit large surface areas, offers a path for molecular transport into the interior of the catalyst, and provides an active surface for catalytic reactions to occur. However, a tradeoff exists between pore size and surface area. Microporous materials facilitate high surface areas but possess reduced pore diameters; this can lead to transport limitations and inadequate reaction along the interior of the catalyst.[59] On the other end of the spectrum macroporous materials offer large pores and comparatively high rates of transport but they exhibit low surface areas. Mesoporous materials offer a balance between surface area and pore size, allowing adequate rates of transport and relatively large surface areas.

1.2.6 Molecular Transport within Catalytic Materials

The actual rate of a reaction is ultimately dependent upon the molecular structure of active sites located on the surface of a catalyst. These surface functional groups govern the reaction rate as defined by the turnover frequency (TOF) of each site. However, in order for a

heterogeneous catalytic reaction to occur, a reactant species must leave the bulk convective flow of the reactor, diffuse through a stagnant layer surrounding the catalyst, and travel through a system of pores to reach the surface of the catalyst. The time required for diffusion is much greater than the time required for reaction; and thus the actual rate of a reaction can be greatly hindered by internal gradients within the pore structure of a catalyst.[60]

Concentration and temperature gradients arise due to mass transport limitations imposed upon the reactant and product species during transport within a catalytic particle.[61] These gradients arise due to the restricted flow of molecular species within the narrow and tortuous pore regions of a catalyst. Transport limitations can alter the experimentally obtained reaction rate, creating an observed or measured rate which differs from its true value. Thus, an effectiveness factor (η) is often utilized to quantify the effect of internal gradients on the true rate of reaction (See **Equation 1-4**).[62]

$$\eta = \frac{\text{Observed Rate of Reaction}}{\text{Rate with no Internal Gradients}} \qquad \textbf{Equation 1-4}$$

The effectiveness factor is obtained by modeling the geometric and characteristic length scales of a catalytic particle to account for internal variations in temperature and concentration. The Thiele modulus is used to account for the internal diffusivity of chemical components within a catalytic particle with a given geometry.[63] **Equation 1-5** lists the generalized Thiele modulus for an *n*th-order reaction of chemical species "*A*" within an isothermal catalytic particle.[64] By definition, the Thiele modulus accounts for the characteristic dimension of the particle (l_c, See **Equation 1-6**), the effective diffusivity ($D_{effective}$), and the catalytic rate constant (k); furthermore, the Thiele modulus is directly related to the effectiveness constant as given by **Equation 1-7**.

$$\emptyset = l_c \sqrt{\frac{(n+1)\mathrm{k}C_A^{n-1}}{2D_{effective}}} \qquad \textbf{Equation 1-5}$$

$$l_c = \frac{\text{Volume of the Catalytic Paritcle}}{Outer\ Surface\ Area\ of\ the\ Particle} \qquad \textbf{Equation 1-6}$$

$$\eta = \tanh(\emptyset)\ /\emptyset \qquad \textbf{Equation 1-7}$$

A plot of the effectiveness factor versus the Thiele modulus is presented in **Figure 1-10a**. For ø<1, the catalytic reaction rate is limited by the material properties of the catalyst; for ø>1 the catalytic reaction is limited by internal mechanisms of diffusion.[65] In order to optimize the effectiveness of a catalyst, one must seek to reduce internal barriers of diffusion such that the entire catalytic particle is utilized. The effective diffusivity is defined by **Equation 1-8** and is dependent upon the porosity of the catalyst (ε), the tortuosity of the pores (τ), and the theoretical diffusivity of a chemical species within straight, cylindrical pores whereby pore diameter is given by d_{pore}. Thus, one can increase diffusion and prevent transport limitations by increasing the average pore size of a catalyst and reducing its tortuosity.

$$D_{eff} = D_A\left(d_{pore}\right)\varepsilon/\tau \qquad \textbf{Equation 1-8}$$

There are three primary methods of diffusion within the pore structure of a catalyst; these include bulk molecular diffusion, Knudsen diffusion, and configurational diffusion (See **Figure 1-9**).[66] As the pore diameter is reduced to sizes approaching that of the reactant molecules, the internal molecular diffusivity is dramatically reduced as molecules begin interacting with both the pore structure of the catalyst and neighboring molecules more frequently.[67] By increasing the pore size of a catalyst through synthetic approaches one can limit the effect of internal diffusion on the reaction rate and promote molecular flux within a catalytic particle.

Furthermore, reconstructive catalytic effects such as sintering are highly problematic for molecular transport within a catalytic particle as they reduce can reduce molecular diffusivity and alter the rate of reaction. *In chapter 2 a hard templating technique will be employed to rationally synthesize highly ordered catalytic supports with tunable pore size on the meso-scale.*

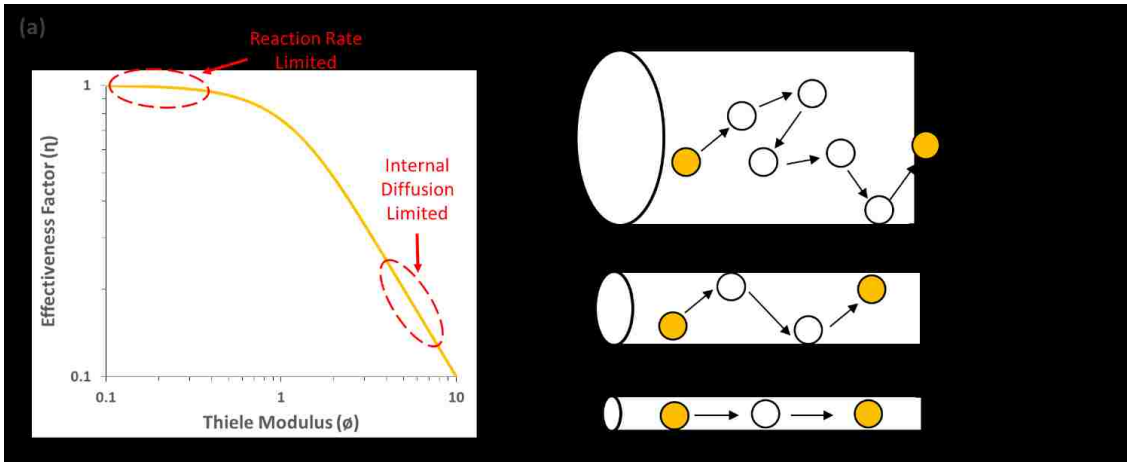

Figure 1-9. Effect of molecular transport limitations on the observed rate of a reaction. **(a)** A logarithmic graph depicting the effectiveness factor (η) versus the generalized Thiele modulus (ø); **(b)** depiction of bulk molecular diffusion; **(c)** depiction of Knudsen based diffusion; **(d)** depiction of configurational based diffusion.

1.2.7 Supported Oxide Surface Functionalities

After IWI and calcination of the supported oxide a range of complex terminal surface functionalities are created. Metal ions with high oxidation states (i.e. oxidation states > M^{+4}) are able to exhibit high coordination numbers and terminate with mono-oxo or poly-oxo surface functionalities (i.e. M=O). This is common for *d*-block transition metals with high valencies such as vanadium, molybdenum, and tungsten. As such, transition metals with high oxidation states provide suitable surface candidates in supported oxide catalysts. [68] Conversely, metal ions with low oxidation states (i.e. oxidation states ≤ M^{+4}) present lower coordination numbers and normally terminate with hydroxyl (i.e. M-OH) and bridging surface

functionalities (i.e. M-O-M). These materials offer suitable candidate supporting oxides (e.g. SiO_2, Al_2O_3, TiO_2, ZrO_2) and often exhibit both Lewis and Brönsted acidity.[69]

Depending on the loading of the surface oxide, different surface chemistries develop. At low loadings, small monomeric mono-oxo and dioxo species exist on the surface (See **Figure 1-10**).[4] As the surface loading is increased, these monomeric species dimerize and polymerize until the surface is coated with a monolayer of the surface oxide. At even higher loadings, the supported oxide begins to form surface crystals and nanoparticles along the surface of the support.[70,71,72] This diverse range of terminal surface species offers a wide range of catalytically active surface sites and are responsible for the effectiveness of supported oxide catalysts.

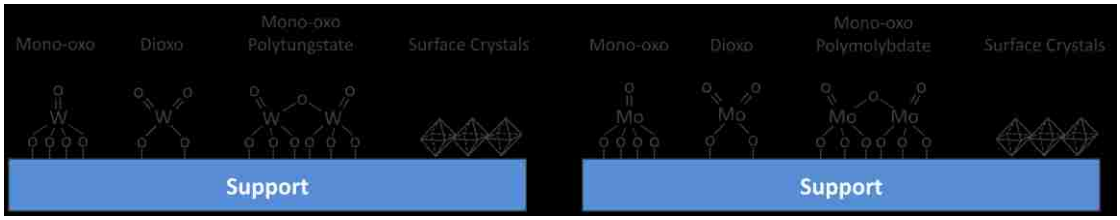

Figure 1-10. A depiction of supported oxides under various loadings: isolated monomer species are present below monolayer coverage; polymers and extensive surface coverage is present near monolayer coverage; monolayers and surface crystals are present at loadings which exceed monolayer coverage.

1.2.8 Mechanisms of Catalytic Reconstruction and Deactivation

Having reviewed the general concepts involved in the production and synthesis of catalytic materials and supported oxides we will now highlight the mechanisms of high temperature reconstruction and deactivation. Catalyst deactivation typically occurs due to poisoning and reconstruction.[73] Examples of reconstruction include: sintering, pore collapse, phase transformation, and leaching. Sintering ensues at elevated temperatures and causes small oxide features to fuse into much larger particles. Phase changes occur during heating or cooling as metastable oxide phases (e.g. tetragonal zirconia and anatase titania[74]) attempt to

reduce their surface and bulk free energies. Additionally, the presence of moisture can leach surface atoms from the oxide and reduce activity.[75] These combined effects result in the collapse of pores, the loss of surface area, and deactivation of the catalyst.

Surface Reconfiguration and Sintering

The onset of catalytic reconfiguration is initiated by a series of surface transformations which facilitate sintering and rearrangement of a catalyst.[76] Atomic surface mobility typically initiates at temperatures ranging from 500-700˚C for most supported oxide systems and is governed by two primary factors; these include the bulk melting point of the material and its crystal size. Surface atoms are bound to a crystal with less cohesive energy than their bulk counterparts. Additionally, surface atoms are typically less coordinated to the crystal than atoms well within the bulk crystal structure. This allows surface atoms to detach from the support, become mobile, and redeposit at another location within the catalytic framework (See **Figure 1-11**). This concept of surface spreading and wetting is the same physical phenomenon which is utilized to disperse the surface oxide along the supporting oxide when preparing a supported catalyst via IWI. However, this phenomenon becomes problematic during high temperature operation as catalysts are only active along their outer surface and any resulting surface reconstruction will rapidly deteriorate catalytic performance.

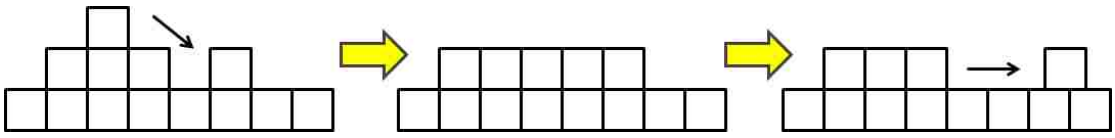

Figure 1-11. Depiction of the spreading of a surface species along the surface of an oxide.

The ability of a surface atom to become mobile is related to its surface free energy as measured by the bulk melting point of an oxide. Surface mobility initiates at the characteristic Hüttig and Tammann temperatures of a bulk material (See **Equations 1-9 and 1-10**).[77] The

Hüttig temperature is defined as the point at which surface atoms become mobile and can either spread or disperse. The Tammann temperature is the temperature at which atoms obtain enough energy to become mobile, spread along the surface, and even transfer from the bulk to the surface of the oxide (See **Figure 1-12**). Thus, atoms in oxides with high surface free energies and correspondingly high Tammann temperatures are less mobile at elevated temperatures and as a result are more resistant to sintering. A list of Hüttig and Tammann temperatures for various oxides is presented in **Table 1-2**.

$$T_{Huttig} \sim {T_{melt}^{bulk}}/{3} \qquad \textbf{Equation 1-9}$$

$$T_{Tammann} \sim {T_{melt}^{bulk}}/{2} \qquad \textbf{Equation 1-10}$$

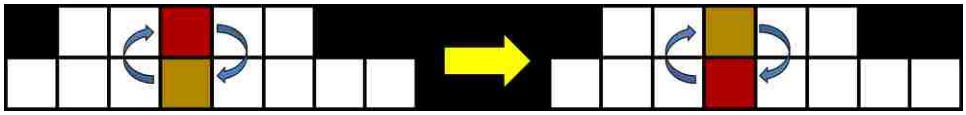

Figure 1-12. Depiction of bulk-to-surface atomic mobility.

Table 1-2. Compilation of melting points, Tammann, and Hüttig temperatures for various oxides.[78, 79]

Oxide [Source]	Melting Point (˚C)	Tammann Temperature (˚C)	Hüttig Temperature (˚C)
V_2O_5 [78]	670	199	---
MoO_3 [78]	795	261	---
WO_3 [78]	1472	599	~491
SiO_2 [25]	1712	719	~570
TiO_2 [79]	1843	922	~614
Al_2O_3 [79]	2054	890	~685
ZrO_2 [79]	2710	1220	~903
MgO [78]	2851	1263	~950

Atoms within small crystallites are bound with less cohesive energy than those found in much larger crystals. As a result, nano-scale crystallites (d < 50 nm) facilitate surface mobility, destabilize and even melt at lower temperatures than corresponding macroscopic crystals.[80] Once mobile, surface atoms often redeposit at more energy favorable locations along the surface of the oxide network and ultimately reduce the surface energy of the

supported oxide. This process is known as sintering and results in the loss of surface area and porosity of the catalyst.[81] Additionally, sintering creates a coarsening effect where atoms in the smallest crystallites feed the growth of larger crystals and fill in the necking regions between the crystallites (See **Figure 1-13**).

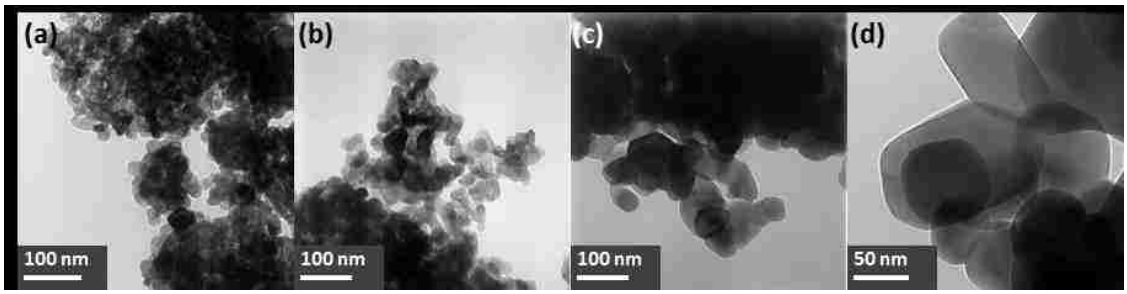

Figure 1-13. Transmission electron microscope images demonstrating various degrees of ZrO_2 sintering after three hour calcinations at: **(a)** 500˚C; **(b)** 600˚C; **(c)** 900˚C; **(d)** 1000˚C. The small crystallites coarsen and feed the growth of the larger crystals when calcined at high temperatures.

The combination of surface reconfiguration and sintering greatly alters the surface functionality of a catalyst when calcining supported oxides to extreme temperatures (T>700˚C). A reduction in surface area of the underlying support causes an increase in surface density of the supported oxide.[82] Supported oxides with low surface loadings present highly dispersed surface species when calcined at low temperatures. At higher calcination temperatures the surface oxide becomes less dispersed as the surface area of the underlying support is reduced. Further increases in calcination temperature collapses the support and results in the formation of a close-packed surface monolayer and the development of surface crystallites (See **Figure 1-14**). Thus, high temperature calcination of a supported catalyst results in a relative increase in surface density of the supported species and a consequential alteration of terminal surface functionalities.

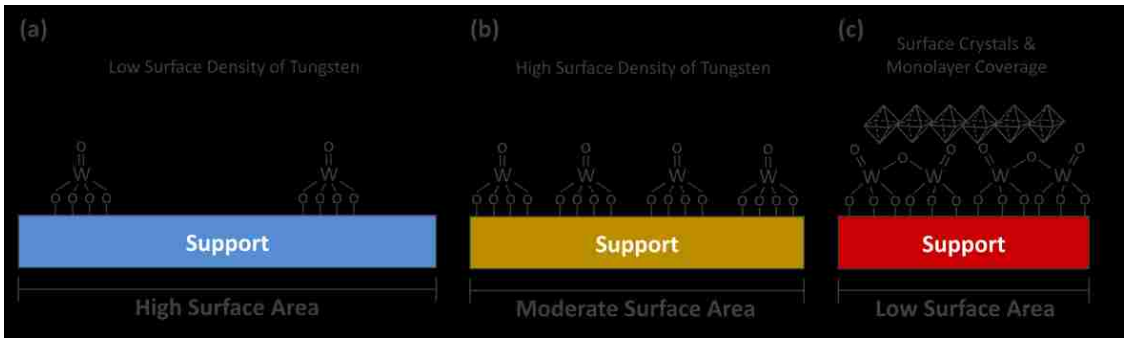

Figure 1-14. Schematic representation of the variation in surface density and surface functionality due to support sintering when calcining a supported catalyst at: **(a)** low temperatures; **(b)** elevated temperatures; **(c)** extreme temperatures.

Phase Transformation

Solid-to-solid phase transformation occurs when a metastable oxide crystal converts to a more stable polymorph. This can be problematic for catalytic materials as this conversion often results in a large reduction in density and can generate macroscopic cracks within a ceramic catalytic monolith.[83] These problems can be exacerbated in processes which involve cyclical periods of heating and cooling such as that observed in catalytic converters and fuel cells. Thus, it is often important to engineer catalytic materials which are resistant to phase deterioration over a prolonged lifetime of cyclical operation.

Phase transformation often nucleates along the surface of a material at heterogeneous points such as oxygen vacancies, surface defects, impurities, and grain boundaries (See **Figure 1-15**).[84] Propagation of the stabile phase is then facilitated by both diffusion[85] and diffusionless[86] mechanisms of conversion. During diffusion based transformation, atomic surface mobility facilitates not only the growth of larger crystallites, but also the growth of undesirable oxide phases. As surface atoms on metastable crystallites become mobile they migrate to neighboring crystallites and feed the growth of heterogeneous phase nuclei.

After development of a stable surface nuclei, the new crystalline phase can rapidly propagate into the bulk of a crystal via diffusionless mechanisms of transformation.[87] This mechanism typically occurs during cooling as internal atoms seek to lower their bulk free energy by transforming to the more stable crystal structure. [88] This process can be extremely rapid as displacive lattice deformations propagate the new phase throughout the crystal via the cooperative movement of atoms. This mechanism is readily observed in large unstabilized oxide monoliths during the development of cracks and twined crystal grains in a process termed martensitic transformation.[89] Furthermore, displacive lattice transformation has been observed not only in large macroscopic crystals but also in oxide nanocrystals.[90]

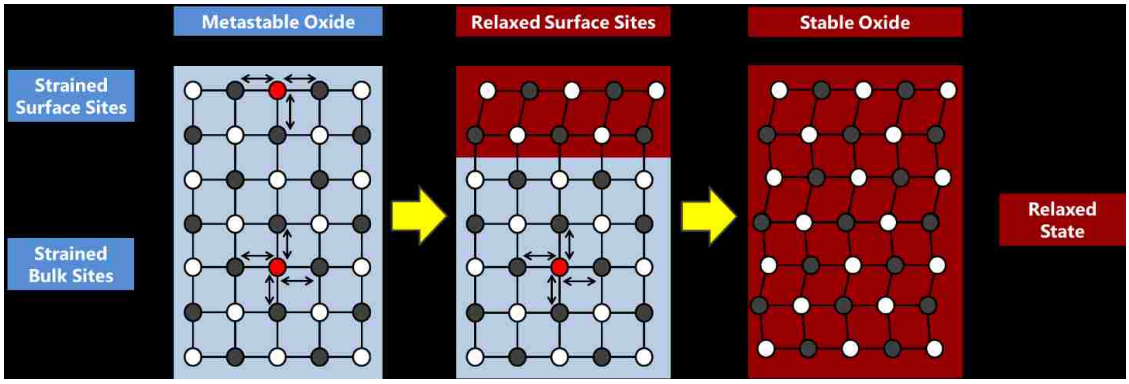

Figure 1-15. Phase transformation from a metastable oxide structure to a stable oxide crystal structure.

The transformation from tetragonal to monoclinic zirconia has been observed to occur via a martensitic phase transformation where surface strains cause atoms to shift their lattice orientation near the surface of the oxide.[91] After nucleation, the monoclinic phase then propagates into to the interior of the crystal.[92] This theory of external to internal phase evolution has been supported by a series of characterization techniques with varying degrees of surface sensitivity (i.e. UV-Raman and Vis-Raman) and comparing these results with bulk sensitive techniques (i.e. X-ray diffraction).[93]

Current Methods of Oxide Stabilization

The most common method of preventing the t-ZrO_2 to m-ZrO_2 phase transformation from occurring is to dope small amounts of an impurity into the bulk region of the crystal.[94] This relieves internal strains and prevents phase transformation from spreading to the interior of the crystal (See **Figure 1-16a**). Solid-oxide fuel cells utilize this concept by doping t-ZrO_2 with ~8 mol% of yittria to form yittria-stabilized zirconia (YSZ).[95] YSZ promotes O^{2-} conductivity within the cell and preserves the stability of the electrolyte; this allows operation of the fuel cell at temperatures ranging from 700-1000˚C for extended periods of time during cyclical operation and without significant performance loss.

Surface stabilization of tetragonal zirconia has been briefly observed when preparing tungstated (WO_3/ZrO_2)[96] and sulfated zirconia (SO_4^{2-}/ZrO_2).[97] The tungsten oxide and sulfate groups in these systems actively cover the surface of the zirconia and inhibit the t-ZrO_2 to m-ZrO_2 phase transformation from occurring. This phase stabilization has been reported to occur at temperatures up to 700˚C and in doing so, preserves the surface area of the system.[98] These phenomena suggest that phase transformation begins along the surface of an oxide and can be prevented by modifying the surface with a second, supported oxide (See **Figure 1-16b**). Conversely, a supported oxide with a low Tammann temperature (i.e. V_2O_5) has been reported to increase sintering and reduce surface area during calcination.[99] Therefore, with the use of an appropriate surface oxide one can either promote or reduce catalytic restructuring.

Another widely discussed method of stabilization[100] suggests that metastable oxide phases can be preserved if the oxide is confined below a critical size (See **Figure 1-16c**).[101] This theory has been applied to explain the existence of various metastable oxide phases (e.g. tetragonal zirconia[102] and anatase titania[103]) at low temperatures.[104] By limiting the crystallite

size below a critical value, it is believed that the surface and bulk free energies of the crystal allow an otherwise unstable phase to exist at temperatures where the phase is not traditionally thermodynamically stable (See **Equation 1-11**). It is reported that as the oxide is calcined to elevated temperatures, the crystallites begin to sinter until the critical crystallite size has been exceeded; this subsequently causes transformation into a more stable phase (e.g. monoclinic zirconia[105] and rutile titania[106]).

$$r_c = \frac{-3(\sigma_1 - \sigma_2)}{(\psi_1 - \psi_2)} \qquad \textbf{Equation 1-11}$$

r_c = Critical crystallite size
ψ_i =Free energy per unit volume of phase i
σ_i = Surface free energy of phase i

This mechanism of size-stabilization assumes spherical crystals with no impurities; a task which is difficult to engineer in practice. Furthermore, this theory assumes that the surface is a truncation of the bulk crystal structure and does not account for the possibility of an amorphous or oxidized layer near the surface. Nevertheless, this theory provides insight into the thermodynamic concepts that are involved in lattice strain and phase transformation of a metastable oxide.

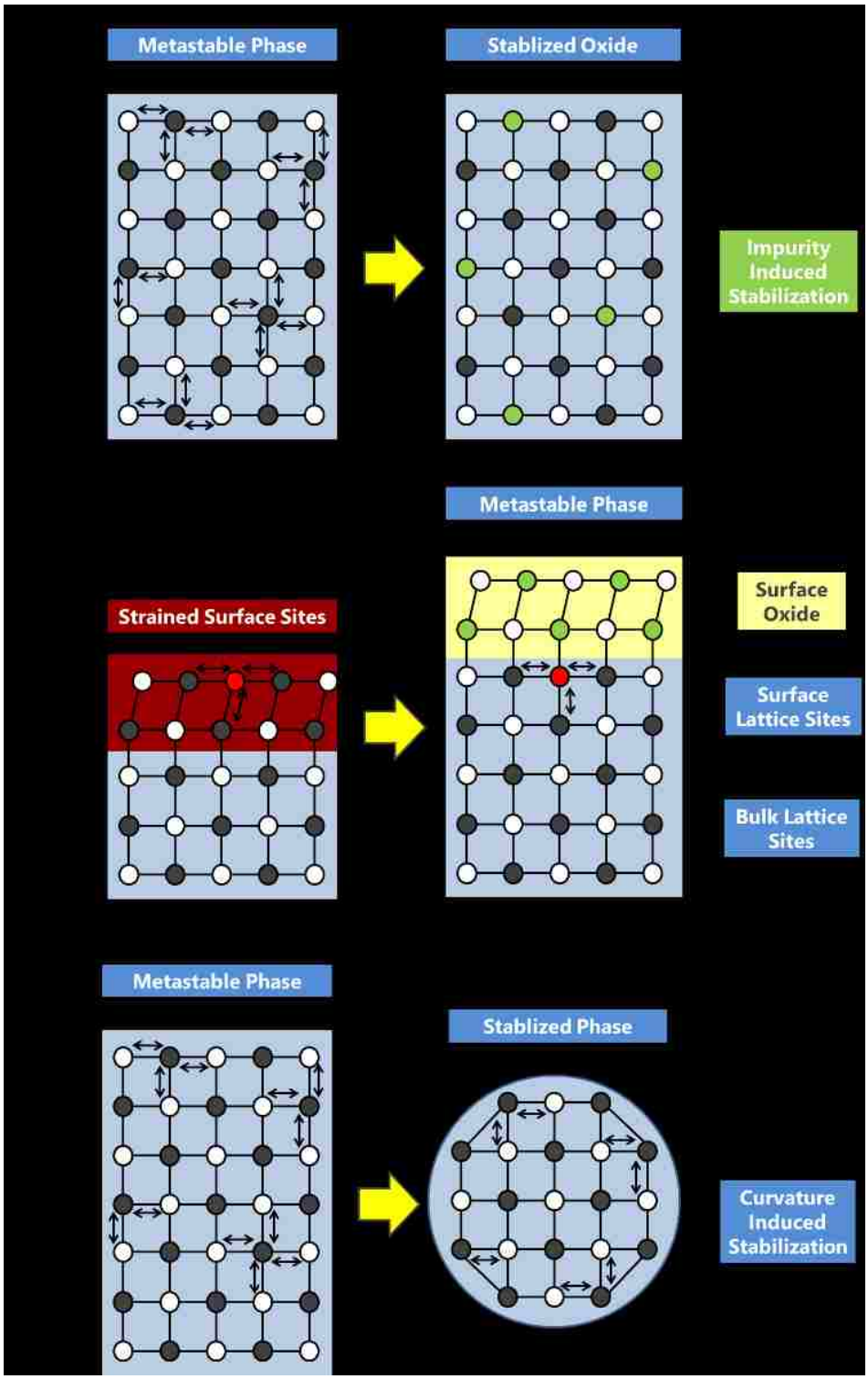

Figure 1-16. Methods of preventing transformation of a metastable oxide including: **(a)** bulk oxide doping; **(b)** surface modification; **(c)** and confinement of crystallite size.

1.2.9 Summary of Background Section

In summary of this review section, many structural methods of catalytic reconfiguration occur during the synthesis and high temperature application of a supported oxide catalyst. We have shown that common methods of synthesizing catalysts offer a wide range of tune-ability in their final structure. Precursor and ligand selection can be utilized to promote scaffolding of a hydroxide during synthesis. Subsequent control of syneresis conditions during drying and calcination can be utilized to retain surface area and pore size of the hydroxide during conversion to a crystalline oxide. Deposition of high valence transition metal precursors via IWI can promote a diverse range of surface chemistry along the surface of a support. However, we have also shown that oxides are susceptible to reconstruction at elevated temperatures due to atomic surface mobility. The low surface energies which facilitate the development of small crystallites, high surface areas, and unique terminal surface functionalities in supported oxides also makes them unstable and susceptible to reconfiguration at elevated temperatures. Atomic surface mobility causes supported oxides to sinter, change phase, and lose catalytically active surface functionality.

Despite the potential for reconstruction, supported oxides are desired for operation at high temperatures. They are currently employed in diverse catalytic applications and under various operating environments including: steam reforming with nickel supported on Al_2O_3 or $AlMgO_4$ spinels,[3] methanol synthesis from H_2, CO_2 and CO over Cu/ZnO catalysts,[107] and the use of tungstated[108] or sulfated zirconia[109] for the skeletal isomerization of alkanes.[110] Oxide catalysts have also established their importance for pollution abatement. Oxides such as zirconia, ceria, and gamma alumina (γ-Al_2O_3) are incorporated in automotive catalysts for the reduction of CO; while oxides such as titania, vanadia, and tungsten oxide are essential for the

selective catalytic reduction of NO_x into N_2.[111] These examples demonstrate the versatility of oxides; yet their methods of stabilization at high temperatures are still not fully understood.

Several methods of oxide stabilization have been experimentally observed in various literature sources. Reconstruction can be mitigated by bulk crystal doping, the incorporation of a surface oxide, and by the size confinement of crystallites. The mechanism of surface modification has shown promise for its ability to promote unique surface functionality, prevent sintering, and inhibit structural phase changes; however, this method of oxide stabilization has not yet been thoroughly investigated. **In this thesis** we demonstrate how a surface oxide can be used to stabilize a metastable catalytic oxide support by decreasing the surface energy of the system, reducing surface strains, and by more fully coordinating the surface of the metastable oxide. In the next section we summarize the chapters contained in this thesis and the work contained therein.

1.3 Chapter Outlines

Chapter 2 Overview

In the next chapter we investigate the synthetic design of three dimensionally ordered mesoporous catalytic supports (3DOm-supports) including carbon, titania, and zirconia. A bottom-up hard templating methodology is utilized for the controlled formation of size tunable mesopores and the promotion of surface area in these materials. Generation of mesoporosity is accomplished by the synthesis of a sacrificial colloidal silica template, subsequent infiltration of the template with a chemical precursor, and removal of the SiO_2 template (See **Figure 1-17**).

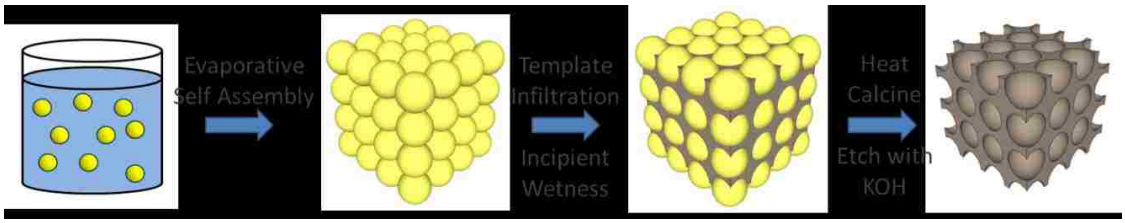

Figure 1-17. Schematic depicting hard templating of a material via colloidal silica templating.

Template synthesis consists of a modified Stöber process.[112] L-lysine is utilized as a buffer to control the rates of hydrolysis and condensation of tetraethyl orthosilicate (TEOS), a common silica precursor.[113] Rapid mixing of the sol-gel based solution allows formation of monodisperse colloidal silica nanoparticles (SiO_2-NPs) ranging in size from 20-50 nm. Evaporation of the solution facilitates the formation of bulk 3DOm SiO_2 colloidal crystal templates. Infiltration, calcination, and alkali etching of the resulting 3DOm SiO_2 templates provides a size tunable methodology for the production of mesoporous catalytic supports. The pore size of the resulting 3DOm material is governed by the initial size of the colloidal SiO_2-NPs.

Characterization of the resulting 3DOm products via N_2 adsorption and transmission electron microscopy (TEM) demonstrates the ability to tune pore size and increase surface area in the templated materials. Additionally, characterization by x-ray diffraction (XRD) of 3DOm TiO_2 and ZrO_2 reveals the inherent stabilization of traditionally metastable oxide phases in the templated materials after high temperature calcination (i.e. anatase titania and tetragonal zirconia). Residual silica from the colloidal template is hypothesized to assist in stabilization of the metastable oxide; a concept that is investigated further in Chapter 3. This work validates hard templating as a viable method of tailoring pore structure and promoting surface area of catalytic oxides while simultaneously facilitating stabilization of metastable phases at elevated temperatures.

Chapter 3 Overview

In Chapter 3, we investigate the concept of metastable oxide stabilization further; a phenomenon that was originally observed in Chapter 2 during the templating of 3DOm TiO_2 and ZrO_2. A series of model supported oxides consisting of SiO_2/TiO_2 and SiO_2/ZrO_2 are prepared via IWI on commercial crystalline and hydroxide based supports (See **Figure 1-18**). XRD characterization of these model supported oxides demonstrates stabilization of both the metastable a-TiO_2 and t-ZrO_2 phases. Increased loadings of the surface oxide are found to facilitate more robust crystal stabilization at elevated temperatures. A series of extended calcination studies shows that the mechanism of surface stabilization breaks down during prolonged calcination at temperatures above the characteristic bulk Tammann temperature of the supporting oxide.

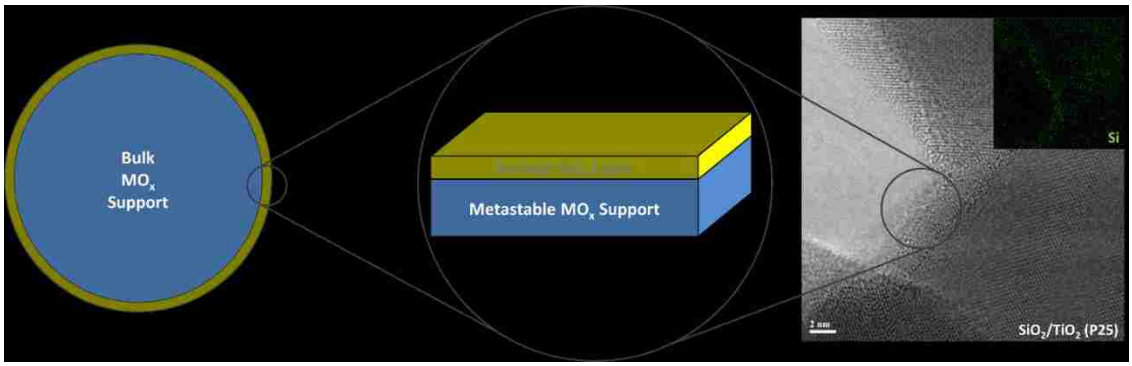

Figure 1-18. Model SiO_2/MO_x samples prepared via IWI for stabilization analysis.

Atomic resolution microscopic imaging (ARM) and energy dispersive x-ray spectroscopic mapping (EDS) of the model supported oxides reveals the presence of an amorphous SiO_2 layer on the surface of the oxides. This surface layer facilitates stabilization of the metastable oxide phase at high temperature by reducing atomic surface mobility of the support. Additionally, N_2 adsorption of the supported oxides demonstrates a resistance to

sintering at elevated temperatures versus unstabilized TiO_2 and ZrO_2 samples. This work validates surface modification as a general method of preserving the crystallinity of a metastable material, as well as, a means of preserving surface area. In Chapter 4 the concept of surface stabilization is examined more fundamentally by studying the interface between two layered oxides.

Chapter 4 Overview

In Chapter 4, a fundamental investigation of the nature of oxide stabilization is conducted by examining the interface between two oxides. A series of uniform thin TiO_2 films ranging in thickness from ~ 20-200 nm are deposited via convective deposition on oxidized silicon wafers (See **Figure 1-19**). XRD characterization of the films confirms stabilization of the anatase phase of titania at elevated temperatures, while corresponding bulk-titania control powders rapidly convert to the more stable rutile phase. The bulk-control powders are observed to convert to the rutile phase at temperatures near the characteristic Hütting temperature of bulk titania ($TiO_2^{Hüttig}$ ~ 610˚C); while films promote stabilization at temperatures nearing the characteristic Tammann temperature ($TiO_2^{Tammann}$ ~ 920˚C). It is proposed that the increased exposure of surface atoms within the powdered TiO_2 samples facilitate mechanisms of low temperature phase transformation which are governed by surface driven atomic mobility. Conversely, stabilization of the films is finally overcome via a combination of surface driven reconfiguration and Tammann based bulk-to-surface mobilization.

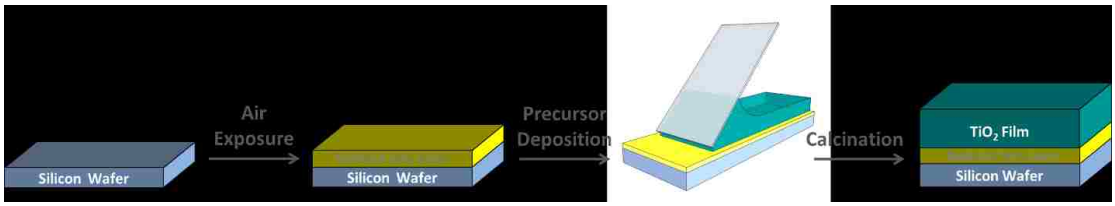

Figure 1-19. Thin film deposition process.

Further analysis with scanning electron microscopy (SEM) reveals the development of sintered crystallites along cracks and defects within films prepared with fast coating rates. These cracked films promote slight increases in the rutile phase as the films are not coherently attached to the substrate. This suggests that TiO_2-substrate coherency assists in stabilization of the metastable phase by limiting sintering and more fully coordinating the surface of the film along the oxide interface. SEM characterization further reveals that development of the rutile phase corresponds to the formation of large surface platelets when approaching the characteristic Tammann temperature of titania. Focused ion beam lithography (FIB) is then utilized to prepare thin slices of the films for depth profiling along the interior of the film. EDS mapping of the resulting slices reveals an absence of homogeneous silicon doping within the film. Thus, anatase stabilization is facilitated primarily by the oxide interface. This work provides a simplified model system which can be used to study the phenomenon of oxide stabilization as was originally observed in Chapters 2 and 3 and offers fundamental insight into the mechanism of stabilization.

Chapter 5 Overview

Surface modification is employed in Chapter 5 for the stabilization of catalytically desirable supported oxides. A series of supported and mixed oxides are prepared via IWI on commercially available crystalline zirconia and zirconium hydroxide based supports. Common catalytically active surface oxides including molybdenum oxide, tungsten oxide, and ceria were

dispersed on the surface of the underlying supports and calcined at temperatures ranging from 500-1000˚C. Characterization of the resulting oxides is conducted to assess stabilization of crystal phase, surface area, and terminal surface functionality.

Thermogravimetric analysis (TGA) is performed to determine the point of hydroxide crystallization during calcination. A combination of XRD and Raman spectroscopy are then used to confirm stabilization of the metastable tetragonal ZrO_2 phase at elevated temperatures (T > 500˚C). Nitrogen adsorption shows a significant increase in surface area for samples prepared on hydroxide based supports versus those synthesized on commercial crystalline supports. Low energy ion scattering (LEIS) confirms that the surface composition of the catalyst remains rich in the original surface oxide at elevated temperatures and facilitates surface based mechanisms of stabilization.

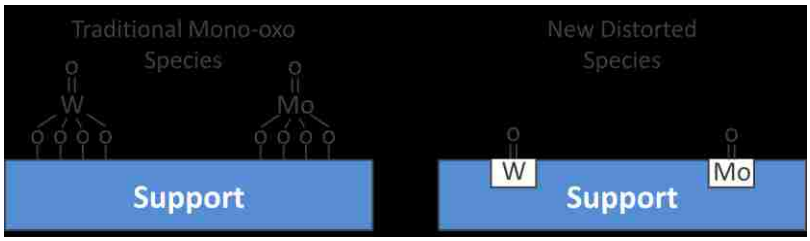

Figure 1-20. Graphic depicting the traditional mono-oxo $O=WO_4$ and $O=MoO_4$ species and a possible structure of the new distorted mono-oxo species.

A combination of dehydrated Raman and infrared (IR) spectroscopy experiments reveal the presence of two distinct surface sties in the supported WO_3/ZrO_2 and MoO_3/ZrO_2 catalysts when synthesized on zirconium hydroxide supports ($Zr(OH)_x$). These terminal surface functionalities include the standard mono-oxo $O=WO_4$ and $O=MoO_4$ surface sites along with the newly discovered distorted mono-oxo $O=WO_x^{Distorted}$ and $O=MoO_x^{Distorted}$ species (See **Figure 1-20**). Acidity characterization via ammonia desorption and IR spectroscopy suggests the distorted mono-oxo sites promote increased acidity. It is proposed that these newly

discovered surface species are embedded along the surface of the support, preserve the metastable tetragonal phase, promote surface area, and simultaneously offer new catalytically active surface sites. These exciting results demonstrate the versatility of surface modification as a means of preserving a metastable supporting oxide while concurrently promoting the formation of new catalytically active surface species.

Chapter 6 Overview

In the final chapter we conclude this thesis with a summary of the insights provided by this work on the nature of metastable oxide stabilization via surface modification. The work presented in this thesis suggests that the concept of oxide stabilization is a general phenomenon which could be utilized in many oxide systems and offers a wide range of future research. A series of extensions are presented for future research projects in order to better understand this concept. A discussion regarding the possible impact of this work is provided and several potential applications of this phenomenon are highlighted. Finally, the work entailed in this thesis will provide the reader with a general background of the methods which can be utilized to stabilize supported oxide catalysts and more generally metastable oxides for a wide range of applications.

1.4 References

[1] Armor, John N. "A History of Industrial Catalysis." *Catalysis Today* 163.1 (2011): 3-9.

[2] Fechete, Ioana, Ye Wang, and Jacques C. Védrine. "The Past, Present and Future of Heterogeneous Catalysis." *Catalysis Today* 189.1 (2012): 2-27.

[3] Chorkendorff, I., and J. W. Niemantsverdriet. "Introduction to Catalysis." *Concepts of Modern Catalysis and Kinetics*. Weinheim: Wiley-VCH, 2003. 1-19.

[4] Wachs, I. E., and C. J. Keturakis. "Monolayer Systems" *Comprehensive Inorganic Chemistry II: From Elements to Applications*. Ed. Jan Reedijk and Kenneth Poeppelmeier. Burlington: Elsevier, 2013. Chapter 7.06, 131-51.

[5] Wachs, Israel E., and Kamalakanta Routray. "Catalysis Science of Bulk Mixed Oxides." *ACS Catalysis* 2.6 (2012): 1235-246.

[6] Wachs, Israel E. "Molecular Structures of Surface Metal Oxide Species: Nature of Catalytic Active Sties in Mixed Metal Oxides." *Metal Oxides: Chemistry and Applications*. Ed. J. L. G. Fierro. Boca Raton, FL: Taylor & Francis, 2006. 1-30.

[7] Tanabe, K. "Industrial Application of Solid Acid–base Catalysts." *Applied Catalysis A: General* 181.2 (1999): 399-434.

[8] Busca, G. "The Surface Acidity of Solid Oxides and Its Characterization by IR Spectroscopic Methods. An Attempt at Systematization." *Physical Chemistry Chemical Physics* 1.5 (1999): 723-36.

[9] Bell, Alexis T., Bruce C. Gates, and Douglas Ray. "Grand Challenge 2: Design and Controlled Synthesis of Catalytic Structures." *Basic Research Needs: Catalysis for Energy: Report from the U.S. Department of Energy, Office of Basic Energy Sciences Workshop, August 6-8, 2007, in Bethesda, Maryland*. Washington, D.C.: Office of Basic Energy Sciences, U.S. Dept. of Energy, 2007. 22-37.

[10] Scheithauer, Markus, Robert K. Grasselli, and Helmut Knözinger. "Genesis and Structure of WO_x/ZrO_2 Solid Acid Catalysts." *Langmuir* 14.11 (1998): 3019-029.

[11] Srinivasan, Ram, Tom Watkins, Camden Hubbard, and Burtron H. Davis. "Sulfated Zirconia Catalysts. The Crystal Phases and Their Transformations." *Chemistry of Materials* 7.4 (1995): 725-30.

[12] Afanador, L. "Titanyl Sulfate Extracted from the Mineral Ilmenite as Mesoporous Catalyst for the Oleic Acid Esterification." *Fuel* 100 (2012): 43-47.

[13] Bradley, D. C., R. C. Mehrotra, and D. P. Gaur. *Metal Alkoxides*. London: Academic, 1978.

[14] Jong, Krijn Pieter De. *Synthesis of Solid Catalysts*. Weinheim: Wiley-VCH, 2009.

[15] Segal, D. "Soft Chemistry Routes to Zirconia Ceramics." *Zirconia Engineering Ceramics: Old Challenges - New Ideas*. 241-49.

[16] Menon, P. G., and B. Delmon. "3.7 Solid-State Reactions." *Preparation of Solid Catalysts*. By G. Ertl, H. Knözinger, and J. Weitkamp. Weinheim: Wiley-VCH, 1999. 109-39.

[17] Schlogl, R. "Chapter 3.1 Fused Catalysts." *Preparation of Solid Catalysts*. By G. Ertl, H. Knözinger, and J. Weitkamp. Weinheim: Wiley-VCH, 1999. 11-28.

[18] Jacobsen, H., and P. Kleinschmit. "3.6 Flame Hydrolysis." *Preparation of Solid Catalysts*. By G. Ertl, H. Knözinger, and J. Weitkamp. Weinheim: Wiley-VCH, 1999. 99-109.

[19] White, Laurence, and George Duffy. "Staff-Industry Collaborative Report Vapor-Phase Production of Colloidal Silica." *Ind. Eng. Chem. Industrial & Engineering Chemistry* 51.3 (1959): 232-38.

[20] Sanchez, C., L. Rozes, F. Ribot, C. Laberty-Robert, D. Grosso, C. Sassoye, C. Boissiere, and L. Nicole. "“Chimie Douce”: A Land of Opportunities for the Designed Construction of Functional Inorganic and Hybrid Organic-inorganic Nanomaterials." *Comptes Rendus Chimie* 13.1-2 (2010): 3-39.

[21] Gupta, Shipra M., and Manoj Tripathi. "A Review on the Synthesis of TiO_2 Nanoparticles by Solution Route”." *Central European Journal of Chemistry* 10.2 (2012): 279-94.

[22] Knözinger, Helmut, and Karl Kochloefl. "Heterogeneous Catalysis and Solid Catalysts." *Ullmann's Encyclopedia of Industrial Chemistry* (2003).

[23] Che, M., O. Clause, and Ch. Marcilly. "Chapter 4.1 Impregnation and Ion Exchange." *Preparation of Solid Catalysts*. By G. Ertl, H. Knözinger, and J. Weitkamp. Weinheim: Wiley-VCH, 1999. 315-40.

[24] Regalbuto, John R. *Catalyst Preparation: Science and Engineering*. Boca Raton: CRC/Taylor & Francis, 2007. 341-372.

[25] Leyrer, J. "Spreading Behavior of Molybdenum Trioxide on Alumina and Silica: A Raman Microscopy Study." *Journal of Catalysis* 124.2 (1990): 349-56.

[26] Schuth, F., and K. Unger. "3.4 Precipitation and Coprecipitation."*Preparation of Solid Catalysts*. By G. Ertl, H. Knözinger, and J. Weitkamp. Weinheim: Wiley-VCH, 1999. 60-84.

[27] Basolo, Fred, and Ronald C. Johnson. *Coordination Chemistry; the Chemistry of Metal Complexes*. New York: W.A. Benjamin, 1964.

[28] Cotton, F. Albert. *Advanced Inorganic Chemistry*. 5th ed. New York: Wiley, 1999.

[29] Clearfield, Abraham. "The Mechanism of Hydrolytic Polymerization of Zirconyl Solutions."*Journal of Materials Research* 5.1 (1990): 161-62.

[30] Clearfield, A. "Crystalline Hydrous Zirconia." *Inorganic Chemistry* 3.1 (1964): 146-48.

[31] Clearfield, A., and P. A. Vaughan. "The Crystal Structure of Zirconyl Chloride Octahydrate and Zirconyl Bromide Octahydrate." *Acta Crystallographica* 9.7 (1956): 555-58.

[32]Ambrosi, Moira. "Bottom-up/top-down Synthesis of Stable Zirconium Hydroxide Nanophases." *Journal of Materials Chemistry* 22 (2012): 23497-3505.

[33] P.D. Southon, J.R. Bartlett, J.L. Woolfrey, B. Ben-Nissan, Formation and characterisation of an aqueous zirconium hydroxide colloid, Chemistry of Materials 14.10 (2002): 4313-4319.

[34] P.D. Southon, J.R. Bartlett, K.S. Finnie, J.L. Woolfrey, B. Ben-Nissan, G.S.K. Kannangara, The formation of zirconium hydroxide nanoparticles from aqueous nitrate solutions, J. Aust. Ceram. Soc. 35.1/2 (1999): 7-12.

[35] P.D. Southon, J.R. Bartlett, J.L. Woolfrey and M.G. Stevens, Evolution of the structure of aqueous zirconia gels during preparation and heating, Ceramic Transactions 81 (1998): 75-80.

[36] Srinivasan, Ram. "Zirconium Oxide Crystal Phase: The Role of the pH and Time to Attain the Final pH

for Precipitation of the Hydrous Oxide." Journal of Materials Research 3.4 (1988): 787-97.

[37] Srinivasan, Ramachandra, Robert De Angelis, and Burton H. Davis. "Factors Influencing the Stability of the Tetragonal Form of Zirconia." Journal of Materials Research 1.04 (1986): 583-88.

[38] Iler, Ralph K. *The Chemistry of Silica: Solubility, Polymerization, Colloid and Surface Properties, and Biochemistry*. New York: Wiley, 1979.

[39] Watanabe, Ryota, Toshiyuki Yokoi, Erina Kobayashi, Yuki Otsuka, Atsushi Shimojima, Tatsuya Okubo, and Takashi Tatsumi. "Extension of Size of Monodisperse Silica Nanospheres and Their Well-ordered Assembly." *Journal of Colloid and Interface Science*360.1 (2011): 1-7.

[40] Turova, Nataliya Ya. *The Chemistry of Metal Alkoxides*. Boston: Kluwer Academic, 2002.

[41] Livage, J., M. Henry, and C. Sanchez. "Sol-gel Chemistry of Transition Metal Oxides." *Progress in Solid State Chemistry* 18.4 (1988): 259-341.

[42] Sanchez, C., J. Livage, M. Henry, and F. Babonneau. "Chemical Modification of Alkoxide Precursors." *Journal of Non-Crystalline Solids* 100.1-3 (1988): 65-76.

[43] Bradley, Donald C. "Metal Alkoxides as Precursors for Electronic and Ceramic Materials."*Chemical Reviews* 89.6 (1989): 1317-322.

[44] De, G., A. Chatterjee, and D. Ganguli. "Zirconia Fibres from the Zirconiumn-propoxide-acetylacetone-water-isopropanol System."*Journal of Materials Science Letters J Mater Sci Lett* 9.7 (1990): 845-46.

[45] Yi, Guanghua, and Michael Sayer. "Sol-Gel Processing of Complex Oxide Films." *American Ceramic Society Bulletin* 70.7 (1991): 1173-1177.

[46] Kim, Seung-Goo, Suk Woo Nam, Sung-Pil Yoon, Sang-Hoon Hyun, Jonghee Han, Tae-Hoon Lim, and Seong-Ahn Hong. "Sol-gel Processing of Yttria-stabilized Zirconia Films Derived from the Zirconium N-butoxide-acetic Acid-nitric Acid-water-isopropanol System." *Journal of Materials Science* 39.8 (2004): 2683-688.

[47] Takahashi, Yasutaka, and Yoshihiro Matsuoka. "Dip-coating of TiO_2 Films Using a Sol Derived from $Ti(O\text{-}i\text{-}Pr)_4$-diethanolamine-$H_2O$-i-PrOH System." *Journal of Materials Science* 23.6 (1988): 2259-2266.

[48] Takahashi, Yasutaka, Katsuhiro Niwa, Keisuke Kobayashi, and Michiyasu Matsuki. "Dip Coating of Zirconia and Mixed Zirconia Films." *Journal of the Ceramic Association, Japan* 95.1106 (1987): 942-948.

[49] Brinker, C. Jeffrey., and George W. Scherer. *Sol-gel Science: the Physics and Chemistry of Sol-gel Processing*. Boston: Academic, 1990.

[50] Davis, P., C. Jeffrey Brinker, and D. Smith. "Pore Structure Evolution in Silica Gel during Aging/drying I. Temporal and Thermal Aging." *Journal of Non-Crystalline Solids*142 (1992): 189-96.

[51] Davis, P., C. Jeffrey Brinker, D. Smith, and R. Assink. "Pore Structure Evolution in Silica Gel during Aging/drying II. Effect of Pore Fluids." *Journal of Non-Crystalline Solids* 142 (1992): 197-207.

[52] Deshpande, R., D. Hua, D. Smith, and C. Brinker. "Pore Structure Evolution in Silica Gel during Aging/drying. III. Effects of Surface Tension." *Journal of Non-Crystalline Solids* 144 (1992): 32-44.

[53] Davis, P., R. Deshpande, D. Smith, C. Brinker, and R. Assink. "Pore Structure Evolution in Silica Gel during Aging/drying. IV. Varying Pore Fluid pH." *Journal of Non-Crystalline Solids* 167.3 (1994): 295-306.

[54] Brinker, C.J., D.M. Smith, R. Deshpande, P.M. Davis, S. Hietala, G.C. Frye, C.S. Ashley, and R.A. Assink. "Sol-gel Processing of Controlled Pore Oxides." *Catalysis Today*14.2 (1992): 155-63.

[55] D'Souza, Lawrence, Andreas Suchopar, Kake Zhu, Denitza Balyozova, Mukundan Devadas, and Ryan M. Richards. "Preparation of Thermally Stable High Surface Area Mesoporous Tetragonal ZrO_2 and Pt/ZrO_2: An Active Hydrogenation Catalyst."*Microporous and Mesoporous Materials* 88.1-3 (2006): 22-30.

[56] Deshmane, Vishwanath G., and Yusuf G. Adewuyi. "Synthesis of Thermally Stable, High Surface Area, Nanocrystalline Mesoporous Tetragonal Zirconium Dioxide (ZrO_2): Effects of Different Process Parameters." *Microporous and Mesoporous Materials* 148.1 (2012): 88-100.

[57] Tsotsas, Evangelos, and A. S. Mujumdar. "Chapter 5. Understanding and Preventing Structural Changes During Drying Gels." *Modern Drying Technology*. Weinheim: Wiley-VCH, 2011. 155-223.

[58] Rouquerol, J., D. Avnir, C. W. Fairbridge, D. H. Everett, J. M. Haynes, N. Pernicone, J. D. F. Ramsay, K. S. W. Sing, and K. K. Unger. "Recommendations for the Characterization of Porous Solids (Technical Report)." *Pure and Applied Chemistry* 66.8 (1994): 1739-758.

[59] Roberts, G. W. "Chapter 9. Heterogeneous Catalysis Revisited. "*Chemical Reactions and Chemical Reactors*. Hoboken, NJ: John Wiley & Sons, 2009. 305-76.

[60] Boudart, Michel. "Chapter 7. Irreducible Transport Phenomena in Chemical Kinetics." *Kinetics of Chemical Processes*. Englewood Cliffs, NJ: Prentice-Hall, 1968. 144-64.

[61] Boudart, Michel, and G. Djéga-Mariadassou. "Chapter 6. Parasitic Phenomena." *Kinetics of Heterogeneous Catalytic Reactions*. Princeton, NJ: Princeton UP, 1984. 194-201.

[62] Chorkendorff, I., and J.W Niemantsverdriet. "5.8.2.1 Transport Limitations and the Thiele Diffusion Modulus." *Concepts of Modern Catalysis and Kinetics*. Weinheim: Wiley-VCH, 2007. 207-15.

[63] Thiele, E. W. "Relation between Catalytic Activity and Size of Particle." *Ind. Eng. Chem. Industrial & Engineering Chemistry* 31.7 (1939): 916-20.

[64] Roberts, G. W. "The Effective Diffusion Coefficient." *Chemical Reactions and Chemical Reactors*. Hoboken, NJ: John Wiley & Sons, 2009. 318-27.

[65] Bird, R. Byron, Warren E. Stewart, and Edwin N. Lightfoot. "17.6 Diffusion and Chemical Reaction Inside a Porous Catalyst: The "Effectiveness Factor"" *Transport Phenomena*. New York: Wiley, 1960. 542-47.

[66] Froment, Gilbert F., and Kenneth B. Bischoff. "3.4 Molecular, Knudsen, and Surface Diffusion in Pores." *Chemical Reactor Analysis and Design*. 3rd ed. New York: Wiley, 1979. 172-76.

[67] Deen, William M. "Chapter 1 Diffusive Fluxes and Material Properties." *Analysis of Transport Phenomena*. New York: Oxford UP, 1998. 25.

[68] Wachs, Israel E. "Recent Conceptual Advances in the Catalysis Science of Mixed Metal Oxide Catalytic Materials." *Catalysis Today* 100.1-2 (2005): 79-94.

[69] Tanabe, Kōzō. *New Solid Acids and Bases: Their Catalytic Properties*. Tokyo: Kodansha, 1989.

[70] Kim, T., A. Burrows, C. Kiely, and I. Wachs. "Molecular/electronic Structure–surface Acidity Relationships of Model-supported Tungsten Oxide Catalysts." *Journal of Catalysis* 246.2 (2007): 370-81.

[71] Ross-Medgaarden, E. I.; Knowles, W. V.; Kim, T.; Wong, M. S.; Zhou, W.; Kiely, C. J.; Wachs, I. E. *J. Catal.* 2008, 256, 108-125.

[72] Zhou, Wu, Elizabeth I. Ross-Medgaarden, William V. Knowles, Michael S. Wong, Israel E. Wachs, and Christopher J. Kiely. "Identification of Active Zr–WO_x Clusters on a ZrO_2 Support for Solid Acid Catalysts." *Nature Chemistry* 1.9 (2009): 722-28.

[73] Boudart, M. "Principles of Heterogeneous Catalysis." *Handbook of Heterogeneous Catalysis*. Ed. G. Ertl, H. Knözinger, and J. Weitkamp. Weinheim: VCH, 1997. 8-9.

[74] Hanaor, Dorian A. H., and Charles C. Sorrell. "Review of the Anatase to Rutile Phase Transformation." *Journal of Materials Science* 46.4 (2011): 855-74.

[75] Kuba, S.; Knözinger, H. *J. Raman Spectrosc*. 2002, 33, 325-332.

[76] Stevenson, Scott A., and Eli Ruckenstein. "Chapter 13. Wetting and Spreading." *Metal-support Interactions in Catalysis, Sintering, and Redispersion*. New York: Van Nostrand Reinhold, 1987. 230-248.

[77] Knözinger, H., and E. Taglauer. "Spreading and Wetting." *Preparation of Solid Catalysts*. Ed. G. Ertl, H. Knözinger, and J. Weitkamp. Weinheim: Wiley-VCH, 1999. 501-26

[78] Carreon, Moises A., and Vadim V. Guliants. "Ordered Meso- and Macroporous Binary and Mixed Metal Oxides." *European Journal of Inorganic Chemistry* 2005.6 (2005): 1189.

[79] Hlavac, J. "IUPAC Melting Temperatures of Refractory Oxides: Part 1." *Pure & Applied Chemistry* 54.3 (1982): 681.

[80] Takagi, Mieko. "Electron-Diffraction Study of Liquid-Solid Transition of Thin Metal Films." *Journal of the Physical Society of Japan J. Phys. Soc. Jpn.* 9.3 (1954): 359-63.

[81] Stevenson, Scott A., and Eli Ruckenstein. "Chapter 11. Mechanisms of Sintering (Migration and Coalescence)." *Metal-support Interactions in Catalysis, Sintering, and Redispersion*. New York: Van Nostrand Reinhold, 1987. 156-86.

[82] Chan, Shirley S., Israel E. Wachs, Lawrence L. Murrell, and Nick C. Dispenziere, Jr. "Laser Raman Characterization of Tungsten Oxide Supported on Alumina: Influence of Calcination Temperatures."*Journal of Catalysis* 92.1 (1985): 1-10.

[83] Stevens, R. *Zirconia and Zirconia Ceramics*. Manchester, U.K.: Magnesium Elektron, 1986.

[84] Chen, I-Wei, and Y-H. Chiao. "Theory and Experiment of Martensitic Nucleation in ZrO_2 Containing Ceramics and Ferrous Alloys." *Acta Metallurgica* 33.10 (1985): 1827-845.

[85] Mercera, P.D.L., J.G. Van Ommen, E.B.M. Doesburg, A.J. Burggraaf, and J.R.H. Ross. "Zirconia as a Support for Catalysts Evolution of the Texture and Structure on Calcination in Air." *Applied Catalysis* 57.1 (1990): 127-148.

[86] Wolten, G. M. "Diffusionless Phase Transformations in Zirconia and Hafnia." *Journal of the American Ceramic Society* 46.9 (1963): 418-422.

[87] Chen, I-Wei, Y-H. Chiao, and K. Tsuzaki. "Statistics of Martensitic Nucleation." *Acta Metallurgica* 33.10 (1985): 1847-859.

[88] P. D. Southon, *Structural Evolution during the Preparation and Heating of Nanophase Zirconia Gels*, Thesis, 7-5 (2000).

[89] Lynch, C. T., F. W. Vahldiek, and L. B. Robinson. "Monoclinic-Tetragonal Transition of Zirconia." *Journal of the American Ceramic Society* 44.3 (1961): 147-48.

[90] Tang, J., F. Zhang, P. Zoogman, J. Fabbri, S.-W. Chan, Y. Zhu, L. E. Brus, and M. L. Steigerwald. "Martensitic Phase Transformation of Isolated HfO_2, ZrO_2, and $Hf_xZr_{1-x}O_2$ ($0<x<1$) Nanocrystals." *Advanced Functional Materials* 15.10 (2005): 1595-602.

[91] Heuer, A. H., and M. Ruhle. "On the Nucleation of Martensitic Transformation in Zirconia (ZrO_2)." *Acta Metallurgica* 33 (1985): 2101-112.

[92] B. Basu, J. Vleugels, and O. Van Der Biest, *Materials Science and Engineering: A*, 366, 338 (2004).

[93] C. Li, and M. Li, *Journal of Raman Spectroscopy*, 33, 301 (2002).

[94] Mercera, P.D.L., J.G. Van Ommen, E.B.M. Doesburg, A.J. Burggraaf, and J.R.H. RoSs. "Stabilized Tetragonal Zirconium Oxide as a Support for Catalysts Evolution of the Texture and Structure on Calcination in Static Air." *Applied Catalysis* 78.1 (1991): 79-96.

[95] Steele, Brian C.H., and Angelika Heinzel. "Materials for Fuel-Cell Technologies." *Nature* 414 (2001): 345-52.

[96] Scheithauer, Markus, Robert K. Grasselli, and Helmut Knozinger. "Genesis and Structure of WO_x/ZrO_2 Solid Acid Catalysts." *Langmuir* 14.11 (1998): 3019-029.

[97] Li, Meijun, Zhaochi Feng, Guang Xiong, Pinliang Ying, Qin Xin, and Can Li. "Phase Transformation in the Surface Region of Zirconia Detected by UV Raman Spectroscopy." *The Journal of Physical Chemistry B* 105.34 (2001): 8107-111.

[98] Srinivasan, Ram, Tom Watkins, Camden Hubbard, and Burtron H. Davis. "Sulfated Zirconia Catalysts. The Crystal Phases and Their Transformations." *Chemistry of Materials* 7.4 (1995): 725-30.

[99] Wachs, Israel E., Franklin D. Hardcastle, and Shirley S. Chan. "Characterization of Supported Metal Oxides by Laser Raman Spectroscopy: Supported Vanadium Oxide on Al_2O_3 and TiO_2." *MRS Proceedings* 111 (1987): 353-58.

[100] Garvie, R. C., and M. F. Goss. "Intrinsic Size Dependence of the Phase Transformation Temperature in Zirconia Microcrystals." *Journal of Materials Science* 21.4 (1986): 1253-257.

[101] Garvie, Ronald C. "The Occurrence of Metastable Tetragonal Zirconia as a Crystallite Size Effect." *The Journal of Physical Chemistry* 69.4 (1965): 1238-243.

[102] Garvie, R. C. "Stabilization of the Tetragonal Structure in Zirconia Microcrystals." The Journal of Physical Chemistry 82.2 (1978): 218-24.

[103] Zhang, Hengzhong, and Jillian F. Banfield. "Thermodynamic Analysis of Phase Stability of Nanocrystalline Titania." *Journal of Materials Chemistry* 8.9 (1998): 2073-076.

[104] Baldinozzi, G., D. Simeone, D. Gosset, and M. Dutheil. "Neutron Diffraction Study of the Size-Induced Tetragonal to Monoclinic Phase Transition in Zirconia Nanocrystals." *Physical Review Letters* 90.21 (2003): 1-4.

[105] Holmes, H. F., E. L. Fuller, and R. B. Gammage. "Heats of Immersion in the Zirconium Oxide-water System." *The Journal of Physical Chemistry* 76.10 (1972): 1497-502.

[106] Hu, Y., H.-L Tsai, and C.-L Huang. "Phase Transformation of Precipitated TiO_2 Nanoparticles." *Materials Science and Engineering: A* 344.1-2 (2003): 209-14.

[107] Schuth, F., and K. Unger. "3.4 Precipitation and Coprecipitation." *Preparation of Solid Catalysts*. Ed. G. Ertl, H. Knözinger, and J. Weitkamp. Weinheim: Wiley-VCH, 1999. 60-62.

[108] Busca, Guido. "Acid Catalysts in Industrial Hydrocarbon Chemistry." *Chemical Reviews* 107.11 (2007): 5366-410.

[109] Davis, Burtron H., Robert A. Keogh, and Ram Srinivasan. "Sulfated Zirconia as a Hydrocarbon Conversion Catalyst." *Catalysis Today* 20.2 (1994): 219-56.

[110] Corma, A. "Inorganic Solid Acids and Their Use in Acid-Catalyzed Hydrocarbon Reactions." *Chemical Reviews* 95.3 (1995): 559-614.

[111] Chorkendorff, I., and J. W. Niemantsverdriet. "Environmental Catalysis." *Concepts of Modern Catalysis and Kinetics*. Weinheim: Wiley-VCH, 2003. 381-404. Print.

[112] Stöber, Werner, Arthur Fink, and Ernst Bohn. "Controlled Growth of Monodisperse Silica Spheres in the Micron Size Range."*Journal of Colloid and Interface Science* 26.1 (1968): 62-69.

[113] Fan, Wei, and Mark A. Snyder. "Hierarchical Nanofabrication of microporous Crystals with Ordered Mesoporosity." Nature Materials 7.12 (2008): 984-91.

Chapter 2: Synthesis of three Dimensionally Ordered Mesoporous (3DOm) Materials

2.1 Abstract

This work investigates conceptual aspects of hard templating as a methodology used for the synthesis of three dimensionally ordered mesoporous (3DOm) adsorptive membranes and pore size tunable catalytic supports. This method of synthesis facilitates the design of mesoporous materials with large surface areas and tunable pore sizes in order to reduce internal transport limitations. Additionally, we reveal an interfacial mechanism which facilitates the stabilization of metastable oxides at elevated temperatures during this sacrificial method of hard templating. This concept of interfacial stabilization is then demonstrated to be a more general phenomenon by preparing and characterizing a series of composite zirconia-silica (ZrO_2/SiO_2) materials by various means of preparation.

We begin by highlighting the essential aspects of wet-chemistry necessary for successful nanocasting of 3DOm materials including zirconia (ZrO_2), titania (TiO_2), and carbon by means of a sacrificial hard templating process with size tunable colloidal silica nanoparticles (SiO_2-NP's). Monodisperse colloidal silica nanospheres ranging in size from 20-50nm were synthesized via a buffered hydrolysis and condensation reaction with tetraethyl orthosilicate (TEOS). Subsequent drying of the as prepared suspensions facilitated convective driven deposition of the SiO_2-NP's and resulted in the formation of 3DOm SiO_2 templates. Solvent based methods of infiltration were then employed to deposit soft chemical precursors within the as made 3DOm SiO_2 nanomolds. High temperature curing and alkali etching of these composite materials facilitated the formation of pore size tunable 3DOm products with hierarchically structured micro-meso-macroporous frameworks.

Dynamic light scattering (DLS) was utilized to screen particle size within a series of wet-chemical precursor solutions and ensured that the degree of oligomerization was within the acceptable range necessary for infiltration of the mesoporous SiO_2 templates. Nitrogen and argon gas adsorption validated this method of templating as a means of producing 3DOm materials with tunable surface area and pore size. Material crystallinity was characterized with X-ray diffraction (XRD) to assess phase composition of the 3DOm metal oxide products. The XRD results suggest that oxide polymorphism is tunable by controlling the degree of template-induced confinement during nucleation, crystallization, and higher-temperature processing of the oxide based materials. Atomic resolution microscopy (ARM) suggests that the 3DOm template assists in the interfacial stabilization of metastable oxide phases.

Apparent stabilization of the tetragonal phase of zirconia (t-ZrO_2) and anatase phase of titania (a-TiO_2) is achievable on the basis of interfacial stabilization between the template (SiO_2) and the templated material. This mechanism of stabilization is then validated by preparing a series of ZrO_2/SiO_2 samples through alternative synthetic routes. This work demonstrates that sacrificial hard templating not only offers a means of engineering tunable 3DOm materials, but can simultaneously stabilize them via template-induced interfacial mechanisms. As such, these materials might be beneficial for catalytic and adsorption based applications which involve high temperatures.

2.2 Introduction

Catalytic materials and adsorbent membranes incorporate a tortuous network of interconnected pores to promote the formation of materials with large surface areas and broad distributions in pore size. These interconnected pores construct a labyrinth of irregular pathways for internal molecular transport, provide a large platform for molecular adsorption,

and facilitate catalytic reactions.[1] However this inherent irregular pore structure often leads to internal transport limitations and molecular congestion which can significantly hinder the performance of a catalyst or adsorbent.[2, 3, 4] To minimize these effects, new synthetic approaches are required to fabricate materials with large surface areas and tunable pore structures in order to optimize the internal molecular diffusivity of processed feedstocks. Additionally, these new methods of synthetic design should incorporate mechanisms of stabilization in order to remain stable during prolonged operation at high temperatures.

Overview of Transport Limitations

Transport limitations present a barrier to optimal material performance when the effective diffusivity (D_{eff}) of the processing flow is reduced (See **Equation 2-1**).[5] The effective molecular diffusivity within a material is dependent upon its average pore diameter (d_{pore}), the overall porosity (ε), its tortuosity (τ), and the processing conditions of the operation. This effective diffusivity can vary greatly from the theoretical molecular diffusivity (D_A) that would be observed had the material consisted of only uniformly straight, cylindrical pores.

Molecular diffusion becomes increasingly congested as the pore dimension of a material approaches that of the affluent molecules within the product and feed streams. As the pore dimension is reduced, molecules begin to experience more frequent collisions with the internal surfaces of the material; this leads to Knudsen based molecular diffusion, which is inherently slower than traditional bulk diffusion.[6] Knudsen diffusion is shown to be directly related to the pore size of a material as demonstrated by **Equation 2-2** where R is the gas constant, T is the process temperature, and M_A is the molecular weight of chemical species "A".[7] Further reduction in pore size leads to even slower configurational mechanisms of diffusion. Thus, it becomes readily apparent that materials which incorporate larger pores are

more able to facilitate increased diffusivity by reducing molecular gridlock within the pore network of the material.

$$D_{eff} = D_A\left(d_{pore}\right)\varepsilon/\tau \qquad \textbf{Equation 2-1}$$

$$D_{A,Knudsen} = \frac{2d_{pore}}{3}\sqrt{\frac{2RT}{\pi M_A}} \qquad \textbf{Equation 2-2}$$

Pore size is divided into three regimes as defined by the International Union of Pure and Applied Chemistry (IUPAC).[8,9,10] Micropores consist of pores with diameters below two nanometers in size; mesopores range in size from 2-50nm in diameter; and finally, macropores consist of pores larger than 50nm. By increasing the pore size of a material one can successfully reduce the effective molecular diffusivity and mitigate transport limitations; however as pore size is increased, the surface area of the material is ultimately reduced, resulting in a diminished capacity for adsorption and fewer catalytically active sites. Thus the development of new synthetic approaches for the design of materials with tailored surface area and pore configuration could facilitate the design of optimally structured materials in order to mitigate internal transport limitations.

Advent of Rationally Designed Mesoporous Materials

In recent years, a series of techniques have been developed to engineer catalysts and adsorbents with tunable porosity in order to reduce transport limitations during industrial processing. These techniques are generally classified as either top-down or bottom-up methods of synthesis.[11] Top-down methods alter the porosity of a material by reconfiguring its current pore structure. This technique typically utilizes a chemical etchant to introduce a new system of mesopores by selectively removing a portion of the material.[12] The top-down

"riving" technique has recently been utilized to promote the formation of small mesopores in catalytically active zeolites and has successfully reduced transport limitations during the prolonged catalytic cracking of crude oil.[13]

Bottom-up synthetic techniques allow direct structuring of a material from its chemical precursors during synthesis. This technique typically incorporates either a soft or hard template to structure chemical precursors within solution.[14] Subsequent crystallization of the material, followed by removal of the scaffolding agent, reveals a molded replica structure of the original chemical template. Soft templating is utilized for the production of large pore zeolites including ZSM-5[15] and MCM-41.[16] Similar methods of soft-chemical templating are used for the production of mesoporous silica's[17] including SBA-15[18] and KIT-6.[19] Chemical chelating groups also act as structure directing agents and have been used to promote both surface area and porosity of materials during bottom-up synthesis.[20]

Bottom-up hard templating techniques often utilize colloidal particles such as spherical carbons and silica's to design a range of products including three dimensionally ordered mesoporous materials (3DOm),[21] core shell materials,[22] and even encapsulated nanorattles.[23] The selection of a size tunable colloidal material such as silica, offers direct tunability of pore size in the final templated material.[24] These techniques offer a promising method of synthesis as they facilitate extensive control of both pore size and surface area in order to produce materials with minimal transport limitations.

Thermodynamic Driven Mechanisms of Reconfiguration

While many newly designed approaches to material synthesis have been devised in recent decades, most of the of the resulting "novel" materials have not been tested or employed at the conditions typical of most industrial scale operations. The advent of rationally

designed materials have revealed significant insight into the solution driven mechanisms of chemical synthesis; however, little research is currently being focused on the rational design of stable materials or stability assessment of these novel materials at elevated temperatures. It is important to bear in mind that regardless of the synthetic method used to manufacture a product, it still remains susceptible to thermodynamic mechanisms of reconfiguration during prolonged operation at high temperatures. Thus, future synthetic techniques should begin to incorporate methods of both stabilization and pore configuration in order to produce stabilized materials with tailored porosity for the reduction of transport limitations.

Overview of this Chapter

This chapter investigates a sacrificial hard templating approach as a means used for the synthetic design of pore size tunable carbon, titania (TiO_2), and zirconia (ZrO_2) materials with three dimensionally ordered mesopores (3DOm). This templated route to synthesis can be used to design materials which limit molecular barriers to diffusion by tailoring the average pore size of the material, promoting its porosity, increasing its surface area, and reducing tortuosity. Additionally, we use ZrO_2 as a case study demonstrate how the application of a hard templated based synthetic approach can facilitate the synergistic stabilization of metastable oxide materials via interfacial mechanisms of surface stabilization. This mechanism of surface stabilization is then further analyzed by preparing a series of supported ZrO_2/SiO_2 samples utilizing various methods of preparation. The discovery of this mechanism of interfacial stabilization provides the fundamental topic of investigation for the remainder of this thesis.

2.3 Materials and Methods

Tetraethyl orthosilicate (TEOS), zirconyl chloride octahydrate ($ZrOCl_2 \bullet 8H_2O$), 70wt% zirconium(IV) propoxide ($Zr(OC_3H_5)_7$) in ethanol, titanium(IV) ethoxide ($Ti(OC_2H_5)_4$), L-lysine,

diethylene glycol, sulfuric acid (H_2SO_4), hydrochloric acid (HCl), sodium hydroxide (NaOH), potassium hydroxide (KOH), and D-glucose were purchased from Sigma-Aldrich and used without further purification.

Synthesis of SiO_2 Nano-Spheres

Spherical silica nanoparticles were synthesized using a seeded growth technique, which produced monodisperse SiO_2 particles ranging from 20-50 nm in diameter.[25] SiO_2 synthesis consisted of a modified Stöber silica process which utilized an amino acid (L-Lysine) as a buffer.[26] Silica seeds were first synthesized from tetraethyl orthosilicate (TEOS), L-lysine, and water resulting in a final molar composition consisting of: x SiO_2 / y lysine / 9500 water / 4x ethanol (where x = 61.4 and y = 1.23). During synthesis, the solution was vigorously stirred at 90˚C for 48 hours in order to fully hydrolyze and condense the SiO_2 into 15 nm seeds. The particle size was then increased to 50 nm by incrementally adding TEOS in three steps, such that the final molar ratio consisted of: x = 1120 and y = 1.23. The suspensions were then dialyzed with water until a pH of ~6.0 was obtained. The SiO_2 volume percent in these solutions ranged from 3.7 - 4.3%. The solutions were then dried at room temperature in order to assemble the particles into highly ordered colloidal crystal templates for nanocasting.

Preparation of 3DOm Materials

A hard templating methodology was utilized to produce 3DOm materials by means of infiltration and subsequent removal of the colloidal silica nano-molds (See **Figure 2-1**). The mold consisted of the ordered colloidal silica templates, as prepared during the buffered hydrolysis and condensation reaction. A chemical precursor was deposited within the colloidal silica template through either an iterative series of incipient wetness infiltration (IWI) steps or a one-pot co-assembly technique in which the colloidal SiO_2 nanospheres were mixed with a

precursor solution and subsequently dried. After infiltration, the samples were typically cured at 500-1000˚C in order to produce an infiltrated composite sample. The silica template was subsequently removed by etching in a 3.0 M KOH solution for 5-72 hours. After etching, the alkali counter ion was removed via a series of iterative rinsing steps whereby the sample was dispersed in de-ionized water, collected via centrifugation, and subsequently redispersed in water. This process was repeated until a neutral pH value was obtained. The samples were then dried at 70˚C for further characterization.

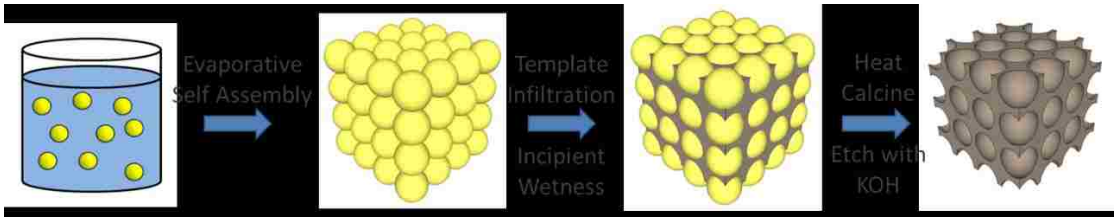

Figure 2-1. Generalized depiction of the 3DOm hard templating methodology utilized for the production of mesoporous materials.

Preparation of 3DOm Carbon

3DOm carbon was prepared via co-assembly of the SiO_2 nanospheres with an aqueous glucose solution. The as made SiO_2 nanosphere solutions were dialyzed in water until a neutral pH was obtained. The dialyzed silica solutions were then diluted with de-ionized water to obtain a SiO_2 volume percent ranging from 3.7-4.3%. Glucose precursor solutions were prepared by diluting 50µL of concentrated H_2SO_4 in 50g of de-ionized water; then 50g of D-glucose was dissolved in the acid solution. The acidified glucose solution was then mixed with the dialyzed 50nm SiO_2 solution to obtain a final glucose concentration ranging from 0.014-0.035g/mL. The samples were then dried at ambient conditions for 3-5 weeks to complete the co-assembly process.

After drying, the samples were heated at 1˚C per minute to 100˚C and soaked for three hours in air; the samples were then heated at 1˚C per minute to 160˚C and soaked for an additional three hours in air. The samples were then placed in a tubular furnace with flowing N_2 gas, heated at 5˚C per minute to 900˚C, and soaked for three hours. The samples were then allowed to cool to room temperature under flowing N_2 gas. The samples were then dissolved in a 30wt% KOH solution under vigorous mixing for three days at ambient conditions. The samples were then collected via centrifugation and the resulting diluent was decanted. The samples were then rinsed with de-ionized water, collected via centrifugation, and re-dispersed in de-ionized water. This process was repeated until a neutral pH was obtained. After the final collection was completed the samples were dried for 12 hours at 70˚C.

Preparation of 3DOm Titania

3DOm titania was prepared via iterative IWI of the SiO_2 nanospheres with an acidified TiO_2 precursor solution. Titanium(IV) ethoxide was hydrolyzed in water by mixing 0.6g of alkoxide with 30mL of de-ionized water. This resulted in the formation of a white precipitate. The solution and precipitate was stirred vigorously for one hour. The precipitated titanium hydroxide gel was then separated via decantation and subsequently dissolved by addition of 0.8g of HCl solution (63.5vol% HCl). This clear precursor solution was then added to a 1.0g portion of dried SiO_2 NP's via nine IWI steps. Between each infiltration step, the powder was dried at 160˚C for 10 minutes and subsequently dried at 100˚C for 24 hours. The composite sample was then calcined at 1˚C per minute to a temperature ranging from 450-773˚C and soaked for five hours. The samples were then etched in a 1.0M aqueous NaOH solution for five days. The resulting 3DOm TiO_2 particles were then separated via decantation, rinsed with H_2O,

and recollected via decantation multiple times until a neutral pH was reached. The 3DOm samples were then dried at 120˚C for further characterization.

Preparation of 3DOm Zirconia

3DOm zirconia was prepared via iterative IWI of the dried colloidal silica nano-templates with a series of zirconium based precursor solutions. Zirconium alkoxide solutions were prepared for IWI by diluting zirconium propoxide ($Zr(OPr)_4$) with ethanol to obtain a final zirconium concentration of 0.3M. Chelation stabilized $Zr(OPr)_4$ solutions were prepared by mixing ethanol, diethylene glycol, and $Zr(OPr)_4$ to obtain a 0.3M zirconium concentration and a 1:2 molar ratio of $Zr(OPr)_4$ to diglycol. Aqueous zirconyl chloride solutions ranging in concentration from 0.1-1.0M were also prepared for IWI. Iterative IWI was performed by drop wise addition of the precursor solution until reaching the incipient wetness point of the SiO_2 template. After IWI, a room temperature drying period was utilized to draw the precursor molecules within the internal pore structure of the SiO_2 template and was followed by further drying at 120˚C. This IWI process was repeated until enough zirconium was added to fill the pore volume of the SiO_2 nanomold. The samples were then calcined at 5˚C per minute to 500˚C, dwelled at the final temperature for three hours, and finally cooled to room temperature. This process was repeated for samples requiring higher temperature calcinations at temperatures ranging from 600-1000˚C.

Preparation of SiO_2-ZrO_2 Co-assembled Materials

A 1.0 M aqueous zirconyl chloride octahydrate stock solution was prepared for co-assembly with the as made silica nanoparticle solutions. The $ZrOCl_2$ solution was mixed with a desired quantity of the SiO_2 nanoparticle suspension in order to form a SiO_2-$ZrOCl_2$ composite

suspension. The zirconium concentration in the composite suspension ranged from 0.75-2.64 wt% and was selected in order to fill 20-100% of the silica's void space with ZrO_2 after calcination. The composite suspensions were then dried for 72 hours at room temperature, forming a SiO_2-$ZrOCl_2$ powdered hydrate. The dried composites were ground with a mortar and pestle and subsequently sieved with a number 40 mesh screen (0.420 mm pores). The samples were then calcined at 5˚C per minute and dwelled at 500˚C for three hours to induce zirconia crystallization. For higher temperature calcination, the co-assembled samples were subsequently calcined in a similar manner at temperatures ranging from 600-1000˚C.

Preparation of Physically Mixed SiO_2 and ZrO_2 Composites

A physical mixture of SiO_2 and ZrO_2 was prepared by grinding a 50nm colloidal silica powder with a hydrated zirconium powder. The hydrated zirconium powder was previously prepared by evaporating a 0.75 wt% $ZrOCl_2$ solution and drying it at 120˚C. The SiO_2 and $ZrOCl_2$ powders were physically ground for 15 minutes using a mortar and pestle to induce surface adhesion. The composite powder was then sieved with a number 40 mesh screen such that particle size remained below 0.420 mm. The powders were then calcined using the methods mentioned above.

Preparation of Unsupported ZrO_2 Control Samples

Unsupported zirconia samples were prepared from an aqueous zirconyl chloride octahydrate ($ZrOCl_2 \bullet 8H_2O$) solution with a zirconium concentration of 0.75 wt%. First, a 1.0 M stock solution was prepared and then subsequently diluted to a desired concentration with de-ionized water. The solution was then dried at room temperature for 72 hours forming a $ZrOCl_2$ hydrated powder. The powder was then ground with a mortar and pestle and sieved with a number 40 mesh screen (0.420 mm pores). Finally, the powders were calcined at 5˚C

per minute to a temperature ranging from 500-1000˚C and dwelled at the final temperature for three hours in order to induce ZrO_2 crystallization.

Characterization

Nitrogen (N_2) was utilized to determine the surface area (S.A.) and pore structure of the resulting 3DOm materials. A Micromeritics ASAP 2020 instrument was employed to measure the volumetric quantity of adsorbed species (cm^3/g STP) retained on the samples during the isothermal adsorption and desorption of gas molecules. Adsorption experiments were conducted at the liquefied temperature of nitrogen (i.e. 77K). The BET theory (Brunauer-Emmett-Teller) was utilized for calculation of surface area.[27] This theory assumes that N_2 adsorbs on the surface of a porous solid in the form of "multimolecular" stacked layers. Calculation of S.A. via the BET theory also accounts for the dynamic equilibrium of adsorbed species with the vapor phase. Pore size distribution within the mesopore range (i.e. 2-50nm) was calculated by using the BJH method (Barrett-Joyner-Halenda) to analyze the desorption portion of the resulting isotherms. [28] The BJH method enables calculation of the critical condensation pressure (P*) necessary for condensation within mesopores by accounting for the thickness of the adsorbed film at a given pressure. Additionally, the Broekhoff-De Boer correction was used to account for the chemical potential of adsorbed species by assuming a cylindrical pore structure.[29]

X-ray diffraction (XRD) was utilized to determine the crystal structure of the as prepared 3DOm oxides. XRD was performed using a Rigaku Miniflex II X-ray diffractometer with Cu K-alpha radiation (K_α=1.5418 Å). The samples were analyzed over the appropriate range (2-theta) necessary to assess the crystallographic structure of each supported oxide. This range included the characteristic t(101), m($11\bar{1}$), and m(111) peaks of zirconia found from 25-

35˚ (2-theta); and the characteristic a(101) and r(110) peaks of titania found in the 20-30˚ region. Analysis of the phase composition of each sample was determined via a weighted average of the integrated characteristic peak intensity of each phase. This was performed for both titania (See **Equation 2-3**) and zirconia (See **Equations 2-4 and 2-5**).[30,31] This calculation resulted in a +/- 3.5 % standard deviation between samples.

$$Volume\ \%_{\ Anatase} = \ 100 * \frac{0.79 I_A}{I_R + 0.79 I_A} \qquad \textbf{Equation 2-3}$$

$$X_{monoclinic} = \frac{I_m(\bar{1}11) + I_m(111)}{I_m(\bar{1}11) + I_m(111) + I_t(101)} \qquad \textbf{Equation 2-4}$$

$$Volume\ \%_{monoclinic} = \frac{1.311\ X_m}{1 + 0.311 X_m} \qquad \textbf{Equation 2-5}$$

$$I_i = \text{Integral intensity of Phase } i$$

The 3DOm products were imaged with various types of electron microscopy. A Hitachi 4300 SE/N scanning electron microscope (SEM) was utilized to collect images of the samples at accelerating voltages ranging from 5-10 kV. The samples were first coated with ~5 nm of iridium via plasma deposition prior to SEM imaging in order to avoid sample charging. A 200 kV JEOL 2000FX transmission electron microscope (TEM), equipped with an Oxford Instruments XEDS system was used to collect images and determine elemental composition via energy dispersive x-ray spectroscopy (EDS). Additionally, an atomic resolution microscope (ARM) was employed to collect high resolution TEM images. The ARM images were collected using a 200 kV aberration-corrected JEOL JEM-ARM200CF instrument. Energy dispersive x-ray mapping (EDS-mapping) was performed during ARM imaging with a Centurio XEDS system. Elemental mapping was performed by detecting the spatial emission of characteristic K-alpha x-rays ($K_{\alpha 1}$) for elements including zirconium (15.7 keV), silicon (1.74 keV), and oxygen (0.52

keV).[32] For TEM imaging, the as prepared samples were deposited on 300 mesh copper microscopy grids with an underlying non-porous carbon film.

Dynamic light scattering (DLS) was utilized to measure the average hydrodynamic radius (R_h) of oligomeric species, small particles, and gels suspended within the metal oxide precursor solutions. A commercial Brookhaven laser spectrometer (BI-9000AT) equipped with a 532nm solid-state laser was utilized to determine the diffusion coefficient (D) of particles in solution via a multichannel digital correlator and processed by the CONTIN Method.[33] The hydrodynamic radius was calculated via the Stokes-Einstein equation: $R_h=K_BT/6\pi\eta D$ where K_B is the Boltzmann constant, η is the viscosity of the solvent, and T is the experimental temperature. The viscosity was approximated as the primary solvent component (ethanol viscosity ~1.074 mPa*S at 25˚C).[34]

2.4 Results and Discussion

Monodisperse colloidal SiO_2 nanospheres where made via a modified Stöber silica process which incorporated TEOS as a silica precursor and an amino acid (L-Lysine) as a buffer. TEOS and similar metal alkoxides found within the transition series remain highly susceptible to hydrolysis and condensation reactions when in the presence of water.[35, 36] These reactions often lead to rapid and highly uncontrolled oligomerization, gelation, and precipitation of hydrated SiO_x gels. Incorporation of L-lysine facilitates the controlled hydrolysis and condensation of TEOS, allowing slow growth of sols within solution by maintaining a basic pH of ~9.[37] Rapid vortex mixing was utilized to twist the condensed gels within solution allowing formation of mondodisperse spherical SiO_2 colloids ranging from ~20-50nm in diameter (See **Figure 2-2**).

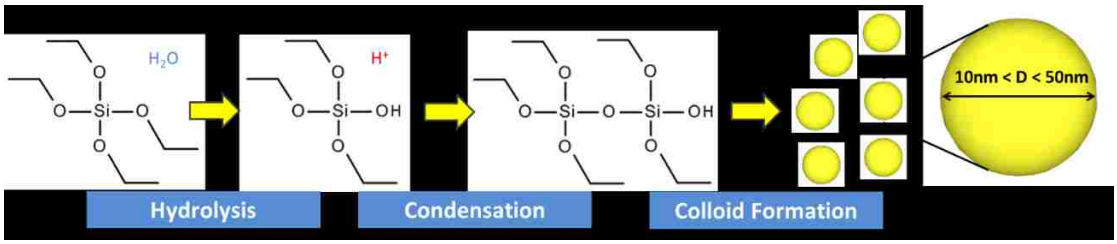

Figure 2-2. The controlled hydrolysis and condensation reaction of TEOS during the formation of colloidal SiO_2 nanoparticles.

A combination of dynamic light scattering and microscopy were utilized to validate the morphology and monodispersity of the as made colloidal SiO_2 nanoparticles. SiO_2 spheres were incrementally grown in size during synthesis by increasing the molar composition of TEOS within the reaction solution (See **Figure 2-3a**). The SiO_2 nanoparticles exhibited a highly monodisperse, spherical morphology when characterized with TEM (See **Figure 2-3b**). Subsequent evaporative drying of the as made colloidal silica solutions facilitated convective driven assembly of the SiO_2 nanoparticles and resulted in large ordered domains of packed SiO_2 nanospheres (See **Figure 2-3c**).

The dried SiO_2 colloidal crystal powders demonstrated a 3DOm structure when analyzed by nitrogen adsorption (See **Figure 2-4**). SiO_2 powders prepared from small SiO_2 particles (e.g. SiO_2 diameter=20nm) exhibited large surface areas (i.e. 231m^2/g) and small pore sizes (i.e. pore width~4nm); conversely SiO_2 powders prepared from larger NP's (e.g. SiO_2 diameter=50nm) exhibited smaller surface areas (i.e. 106m^2/g) but larger pore sizes (i.e. pore width~9nm). Thus, by tuning the diameter of the as made SiO_2 NP's one can tune both the surface area and pore size of the resulting powder.

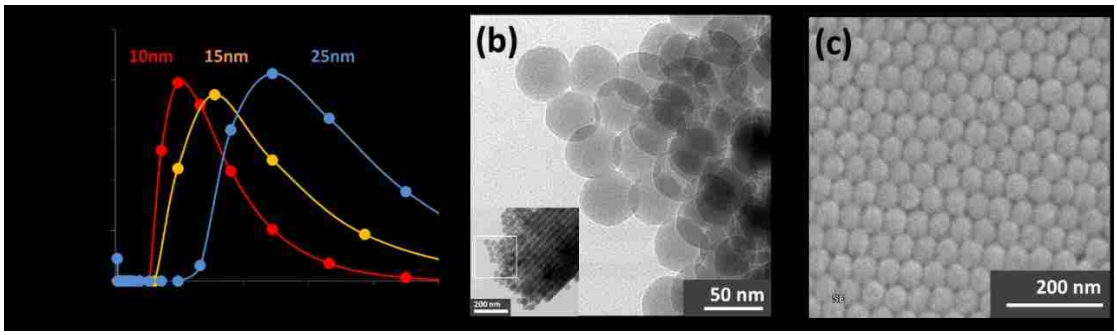

Figure 2-3. Figures demonstrating size control, morphology, and monodispersity of colloidal silica nanoparticles. **(a)** dynamic light scattering measurements of colloidal silica solutions with SiO_2 diameters ranging from 20-50nm; **(b)** TEM image of 40nm silica, a larger view of the particle is presented in the inset; **(c)** SEM image of 34nm colloidal silica nanospheres.

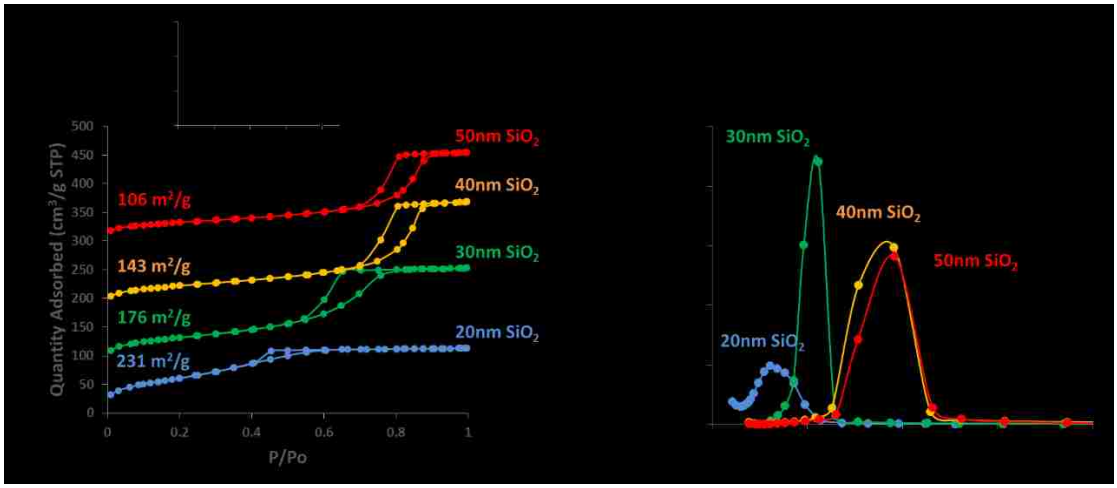

Figure 2-4. N_2 adsorption characterization of size tunable SiO_2-NP's ranging in diameter from 20-50nm. Data includes **(a)** adsorption and desorption isotherms shifted along the y-axis and the resulting BET surface areas (inset); **(b)** BJH pore volume of sintered SiO_2.

High temperature calcination of the 3DOm colloidal SiO_2 powders initiates sintering and results in the loss of both surface area and pore size. When calcining 50nm SiO_2 powders for three hours at 500˚C, a surface area of 106m^2/g is obtained; by raising the temperature to 1000˚C, the powder rapidly sinters and presents a surface area of 50m^2/g (See **Figure 2-5a**). This corresponds to a reduction in pore size as characterized via BJH analysis of the desorption branch of the corresponding isotherms (See **Figure 2-5b**).

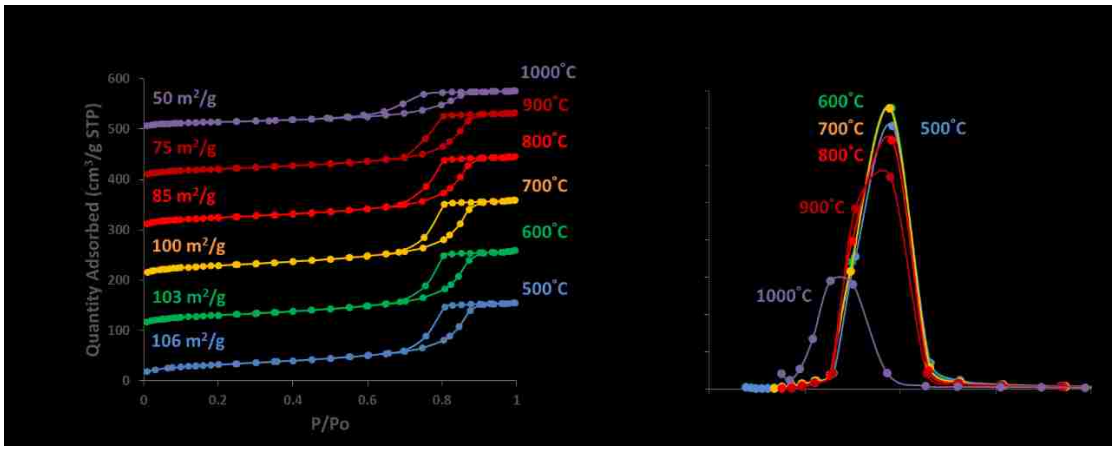

Figure 2-5. N_2 adsorption characterization of sintered 50nm SiO_2 nanoparticles calcined at temperatures ranging from 500-1000˚C for three hours. Data includes **(a)** adsorption and desorption isotherms (shifted along the y-axis); **(b)** BJH pore volume of sintered SiO_2 powders.

Characterization of 3DOm Carbons

Evaporative deposition of 50nm SiO_2 nanoparticles along with a carbon precursor solution facilitated direct one-pot co-assembly of 3DOm carbons. An aqueous glucose precursor solution was utilized for co-assembly due to its stability and resistance to precursor aggregation. This allowed time for the precursor to successfully infiltrate within the pore space of the SiO_2 NP's during evaporative drying (See **Figure 2-6a**). After carbonization and etching, a 3DOm carbon product was revealed (See **Figure 2-6b**). Characterization via N_2 adsorption validated the 3DOm nature of the porous carbons. Large hysteresis loops were observed between the adsorption and desorption branches of the isotherms, signifying the presence of mesopores (See **Figure 2-6c**). Mesoporosity was further confirmed via BJH analysis which shows a 3DOm pore size on the order of 50nm, roughly equal to the original diameter of the SiO_2 nanoparticles (See **Figure 2-6d**).

Calculation of the BET surface area in the 3DOm samples demonstrates that the surface area can be tuned by altering the glucose concentration within solution (See **Figure 2-6c**). Variation in glucose concentration from 0.014 to 0.035g/mL alters the degree of precursor

condensation during synthesis and results in systematic variation in microporosity in the 3DOm carbons. Thus, the solution space for precursor preparation provides an additional handle for tuning surface area within the walls of the 3DOm carbon samples. These findings validate hard templating as a means of directly synthesizing mesoporous materials with colloidal silica nanospheres.[38,39]

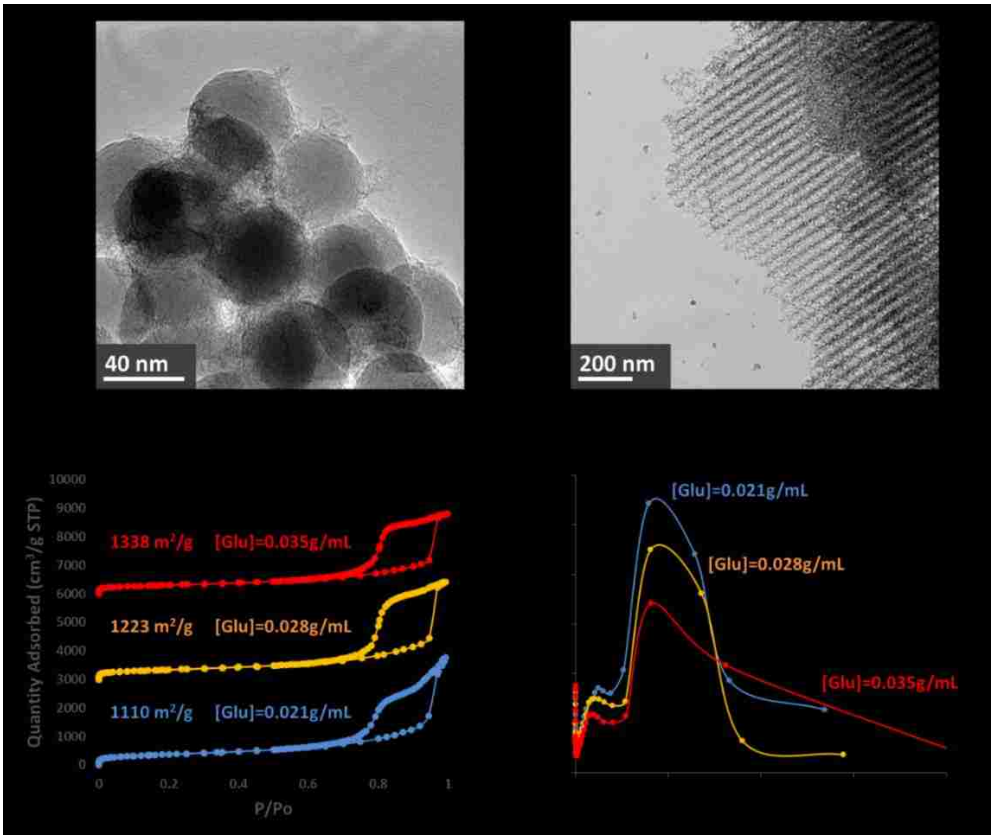

Figure 2-6. Characterization of the 3DOm carbon samples: **(a)** TEM image of a composite sample consisting of 50nm SiO_2 NP's and carbon after carbonization under flowing N_2 at 900˚C; **(b)** TEM image of a 3DOm carbon sample after removal of the template; **(c)** Nitrogen adsorption isotherms of 3DOm carbons prepared via coassembly; **(d)** BJH pore size distribution of 3DOm carbons. *Isotherm data and sample preparation was conducted in collaboration with Dr. Zheng Tian.*

Characterization of 3DOm Titania

IWI of the colloidal SiO_2 nanospheres with a TiO_2 precursor solution facilitated the formation of 3DOm titania. The precursor solution was observed to decorate the surface of

the SiO_2 NPs and infiltrate the internal pore structure of the powder as demonstrated in **Figure 2-7a**. Stabilization of the metastable anatase TiO_2 phase was observed after high temperature calcination of the composite TiO_2/SiO_2 materials. This is confirmed by the presence of the anatase (101) peak at ~25.3˚ (2θ) in the composite TiO_2/SiO_2 samples after 773˚C calcination (See **Figure 2-7b**). Untemplated TiO_2 control powders prepared from the same precursor solution were shown to rapidly convert the rutile phase after calcination at 773˚C as noted by the presence of the r(110) peak at ~27.5˚ (2θ).

Removal of the 3DOm template via alkali etching revealed the presence of a 3DOm TiO_2 honeycomb structure (See **Figure 2-7c**). Characterization of the 3DOm titanias with nitrogen adsorption revealed the presence of hysteresis loops between the adsorption and desorption branches of the isotherms (See **Figure 2-7d**). Hysteresis loops form as a result of capillary condensation of N_2 within mesopores and signifies the presence of mesoporosity within the templated samples. Mesoporosity was also confirmed via BJH analysis of the desorption portion of the isotherm (See inset of **Figure 2-7d**). Thus, 3DOm TiO_2 templating facilitated not only the control of porosity but also the stabilization of the metastable anatase phase of titania.

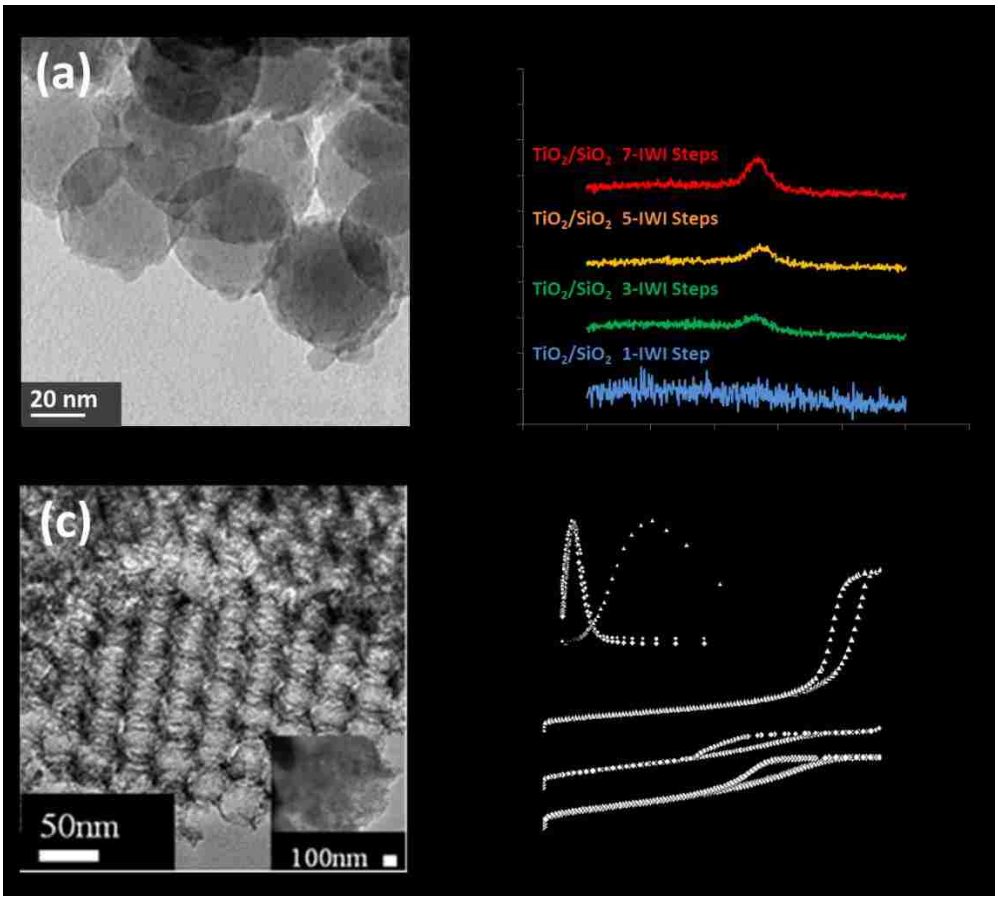

Figure 2-7. Characterization during preparation of 3DOm TiO_2: **(a)** TEM image of a composite TiO_2/SiO_2 sample; **(b)** XRD comparison of TiO_2/SiO_2 composite samples calcined at 773˚C with an untemplated TiO_2 control powder calcined at 773˚C; **(c)** TEM image of a 3DOm TiO_2 sample after removal of the template; **(d)** N_2 adsorption isotherms and BJH pore size distribution (inset) collected from 3DOm TiO_2 samples. *Isotherm data and sample preparation was conducted in collaboration with Qianying Guo.*

3DOm Zirconia – A Case Study in Hard Templating

In order to successfully template the 3DOm SiO_2 powders with a second material, one must first infiltrate the silica molds with a chemical precursor. This is often achieved via a solvent based route which utilizes multiple IWI steps to deposit the precursor[40] or via submersion of the mold within a precursor solution and subsequent hydrothermal growth of the second material within the 3DOm template.[41,42] After infiltration, the precursor is often

cured at elevated temperatures to induce crystallization. The SiO_2 mold is then subsequently removed via alkali etching (e.g. KOH or NaOH).

In order to successfully accomplish infiltration of a 3DOm template with a chemical precursor, one must first select a precursor that does not extensively aggregate or agglomerate within solution. A series of chemical precursors were utilized to attempt infiltration of the 3DOm SiO_2 molds; these materials include metal alkoxides, chelated metal alkoxides, and metal oxy-halides. Dynamic light scattering was used to assess particle size in solution to determine if the chemical precursor was small enough to be deposited within the pore structure of the 3DOm SiO_2 nanomolds (See **Figure 2-8**).

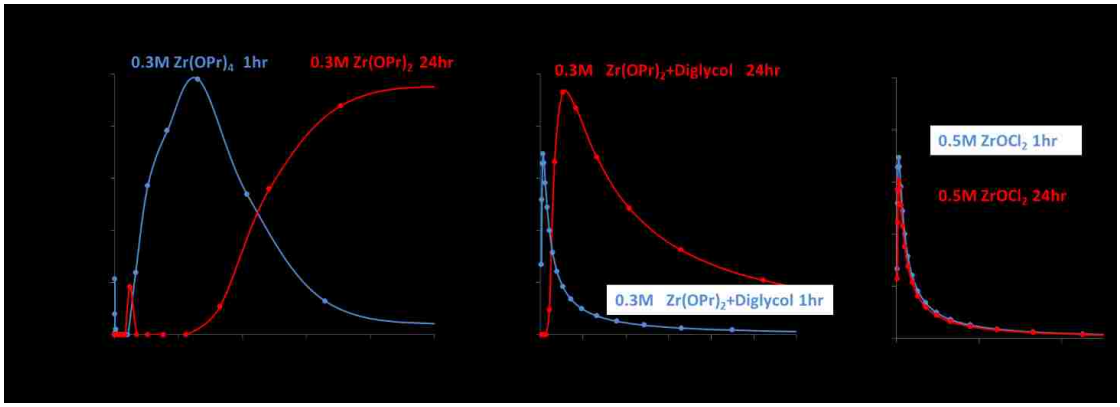

Figure 2-8. Dynamic light scattering measurements of ZrO_2 precursor solutions. **(a)** DLS of 0.3M zirconium propoxide solutions; **(b)** DLS of 0.3M zirconium propoxide solutions stabilized with diglycol; **(c)** DLS of aqueous zirconyl chloride solutions.

Rapid gelation of unstabilized metal alkoxides was observed simply by diluting commercial $Zr(OPr)_4$ solutions with ethanol under ambient conditions; this was confirmed with DLS as the particle size within a 0.3M $Zr(OPr)_4$ solution was found to be hundreds of nanometers in size (See **Figure 2-8a**). Transition metal alkoxides are highly susceptible to hydrolysis and condensation reactions in the presence of moisture and rapidly precipitate by the addition of even trace quantities of water.[43] Thus, alkoxide gelation prevented successful

infiltration of the SiO_2 nanomolds as the chemical precursors were confined in large suspended gels much larger than the 3DOm SiO_2 pore structure.

Polydentate ligands such as acetylacetonate,[44,45] acetic acid,[46] alkanolamines,[47] and diols[48] can be used to control the rate of hydrolysis and condensation during the production of metal oxides.[49] Multi-dentate ligands bind to the central metal atom at several points and sterically hinder condensation reactions from occuring.[50] Thus diglycol, a multi-dentate chelating group, was mixed with the 0.3M $Zr(OPr)_4$ solution in order to bind with the central zirconium atom in the complex and prevent condensation during infiltration of the 3DOm SiO_2 templates.[51] This technique was successful in limiting growth of the $Zr(OPr)_4$ gel within solution as particles only a few nanometers in size were detected with DLS (See **Figure 2-8b**). However, the $Zr(OPr)_4$ solution was found to slowly oligomerize over the course of time forming small particles on the order of ~8nm.

Zirconyl chloride octahydrate ($ZrOCl_2 \bullet 8H_2O$) and zirconium(IV) oxynitrates ($ZrO(NO_3)_2 \bullet xH_2O$) were found most suitable for infiltration of the 3DOm SiO_2 templates. These materials remain highly acidic in solution due to the presence of counter ions, which inhibit condensation. Particle size in solution was observed to be only ~1nm as measured by DLS (See **Figure 2-8c**). Furthermore, the solutions remained stable for several days without significant precursor condensation. Thus, these materials were utilized for infiltration of the 3DOm SiO_2 templates (See **Figure 2-9a**).

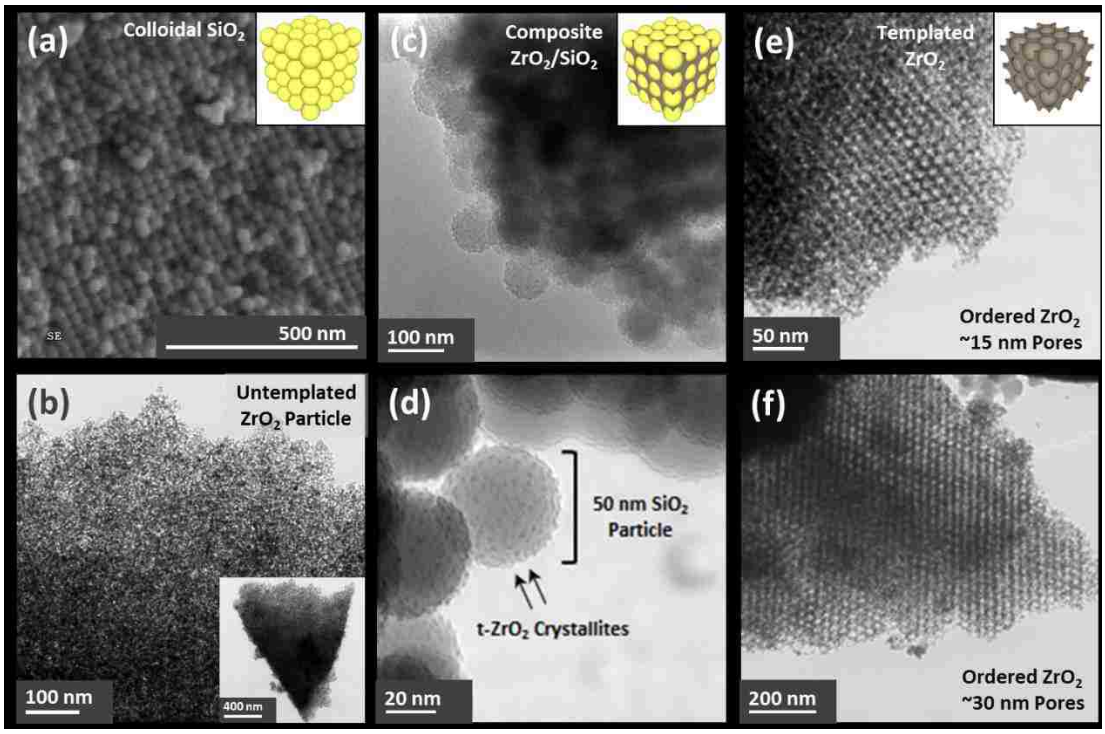

Figure 2-9. Microsocpy images of various silica and zirconia materials calcined for three hours at 500˚C. **(a)** SEM image of colloidal SiO_2 templates; **(b)** TEM image of ZrO_2 prepared from a 0.3M $Zr(OPr)_4$ precursor solution; **(c)** TEM of a composite ZrO_2/SiO_2 sample; **(d)** A TEM image of a composite ZrO_2/SiO_2 sample which demonstrates ZrO_2 surface decoration; **(e)** A TEM image of a ZrO_2 particle templated from a 20nm colloidal SiO_2 template; **(f)** A TEM image of ZrO_2 particle templated from a 30nm colloidal SiO_2 template.

Zirconia control powders were prepared by evaporative drying of 1.0M $ZrOCl_2$ solutions and subsequently calcined at temperatures ranging from 500-1000˚C. This produced untemplated ZrO_2 powders with a rough and disordered morphology (See **Figure 2-9b**). 3DOm ZrO_2 powders were prepared in a similar process used during the preparation of 3DOm TiO_2 materials. 1.0M $ZrOCl_2$ solutions were infiltrated within the 3DOm SiO_2 molds via iterative IWI. Subsequent calcination, resulted in the formation of decorated ZrO_2/SiO_2 composite samples (See **Figure 2-9c** and **Figure 2-9d**). Removal of the 3DOm SiO_2 template revealed the presence of 3DOm ZrO_2 materials with an ordered honeycomb morphology and some additional untemplated ZrO_2 particles (See **Figure 2-9e** and **Figure 2-9f**).

A 3DOm ZrO_2 powder was prepared by templating a 30nm colloidal SiO_2 powder with a 1.0M $ZrOCl_2$ solution. **Figure 2-10a** presents the adosorption and desorption isotherms of this sample versus an untemplated ZrO_2 control powder, as characterized by means of N_2 adsorption. The untemplated control powder had a low surface area of only $16m^2/g$ while the 3DOm ZrO_2 sample presented a surface area of to $178m^2/g$; over an order of magnitude larger than the control sample. Additionally, a much larger hysteresis volume was presented by the 3DOm sample; this validates templating as a means of promoting mesoporosity. BJH analysis confirmed that the templated ZrO_2 sample exhibited a significant promotion in mesopore content within the 20nm pore range (See **Figure 2-10b**). These results validate 3DOm templating as a means of synthesizing pore size tunable materials with large surface areas.

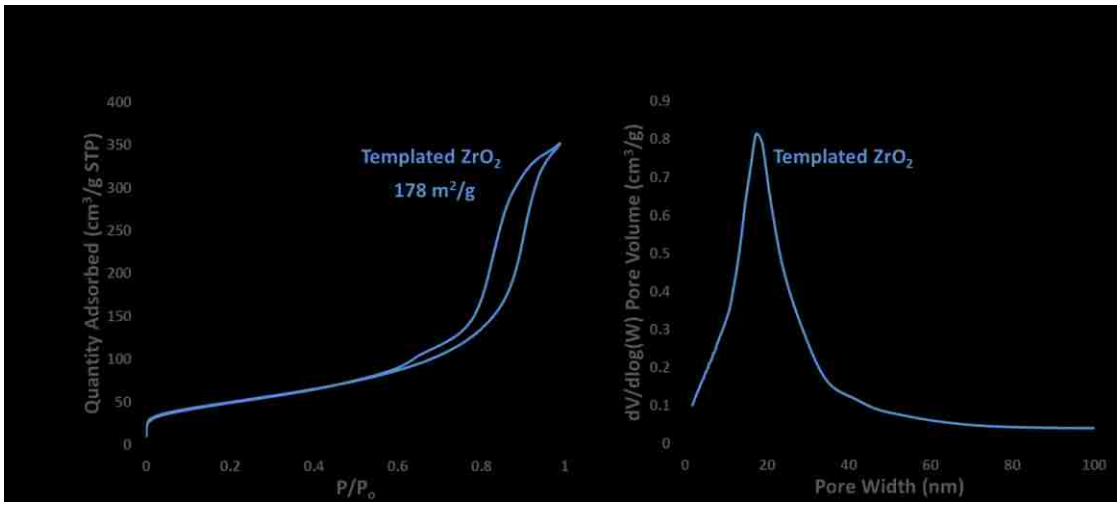

Figure 2-10. N_2 adsorption characterization of an untemplated ZrO_2 control sample and a 3DOm ZrO_2 sample prepared via hard templating with a ~30nm SiO_2 colloidal crystal template. **(a)** Measured adsorption and desorption isotherms of the samples. **(b)** BJH analysis of the corresponding isotherms.

XRD was used to assess the phase content in templated versus untemplated ZrO_2 samples. The tetragonal phase of zirconia developed after calcination at 500˚C in the unsupported $ZrOCl_2$ samples. This is observed by the formation of the t(101) peak in the 30˚ (2-theta) region of the diffractogram presented in **Figure 2-11**. As the unsupported ZrO_2 is

calcined to higher temperatures the t(101) peak is shown to shift to lower 2-theta values. This is a result indicative of uniform crystalline strain caused by the phase transformation to m-ZrO_2. The development of m-ZrO_2 effectively distorts the atomic lattice of the t-ZrO_2 crystals and shifts the tetragonal peak. The monoclinic phase of zirconia quickly develops when calcining unsupported ZrO_2 at temperatures ranging from 500-700˚C. This is observed by the formation of peaks in the 28˚ and 31.5˚ (2-theta) region of the diffractogram. These peaks correspond to the monoclinic m($\bar{1}$11) and m(111) planes respectively.[52] The onset of m-ZrO_2 formation corresponds to a reduction of the t(101) peak and signifies transformation of the metastable t-ZrO_2 phase into the more thermodynamically favorable m-ZrO_2 phase. Calcination above 800˚C transforms the sample into nearly pure m-ZrO_2.

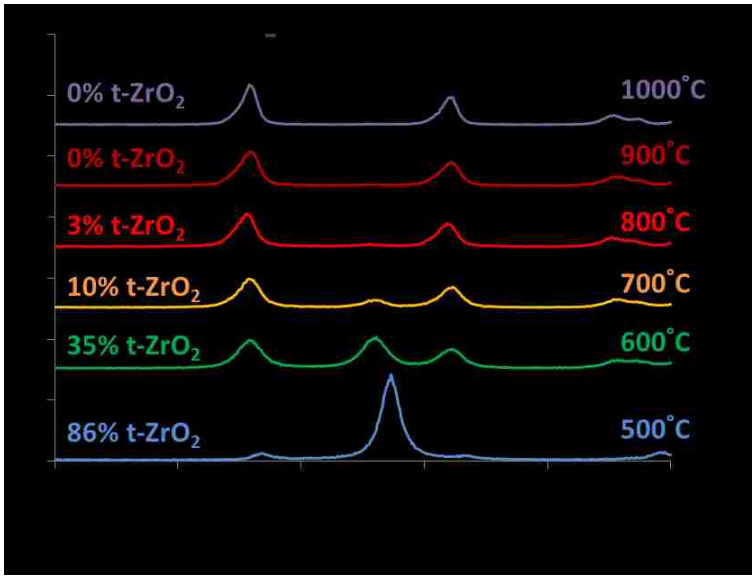

Figure 2-11. Unsupported zirconia dried from a $ZrOCl_2$ precursor solution and calcined to 500˚C. The sample was then subsequently calcined to higher temperatures ranging from 600-1000˚C.

The phase evolution of the templated ZrO_2 materials was assessed at temperatures ranging from 500-1000˚C using XRD. Both the un-etched ZrO_2/SiO_2 composite sample (See

Figure 2-12a) and the etched sample (See **Figure 2-12b**) demonstrated the ability to stabilize the tetragonal phase even after calcination at 1000˚C. This was noted by the preservation of the t(101) peak and limited development of the monoclinic peaks when comparing **Figure 2-11** to **Figure 2-12**. This demonstrates that the SiO_2 template actively mitigated the t-ZrO_2 to m-ZrO_2 phase transformation from occurring. It is hypothesized that silica doping is responsible for stabilization of the tetragonal phase in the etched sample. The residual silica likely grafts to the surface ZrO_2 hydroxyl groups, stabilizing the surface of the metastable ZrO_2 phase.[53]

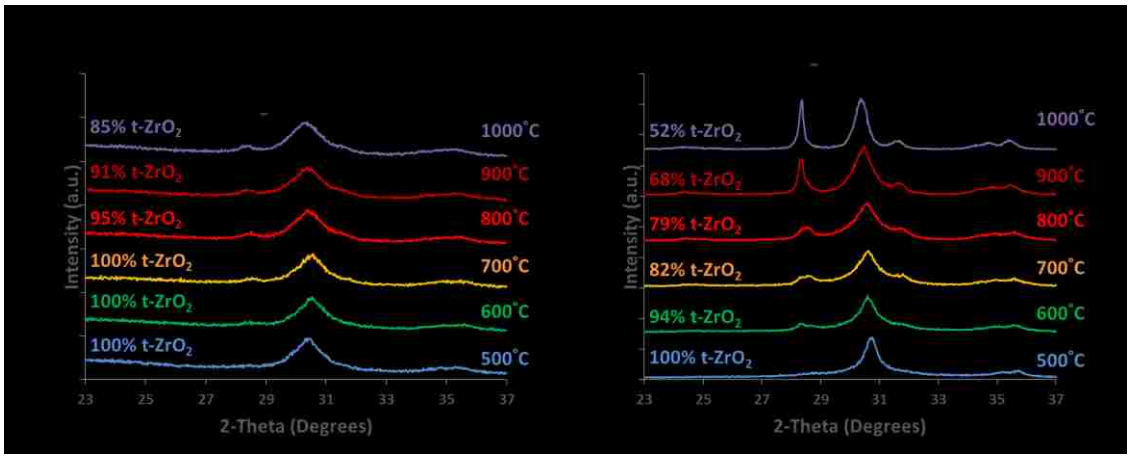

Figure 2-12. XRD of **(a)** a composite ZrO_2/SiO_2 prepared via incipient wetness with a $ZrOCl_2$ solution and a colloidal SiO_2 template; **(b)** a templated ZrO_2 sample after calcination and etching.

A one-pot synthetic co-assembly technique was conducted in order to produce ZrO_2/SiO_2 composite samples for further analysis of t-ZrO_2 preservation when in contact with SiO_2. Enough zirconium was present in solution to fill 20% of the silica's void space with ZrO_2 after drying and calcination. This ratio ensured that upon drying of the solution, the ZrO_2 would be in full contact with the silica nanoparticles. This co-assembly technique demonstrated t-ZrO_2 phase stabilization up to 1000˚C without the development of m-ZrO_2 (See **Figure 2-13a**).

A physical mixture of SiO_2 and ZrO_2 was prepared by mixing the hydrated $ZrOCl_2$ powder (i.e. $ZrOH_x$ as dried from the 0.75 wt% $ZrOCl_2$ solution) and a dried 50nm colloidal silica

powder. Enough hydrated $ZrOH_x$ powder was mixed with the silica in order to fill 100% of the silica's void space with ZrO_2 after calcination. This preparation technique was found to stabilize the tetragonal phase of zirconia only slightly, as the t(101) peak was still preserved at 1000˚C (See **Figure 2-13b**). A large amount of m-ZrO_2 had developed in these samples and is likely due the transformation of excess t-ZrO_2 particles which were not direct contact with the silica.

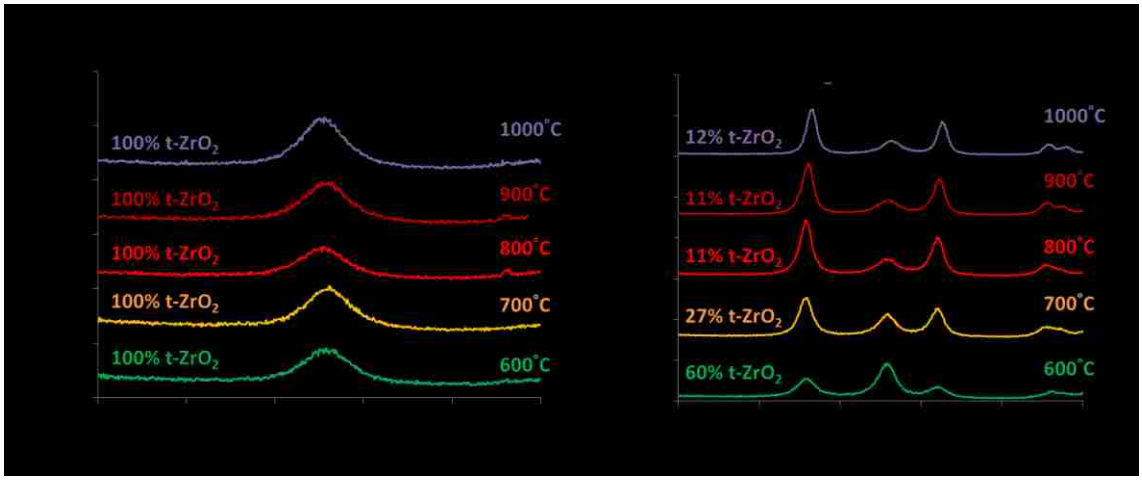

Figure 2-13. XRD data of **(a)** ZrO_2/SiO_2 composite samples prepared via coassembly of a $ZrOCl_2$ solution and colloidal SiO_2 particles. The samples were calcined to 550˚C to induce crystallization of ZrO_2 and subsequently calcined to higher temperatures ranging from 600-1000˚C; **(b)** ZrO_2/SiO_2 prepared from a physical mixture of $ZrOH_x$ powder and 50nm colloidal SiO_2 powder. The samples were calcined to 550˚C to induce crystallization of the ZrO_2. The samples were then subsequently calcined to higher temperatures ranging from 600-1000˚C.

Summary of t-ZrO_2 Stabilization

The unsupported zirconia sample was found to rapidly transform into m-ZrO_2 when calcined from 500-800˚C (See **Figure 2-14**). The tetragonal phase was not detected in this sample after calcination at 1000˚C. The presence of silica was found to preserve the tetragonal phase in the ZrO_2/SiO_2 composite samples prepared by means of physical powder mixing, incipient wetness, and co-assembly. The co-assembly method provided the best technique for stabilization as the monoclinic phase was not detected after calcination to 1000˚C. This sample utilized a relatively low loading of ZrO_2 (i.e. 20% of the SiO_2 void space) and evenly distributed

the ZrO_2 throughout the SiO_2 template during the co-assembly process. Similarly, only a small amount of m-ZrO_2 was detected after calcination at 1000˚C in samples prepared via IWI (See **Figure 2-14**). The IWI process allows significant deposition of the ZrO_2 precursor into the void space of the 3DOm SiO_2 template and provides thorough contact between the ZrO_2 and SiO_2. By simply preparing a physical mixture of $ZrOCl_2$ and SiO_2 powders, approximately 10% of the zirconia could be preserved as t-ZrO_2, even after calcination to 1000˚C. However, this sample exhibited a significant transformation from t-ZrO_2 to m-ZrO_2. Only limited contact between the ZrO_2 precursor and the SiO_2 template can be achieved by physically mixing the two powders. It is believed that the SiO_2 phase interacts with ZrO_2 surface hydroxyls and stabilizes the surface of the metastable t-ZrO_2 phase by more fully coordinating the zirconia.

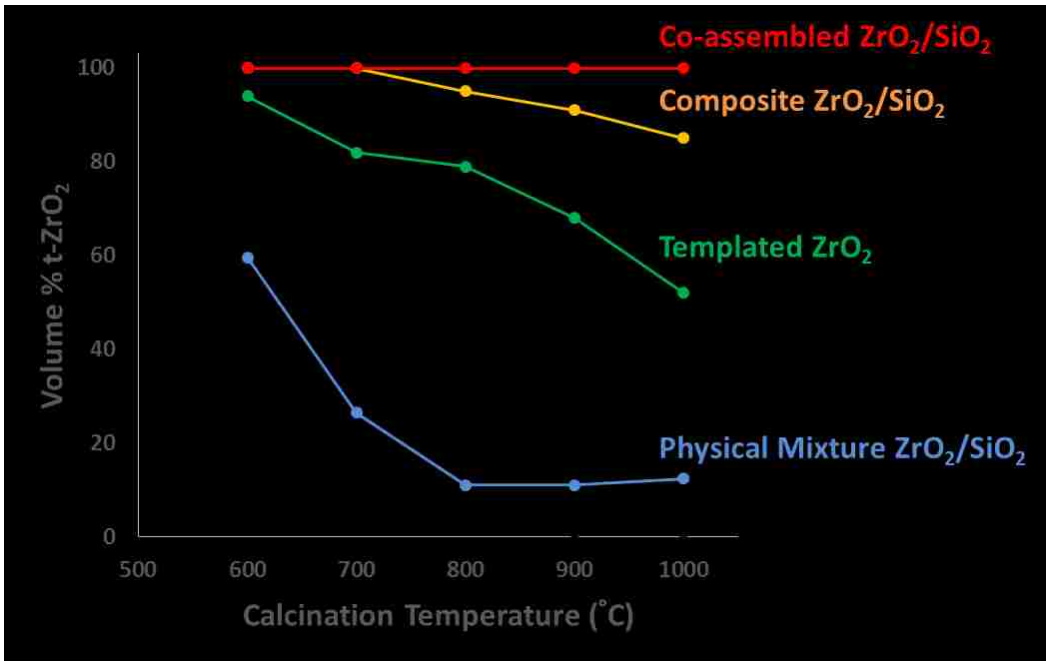

Figure 2-14. Compiled XRD data calculating the volume fraction of the tetragonal phase of ZrO_2 in various ZrO_2 and ZrO_2/SiO_2 samples.

These results support the theory that a metastable oxide such as t-ZrO_2 can be stabilized by the incorporation of a surface oxide to limit surface strains, coordinate the

surface, and stabilize the material at high temperatures. This was best demonstrated in the samples that most readily dispersed the ZrO_2 precursor along the silica's surface. The physical mixing technique provided a transitional scenario as it demonstrated stabilization of t-ZrO_2 at high temperatures but still allowed the development of m-ZrO_2. This development of m-ZrO_2 is likely a result of limited contact between the two oxides. These general concepts could be applied for the stabilization of other catalytic materials at high temperatures.

Generalization of Surface Stabilization

Interfacial surface stabilization was observed for both titania and zirconia during IWI of 3DOm colloidal SiO_2 templates (See **Figure 2-7b** and **Figure 2-12a**). Therefore, interfacial stabilization is a general phenomenon between mesoporous oxides and a second supporting phase. High resolution microscopy demonstrated the affinity for interfacial stabilization of both the TiO_2/SiO_2 and ZrO_2/SiO_2 samples (See **Figure 2-15**). The metastable oxide phases were located in the SiO_2 crevices (See **Figure 2-15a**), maximizing contact with the SiO_2 layer. Additionally, the amorphous SiO_2 layer was observed to coat the surface of the TiO_2 nanocrystals (See **Figure 2-15d**), confirming interfacial contact as a stabilization phenomenon.

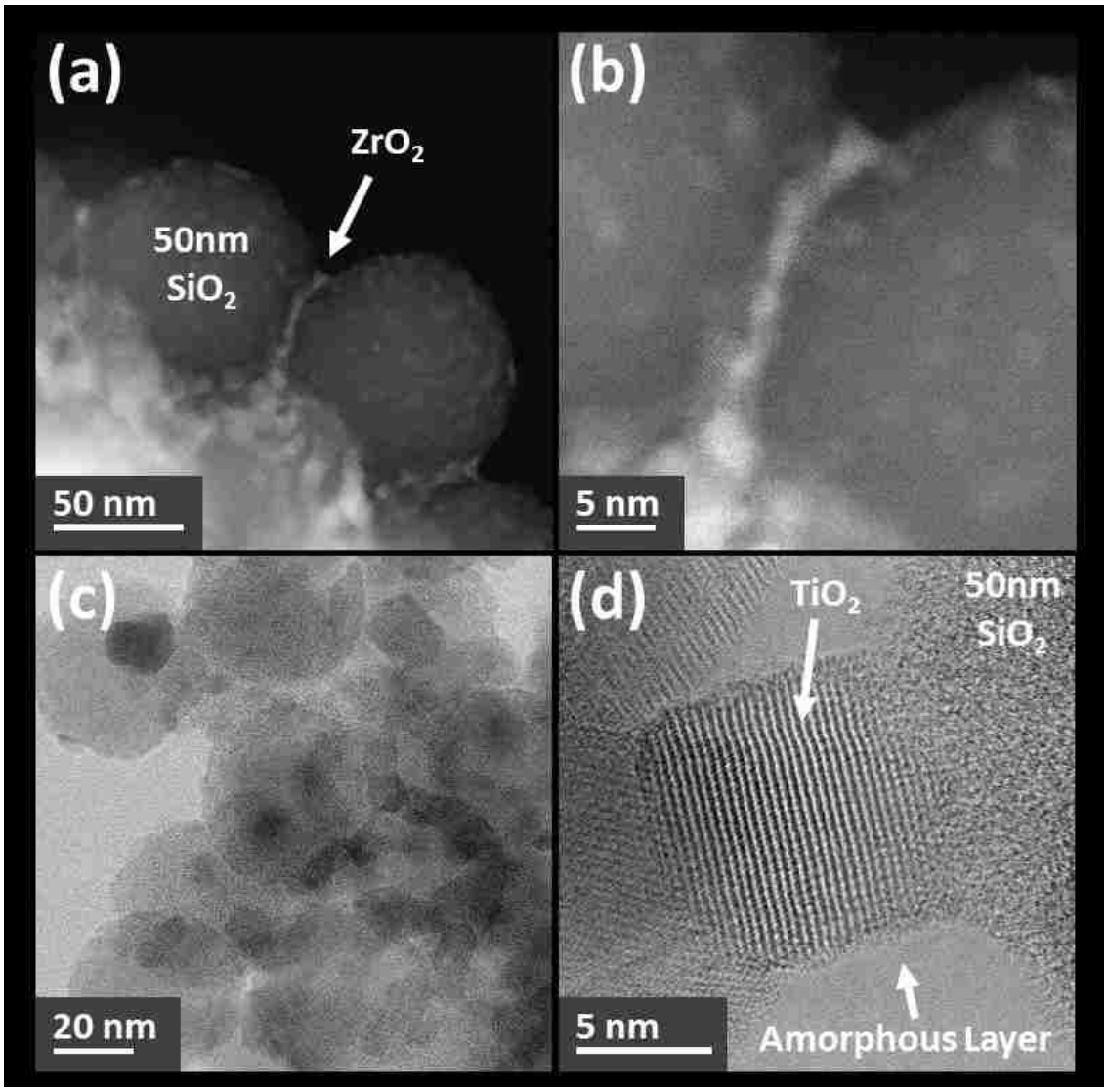

Figure 2-15. ARM of the composite ZrO_2/SiO_2 and TiO_2/SiO_2 samples prepared via IWI reveal the large contact area of the metastable oxide with the SiO_2 template. **(a-b)** ZrO_2/SiO_2 prepared via IWI and calcined at 600˚C. **(c-d)** TiO_2/SiO_2 prepared via IWI and calcined at 773˚C.

2.5 Conclusions

Mesoporous templating was demonstrated as a valid synthetic approach for the production of 3DOm carbon, titania, and zirconia. Size tunable colloidal SiO_2 nanoparticles ranging in size form 20-50nm were synthesized via a buffered hydrolysis and condensation reaction. The resulting 3DOm colloidal crystal templates were subsequently infiltrated with

chemical precursors, cured at elevated temperatures, and subsequently etched away to reveal molded 3DOm materials. By altering the diameter of the colloidal SiO_2 nanospheres, one can successfully tune the surface area and pore size of the resulting 3DOm product. This synthesis route provides a direct means of optimizing the internal pore structure of a material in order to reduce transport limiting effects during catalytic and adsorbent processing. Additionally, the incorporation of a hard template was observed to stabilize metastable crystal structures including the t-ZrO_2 and a-TiO_2 phase. This concept was demonstrated further by preparing a series of ZrO_2/SiO_2 samples. It is hypothesized that the SiO_2 template acts to more fully coordinate the surface of the metastable oxide phase, graft with surface hydroxyl groups, and prevent phase transformation from initiating at the surface of the oxide. Thus, hard templating provides a means for tuning surface area, pore size, and polymorphism during the production of 3DOm products.

2.6 References

[1] Chorkendorff, I., and J.W Niemantsverdriet. "5.8.2.1 Transport Limitations and the Thiele Diffusion Modulus." *Concepts of Modern Catalysis and Kinetics*. Weinheim: Wiley-VCH, 2007. 207-15.

[2] Boudart, Michel. "Chapter 7. Irreducible Transport Phenomena in Chemical Kinetics." *Kinetics of Chemical Processes*. Englewood Cliffs, NJ: Prentice-Hall, 1968. 144-64.

[3] Boudart, Michel, and G. Djéga-Mariadassou. "Chapter 6. Parasitic Phenomena." *Kinetics of Heterogeneous Catalytic Reactions*. Princeton, NJ: Princeton UP, 1984. 194-201.

[4] Bird, R. Byron, Warren E. Stewart, and Edwin N. Lightfoot. "17.6 Diffusion and Chemical Reaction Inside a Porous Catalyst: The "Effectiveness Factor"" *Transport Phenomena*. New York: Wiley, 1960. 542-47.

[5] Roberts, G. W. "The Effective Diffusion Coefficient." *Chemical Reactions and Chemical Reactors*. Hoboken, NJ: John Wiley & Sons, 2009. 318-27.

[6] Deen, William M. "Chapter 1 Diffusive Fluxes and Material Properties." *Analysis of Transport Phenomena*. New York: Oxford UP, 1998. 25.

[7] Froment, Gilbert F., and Kenneth B. Bischoff. "3.4 Molecular, Knudsen, and Surface Diffusion in Pores." *Chemical Reactor Analysis and Design*. 3rd ed. New York: Wiley, 1979. 172-76.

[8] Rouquerol, J., D. Avnir, C. W. Fairbridge, D. H. Everett, J. M. Haynes, N. Pernicone, J. D. F. Ramsay, K. S. W. Sing, and K. K. Unger. "Recommendations for the Characterization of Porous Solids (Technical Report)." *Pure and Applied Chemistry* 66.8 (1994): 1739-758.

[9] Sing, K. S. W. "Reporting Physisorption Data for Gas/solid Systems with Special Reference to the Determination of Surface Area and Porosity (Provisional)." *Pure and Applied Chemistry* 54.11 (1982): 2201-2218.

[10] Sing, K. S. W. "Reporting Physisorption Data for Gas/solid Systems with Special Reference to the Determination of Surface Area and Porosity (Recommendations 1984)." *Pure and Applied Chemistry*57.4 (1985): 603-05.

[11]Schüth, Ferdi. "Endo- and Exotemplating to Create High-Surface-Area Inorganic Materials." *Angewandte Chemie International Edition Angew. Chem. Int. Ed.* 42.31 (2003): 3604-622.

[12] García-Martínez, Javier, Marvin Johnson, Julia Valla, Kunhao Li, and Jackie Y. Ying. "Mesostructured Zeolite Y—high Hydrothermal Stability and Superior FCC Catalytic Performance." *Catal. Sci. Technol. Catalysis Science & Technology* 2.5 (2012): 987-94.

[13]Li, Kunhao, Julia Valla, and Javier Garcia-Martinez. "Realizing the Commercial Potential of Hierarchical Zeolites: New Opportunities in Catalytic Cracking." *ChemCatChem* 6.1 (2013): 46-66.

[14]Schüth, Ferdi. "Non-siliceous Mesostructured and Mesoporous Materials †." *Chemistry of Materials Chem. Mater.* 13.10 (2001): 3184-195.

[15] Argauer, Robert J., and George R. Landolt. Crystalline Zeolite Zsm-5 and Method of Preparing the Same. Mobil Oil Corporation, assignee. Patent 3,702,886. 14 Nov. 1972.

[16] Beck, J. S., J. C. Vartuli, W. J. Roth, M. E. Leonowicz, C. T. Kresge, K. D. Schmitt, C. T. W. Chu, D. H. Olson, E. W. Sheppard, S. B. Mccullen, J. B. Higgins, and J. L. Schlenker. "A New Family of Mesoporous Molecular Sieves Prepared with Liquid Crystal Templates." *J. Am. Chem. Soc. Journal of the American Chemical Society* 114.27 (1992): 10834-0843.

[17] Wan, Ying, and Zhao. "On the Controllable Soft-Templating Approach to Mesoporous Silicates." *Chemical Reviews Chem. Rev.*107.7 (2007): 2821-860.

[18] Zhao, Dongyuan, Qisheng Huo, Jianglin Feng, Bradley F. Chmelka, and Galen D. Stucky. "Nonionic Triblock and Star Diblock Copolymer and Oligomeric Surfactant Syntheses of Highly Ordered, Hydrothermally Stable, Mesoporous Silica Structures."*J. Am. Chem. Soc. Journal of the American Chemical Society* 120.24 (1998): 6024-036.

[19] Kleitz, Freddy, Shin Hei Choi, and Ryong Ryoo. "Cubic *Ia3d* Large Mesoporous Silica: Synthesis and Replication to Platinum Nanowires, Carbon Nanorods and Carbon Nanotubes" *Chemical Communications* 17 (2003): 2136-2137.

[20] Deshmane, Vishwanath G., and Yusuf G. Adewuyi. "Synthesis of Thermally Stable, High Surface Area, Nanocrystalline Mesoporous Tetragonal Zirconium Dioxide (ZrO_2): Effects of Different Process Parameters." *Microporous and Mesoporous Materials* 148.1 (2012): 88-100.

[21]Chen, Huiyong, James Wydra, Xueyi Zhang, Pyung-Soo Lee, Zhuopeng Wang, Wei Fan, and Michael Tsapatsis. "Hydrothermal Synthesis of Zeolites with Three-Dimensionally Ordered Mesoporous-Imprinted Structure." *J. Am. Chem. Soc. Journal of the American Chemical Society* 133.32 (2011): 12390-2393.

[22] Joo, Sang Hoon, Jeong Young Park, Chia-Kuang Tsung, Yusuke Yamada, Peidong Yang, and Gabor A. Somorjai. "Thermally Stable Pt/mesoporous Silica Core–shell Nanocatalysts for High-temperature Reactions." *Nature Materials Nat Mater* 8.2 (2008): 126-31.

[23]Arnal, Pablo M., Massimiliano Comotti, and Ferdi Schüth. "High-Temperature-Stable Catalysts by Hollow Sphere Encapsulation."*Angewandte Chemie Angew. Chem.* 118.48 (2006): 8404-407.

[24]Stein, Andreas. "Sphere Templating Methods for Periodic Porous Solids." *Microporous and Mesoporous Materials* 44-45 (2001): 227-39.

[25] Fan, Wei, Mark A. Snyder, Sandeep Kumar, Pyung-Soo Lee, Won Cheol Yoo, Alon V. Mccormick, R. Lee Penn, Andreas Stein, and Michael Tsapatsis. "Hierarchical Nanofabrication of microporous Crystals with Ordered Mesoporosity." *Nature Materials Nat Mater* 7.12 (2008): 984-91.

[26] Stöber, Werner, Arthur Fink, and Ernst Bohn. "Controlled Growth of Monodisperse Silica Spheres in the Micron Size Range."*Journal of Colloid and Interface Science* 26.1 (1968): 62-69.

[27] Brunauer, Stephen, P. H. Emmett, and Edward Teller. "Adsorption of Gases in Multimolecular Layers." *J. Am. Chem. Soc. Journal of the American Chemical Society* 60.2 (1938): 309-19.

[28] Barrett, Elliott P., Leslie G. Joyner, and Paul P. Halenda. "The Determination of Pore Volume and Area Distributions in Porous Substances. I. Computations from Nitrogen Isotherms." *J. Am. Chem. Soc. Journal of the American Chemical Society* 73.1 (1951): 373-80.

[29] Webb, Paul, and Clyde Orr. *Analytical Methods in Fine Particle Technology*. Norcross, GA: Micromeritics Instrument, 1997.

[30] Spurr, R. A., and Howard Myers. "Quantitative Analysis of Anatase-Rutile Mixtures with an X-Ray Diffractometer." *Analytical Chemistry* 29.5 *(*1957): 760-762.

[31] Toraya, H., M. Yoshimura, and S. Somiya. "Calibration Curve for Quantitative Analysis of the Monclinic-tetragonal ZrO_2 System by X-ray Diffraction." *Journal of the American Ceramic Society* 67.6 (1984): C-119--121.

[32] Bearden, J. A. "X-Ray Wavelengths." *Reviews of Modern Physics Rev. Mod. Phys.* 39.1 (1967): 78-124.

[33] Provencher, Stephen W. "A Constrained Regularization Method for Inverting Data Represented by Linear Algebraic or Integral Equations." *Computer Physics Communications* 27.3 (1982): 213-27.

[34] Lide, David R. "Section 6: Fluid Properties - Viscosity of Liquids." *CRC Handbook of Chemistry and Physics: A Ready-reference Book of Chemical and Physical Data*. 85th ed. Boca Raton, FL: CRC, 2004. 6-203--205.

[35] Iler, Ralph K. *The Chemistry of Silica: Solubility, Polymerization, Colloid and Surface Properties, and Biochemistry*. New York: Wiley, 1979.

[36] Bradley, D. C., R. C. Mehrotra, and D. P. Gaur. *Metal Alkoxides*. London: Academic, 1978.

[37] Davis, Tracy M., Mark A. Snyder, John E. Krohn, and Michael Tsapatsis. "Nanoparticles in Lysine−Silica Sols." *Chemistry of Materials Chem. Mater.* 18.25 (2006): 5814-816.

[38] Tian, Zheng, and Mark A. Snyder. "Hard Templating of Symmetric and Asymmetric Carbon Thin Films with Three-Dimensionally Ordered Mesoporosity." *Langmuir* 30.32 (2014): 9828-837

[39] Tian, Zheng, and Mark A. Snyder. "Nanocasting of Carbon Films with Interdigitated Bimodal Three-Dimensionally Ordered Mesopores by Template-Replica Coassembly." *Langmuir* 30.41 (2014): 12411-2420.

[40] Kim, Sung Soo, Hyung Ik Lee, Jeong Kuk Shon, Jae Young Hur, Min Suk Kang, Sang Soo Park, Soo Sung Kong, Ji Ae Yu, Miran Seo, Donghao Li, Santosh Singh Thakur, and Ji Man Kim. "Preparation of Highly Ordered Mesoporous TiO_2 Materials with Crystalline Framework from Different Mesostructured Silica Templates via Nanoreplication." *Chem. Lett. Chemistry Letters*37.2 (2008): 140-41.

[41] Bian, Zhenfeng, Jian Zhu, Jing Wen, Fenglei Cao, Yuning Huo, Xufang Qian, Yong Cao, Meiqing Shen, Hexing Li, and Yunfeng Lu. "Single-Crystal-like Titania Mesocages." *Angewandte Chemie Angew. Chem.* 123.5 (2010): 1137-140.

[42] Crossland, Edward J. W., Nakita Noel, Varun Sivaram, Tomas Leijtens, Jack A. Alexander-Webber, and Henry J. Snaith. "Mesoporous TiO_2 Single Crystals Delivering Enhanced Mobility and Optoelectronic Device Performance." *Nature* 495.7440 (2013): 215-19.

[43] Turova, Nataliya Ya. *The Chemistry of Metal Alkoxides*. Boston: Kluwer Academic, 2002.

[44] De, G., A. Chatterjee, and D. Ganguli. "Zirconia Fibres from the Zirconiumn-propoxide-acetylacetone-water-isopropanol System."*Journal of Materials Science Letters J Mater Sci Lett* 9.7 (1990): 845-46.

[45] Yi, Guanghua, and Michael Sayer. "Sol-Gel Processing of Complex Oxide Films." *American Ceramic Society Bulletin* 70.7 (1991): 1173-1177.

[46] Kim, Seung-Goo, Suk Woo Nam, Sung-Pil Yoon, Sang-Hoon Hyun, Jonghee Han, Tae-Hoon Lim, and Seong-Ahn Hong. "Sol-gel Processing of Yttria-stabilized Zirconia Films Derived from the Zirconium N-butoxide-acetic Acid-nitric Acid-water-isopropanol System." *Journal of Materials Science* 39.8 (2004): 2683-688.

[47] Takahashi, Yasutaka, and Yoshihiro Matsuoka. "Dip-coating of TiO_2 Films Using a Sol Derived from $Ti(O\text{-}i\text{-}Pr)_4$-diethanolamine-$H_2O$-i-PrOH System." *Journal of Materials Science* 23.6 (1988): 2259-2266.

[48] Takahashi, Yasutaka, Katsuhiro Niwa, Keisuke Kobayashi, and Michiyasu Matsuki. "Dip Coating of Zirconia and Mixed Zirconia Films." *Journal of the Ceramic Association, Japan* 95.1106 (1987): 942-948.

[49] Brinker, C. Jeffrey., and George W. Scherer. *Sol-gel Science: the Physics and Chemistry of Sol-gel Processing*. Boston: Academic, 1990.

[50] Bradley, Donald C. "Metal Alkoxides as Precursors for Electronic and Ceramic Materials." *Chemical Reviews Chem. Rev.* 89.6 (1989): 1317-322.

[51] Basolo, Fred, and Ronald C. Johnson. *Coordination Chemistry; the Chemistry of Metal Complexes*. New York: W.A. Benjamin, 1964.

[52] Toraya, H., M. Yoshimura, and S. Somiya. "Calibration Curve for Quantitative Analysis of the Monclinic-tetragonal ZrO_2 System by X-ray Diffraction." *Journal of the American Ceramic Society* 67.6 (1984): C-119-121.

[53]Louis, C., and M. Che. "4.1.2 Anchoring and Grafting of Coordination Metal Complexes onto Oxide Surfaces." *Preparation of Solid Catalysts*. By G. Ertl, H. Knözinger, and J. Weitkamp. Weinheim: Wiley-VCH, 1999. 341-55.

Chapter 3: Stabilization of Metastable Oxides

3.1 Abstract

This work provides a conceptual framework which can be employed for the stabilization of metastable catalytic oxides at high temperatures by means of the incorporation of a second, supported oxide along the surface of a metastable support. This phenomenon is demonstrated by stabilizing both the tetragonal phase of zirconia (t-ZrO_2) and the anatase phase of titania (a-TiO_2) at elevated temperatures (T>500˚C) via utilization of a silica (SiO_2) layer to prevent oxide reconfiguration. Model supported oxides (SiO_2/MO_x) were prepared via incipient wetness impregnation (IWI) with tetraethyl orthosilicate (TEOS) to deposit SiO_2 loadings ranging from 5-15 wt% on the surface of commercial catalytic oxides (Degussa TiO_2 and ZrO_2) and zirconium hydroxides (MEL Chemicals). After IWI, the samples were calcined at temperatures ranging from 500-1000˚C and characterized with X-ray diffraction (XRD), N_2 adsorption, and atomic resolution microscopy (ARM) to assess reconstruction at elevated temperatures. Results demonstrate that both the crystal structure and surface area of the underlying metastable support is stabilized with low SiO_2 loadings (5wt%); while increased SiO_2 loadings (15wt%) facilitate more robust stabilization. Stabilization is observed to deteriorate when calcining for prolonged durations above the characteristic Tammann temperature of the supporting oxide. It is proposed that incorporation of a surface oxide acts to stabilize the metastable supporting oxide by more fully coordinating its exterior and limiting atomic surface mobility. This mechanism of surface stabilization could lead to the development of more robust catalysts for high temperature applications.

3.2 Introduction

Metal oxides utilize oxygen and metal atoms to form materials used in diverse applications including catalysts, fuel cells, photovoltaics, and paints.[1,2,3] Oxides are often employed in applications which involve high temperatures (500-1000˚C) and cyclical periods of operation, such as automotive catalysts and solid-oxide fuel cells.[4] The versatility of MO_x's are due in part to the palette of elements provided by the periodic table and the resulting spectrum of chemistries they exhibit. The commercial, mass production of metal oxides is typically performed by either high temperature flame hydrolysis techniques[5] or soft-chemical solution based approaches.[6] These processes facilitate the tailored control of material properties including crystalline phase, elemental composition, surface area, and pore structure; however, most oxides remain susceptible to methods of high temperature reconfiguration. Thus, oxides must be carefully engineered in order to maintain their stability, function, and surface chemistry in the harsh environments in which they are employed.

Commercial Production of Metal Oxides

Flame hydrolysis is employed during the commercial production of bulk quantities of crystalline oxides for use as adsorbents, catalytic supports, and additives in diverse applications ranging from paints to toothpastes and tires. This process is utilized to manufacture oxides including fumed silica and Degussa P25 TiO_2.[7] High temperature flame hydrolysis techniques facilitate control of product morphology by adjusting the temperature and residence time during the combustion of spray-atomized oxide precursors within a tubular furnace. This comprehensive control of processing parameters facilitates the continuous fabrication of oxides with high surface areas and metastable crystal structures, which are often unable to be produced via traditional solid-state quenching techniques.[8]

Soft chemical or "Chimie-Douche" based synthetic approaches allow either the direct nucleation and crystallization of oxide crystals in solution or the formation of a hydroxide gel which can be subsequently converted to a crystalline oxide by means of calcination at low-to-moderate temperatures.[9] This technique is often beneficial for wash coating ceramic monoliths with a thin catalytic film.[10] The ability of a soft chemical oxide precursor to crystallize in solution is dependent upon the nature of its valence electrons. Transition metals with partially filled d-orbitals are particularly susceptible to complex formation in solution. This typically results in the formation of oligomers or gels which require a heating step to facilitate crystallization.[11] Subsequent drying, syneresis, and calcination allows the crystallization of oxides composed of small crystallites with moderate surface areas and metastable crystal structures.

Oxide Reconstruction due to Atomic Mobility

Commercially produced oxides remain susceptible to high temperature reconstructive processes including phase transformation, sintering, and pore collapse.[12] These mechanisms of transformation typically initiate along the surface of a material, as surface atoms are bound with less cohesive energy than corresponding bulk lattice atoms and can mobilize at lower temperatures.[13] Atomic surface mobility typically initiates at the characteristic Hüttig temperature of a bulk material; which is approximated as one third of the bulk melting point of a solid (See **Equation 2-1**). Higher temperatures facilitate even more dynamic mechanisms of atomic mobility including bulk-to-surface translations, as defined by the characteristic Tammann temperature of a bulk solid (See **Equation 2-2**).

$$T_{Huttig} \sim {T_{melt}^{bulk}}/{3} \quad \textbf{Equation 2-1}$$

$$T_{Tammann} \sim {T_{melt}^{bulk}}/{2} \quad \textbf{Equation 2-2}$$

The reduction of an oxide's crystallite size increases its overall surface area and makes an oxide more desirable for catalytic and adsorbent based applications. However, a reduction in crystallite size also accelerates the onset of atomic surface mobility and can lead to mechanisms of catalytic reconstruction such as sintering.[14] This phenomenon can greatly reduce the surface area of a material at elevated temperatures. As crystallite size is reduced to the nanometer scale, less cohesive energy binds atoms within the material and surface atoms are more likely to mobilize. This makes the material more susceptible to reconfiguration and can even reduce its melting point.[15] Thus, it is necessary to incorporate mechanisms of stabilization to preserve surface area and make oxides more resistant to sintering.

Metastable Oxides

Crystalline materials exhibit a wide range of morphological crystallographic structures.[16] The stability of a given crystal structure is dependent upon elemental composition, processing conditions, and environmental conditions. Polymorphic phase transformations occur by either displacive or reconstructive methods of atomic transformation.[17] This occurs during the transformation of metastable oxide structures including the anatase phase of titania[18] and the tetragonal phase of zirconia to more stable crystal structures including the rutile TiO_2 and monoclinic ZrO_2 phase.[19] This can lead to cracking in ceramic monoliths and performance loss in fuel cells.[4]

Metastable crystal structures are typically stabilized by the incorporation of aliovalent dopants such as Y^{3+}, Ca^{2+}, and Mg^{2+} to relax internal strains within the bulk structure of a

crystal. Doping prevents surface driven phase transformation from propagating into the internal region of the lattice.[20] Another widely discussed method of preserving metastable crystal structures is to reduce the crystallite size below a critical radius in order to effectively balance the surface and bulk free energies of the crystal. This facilitates the stabilization of metastable crystal structures at conditions in which they would typically be unstable.[21,22,23] A similar method of phase stabilization has been reported by maintaining coherency along crystallite-to-crystallite grain boundaries. This interfacial contact is reported to induce a pressure upon neighboring crystallites that prevents phase transformation via crystallite confinement.[24,25] Lastly, a method of surface modification has been reported to stabilize metastable supported catalysts. The addition of a surface oxide in these studies likely hinders atomic surface mobility of the supporting oxide, invites surface doping, and reduces grain propagation via confinement; all of which assist in the promotion of the metastable phase of the underlying support.[26,27,28]

Overview of this Study

This study seeks to more fundamentally examine the mechanisms employed during the stabilization of supported oxides. This is accomplished by examining the crystalline phase composition and structural reconfiguration of model supported oxides prepared from crystalline and hydroxide based commercial supports including SiO_2/TiO_2-crystalline, SiO_2/ZrO_2-crystalline, and SiO_2/ZrO_2-hydroxide. In these systems, the application of a 5-15wt% surface SiO_2 layer is demonstrated to stabilize traditionally metastable oxide phases including anatase TiO_2 and tetragonal ZrO_2 after high temperature calcination (T>500˚C).

Structural and mechanistic insight provided by x-ray diffraction, nitrogen adsorption, and atomic resolution microscopy suggests that the SiO_2 layer helps to more fully coordinate

the support, limits atomic surface mobility, stabilizes metastable crystallites, and limits sintering in comparison to unsupported oxides. Additionally, we directly correlate the mechanisms of atomic surface mobility to characteristic bulk material properties including the Hüttig and Tammann temperature. These properties are shown to govern the extent of surface mobilization and ultimately material reconfiguration. The concepts discussed in this study can be utilized to facilitate the formation of more robust catalytic materials for high temperature applications.

3.3 Experimental

Materials

Commercial catalytic supporting oxides (MO_x) including TiO_2 (Degussa P25) and ZrO_2 (Degussa VP Zikonoxid) were purchased for preparation of model supported oxides (SiO_2/MO_x) via incipient wetness impregnation (IWI). Additionally, an amorphous zirconium hydroxide (MEL Chemicals XZO-631-01) was utilized for direct preparation of supported zirconium oxides from a ZrO_2 precursor. Tetraethyl orthosilicate (TEOS) and ethanol (200 proof) were purchased from Sigma-Aldrich and used without further preparation.

Preparation of Supported oxides

A series of supported and unsupported oxides were prepared via IWI and subsequent calcination. Prior to IWI, the supports were dried at 120˚C to remove physisorbed surface moisture and subsequently transferred to a glove box. The incipient wetness point of the dried oxide powder was first determined via incremental addition of ethanol (200 proof) in small aliquots until reaching the incipient wetness point of the support. The resulting solution volume provided a suitable amount of fluid necessary to completely fill the pore volume of the as dried powders.

IWI was then performed by measuring a desired amount of TEOS within the glove box and subsequently diluted with anhydrous ethanol in order to form a silica precursor solution. The total volume of the precursor solution was consistent with that necessary to fill the pore structure of the support and avoid surpassing the incipient wetness point of the powder. The precursor solution was added to the support in small incremental aliquots and the resulting powder was vigorously stirred. An appropriate amount of TEOS was incorporated in the solution in order to form a supported SiO_2/MO_x sample with a final SiO_2 composition ranging from 5-15 weight percent.

The infiltrated samples were allowed to dry at ambient conditions within the glovebox overnight and further dried at 120˚C for several hours. The supported and unsupported oxides were then briefly sieved with a size 40 mesh (0.42 mm) and calcined at 5˚C per minute to a final dwelling temperature ranging from 500-1000˚C. Upon reaching the final dwelling temperature, the samples were held in static air for a period ranging from three to 24 hours. The samples were then allowed to cool to ambient temperatures and subsequently characterized.

Characterization

Oxide crystallinity was examined using a Rigaku Miniflex II X-ray diffractometer, which utilized Cu K-alpha radiation (K_α=1.5418 Å). The powdered samples were loaded in a dimpled silicon holder and analyzed over the appropriate range necessary to assess the phase content of each supported oxide. This included the characteristic t(101), m($11\bar{1}$), and m(111) peaks of zirconia within the range of 25-35˚ (2-theta); and the characteristic a(101) and r(110) peaks of titania found in the 20-30˚ region. A sample rotation of 0.5˚ per minute was utilized for analysis.

Analysis of the phase composition of each sample was determined via a weighted average of the integrated characteristic peak intensity of each phase (See **Equations 3-1 and 3-2**).[29,30] This calculation resulted in a +/- 3.5 % standard deviation between samples.

$$Volume\ \%_{\ Anatase} = \ 100 * \frac{0.79 I_A}{I_R + 0.79 I_A} \qquad \textbf{Equation 3-1}$$

$$X_{monoclinic} = \frac{I_m(\bar{1}11) + I_m(111)}{I_m(\bar{1}11) + I_m(111) + I_t(101)} \qquad \textbf{Equation 3-2}$$

$$Volume\ \%_{monoclinic} = \frac{1.311\ X_m}{1 + 0.311 X_m} \qquad \textbf{Equation 3-3}$$

$$I_i = \text{Integral intensity of Phase } i$$

Surface area and pore volume was analyzed with nitrogen adsorption as measured with a Micromeritics ASAP 2020 instrument. Surface area was calculated using the BET theory (Brunauer-Emmett-Teller).[31] The BET theory assumes N_2 adsorbs on the surface of a solid in multiple layers and the adsorbed molecules are in dynamic equilibrium with the vapor phase. Pore size distribution was calculated using the BJH method (Barrett-Joyner-Halenda) to analyze the desorption portion of the resulting isotherms. [32] Lastly, the Broekhoff-De Boer correction was used to account for the chemical potential of adsorbed species within a cylindrical pore structure. [33]

Atomic resolution microscopic (ARM) images were collected with a 200 kV aberration-corrected JEOL JEM-ARM200CF microscope. For imaging purposes, the as prepared samples were deposited on 300 mesh copper microscopy grids with a non-porous carbon film underlying the grid. Energy dispersive x-ray mapping (EDS-mapping) was performed with a Centurio XEDS system. Mapping was performed by detecting the spatial emission of

characteristic K-alpha ($K_{\alpha 1}$) x-rays for elements including titanium (4.51 keV), silicon (1.74 keV), and oxygen (0.52 keV).[34]

3.4 Results and Discussion

Surface Stabilization of Titania

Characterization of the as received commercial P25 titania powder shows a composition of approximately 87 vol.% a-TiO_2 and 13 vol.% r-TiO_2 as measured by XRD. **Figure 3-1a** demonstrates the conversion of this sample from the predominantly metastable anatase phase to the more stable rutile phase after three hour calcinations at temperatures ranging from 500-1000˚C. This phase transformation is noted by the diminishing characteristic anatase (101) peak located at approximately 25.1˚ (2-theta) and the development of the rutile (110) peak at ~27.6˚ (2-theta). This phase transformation rapidly occurs at temperatures ranging from 600-800˚C and results in the formation of a sample consisting entirely of the rutile phase.

Supported SiO_2/TiO_2 samples showed a resistance to phase transformation after calcination at elevated temperatures. A 5wt% SiO_2 loading prevented development of the rutile phase and stabilized the anatase TiO_2 crystal structure when calcining at 700˚C (See **Figure 3-1b**). At 1000˚C the rutile phase began developing but was inhibited by incorporation of the silica layer. An increased loading of silica (15wt% SiO_2/TiO_2) promoted more robust stabilization of the anatase phase at extreme temperatures (1000˚C) as demonstrated in **Figure 3-1c**. Thus, the addition of a surface SiO_2 layer can be utilized to stabilize the metastable a-TiO_2 phase and mitigate formation of the rutile phase (See **Figure 3-1d**).

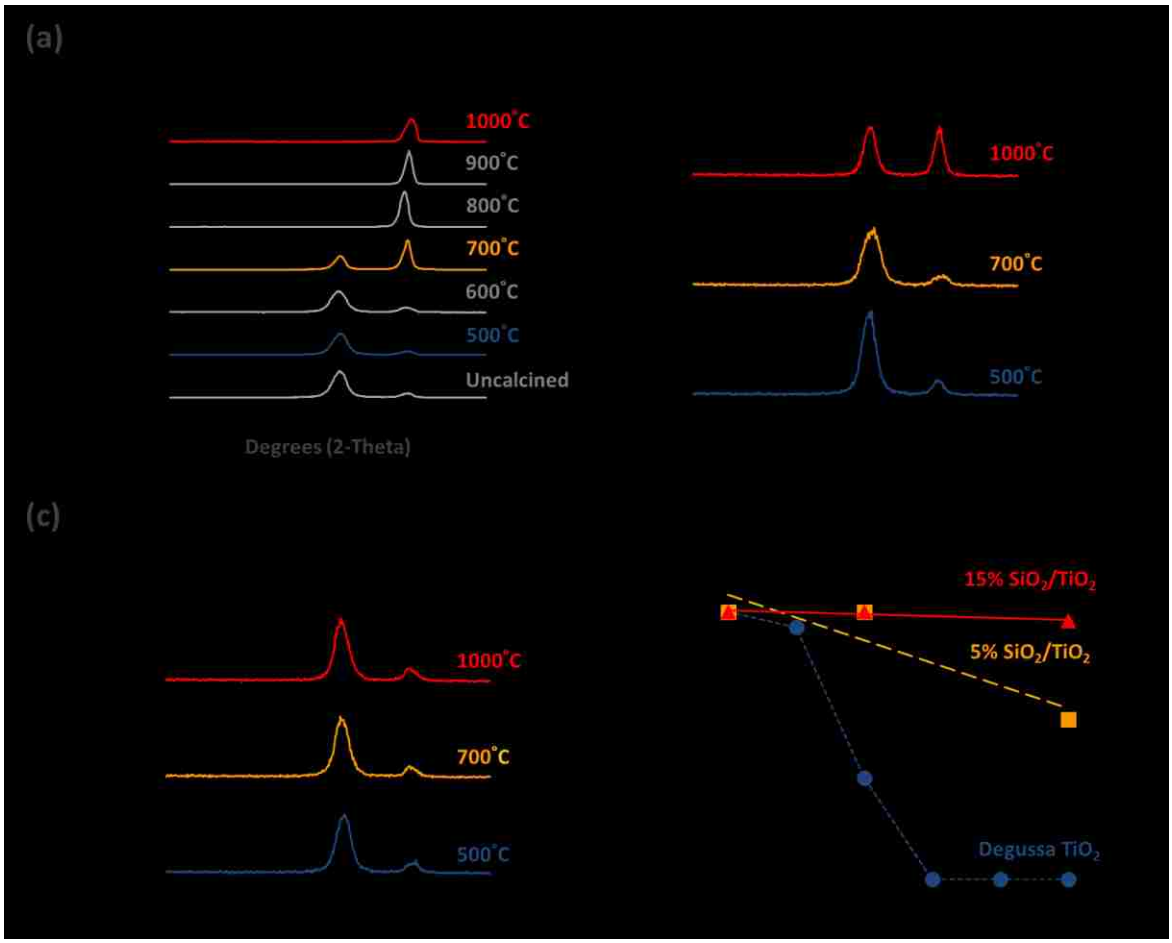

Figure 3-1. XRD characterization of commercial P25 titania and 5-15wt% SiO_2/TiO_2 samples after three hour calcination at temperatures ranging from 500-1000˚C. Panels include: **(a)** XRD characterization of commercial P25 titania; **(b)** XRD characterization of 5wt% SiO_2/TiO_2 samples; **(c)** XRD characterization of 15wt% SiO_2/TiO_2 samples; **(d)** calculated volume percentage of the metastable anatase phase.

ARM images show the presence of an amorphous oxide layer coating the surface of the stabilized SiO_2/TiO_2 samples (See **Figure 3-2**). The amorphous layer is visible with silica loadings ranging from 5-15wt% and and temperatures ranging from 500˚C to 1000˚C. Further characterization of the amorphous layer with EDS mapping confirms it is rich in silicon content and exists as an amorphous oxide layer. This is demonstrated in **Figure 3-3** by an increased concentration of the silicon k-alpha signal when looking top-down along the edge of the TiO_2

crystal. The presence of this oxide layer assists in the stabilization of the metastable anatase phase as characterized with XRD.

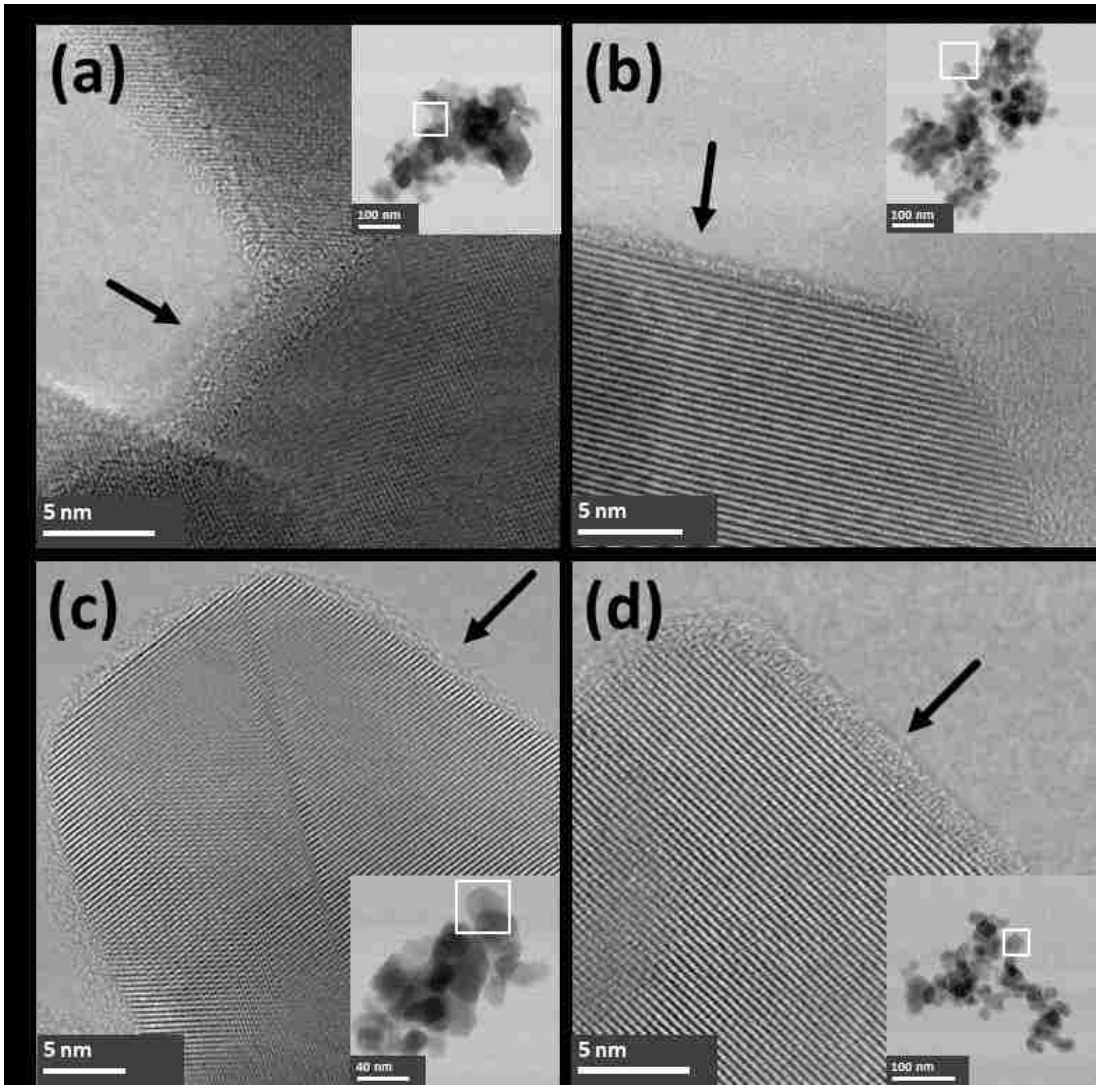

Figure 3-2. ARM images of highlighting the amorphous silica layer in SiO_2/TiO_2 supported samples prepared after three hour calcination. **(a)** 5wt% SiO_2/TiO_2 sample calcined at 1000˚C, inset: image of larger particle; **(b)** 15wt% SiO_2/TiO_2 sample calcined at 1000˚C, inset: image of larger particle; **(c)** 5wt% SiO_2/TiO_2 sample calcined at 500˚C, inset: image of larger particle; **(d)** 15wt% SiO_2/TiO_2 sample calcined at 500˚C, inset: image of larger particle.

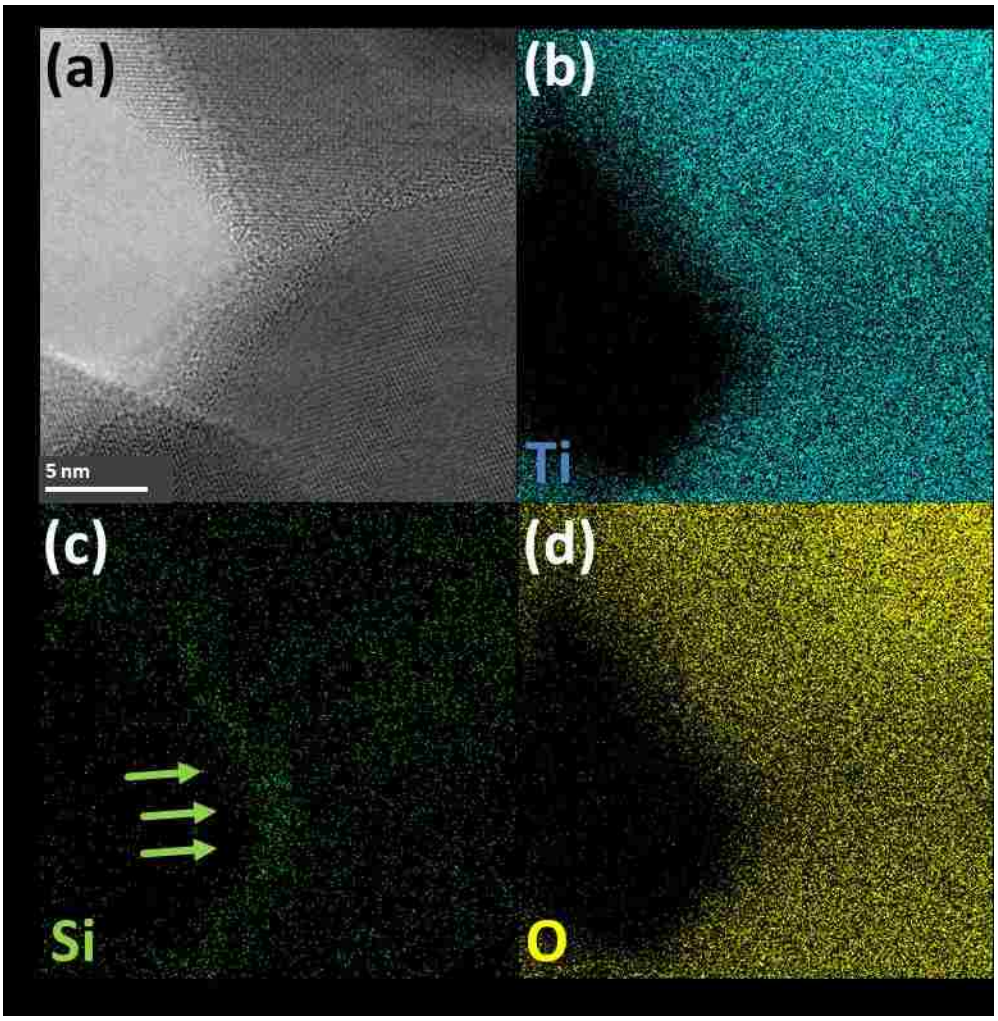

Figure 3-3. EDS mapping demonstrating the surface rich nature of the silicon in the 5wt% SiO_2/TiO_2 sample calcined at 1000˚C for three hours. Images depict: **(a)** ARM image of a crystal; **(b)** titanium K-alpha detection; **(c)** silicon K-alpha detection along the surface of the crystal; **(d)** oxygen K-alpha detection.

The extent of surface stabilization was examined after prolonged calcinations at 700˚C and 1000˚C in order to examine the potential for reconfiguration over extended periods of time. Minimal variation in crystal structure was observed in the SiO_2/TiO_2 samples when calcining at 700˚C for 24 hours. This is established in **Figure 3-4a** as the a(101) peak remains proportionately large relative to the r(110) peak; additionally the calculated phase composition varies by only 1-2% in comparison to that observed after a three hour calcination

time. However, the mechanism of surface stabilization is observed to eventually break down when calcining for prolonged durations of time at 1000˚C, as is shown by the absence of the a(101) peak in **Figure 3-4b**.

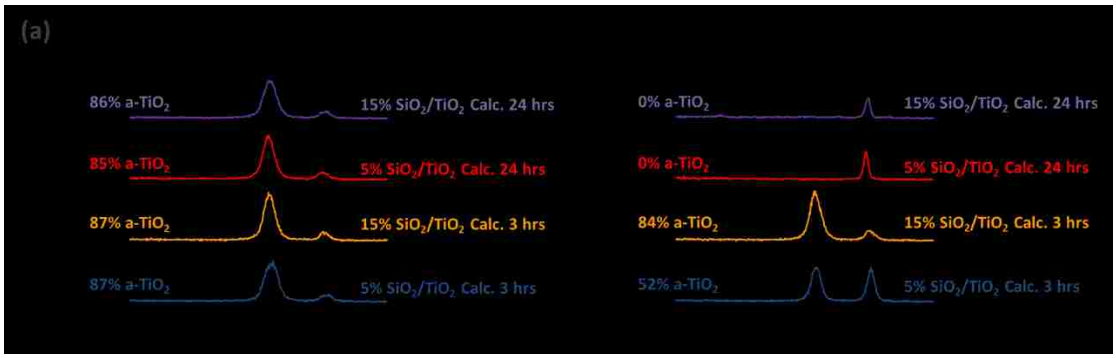

Figure 3-4. XRD characterization of supported SiO_2/TiO_2 samples after prolonged (24 hour) calcination at elevated temperatures: **(a)** extended calcination at 700˚C; **(b)** extended calcination at 1000˚C.

Characterization of the samples with N_2 adsorption was performed in order to assess the degree of sintering and pore collapse after calcination. **Figure 3-5** presents the adsorption and desorption isotherms of commercial P25 and the 5-15wt% SiO_2/TiO_2 samples after calcination. The commercial sample contains minimal mesoporosity as noted by small hysteresis loops in the isotherm and a broad distribution in pore width (See **Figure 3-5a**). The pore volume within the mesopore and small macropore range (dia. < 150nm) of the commercial titania sample rapidly decays after calcination at 1000˚C. This corresponds to a transformation from a type IV isotherm to a type II isotherm as defined by the International Union of Pure and Applied Chemistry (IUPAC).[35,36,37] Calcination of the unsupported titania sample at 1000˚C rapidly sinters the sample from its original BET surface area of 54m^2/g to a value of only 2m^2/g (See **Figure 3-5d**).

The 5wt% SiO_2/TiO_2 sample demonstrates a promotion in pore volume and significant increase in mesoporosity as observed in **Figure 3-5b**. This is observed by a larger hysteresis and pronounced increase in porosity. Additionally, this mesoporosity is maintained even after calcination at 1000˚C as noted by the presence of a type IV isotherm. Similar results are observed with the 15wt% SiO_2/TiO_2 sample (See **Figure 3-5c**); in this sample an increased SiO_2 loading is observed to promote mesoporosity, yet to a lesser extent than the 5wt% SiO_2/TiO_2 sample. Calculation of the BET surface area shows that the supported samples maintain similar surface areas at moderate temperatures (500-700˚C) and a pronounced increase in surface area at 1000˚C, versus the unsupported sample (See **Figure 3-5d**).

These findings suggest that the incorporation of a surface SiO_2 layer alters the pore structure and surface area of the commercial titania at moderate temperatures (500-700˚C) by way of exterior surface decoration of the crystals. At low loadings the silica coats the TiO_2 crystals, reduces the space between neighboring and interconnected crystallites, and facilitates the creation of small mesopores (See **Figure 3-2**). After 1000˚C calcination, the presence of the silica hinders neighboring crystals from coalescing and promotes both porosity and surface area by providing separation between crystallites. At higher loadings further addition of silica acts to fill the pore space between crystallites and results in less pore volume versus that observed with lower SiO_2 loadings. As such, an optimal loading of silica can facilitate the promotion of both surface area and pore structure of titania at elevated temperatures; however, additional loadings can result in pore blockage.

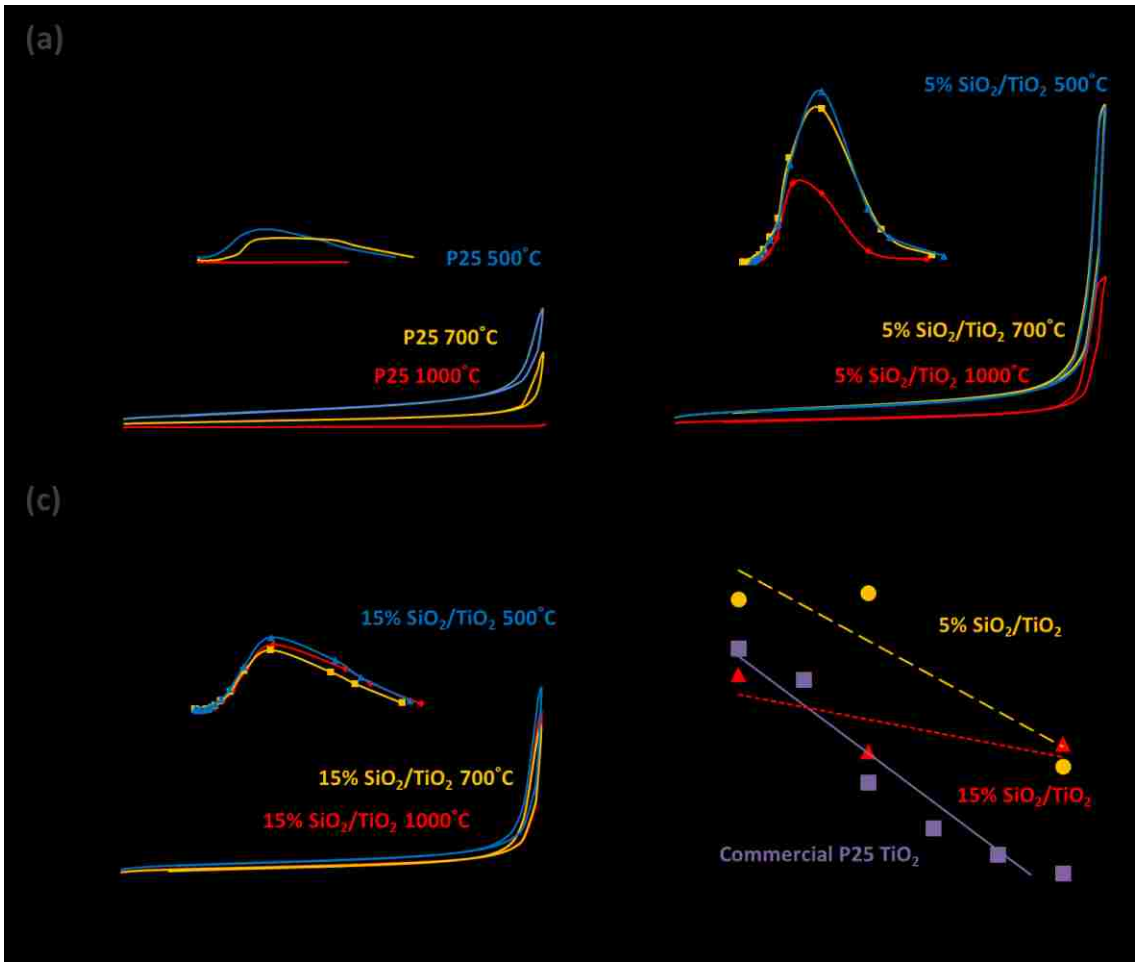

Figure 3-5. Nitrogen adsorption characterization of commercial titania and supported SiO_2/TiO_2 samples after three hour calcination at 500, 700, and 1000˚C: **(a)** N_2 isotherms of P25 titania, inset: calculated pore volume; **(b)** N_2 isotherms of 5wt% SiO_2/TiO_2 samples, inset: calculated pore volume; **(c)** N_2 isotherms of 15wt% SiO_2/TiO_2 samples, inset: calculated pore volume; **(d)** comparison of BET surface area of the samples versus calcination temperature.

Surface Stabilization of Zirconia

A similar mechanism of metastable oxide stabilization was observed when utilizing a surface silica layer to stabilize the metastable tetragonal phase of zirconia at elevated temperatures. XRD characterization of the as received Degussa ZrO_2 powder reveals an initial phase composition of 64 vol.% t-ZrO_2 and 36 vol.% m-ZrO_2. **Figure 3-6a** demonstrates the evolution of this commercial ZrO_2 sample from the metastable tetragonal phase to the more thermodynamically stable monoclinic phase after three hour calcinations. Phase

transformation is observed by the diminishing characteristic tetragonal (101) peak located at approximately 30.5˚ (2-theta) and the development of the characteristic monoclinic ZrO_2 peaks, including the m($11\bar{1}$) peak located at ~28.3˚ and the m(111) peak at ~31.6˚ (2-theta).

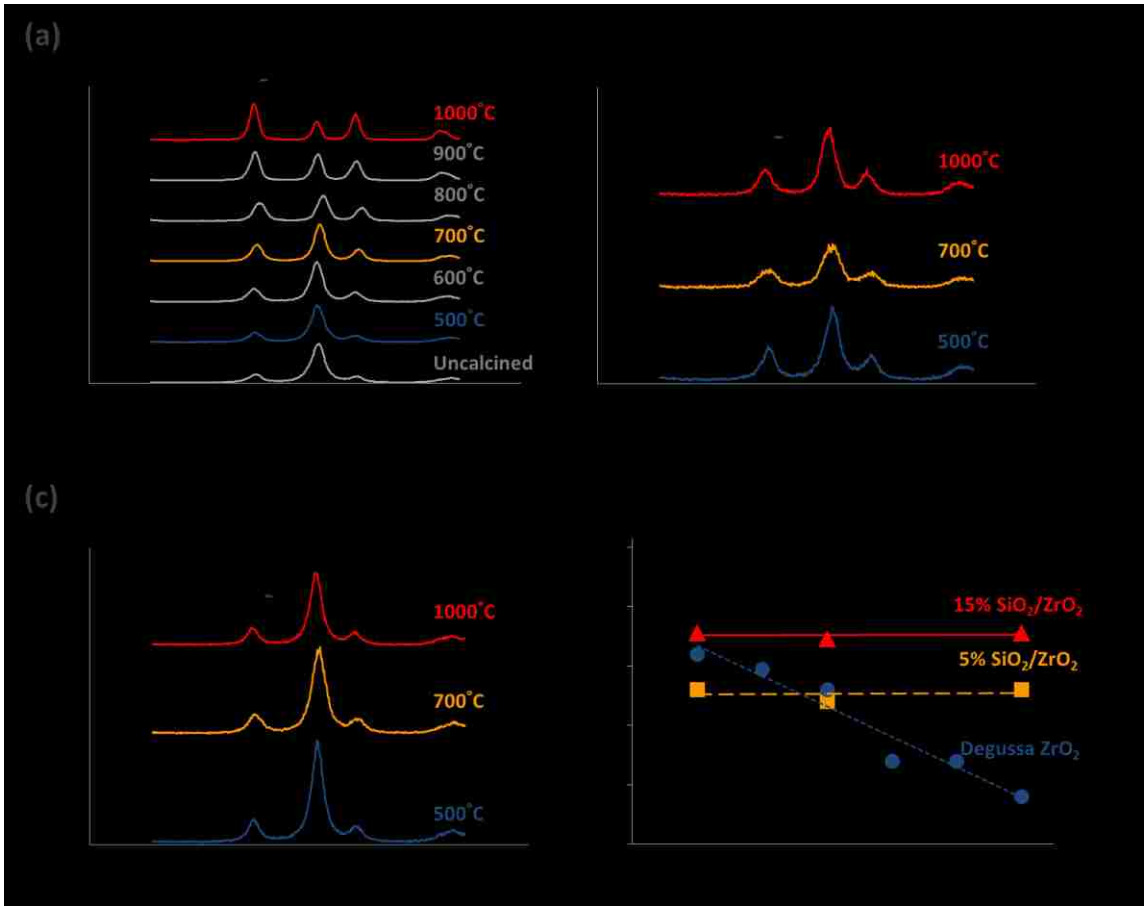

Figure 3-6. XRD characterization of commercial ZrO_2 and 5-15wt% SiO_2/ZrO_2 samples after three hour calcination at temperatures ranging from 500-1000˚C. Panels include: **(a)** XRD characterization of commercial ZrO_2; **(b)** XRD characterization of 5wt% SiO_2/ZrO_2 samples; **(c)** XRD characterization of 15wt% $SiO_2/ZriO_2$ samples; **(d)** calculated volume percentage of the metastable tetragonal phase.

Addition of a silica surface layer facilitated a resistance to phase transformation in the supported SiO_2/ZrO_2 samples after high temperature calcination. A 5wt% SiO_2 loading limited development of the monoclinic ZrO_2 phase as noted by the relative intensities of the t(101) peak to that presented by the m($11\bar{1}$) and m(111) peaks; this is observed when comparing the

XRD diffractograms presented in **Figure 3-6a** and **Figure 3-6b**. Similar results were observed when increasing the silica loading to 15wt%. (See **Figure 3-6c**). Calculation of the corresponding phase compositions shows a substantial promotion of the tetragonal phase in the supported samples at 1000˚C relative to that observed in the unsupported commercial sample (See **Figure 3-6d**).

In order to assess the robustness of ZrO_2 stabilization and the long-term potential for reconfiguration, the stabilized SiO_2/ZrO_2 samples were calcined for prolonged periods of time at 700˚C and 1000˚C. When calcining at 700˚C for 24 hours, minimal variation in crystal structure was observed in both the 5wt% and 15wt% SiO_2/ZrO_2 samples (See **Figure 3-7a**). After an extended calcination time at 700˚C the t(101) peak remains proportionately large relative to the m($11\bar{1}$) and m(111) peaks. The calculated phase composition varies by only 1-3% in comparison to that observed after a three hour period of calcination; suggesting robust stabilization of the tetragonal phase during prolonged 700˚C calcination.

Calcination at 1000˚C for an extended period of time facilitates further surface stabilization with only limited phase transformation (See **Figure 3-7b**). With a 5wt% SiO_2 loading a gradual transformation to the monoclinic phase as is observed during extended calcination at 1000˚C. However, when increasing the SiO_2 loading to 15wt%, a majority of the crystal structure (59% by volume) is stabilized as the metastable tetragonal phase during prolonged calcination at 1000˚C. Thus, with adequate dispersion of surface SiO_2 the metastable tetragonal phase can be stabilized at extreme temperatures for prolonged durations of time.

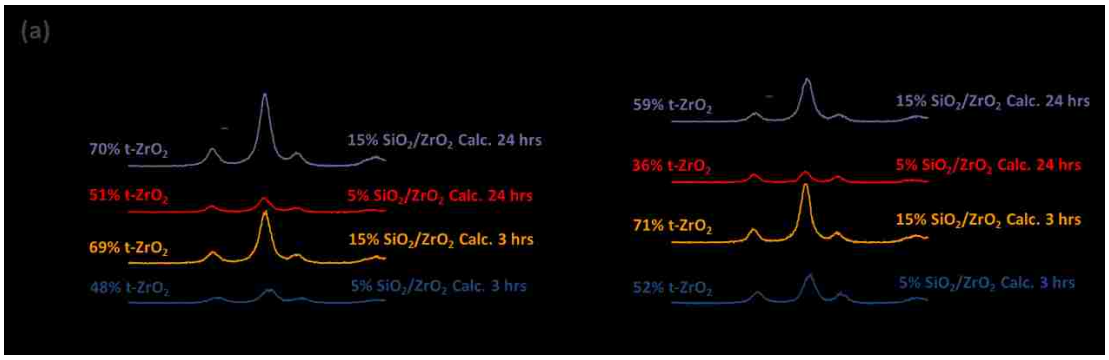

Figure 3-7. XRD characterization of supported SiO_2/ZrO_2 samples after prolonged (24 hour) calcination at elevated temperatures: **(a)** extended calcination at 700˚C; **(b)** extended calcination at 1000˚C.

The commercial ZrO_2 and supported SiO_2/ZrO_2 samples were characterized with N_2 adsorption in order to assess the degree of sintering and pore collapse after calcination (See **Figure 3-8**). The as received Degussa ZrO_2 sample presents moderate surface area (64 m^2/g) and minimal mesoporosity as demonstrated in **Figure 3-8a**. Subsequent calcination of the ZrO_2 control sample at 1000˚C facilitates pore collapse and a large reduction in surface area from 64m^2/g to 14m^2/g. This corresponds to the transformation from a type IV to type II isotherm.

The addition of surface SiO_2 is observed to promote the extent of mesoporosity for both a 5wt% (See **Figure 3-8b**) and 15wt% loading (See **Figure 3-8c**), as noted by an increased pore volume and larger hysteresis size. After calcination at 500˚C the supported SiO_2/ZrO_2 samples exhibit lower surface areas than the ZrO_2 control sample. It is likely that the SiO_2 acts to promote the formation of mesoporosity by reducing the space between crystallites but also acts to limit surface area by blocking smaller micropores. However, after high temperature calcination the surface area and pore structure of the unsupported sample rapidly collapses (See **Figure 3-8d**) while silica stabilizes both the surface area and pore structure in the supported samples. Thus, the incorporation of silica along the commercial zirconia reduces the

surface area to some extent after low temperature calcination but can be utilized to promote surface area for high temperature applications.

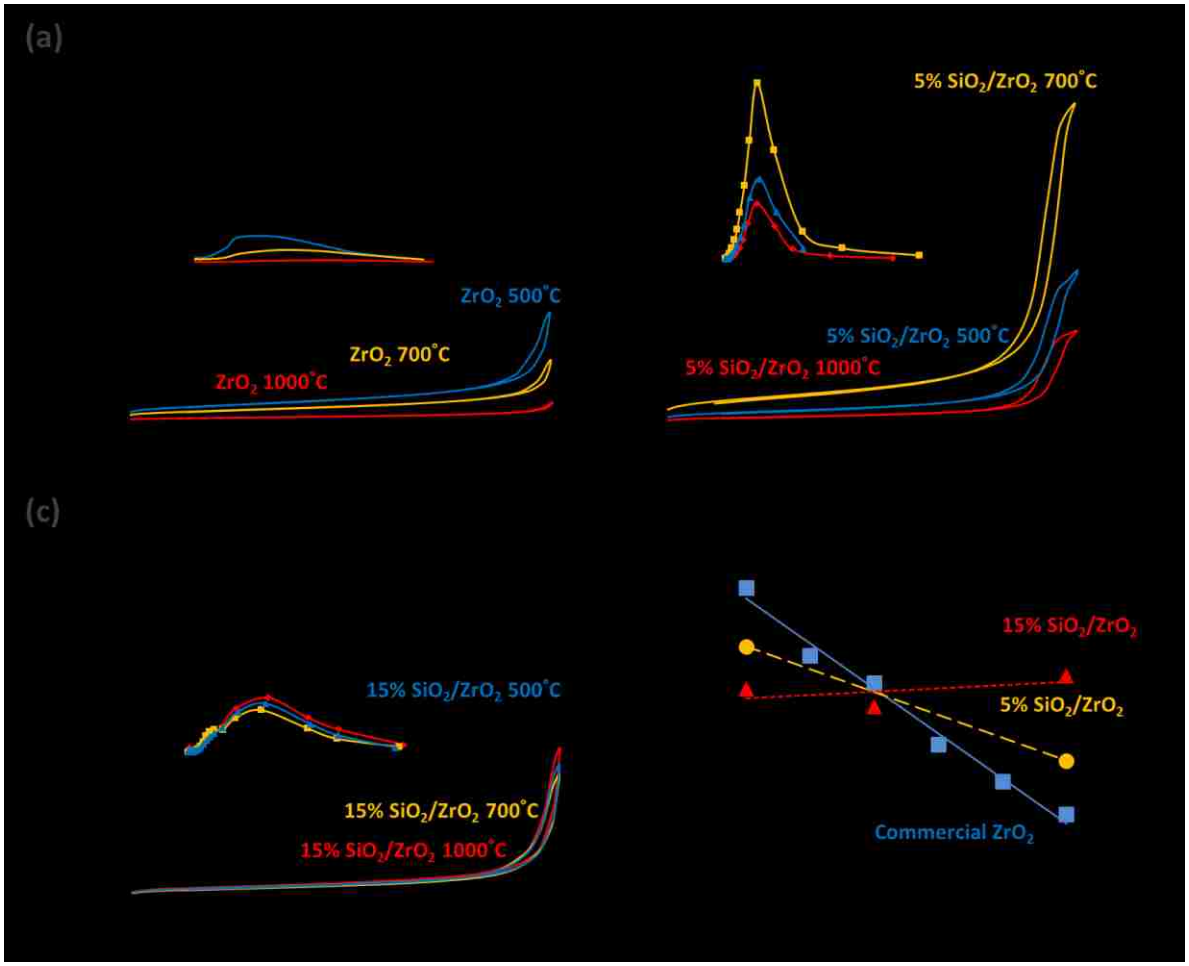

Figure 3-8. Nitrogen adsorption characterization of commercial Degussa ZrO_2 and supported SiO_2/ZrO_2 samples after three hour calcination at 500, 700, and 1000˚C: **(a)** N_2 isotherms of commercial ZrO_2, inset: calculated pore volume; **(b)** N_2 isotherms of 5% SiO_2/ZrO_2 samples, inset: pore volume; **(c)** N_2 isotherms of 15% SiO_2/ZrO_2 samples, inset: pore volume; **(d)** comparison of BET surface area of the samples versus calcination temperature.

Surface Stabilization of Zirconium Hydroxide

The mechanism of surface stabilization was further assessed by preparing supported SiO_2/ZrO_2 samples using zirconium hydroxide as a support. XRD characterization of the as received commercial zirconium hydroxide powder demonstrates the hydroxide is initially amorphous prior to calcination (See **Figure 3-9a**). Calcination of the hydroxide for three hours

at 500˚C facilitates crystallization of the m-ZrO_2 phase as is noted by development of the characteristic m($11\bar{1}$) peak at ~28.3˚ and the m(111) peak at ~31.6˚ (2-theta). Higher temperature calcination facilitates peak sharpening and more pronounced development of the monoclinic phase.

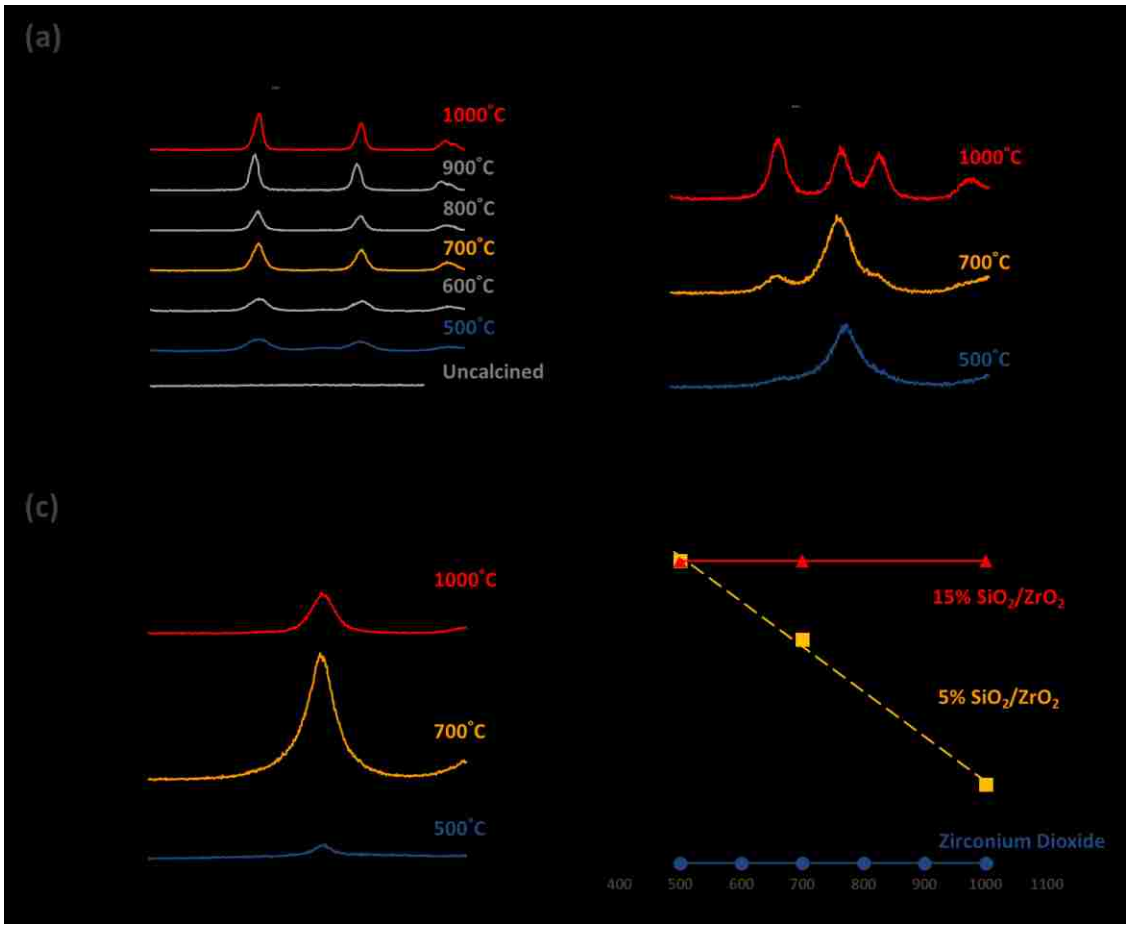

Figure 3-9. XRD characterization of commercial zirconium hydroxide and 5-15wt% SiO_2/ZrO_2 samples after three hour calcination at temperatures ranging from 500-1000˚C. Panels include: **(a)** XRD characterization of ZrO_2 as prepared from a commercial hydroxide; **(b)** XRD characterization of 5wt% SiO_2/ZrO_2 samples; **(c)** XRD characterization of 15wt% $SiO_2/ZriO_2$ samples; **(d)** calculated volume percentage of the metastable tetragonal phase.

The addition of silica to the amorphous zirconium hydroxide via IWI with TEOS has shown the ability to stabilize the tetragonal ZrO_2 phase (See **Figure 3-9b**). This is noted by the direct formation of the t(101) peak at ~30.5˚ 2-theta when preparing a 5wt% SiO_2/ZrO_2.

Increasing the calcination temperature leads to gradual formation of the monoclinic phase at extreme temperatures, yet still maintains a large portion of the t-ZrO_2 phase relative to the unsupported sample. More robust stabilization of the t-ZrO_2 phase is demonstrated when increasing the SiO_2 loading, as is demonstrated in **Figure 3-9c**. With a 15wt% SiO_2 loading, development of the m-ZrO_2 phase is suppressed even after calcination at 1000˚C. **Figure 3-9d** presents the calculated t-ZrO_2 volumetric composition exhibited by the hydroxide based zirconium samples. These findings confirm surface stabilization can be utilized to stabilize a metastable phase when synthesizing a supported oxide directly from a hydroxide based precursor.

The hydroxide based SiO_2/ZrO_2 samples were calcined for prolonged durations and subsequently characterized with XRD in order to assess the long-term potential for reconfiguration. When calcining at 700˚C and 1000˚C for extended durations, samples with low SiO_2 loadings began to gradually convert from the tetragonal to the monoclinic phase (See **Figure 3-10**). However, higher SiO_2 loadings were able to stabilize the tetragonal phase even after extended calcination at 1000˚C. These results suggest adequate surface dispersion of the supported oxide is required for stabilization at prolonged durations.

Characterization of the hydroxide based samples was performed with N_2 adsorption to assess surface area and pore structure (See **Figure 3-11**). When dried at 250˚C the uncrystallized commercial zirconium hydroxide presented a measured surface area of 272m^2/g. Calcination at higher temperatures resulted in crystallization and a large reduction in surface area. The hydroxide exhibited a stepped type IV isotherm at 500˚C and converted to

a type II isotherm at 1000˚C, as the internal pore structure collapsed during calcination (See **Figure 3-11a**).

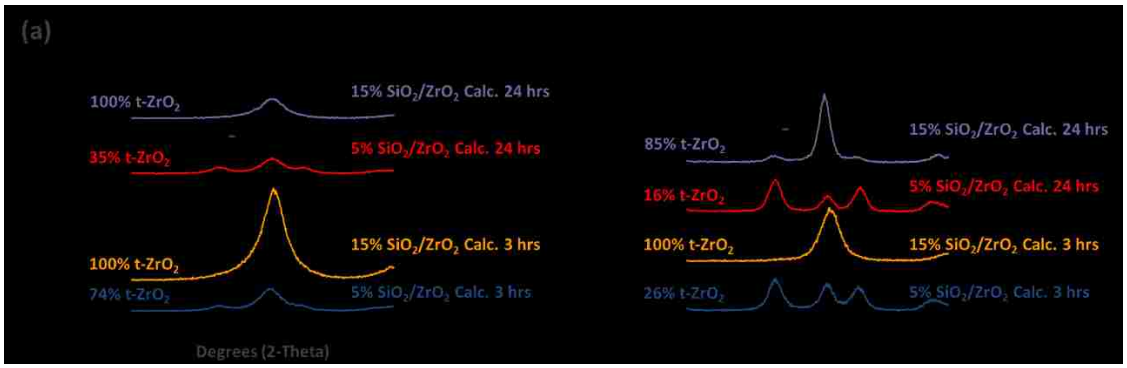

Figure 3-10. XRD characterization of hydroxide supported SiO_2/ZrO_2 samples after prolonged (24 hour) calcination at elevated temperatures: **(a)** 24 hour calcination at 700˚C; **(b)** 24 hour calcination at 1000˚C.

Addition of 5-15wt% silica delays the onset of pore collapse and facilitates structural rigidity of the hydroxide based samples (See **Figure 3-11b** and **Figure 3-11c**). This is demonstrated by an increase pore volume and preservation of the hysteresis after high temperature calcination. Analysis of the BET surface area shows that incorporation of surface silica greatly improves the surface area of the supported samples versus the commercial control (See **Figure 3-11d**). Surface area was more than doubled in the supported samples at all temperatures analyzed.

Zirconium hydroxide consists of a low density amorphous network of hydrated zirconium atoms. This low density structure facilitates large BET surface areas prior to high calcination. However during calcination, rapid dehydration and condensation reactions facilitate large structural densification of the hydroxide; this ultimately results in crystallization. Addition of SiO_2 to the hydroxide framework likely limits the regional extent of dehydration and condensation reactions, prevents pore collapse during syneresis, and effectively scaffolds the hydroxide.[38,39,40,41,42] Thus, surface stabilization of a hydroxide with

SiO_2 facilitates not only promotion of the metastable phase but also a large increase in surface area and pore structure.

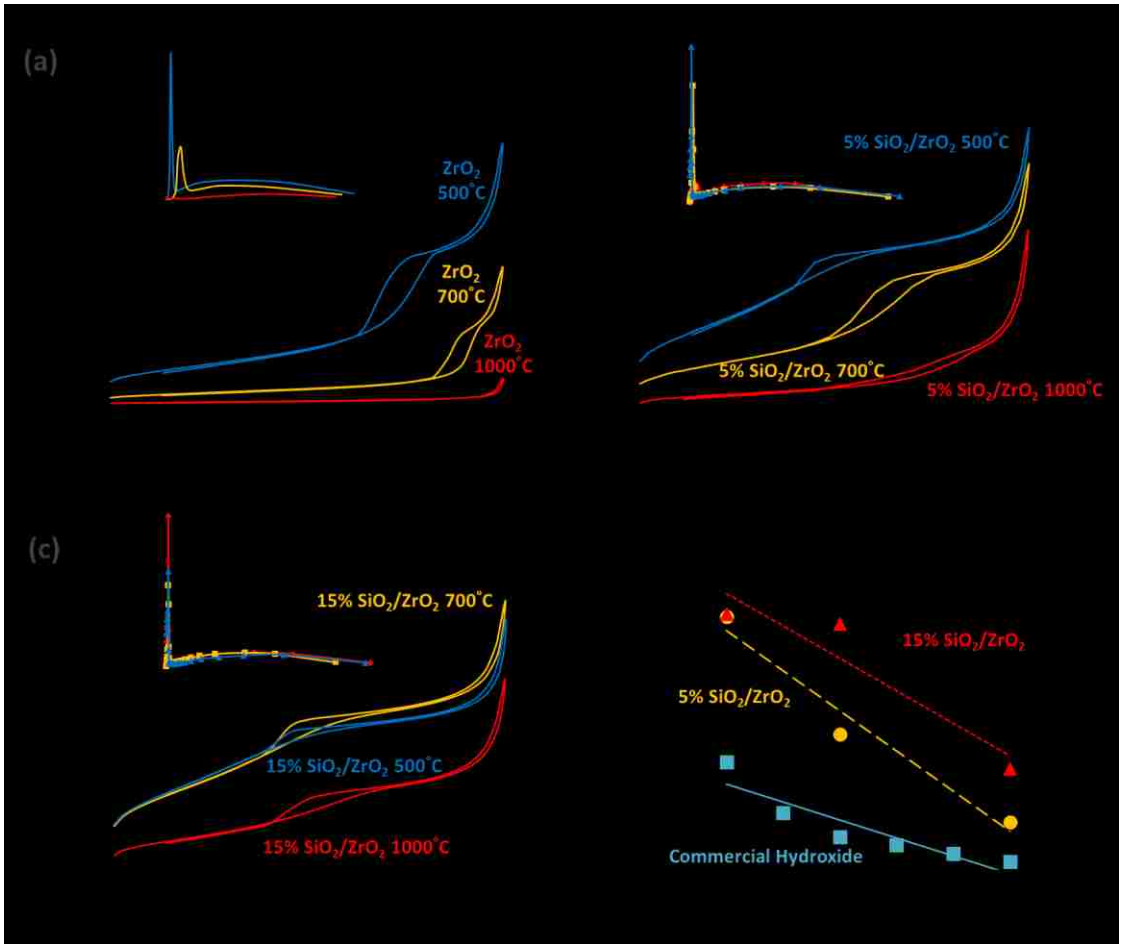

Figure 3-11. Nitrogen adsorption characterization of commercial zirconium hydroxide and supported SiO_2/ZrO_2 samples after three hour calcination at 500, 700, and 1000˚C: **(a)** N_2 isotherms of commercial ZrO_2 prepared from a commercial zirconium hydroxide, inset: calculated pore volume; **(b)** N_2 isotherms of 5wt% SiO_2/ZrO_2 samples, inset: pore volume; **(c)** N_2 isotherms of 15wt% SiO_2/ZrO_2 samples, inset: pore volume; **(d)** comparison of BET surface area of the samples versus calcination temperature.

Mechanism of Surface Stabilization as a General Phenomenon

It is proposed that a mechanism of surface stabilization occurs in all systems analyzed in this study (i.e. SiO_2/TiO_2, SiO_2/ZrO_2, and SiO_2/ZrO_2-hydroxide). The incorporation of a

second, supported oxide was observed to stabilize metastable oxide crystal structures, limit sintering, and prevent high temperature reconstruction. Mechanisms of oxide reconstruction initiate along the surface of a material when surpassing its characteristic Hüttig temperature and rapidly accelerate when heating above the Tammann temperature of a material.[43] The Hüttig temperature is the temperature at which surface atoms obtain enough energy to become mobile and spread along the surface; while the Tammann temperature is the temperature at which atoms obtain enough energy to transfer from the bulk to the surface of a crystal. Thus, the addition of a supported layer can be used to inhibit the atomic surface mobility of a metastable material and prevent both phase transformation and sintering from occurring. This is accomplished by more fully coordinating surface atoms of a metastable support and increasing atomic cohesion with the rest of the crystal.

In the SiO_2/TiO_2 system the mechanism of surface stabilization is effective for extended periods of time at moderate temperatures (700˚C) and for short intervals at more elevated temperatures (See **Figure 3-4**). At 700˚C the SiO_2/TiO_2 system is below the Tammann temperature of both silica ($SiO_2^{Tammann}$ ~720˚C) and titania ($TiO_2^{Tammann}$ ~920˚C); yet above their corresponding Hüttig temperatures (See **Table 3-1**). At this temperature the onset of surface mobility has begun and sintering ensues; however, minimal phase transformation occurs as the surface is stabilized by the SiO_2 layer. An increased loading of silica provides more robust stabilization of the metastable support as it more adequately covers the surface. At 1000˚C the sample is above the characteristic Tammann temperature of both silica and titania. This facilitates a gradual phase transformation over the course of several hours as the advent of bulk-to-surface transitions disrupt the mechanism of surface stabilization.

Table 3-1. Compilation of melting points, Tammann, and Hüttig temperatures for relevant oxides.[44,45]

Oxide [Source]	Melting Point (˚C)	Tammann Temperature (˚C)	Hüttig Temperature (˚C)
SiO_2 [25]	1712	719	~570
TiO_2 [30]	1843	922	~614
ZrO_2 [31]	2710	1220	~903

The supported SiO_2/ZrO_2 samples underwent a similar surface stabilization phenomenon as that observed in the SiO_2/TiO_2 system. SiO_2 successfully stabilized the metastable tetragonal phase of zirconia and limited the degree of sintering versus unsupported zirconia samples (See **Figure 3-6 and 3-8**). Furthermore, SiO_2 was able to scaffold zirconium hydroxides during crystallization and dramatically stabilized both the surface area of the material and promoted formation of the metastable tetragonal phase (See **Figure 3-9 and 3-11**). Thus, surface stabilization can be used not only to stabilize a metastable crystalline oxide, but promote formation of the metastable phase during synthesis, scaffold it's surface area, and stabilize the material at high temperatures.

When comparing the SiO_2/ZrO_2 system to the SiO_2/TiO_2 system, silica stabilizes the metastable t-ZrO_2 phase more readily than the a-TiO_2 phase. This is noted by preservation of the tetragonal phase even after calcination for extended periods of time at 1000˚C (See **Figures 3-7 and 3-10**); whereas the a-TiO_2 structure is completely converted to the rutile phase during prolonged calcination at 1000˚C (See **Figure 3-4**). ZrO_2 has a higher Tammann temperature ($ZrO_2^{Tammann}$ ~1200˚C) than TiO_2, allowing more robust stabilization at elevated temperatures. Thus, addition of SiO_2 limits reconstruction when heating above the characteristic Hüttig temperature of an oxide and reconfiguration occurs closer to the characteristic bulk Tammann Temperature of the material.

3.5 Conclusions

A generalized mechanism of surface stabilization was demonstrated by utilizing SiO_2 to stabilize common metastable oxide crystal structures (i.e. a-TiO_2 and t-ZrO_2). The incorporation of a supported oxide layer via IWI with TEOS stabilized both the phase and surface area of model supported oxide systems including SiO_2/TiO_2, SiO_2/ZrO_2, and SiO_2/ZrO_2-hydroxide. More robust stabilization was observed when increasing the SiO_2 loading from 5wt% to 15wt%. It is hypothesized that the small crystallite structure of the unsupported oxide allows rapid phase transformation and sintering when heating above the characteristic Hüttig temperature of the oxide ($T^{Hüttig}$ ~600˚C). Addition of a surface layer limits atomic surface mobility of the metastable support and prevents mechanisms of reconstruction when heating above the Hüttig temperature. This method of stabilization persists when calcining at temperatures below the characteristic Tammann temperature of the oxide for extended periods of time. Stabilization ultimately breaks down when heating above the characteristic Tammann temperature of the oxide, as bulk-to-surface mobility rapidly promotes reconfiguration. This is a general method of stabilization that can be utilized in applications which operate at elevated temperatures.

3.6 References

[1] O'Neill, Brandon J., David H. K. Jackson, Jechan Lee, Christian Canlas, Peter C. Stair, Christopher L. Marshall, Jeffrey W. Elam, Thomas F. Kuech, James A. Dumesic, and George W. Huber. "Catalyst Design with Atomic Layer Deposition." *ACS Catal. ACS Catalysis* 5.3 (2015): 1804-825.

[2] Jiang, Changyun, Man Yin Leung, Wei Ling Koh, and Yuning Li. "Influences of Deposition and Post-annealing Temperatures on Properties of TiO_2 Blocking Layer Prepared by Spray Pyrolysis for Solid-state Dye-sensitized Solar Cells." *Thin Solid Films*519.22 (2011): 7850-854.

[3] Verbruggen, Sammy W., Shaoren Deng, Mert Kurttepeli, Daire J. Cott, Philippe M. Vereecken, Sara Bals, Johan A. Martens, Christophe Detavernier, and Silvia Lenaerts. "Photocatalytic Acetaldehyde Oxidation in Air Using Spacious TiO_2 Films Prepared by Atomic Layer Deposition on Supported Carbonaceous Sacrificial Templates." *Applied Catalysis B: Environmental* 160-161 (2014): 204-10.

[4] Stevens, R. *Zirconia and Zirconia Ceramics*. Manchester, U.K.: Magnesium Elektron, 1986.

[5] Jacobsen, H., and P. Kleinschmit. "3.6 Flame Hydrolysis." *Preparation of Solid Catalysts*. By G. Ertl, H. Knözinger, and J. Weitkamp. Weinheim: Wiley-VCH, 1999. 99-109.

[6] Sanchez, C., L. Rozes, F. Ribot, C. Laberty-Robert, D. Grosso, C. Sassoye, C. Boissiere, and L. Nicole. ""Chimie Douce": A Land of Opportunities for the Designed Construction of Functional Inorganic and Hybrid Organic-inorganic Nanomaterials." *Comptes Rendus Chimie* 13.1-2 (2010): 3-39.

[7] White, Laurence, and George Duffy. "Staff-Industry Collaborative Report Vapor-Phase Production of Colloidal Silica." *Ind. Eng. Chem. Industrial & Engineering Chemistry* 51.3 (1959): 232-38.

[8] Segal, D. "Soft Chemistry Routes to Zirconia Ceramics." *Zirconia Engineering Ceramics: Old Challenges - New Ideas*. 241-49.

[9] Gupta, Shipra M., and Manoj Tripathi. "A Review on the Synthesis of TiO_2 Nanoparticles by Solution Route"." *Central European Journal of Chemistry* 10.2 (2012): 279-94.

[10] Chorkendorff, I., and J.W Niemantsverdriet. "10.2.1.1 Catalytic Converter." *Concepts of Modern Catalysis and Kinetics*. 2nd ed. Weinheim: Wiley-VCH, 2007. 385-87.

[11] Basolo, Fred, and Ronald C. Johnson. *Coordination Chemistry; the Chemistry of Metal Complexes*. New York: W.A. Benjamin, 1964.

[12] Stevenson, Scott A., and Eli Ruckenstein. "Chapter 11. Mechanisms of Sintering (Migration and Coalescence)." *Metal-support Interactions in Catalysis, Sintering, and Redispersion*. New York: Van Nostrand Reinhold, 1987. 156-86.

[13] Knözinger, H., and E. Taglauer. "Spreading and Wetting." *Preparation of Solid Catalysts*. Ed. G. Ertl, H. Knözinger, and J. Weitkamp. Weinheim: Wiley-VCH, 1999. 501-26

[14] Mercera, P.D.L., J.G. Van Ommen, E.B.M. Doesburg, A.J. Burggraaf, and J.R.H. Ross. "Zirconia as a Support for Catalysts Evolution of the Texture and Structure on Calcination in Air." *Applied Catalysis* 57.1 (1990): 127-148.

[15] Takagi, Mieko. "Electron-Diffraction Study of Liquid-Solid Transition of Thin Metal Films." *Journal of the Physical Society of Japan J. Phys. Soc. Jpn.* 9.3 (1954): 359-63.

[16] Dana, James Dwight, Edward Salisbury Dana, Charles Palache, Harry Berman, and Clifford Frondel. *The System of Mineralogy*. New York: Wiley, 1944.

[17] Kingery, W. D. "Polymorphism." *Introduction to Ceramics*. New York: John Wiley & Sons, 1960. 133-239.

[18] Zhang, Hengzhong, and Jillian F. Banfield. "Thermodynamic Analysis of Phase Stability of Nanocrystalline Titania." *Journal of Materials Chemistry* 8.9 (1998): 2073-076.

[19] Garvie, R. C. "Stabilization of the Tetragonal Structure in Zirconia Microcrystals." The Journal of Physical Chemistry 82.2 (1978): 218-24.

[20] Stevens, R. *Zirconia and Zirconia Ceramics*. Manchester, U.K.: Magnesium Elektron, 1986.

[21] Garvie, R. C., and M. F. Goss. "Intrinsic Size Dependence of the Phase Transformation Temperature in Zirconia Microcrystals." *Journal of Materials Science* 21.4 (1986): 1253-257.

[22] Garvie, Ronald C. "The Occurrence of Metastable Tetragonal Zirconia as a Crystallite Size Effect." *The Journal of Physical Chemistry* 69.4 (1965): 1238-243.

[23] Garvie, R. C. "Stabilization of the Tetragonal Structure in Zirconia Microcrystals." The Journal of Physical Chemistry 82.2 (1978): 218-24.

[24] Garvie, R. C., R. H. Hannink, and R. T. Pascoe. "Ceramic Steel?" *Nature* 258.5537 (1975): 703-04.

[25] Harmer, M. P. "The Phase Behavior of Interfaces." *Science* 332.6026 (2011): 182-83.

[26] Li, Meijun, Zhaochi Feng, Pinliang Ying, Qin Xin, and Can Li. "Phase Transformation in the Surface Region of Zirconia and Doped Zirconia Detected by UV Raman Spectroscopy." *Phys. Chem. Chem. Phys. Physical Chemistry Chemical Physics* 5.23 (2003): 5326.

[27] Li, Can, and Meijun Li. "UV Raman Spectroscopic Study on the Phase Transformation of ZrO_2, Y_2O_3-ZrO_2 and SO_2^4/ZrO_2." *J. Raman Spectrosc. Journal of Raman Spectroscopy* 33.5 (2002): 301-08.

[28] Li, Meijun, Zhaochi Feng, Guang Xiong, Pinliang Ying, Qin Xin, and Can Li. "Phase Transformation in the Surface Region of Zirconia Detected by UV Raman Spectroscopy." *The Journal of Physical Chemistry B J. Phys. Chem. B* 105.34 (2001): 8107-111.

[29] Spurr, R. A., and Howard Myers. "Quantitative Analysis of Anatase-Rutile Mixtures with an X-Ray Diffractometer." *Analytical Chemistry* 29.5 *(*1957): 760-762.

[30] Toraya, H., M. Yoshimura, and S. Somiya. "Calibration Curve for Quantitative Analysis of the Monclinic-tetragonal ZrO_2 System by X-ray Diffraction." *Journal of the American Ceramic Society* 67.6 (1984): C-119-121.

[31] Brunauer, Stephen, P. H. Emmett, and Edward Teller. "Adsorption of Gases in Multimolecular Layers." *J. Am. Chem. Soc. Journal of the American Chemical Society* 60.2 (1938): 309-19.

[32] Barrett, Elliott P., Leslie G. Joyner, and Paul P. Halenda. "The Determination of Pore Volume and Area Distributions in Porous Substances. I. Computations from Nitrogen Isotherms." *J. Am. Chem. Soc. Journal of the American Chemical Society* 73.1 (1951): 373-80.

[33] Webb, Paul, and Clyde Orr. *Analytical Methods in Fine Particle Technology*. Norcross, GA: Micromeritics Instrument, 1997.

[34] Bearden, J. A. "X-Ray Wavelengths." *Reviews of Modern Physics Rev. Mod. Phys.* 39.1 (1967): 78-124.

[35] Lowell, S., Joan E. Shields, Martin A. Thomas, and Matthias Thommes.*Characterization of Porous Solids and Powders: Surface Area, Pore Size, and Density*. Dordrecht: Kluwer Academic, 2004.

[36] Sing, K. S. W. "Reporting Physisorption Data for Gas/solid Systems with Special Reference to the Determination of Surface Area and Porosity (Provisional)." *Pure and Applied Chemistry* 54.11 (1982): 2201-2218.

[37] Sing, K. S. W. "Reporting Physisorption Data for Gas/solid Systems with Special Reference to the Determination of Surface Area and Porosity (Recommendations 1984)." *Pure and Applied Chemistry* 57.4 (1985): 603-05.

[38] Brinker, C. Jeffrey., and George W. Scherer. *Sol-gel Science: the Physics and Chemistry of Sol-gel Processing*. Boston: Academic, 1990.

[39] Davis, P., C. Jeffrey Brinker, and D. Smith. "Pore Structure Evolution in Silica Gel during Aging/drying I. Temporal and Thermal Aging." *Journal of Non-Crystalline Solids*142 (1992): 189-196.

[40] Davis, P., C. Jeffrey Brinker, D. Smith, and R. Assink. "Pore Structure Evolution in Silica Gel during Aging/drying II. Effect of Pore Fluids." *Journal of Non-Crystalline Solids* 142 (1992): 197-207.

[41] Deshpande, R., D. Hua, D. Smith, and C. Brinker. "Pore Structure Evolution in Silica Gel during Aging/drying. III. Effects of Surface Tension." *Journal of Non-Crystalline Solids* 144 (1992): 32-44.

[42] Davis, P., R. Deshpande, D. Smith, C. Brinker, and R. Assink. "Pore Structure Evolution in Silica Gel during Aging/drying. IV. Varying Pore Fluid pH." *Journal of Non-Crystalline Solids* 167.3 (1994): 295-306.

[43] Stevenson, Scott A., and Eli Ruckenstein. "Chapter 13. Wetting and Spreading." *Metal-support Interactions in Catalysis, Sintering, and Redispersion*. New York: Van Nostrand Reinhold, 1987. 230-248.

[44] Carreon, Moises A., and Vadim V. Guliants. "Ordered Meso- and Macroporous Binary and Mixed Metal Oxides." *European Journal of Inorganic Chemistry* 2005.6 (2005): 1189.

[45] Hlavac, J. "IUPAC Melting Temperatures of Refractory Oxides: Part 1." *Pure & Applied Chemistry* 54.3 (1982): 681.

Chapter 4: Interfacial Stabilization of Metastable Oxide Films

4.1 Abstract

This work demonstrates a phenomenon which preserves the traditionally metastable anatase crystal structure of titania (TiO_2) at elevated temperatures (T > 500˚C) along an oxide/oxide interface. To explore this concept, uniform TiO_2 films ranging in thickness from ~20 to 200nm were prepared using a convective deposition process to coat the surface of oxidized silicon wafers (TiO_2/SiO_2-Wafers). A chelated titanium(IV) butoxide solution was utilized during this process in order to form a gelled titania precursor film. Subsequent calcination of the films facilitated crystallization and stabilization of the anatase phase of titania, while corresponding bulk-titania control powders rapidly converted to the more stable rutile phase, as characterized by X-ray diffraction. This mechanism of stabilization is further investigated using focused ion beam lithography (FIB), atomic resolution microscopy (ARM), and energy dispersive x-ray spectroscopic mapping (EDS). Results indicate that the interface provided by the oxidized silicon wafer allows the film to more fully coordinate along the substrate, while neighboring TiO_2 crystallites are coherently confined in a two-dimensional arrangement within the film. This reduced dimensionality acts to inhibit rutile grain propagation by limiting the number of neighboring crystallites versus that observed in bulk control powders; which, traditionally consist of three-dimensionally aggregated crystallites. The combination of these effects reduces the amount of exposed TiO_2 surface area and thus preserves the metastable anatase phase during calcination by mitigating atomic surface mobility. ARM imaging and EDS mapping shows the presence of an amorphous SiO_2 layer along the Si substrate and the absence of homogenous Si doping within the TiO_2 layer. Rutile grain

growth accelerates when exceeding the Tammann temperature of the oxide ($TiO_2^{Tammann}$~920˚C), as bulk-to-surface mobilization allows rapid lateral growth of rutile grains. This method of film stabilization is thought to be a general phenomenon similar to that observed in supported oxide systems (See Chapter 3) and has direct use in applications including: dye-sensitized solar cell boundary layers, TiO_2-based pollution abatement coatings, UV-filters, and supported catalysts.

4.2 Introduction

Transition metal oxide films are utilized in a wide range of applications including catalysis, dye-sensitized solar cells (DSSC), pollution abatement technologies, gas sensors, and hydrothermally stable protective layers.[1,2,3] The unique chemical, electronic, optical, and structural properties of transition metal oxides provide a diverse palette of materials which offer selective control of properties including: refractive index,[4] roughness,[5,6] gas permeability,[7] band gap,[8] catalytic performance,[9,10] and stability.[11] The inherent low surface energies characteristic of most oxides enable increased atomic surface mobility, which permits oxides to spread and coat substrates at moderate temperatures.[12] These properties allow oxides to be readily dispersed as films with tunable thicknesses ranging from sub monolayer catalytic coatings, to thick macroscopic crystalline films. However, low surface energies and corresponding high surface mobility's also make oxide films susceptible to low temperature methods of reconfiguration. As a result, it is necessary to assess mechanisms of oxide film stabilization for high temperature applications.

Film Preparation Methods

Oxide films are typically synthesized using a chemical precursor which is deposited onto a substrate via dip-coating,[13,14] convective deposition,[15] spin coating,[16] and atomic layer

deposition.[17] After preparation, the precursor film is often calcined at elevated temperatures (T > 400˚C) in order to promote crystallization. However, during the process of calcination, oxides undergo dramatic physical and chemical changes which alter the structure and inherent properties of the film. These changes include: hydrolysis, condensation, syneresis, crystallization, phase transformation, and sintering.[18] As a result these effects must be carefully accounted for in order to engineer films with desired properties.

Gel Reconstruction Effects

There are many drawbacks related to thermal reconstruction of the precursor gel during calcination. As the precursor is heated it begins to hydrolyze, evolve water, condense, and densify in a process known as syneresis.[19,20,21,22,23] These changes result in a large density reduction as the gel condenses upon itself and initiates crystal nucleation.[24] Syneresis typically results in the formation of a matrix of interconnected crystallites on the order of ~10-100nm; as opposed to large single crystal monolith's. Upon further temperature elevation additional methods of thermal reconstruction including sintering, atomic surface migration, and phase change begin to occur.[25] These processes can be problematic in film preparation as the topological and chemical structure of the film is constantly reconfiguring.

Metastable Oxide vs. Stable Oxides

Oxides often undergo a phase transformation from a metastable crystal structure (e.g. anatase titania) to a more stable crystalline phase (e.g. rutile titania) above ~500˚C.[26] This process typically initiates along the surface of a crystal as opposed to within the bulk, as the surface of the oxide is not fully coordinated to a rigid matrix of neighboring crystalline atoms; but rather coordinated by a diverse range of surface species (e.g. M-OH, $M(=O)_x$, M-O-M etc).[27] As a result of this, surface atoms are bound with less cohesive energy than bulk lattice atoms

and are more readily able to become mobile, reconfigure, and even melt at low temperatures.[28,29] This lack of cohesion invites the development of surface strains, defect sites, and surface amorphization during calcination; all of which likely assist in the propagation of phase transformation along the surface of the oxide. As such, it is desirable to limit surface area in order to preserve metastable crystal states.

General Methods of Metastable Oxide Stabilization

The most widely recognized method of preventing phase evolution from occurring in bulk oxides entails the use of aliovalent dopants (e.g. Y^{3+}, Ca^{2+}, Mg^{2+} etc.) to relax internal strains within a crystal and to prevent phase transformation from propagating throughout the bulk of the crystalline lattice.[30] Another widely discussed method of preserving metastable crystal structures is to reduce the crystallite size below a critical radius in order to effectively balance the surface and bulk free energies of the crystal.[31,32,33] Similarly, phase stabilization has been reported by maintaining coherency along crystallite-to-crystallite grain boundaries. This interfacial contact is reported to induce a pressure upon neighboring crystallites that prevents phase transformation via confinement within a crystallite matrix.[34,35,36] Finally, a method of surface stabilization has been reported in the study of supported catalytic oxides (See Chapter 3). The addition of a surface oxide in these studies likely hinders atomic surface mobility of the supporting oxide, invites surface doping, and reduces grain propagation via confinement; all of which assist in the promotion of the metastable phase in the underlying support.[37,38,39]

Literature review of Current Thin Film Stabilization

Metalorganic chemical vapor deposition (MOCVD) has shown the ability to prepare metastable oxide films.[40] This approach allows direct epitaxial growth of metastable oxide

phases along a substrate's pre-existing lattice registration. This technique promotes stabilization by limiting porosity and surface area of the film and thus and increases coherency of neighboring crystals. However, utilizing this technique requires an extensive experimental apparatus, adequate environmental control, and the use of pristine crystalline substrates. Similar stabilization phenomenon has been observed on crystalline Si(100) surfaces prepared via more rapid dip-coating and spin coating techniques.[41,42] However, in these systems, characterization of the mechanism of stabilization and the possibility of a native oxide layer existing along the surface of the substrate remains unaccounted for.

Overview of this Study

This study seeks to more fundamentally examine the mechanisms employed during the stabilization of supported oxides (See Chapter 3) using a model thin film system. This is accomplished by examining the crystalline phase composition of thin TiO_2 films (thickness ~20-200 nm) deposited on oxidized silicon wafers. In this system, the oxide/oxide interface (TiO_2/SiO_2-Wafer) is demonstrated to stabilize the traditionally metastable anatase TiO_2 phase during high temperature calcination (T > 500˚C). Mechanistic insight suggests that the SiO_2 substrate helps to more fully coordinate the TiO_2 crystallites, promotes particle-to-particle coherency, and limits sintering via reduction in dimensionality to that of a two-dimensional film. These concepts of oxide stabilization are currently useful in applications as diverse as catalysis, DSSC boundary layers, and hydrothermal coating applications. In chapter 5 these concepts will be employed to stabilize catalytic materials with unique surface chemistries.

4.3 Materials and Methods

Materials

The following reagents were obtained from Sigma-Aldrich and used without further purification: sulfuric acid (H_2SO_4, 98 wt %), ethyl acetoacetate ($CH_3COCH_2COOC_2H_5$, ≥ 99.8 wt %), 2,4-pentadione ($CH_3COCH_2COCH_3$, > 99 wt %), 2,3-butanedione ($CH_3COCOCH_3$, 97 wt %), and titanium(IV) butoxide ($Ti(OBu)_4$, 97 wt %). Hydrogen peroxide (H_2O_2, 30 wt %) and 200 proof ethanol were obtained from Fisher Scientific. Single crystal silicon (100) wafers were purchased from Silicon Quest International.

Substrate Preparation

Commercial silicon (Si) wafers were used as a supporting substrate for the deposition of titania films. Prior to film deposition, the wafers were immersed in a piranha cleaning solution consisting of 98wt% sulfuric acid and 30 wt % hydrogen peroxide mixed in a 3:1 volume ratio. The wafers were submerged for at least 12 hours in order to remove organic surface residue and to simultaneously hydroxylate the surface of the Si-wafer. The cleaned superhydrophilic wafers were then rinsed with deionized water in order to remove residual acid content from the surface of the substrates. The silicon wafers were then oxidized via calcination in static air by heating at 5˚C per minute to 800˚C and maintaining a three hour dwell time. This process facilitated the development of a thin oxidized silica (SiO_2) layer along the surface of the silicon wafer. The thickness of the SiO_2 layer was subsequently measured with a variable angle spectroscopic ellipsometer to ensure consistency of the SiO_2 thickness (17+/-3 nm) between substrates.

Preparation of Precursor Solutions

Ethanol based $Ti(OBu)_4$ precursor solutions were prepared utilizing multi-dentate chelating ligands including: ethyl acetoacetate, 2,4-pentadione, and 2,3-butanedione to limit hydrolysis and condensation of the alkoxide. The stabilized precursors were prepared by first mixing ethyl acetoacetate, 2,4-pentadione, and 2,3-butanedione (8/1/1.2 molar ratio) in a sealed container. The alkoxide precursor (~14.2 moles) was then measured separately and added to the solution of stabilizing ligands under vigorous stirring. Finally, the solution was diluted with ethanol to reach a final molar composition consisting of: 8/1/1.2/14.2/641 of each respective component. The stabilized precursor solution was then vigorously stirred for at least one hour before depositing via convective deposition on the oxidized silica substrate.

Convective Deposition of Oxide Films

Thin TiO_2 films with tunable thickness were deposited via convective deposition on the oxidized silicon wafers using a modified syringe pump apparatus as reported elsewhere.[43] The oxidized wafer was mounted horizontally along the syringe pump and slowly swiped under a stationary glass slide mounted at a 45˚ angle relative to the substrate. The edge of the glass slide was covered with a piece of Parafilm. A 10-50 µL aliquot of the chelated TiO_2 precursor solution was dispensed under the coating blade, forming a meniscus between the substrate and the blade. After deposition of the solution, the coating process was initiated, allowing the precursor solution to be deposited along the oxidized silicon wafer at a coating rate ranging from 0.12–1.2 centimeters per minute. This resulted in the formation of a gelled alkoxide-based TiO_2 precursor film. The film was then calcined at 5˚C per minute to a temperature ranging from 500-1000˚C and subsequently dwelled at the final temperature for three hours.

Characterization

Ellipsometry measurements were conducted on the Si-wafers to measure SiO_2 thickness using a V-vase variable angle spectroscopic ellipsometer from J.A. Woollam Company, Inc. The data was analyzed using a WVASE32 software package. After preparing the TiO_2/SiO_2 films, the oxide crystallinity was examined using a Rigaku Miniflex II X-ray diffractometer utilizing Cu K-alpha radiation (K_α=1.5418 Å). Prior to imaging, samples were first coated with 4 nm of Ir using a plasma deposition instrument to avoid charging. Scanning electron microscopy (SEM) images were collected using a Hitachi 4300 SE/N with accelerating voltages ranging from 5-10 kV. Transmission electron microscopy (TEM) images were collected with a JEOL 2000FX microscope. Atomic resolution microscopy (ARM) images were collected with a JEOL JEM-ARM-200CF microscope equipped with a Centurio XEDS system.

Focused ion beam lithography (FIB-Lithography) was performed using a Scios DualBeam FIB instrument from FEI to prepare thin slices (Thickness<100 nm) of the calcined TiO_2/SiO_2 wafers for cross sectional depth profiling and further characterization. The sample was inserted in the FIB and a layer of Pt was deposited via E-beam deposition and subsequent ion beam deposition to create a rigid backbone along the surface of the TiO_2 film. A cross section was then prepared using Ga ion etching at currents ranging from 1-7 nA. Next, the thin film coupon was removed via *in situ* lift out and placed via Pt deposition onto a copper grid for characterization.

4.4 Results and Discussion

Overview of Thin Film Preparation: SiO_2 formation, Deposition Process, and Calcination

Preparation of uniform thin-TiO_2 films was accomplished via three primary steps: (a) oxidation of the silicon substrate; (b) deposition of a chelated $Ti(OBu)_4$ precursor solution; (c)

crystallization of the TiO_2 precursor layer (See **Figure 4-1**). Preliminary calcination of the silicon wafer offered a mechanism of controlled oxide growth along the surface of the silicon wafer. This facilitated the development of a uniform SiO_2 surface for the eventual deposition of a crack-free titania layer and further characterization of the resulting oxide interface.

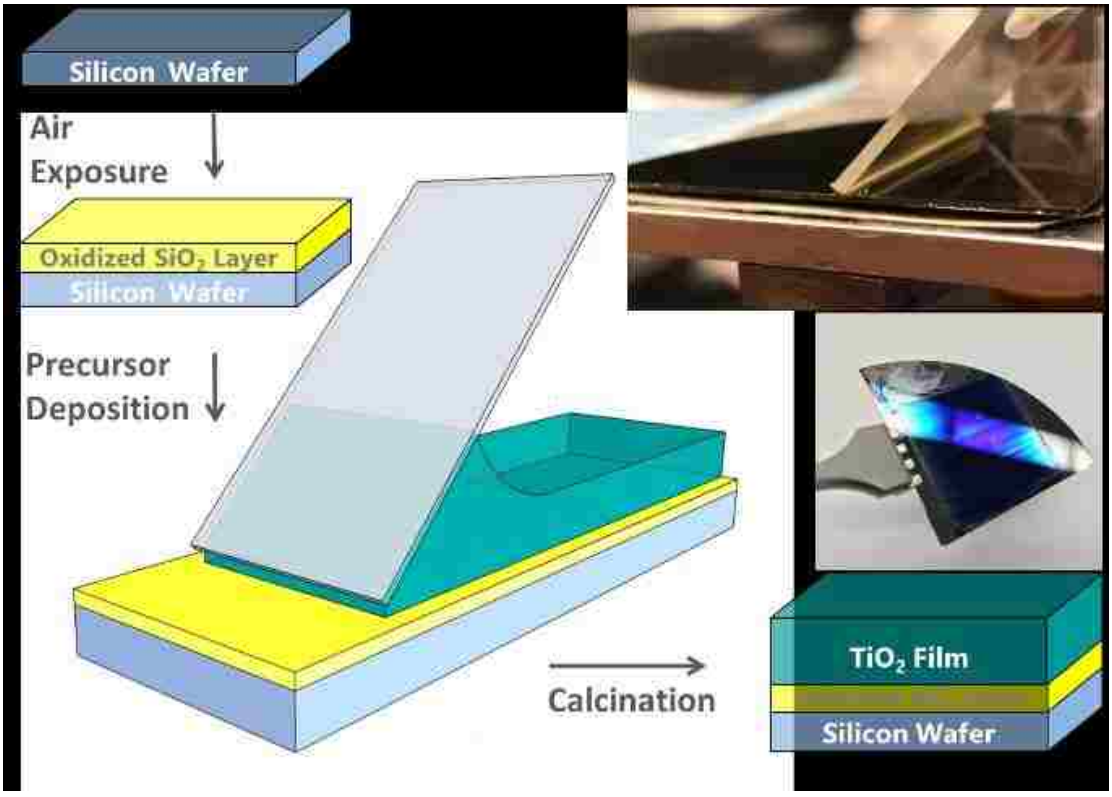

Figure 4-1. Schematic depicting Si-Wafer oxidation, the convective deposition process, and resulting TiO_2 thin films.

Ellipsometry Measurements

Pure silicon is known to undergo rapid oxidation when exposed to atmospheric oxygen.[44] Exposure to air generates a native oxide layer on the order of several nanometers thick; while calcination under controlled conditions offers further growth of this oxidized layer. The silicon substrates were calcined in air for several hours prior to film deposition in order to

ensure consistent thickness of the SiO_2 layer. This step resulted in the production of flat, oxidized silicon substrates with reproducible thickness.

Ellipsometry was utilized to measure growth of the SiO_2 layer with increasing calcination temperature (See **Figure 4-2a**). Prior to calcination the native oxide layer was measured to be 1.7+/-0.1 nm thick. Rapid oxidation occurred when calcining above 500˚C and allowed controlled growth of an oxide layer tens of nanometers thick. Conversely, high temperature calcination at 1000˚C in an inert nitrogen atmosphere resulted in minimal oxide formation (SiO_2 Thickness = 3.4+/-0.1 nm). Calcination at 800˚C for three hours was found to produce a flat substrate with a reproducibly thick oxide layer (SiO_2 Thickness = 19.3+/-3 nm). This calcination regime was utilized for the production of oxidized silicon substrates with reproducible thickness and eventual coating with the TiO_2 precursor solution. Growth of oxide thickness after successive three hour calcinations at 800˚C was measured with ellipsometry (See **Figure 4-2b**). The oxide layer was found to grow in a linear fashion with successive calcinations.

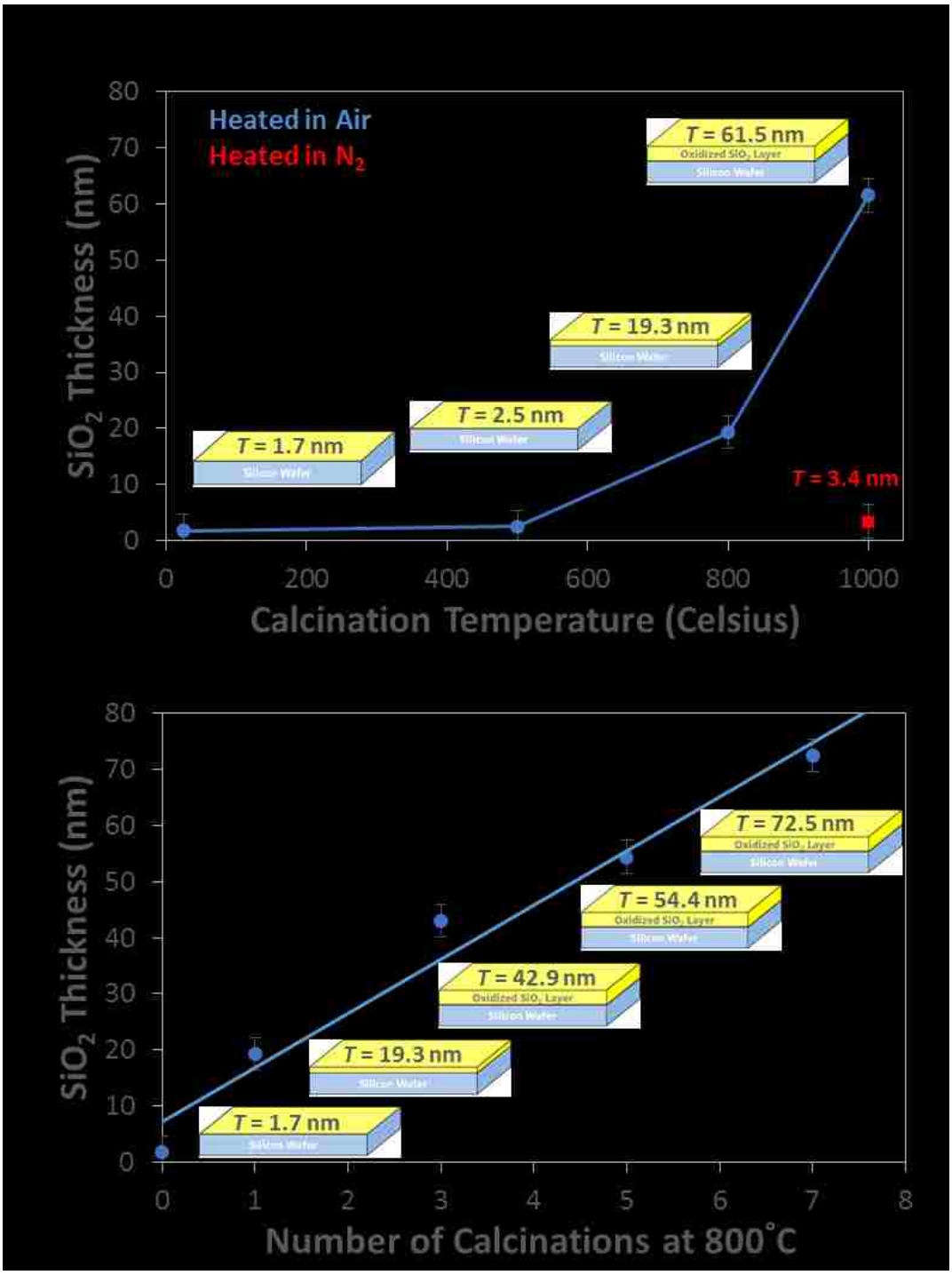

Figure 4-2. Ellipsometery measurements on silicon wafers: **(a)** silicon oxide thickness after calcination at each temperature; **(b)** silicon oxide thickness after iterative calcinations at 800˚C. Each calcination utilized a 5˚C per minute ramp rate under atmospheric conditions and three hour dwell time.

Metal Alkoxide Selection and Chelation Chemistry

Titanium(IV) butoxide was utilized for film deposition due to its ability to gel and subsequently crystallize via calcination.[45] Large butoxide ligands surround the central titanium atom in this complex and provide steric hindrance, which delays the onset of hydrolysis.[46] Additionally, a variety of multidentate chelating groups (i.e. acetoacetate, 2,4-pentadione, 2,3-butanedione) were utilized in the precursor solution to stabilize the metal alkoxide and limit the extent of hydrolysis during film deposition.[47,48] These additives resulted in a precursor that was relatively stable in the presence of air and allowed uniform film deposition prior to gelation.

Effect of Coating Speed on Film Uniformity

The effect of coating speed on crack propagation was analyzed in order to ensure the reproducible production of uniform thin films. Coating speed was varied from 0.12-1.2 centimeters per minute during deposition. As the blade swept along the silicon wafer, the volatile contents within the solution dried and formed a tacky titanium hydroxide based precursor gel. The films were subsequently calcined and analyzed with SEM to assess film uniformity. Slow coating rates allowed the formation of a combination of small spherical and large plate shaped crystallites. The large crystallites spanned several hundred nanometers in size and were noticeably absent with fast deposition rates. Faster coating speeds also resulted in thinner films and limited the convection time allowed for titania precursor molecules to assemble along the advancing gelation line. These films were typically more uniform in thickness, exhibited limited defects, and generated minimal crack formation (See **Figure 4-3**).

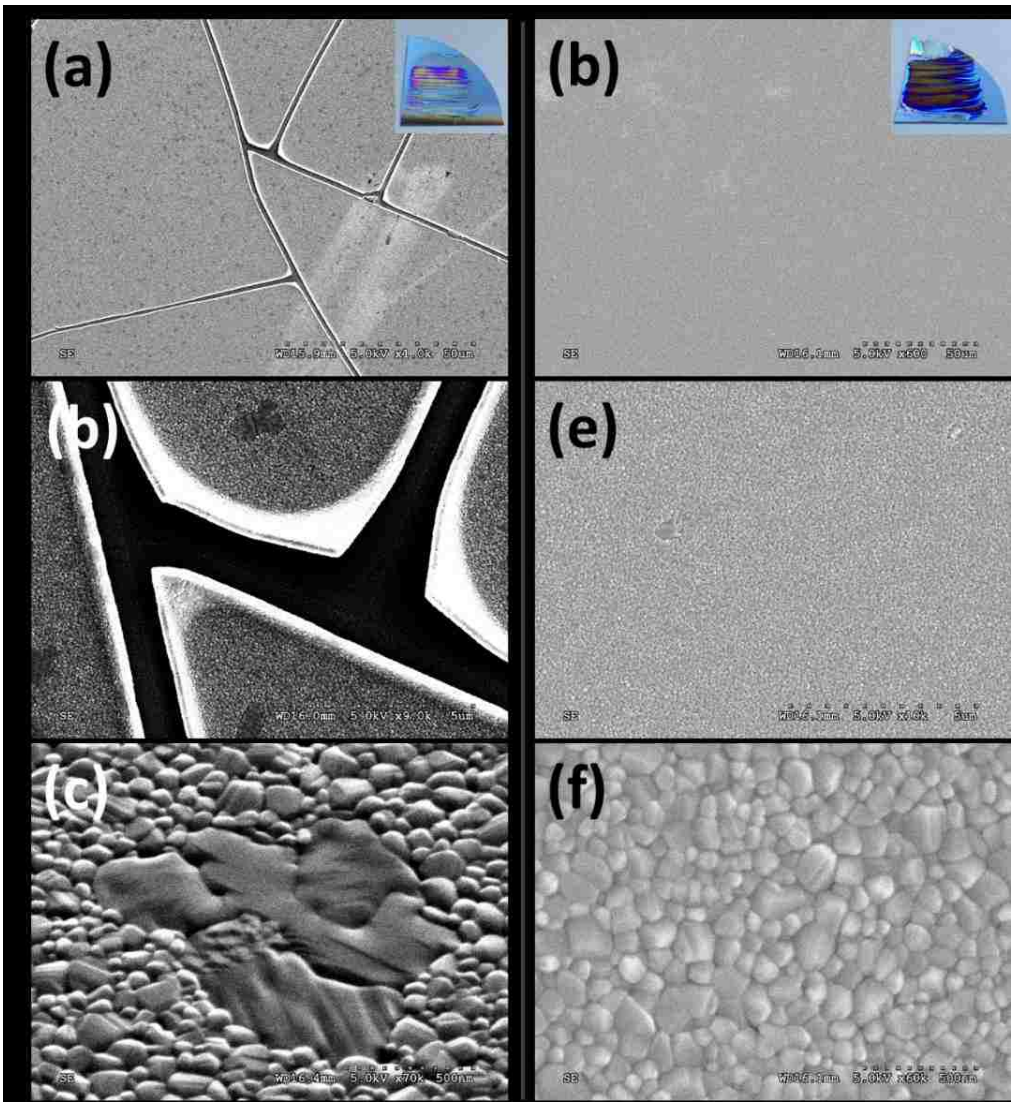

Figure 4-3. SEM images of thin TiO_2 films prepared via convective deposition of 50 µL aliquots of solution and subsequent three hour calcination at 800˚C. Coating rates utilized are as follows: **(a-c)** 0.12 cm/min; **(d-f)** 1.2 cm/min.

Films prepared with slow coating rates were thicker, more susceptible to crack formation, and produced a large number of macroscopic striations. Slow coating rates facilitate longer convection times, which allow increased precursor flow to the gelation line and the likelihood of local flux inhomogeneity's. As a result of these instabilities, convective deposition processes utilizing lower coating rates are typically reported to produce increased cracks and striations.[49] Additionally, thicker films undergo substantial shrinkage as capillary

effects and syneresis acts to contract the alkoxide based gel upon itself; this results in rending of the gel prior to crystallization. As a result of these findings a 1.2 centimeter per minute coating speed was utilized as the optimal coating rate for gel deposition.

Macroscopic crack development was distinguishable by the formation of colored striations running perpendicular to the coating direction. Slow coating rates facilitated cracks spanning the entire width of a film while fast coating rates only left small tears along a film's outer edges. Upon further investigation with SEM, these cracks and striations had peeled from the surface of the substrate and left a thin line of residual titania along the silica's surface (See **Figure 4-4**). This suggests that the film had once covered the entire substrate; however, syneresis and drying had facilitated an elastic contraction along defects and propagated the formation of cracks. Further calcination resulted in sintering and shrinkage of the elevated portions of the film, as is noticed by the curling and thickening of these elevated regions. These elevated portions were typically several hundred nanometers thicker than the film and contained the presence of larger plate shaped crystallites.

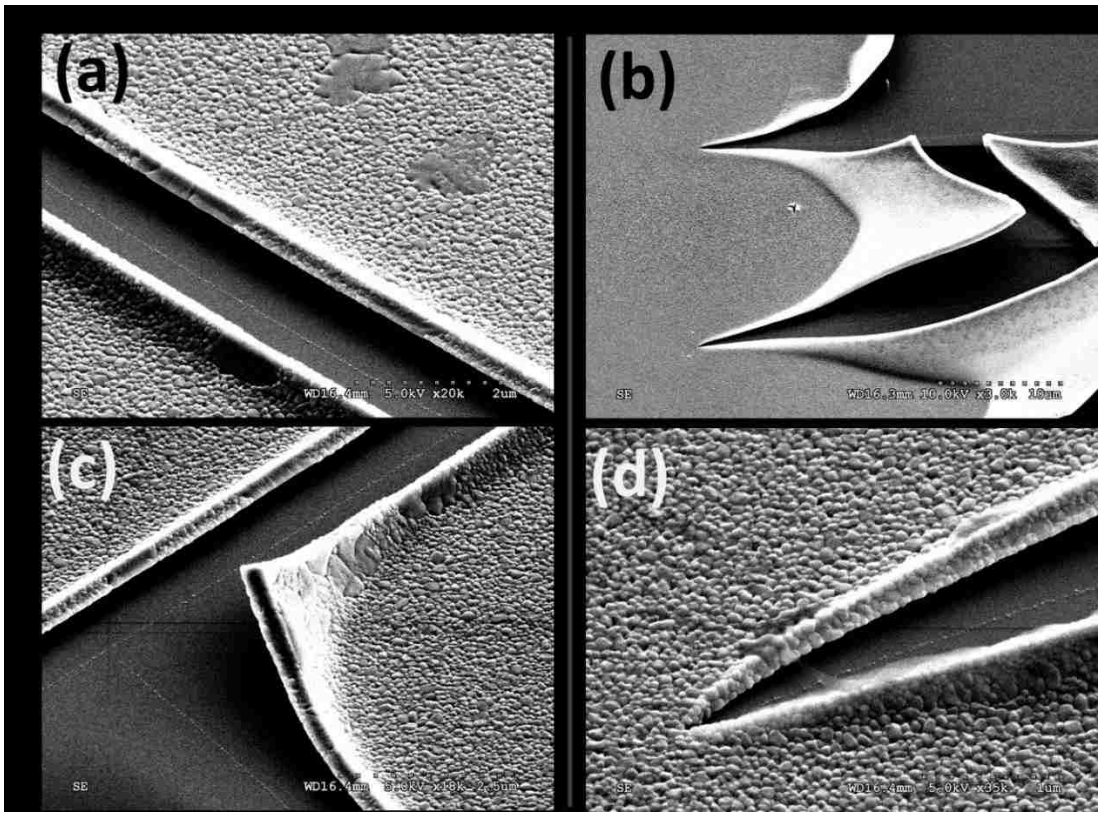

Figure 4-4. SEM images of striations and cracks in TiO_2 films prepared via deposition of 50 µL aliquots of solution and subsequent three hour calcination at 800˚C in air. Coating rates utilized: **(a)** 0.12 cm/min; **(b)** 1.2 cm/min; **(c)** additional view of a 0.12 cm/min film; **(d)** additional view of a 1.2 cm/min film.

Effect of Coating Speed

Slower coating rates facilitated increased development of the rutile phase of titania (See **Figure 4-5**). This is observed by the presence of the rutile (100) peak at approximately 28.1˚ (2-theta). Conversely, the rutile phase was noticeably absent in films prepared with fast coating speeds. Thus, the rutile phase was promoted in thick films containing many cracks. Formation of this phase likely occurs along defects in the elevated portions of the film, as these regions are not coherently adhered to the film, act more traditionally like bulk titania, and are more susceptible to sintering than surface crystals. This promotes the formation of larger

plate-like crystallites and invites additional mechanisms of surface driven phase transformation.

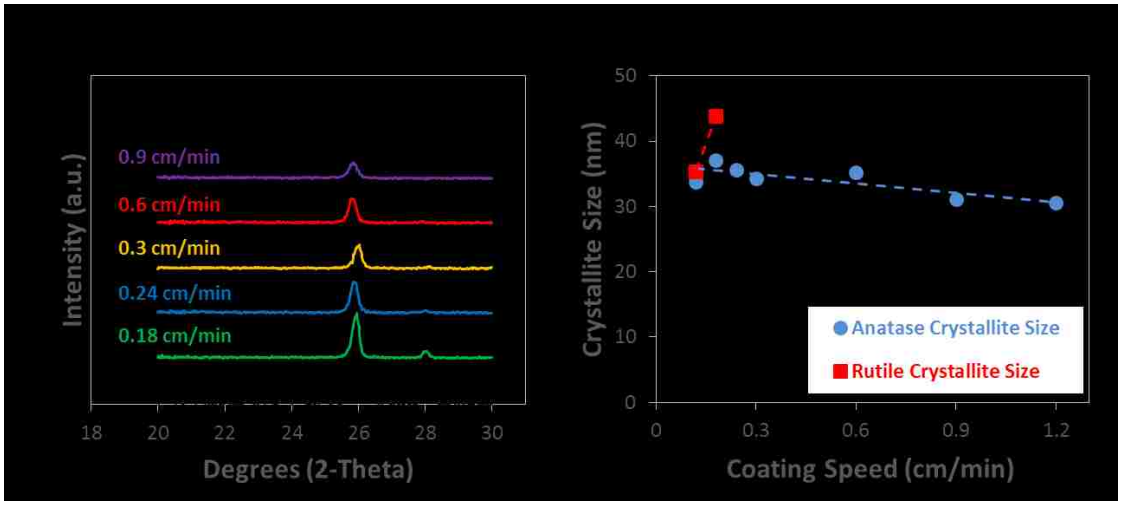

Figure 4-5. XRD characterization of thin film titania samples prepared via convective deposition at different coating rates. **(a)** X-ray diffractogram; **(b)** Scherrer analysis of crystallite size. The films were prepared with a 50 µL aliquot of precursor solution and calcined at 800˚C for three hours.

Intensities of the anatase (101) peak appear sharper for samples prepared with slow coating rates (**See Figure 4-5a**). This suggests that slow deposition rates facilitate larger crystallites and therefore thicker films than those prepared via fast coating speeds. This is supported by the presence of the large plate shaped crystals observed in the SEM images (See **Figure 4-3a**). The Scherrer equation was used to assess qualitative crystallite size based upon the characteristic peak intensity of each phase (See **Equation 4-1**).[50] The calculated size of the anatase crystallites suggests a slight size reduction occurs when the coating speed was increased. Additionally, Scherrer analysis suggests that rutile crystallites were slightly larger than anatase crystallites. This follows the thermodynamic theory proposed by R.C. Garvie which suggests that larger crystallites prefer the thermodynamically more stable structure (i.e. rutile titania).[31-34] However, the calculated Scherrer size provides only a qualitative

approximation of crystallite size for spherical crystallites below ~100 nm in diameter and does not accurately account for the large plate crystallites which span several hundred nanometers in size. The platelets are highly anisotropic in shape and thus have significantly different shape factors (k) than the smaller, more spherical crystallites.[51]

$$\tau = \frac{K\lambda}{\beta cos\theta} \qquad \textbf{Equation 4-1}$$

$$\tau = \text{mean size of crystalline domains}$$

$$k = \text{Shape factor } (0.9)$$

$$\lambda = \text{ Wavelenth}$$

$$\beta = \text{Line broadening at full widht half maxium intensity (FWHM)}$$

$$\theta = \text{Bragg angle}$$

Effect of Calcination Temperature on Phase

A series of films and bulk titania powders were prepared to study the effect of calcination temperature on phase composition. Thin films were prepared using 20 µL aliquots of precursor solution and coating speeds of 1.2 centimeters per minute in order to reduce the presence of defects and striations. The samples were heated at temperatures ranging from 500-1000˚C and characterized with XRD. Bulk titania powders initially produced the anatase phase when calcined at 500˚C but rapidly converted to the rutile phase at 700˚C (See **Figure 4-6a**). Conversely the TiO_2 films exhibited the anatase phase at all temperatures while development of the rutile crystal structure was only observed at 900˚C and above (See **Figure 4-6b**). This provides direct evidence of the interfacial stabilization of the anatase phase of titania when in direct contact with the SiO_2 interface.

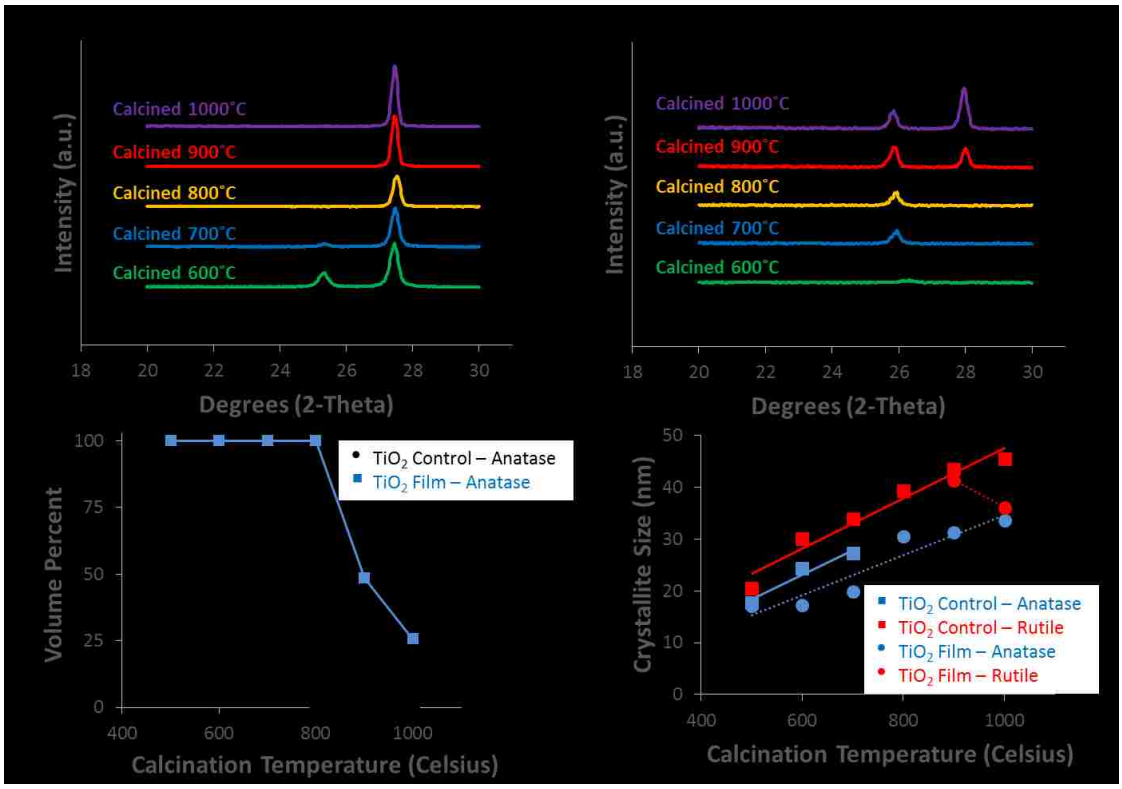

Figure 4-6. XRD characterization of bulk titania powders and thin TiO_2 films. Films were prepared with a 20 µL aliquot of precursor solution and a coating speed of 1.2 centimeters per minute. Samples were drying and calcined at various temperatures **(a)** XRD of bulk TiO_2 control powder; **(b)** XRD of TiO_2 film diffractograms; **(c)** weighted average of phase composition; **(d)** calculated Scherrer crystallite size.

Calculation of the volume percentage of each crystal structure (**See Equation 4-2**) was performed by integrating the characteristic peak intensities of each corresponding phase (i.e. the rutile (110) and anatase (101) peaks).[52] This provides an approximate weighted average of the volume percentage of each crystal structure. Powdered titania rapidly converts to the rutile structure at temperatures near the characteristic Hüttig temperature of titania ($TiO_2^{Hüttig}$ ~ 610˚C). At this temperature surface atoms in bulk single crystals have enough energy to become mobile and rearrange. The aggregated nature of small crystallites within the powdered titania samples promotes surface area and presents a large number of exposed surface atoms. This facilitates increased atomic mobility and allows the anatase crystallites to

feed rutile grains. This results in rapid low temperature phase transformation (See **Figure 4-6c**). Additionally, the small nature of the crystallites within the powder likely promotes Hüttig based atomic transport at temperatures slightly lower than the standard Hüttig temperature of bulk single crystals, as atoms within a small crystallite are bound with less cohesive energy than those bound within larger crystals.[29]

$$Volume\ \%_{Anatase} = 100 * \frac{0.79 I_A}{I_R + 0.79 I_A} \qquad \textbf{Equation 4-2}$$

$$I_i = \text{Integral intensity of Phase } i$$

The TiO_2 films stabilize the anatase crystal structure at much higher temperatures than powdered titania as each individual TiO_2 crystallite within a film is coherently adhered to both the SiO_2 substrate and neighboring crystallites. This leaves fewer exposed surface atoms and greatly reduces the rearrangement of atoms at low temperatures. Evaluation of the characteristic peak intensities shows that the stability of anatase crystals within a film finally breaks down when approaching the characteristic Tammann temperature of bulk titania ($TiO_2^{Tammann}$ ~ 920˚C). At this temperature atoms within a bulk crystal have enough energy to become mobile and facilitate bulk-to-surface transport; this atomic mobility rapidly propagates development of the rutile phase of titania within the films. Thus, the interface provided between the substrate and the TiO_2 layer effectively acts to delay the onset of phase transformation by limiting mechanisms of surface reconstruction.

Scherrer analysis of crystallite size shows that anatase crystallites trend systematically smaller than the rutile crystallites in both the powdered and thin film samples; as predicted thermodynamically by Garvie.[31-34] Additionally, the rutile crystallite size within powdered TiO_2 samples trends systematically larger than that observed in the films. This qualitative data suggests that rutile particle growth is faster in powdered based titania samples as the matrix

of agglomerated crystallites allows more rapid growth of the rutile phase. This supports the concept that the rutile phase is promoted in powdered samples via surface driven mechanistic growth at temperatures near the Hüttig temperature; whereas the films experience surface driven growth only of the anatase phase at temperatures below 800˚C followed by Tammann based growth at higher temperatures.

Iterative Deposition of Titania

TiO_2 films were prepared via iterative convective depositions of the titania precursor solution followed by intermittent calcination between deposition steps. These experiments were conducted in order to assess the mechanism of phase evolution when increasing thickness of the TiO_2 layer. A deposition rate of 1.2 centimeters per minute was utilized to deposit 20 μL aliquots of solution on each substrate, while intermittent three hour calcinations at 800˚C were performed (See **Figure 4-7**). These multicoated samples were subsequently characterized with XRD, broken into quarters, and each piece was further calcined at temperatures ranging from 800-1000˚C. Sequential deposition and calcination allowed the formation of uniform films with limited defects and striations (See **Figure 4-7a**). SEM characterization of the films prepared via iterative deposition shows multiple layers of stacked crystallites. This can be observed along cracks located at the outer edge of the film.

XRD was utilized to assess phase composition between iterative depositions and subsequent calcinations of the thick TiO_2 films (See **Figure 4-7c**). Thick films stabilized the anatase phase after successive calcinations at 800˚C as is noted by the presence of the anatase (101) peak and absence of the rutile (110) peak. After ten depositions and cyclical calcinations the film was then heated to higher temperatures ranging from 800-1000˚C (See **Figure 4-7d**). At these temperatures the film began to more rapidly convert to the rutile phase. Thus,

anatase phase stabilization was once again observed in TiO_2 films prepared via multiple depositions and calcinations at 800˚C. This was followed by destabilization of the anatase structure when approaching the characteristic Tammann temperature of titania.

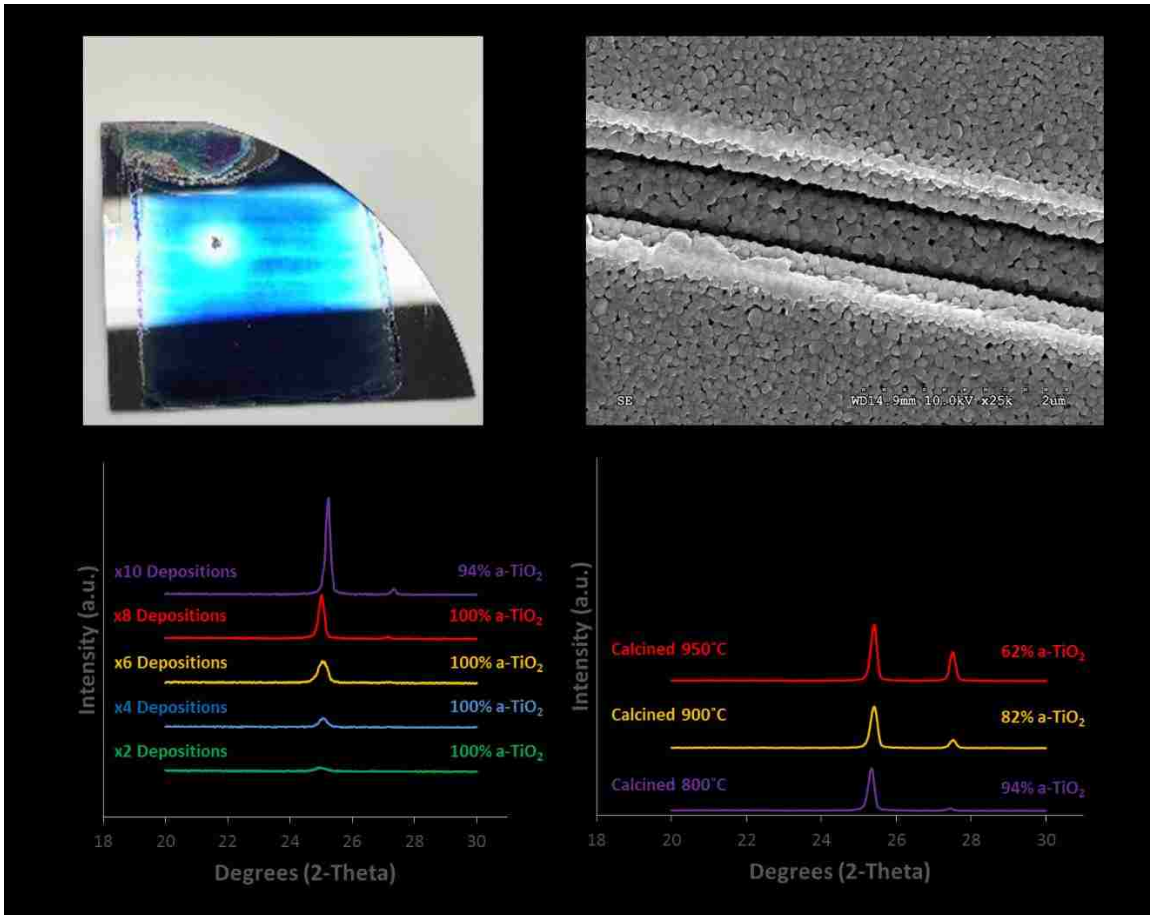

Figure 4-7. XRD and SEM characterization of a TiO_2 film after multiple iterative depositions with 20 µL of precursor solution and intermittent three hour calcinations at 800-1000˚C. **(a)** XRD of the film after intermittent deposition and 800˚C calcination; **(b)** XRD of the thin film after ten depositions and subsequent high temperature calcination 800-1000˚C; **(c)** image of a film after 5 successive depositions; **(d)** SEM image depicting the resulting layers of crystallites.

Temperature Effect on Rutile Grain Growth

SEM characterization of the iteratively deposited films after high temperature calcination (800-1000˚C) shows the rapid growth of crystalline platelets (See **Figure 4-8**). Formation of these platelets corresponds to development of the rutile phase as characterized

by XRD (See **Figure 4-7d**). After calcination at 800-900˚C the films are comprised of small anatase crystallites with limited platelet formation. Crystallite size increases only slightly when increasing the calcination temperature from 800 to 900˚C. Calcination above the characteristic Tammann temperature of titania rapidly forms large plates along the surface of the film. By 1000˚C the entire film has converted from small crystallites into large rutile plates. These findings suggest that the primary mechanism of phase transformation at low temperatures is surface mobilization whereas a new mechanism of transformation rapidly develops between 800-1000˚C.

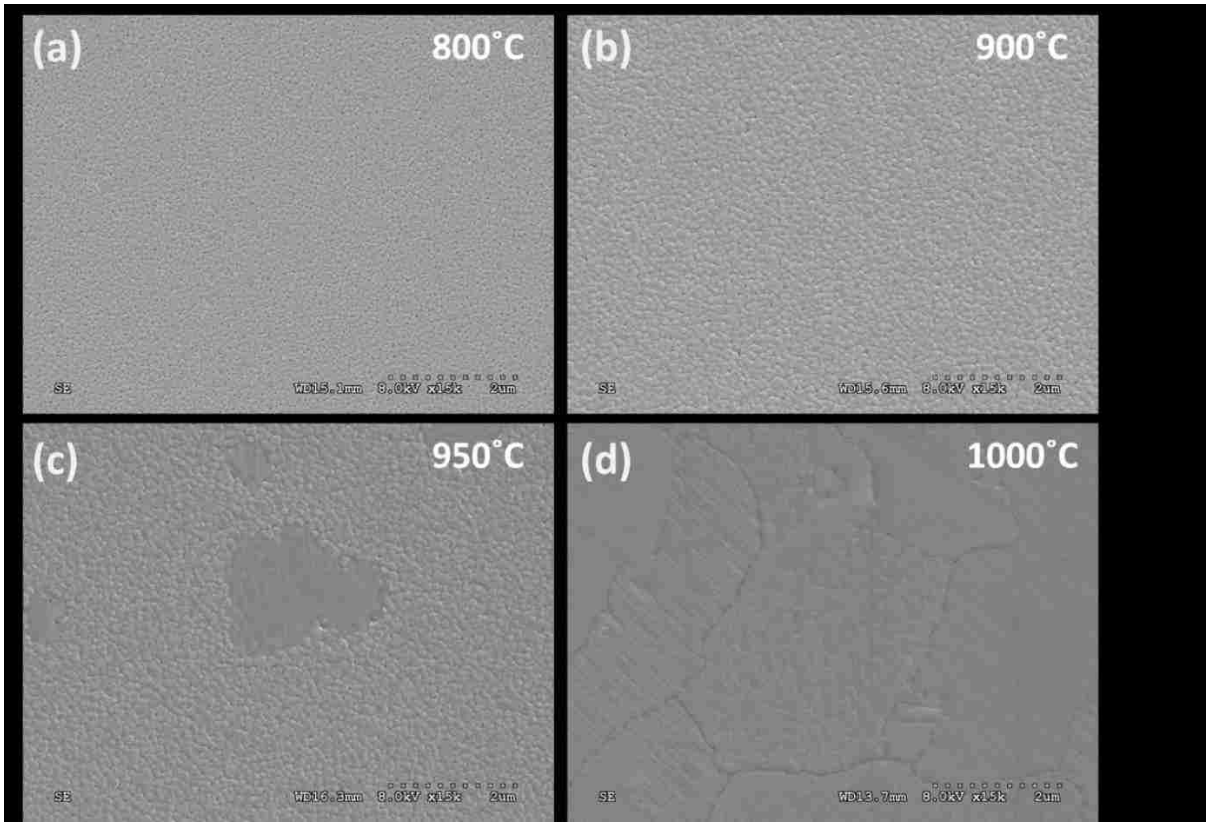

Figure 4-8. SEM images of TiO_2 films prepared via ten iterative deposition steps, cyclical calcination at 800˚C, followed by additional high temperature calcination at a temperature ranging from 800-1000˚C.

FIB Preparation

Focused ion beam lithography was utilized to cut thin slices or "coupons" from selected films in order to assess TiO_2 thickness, perform depth profiling based characterization, and to mechanistically study the transformation from anatase to rutile titania (See **Figure 4-9**). The lithography process included the traditional steps for coupon removal including ion milling, *in situ* lift out, thinning of the wafer via further milling, and attachment to a copper sample grid (See **Figure 4-10**). This process resulted in the formation of thin coupons less than 100 nm thick, 7 microns tall, and 25 microns wide. Focused ion beam lithography was performed on two samples: 1) a thin TiO_2 film prepared via deposition of 20 µL of precursor solution at a coating rate of 1.2 centimeters per minute and subsequently calcined for three hours at 800˚C; 2) a thick film prepared via ten iterative 20 µL depositions at coating rates of 1.2 centimeters per minute followed by calcination for three hours at 950˚C.

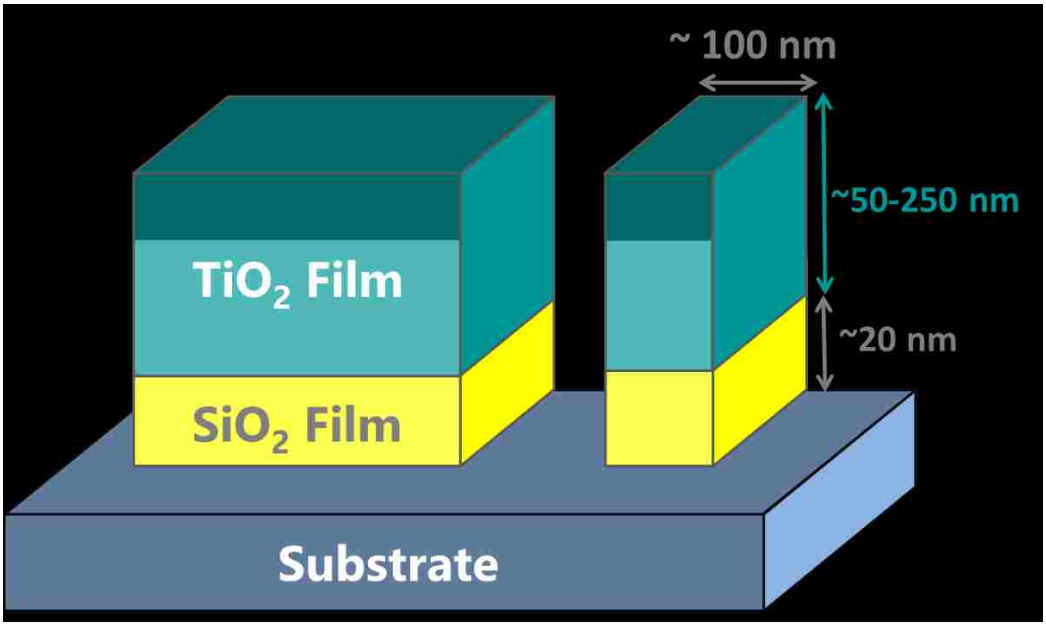

Figure 4.9. FIB lithography schematic for preparation of TiO_2 coupons.

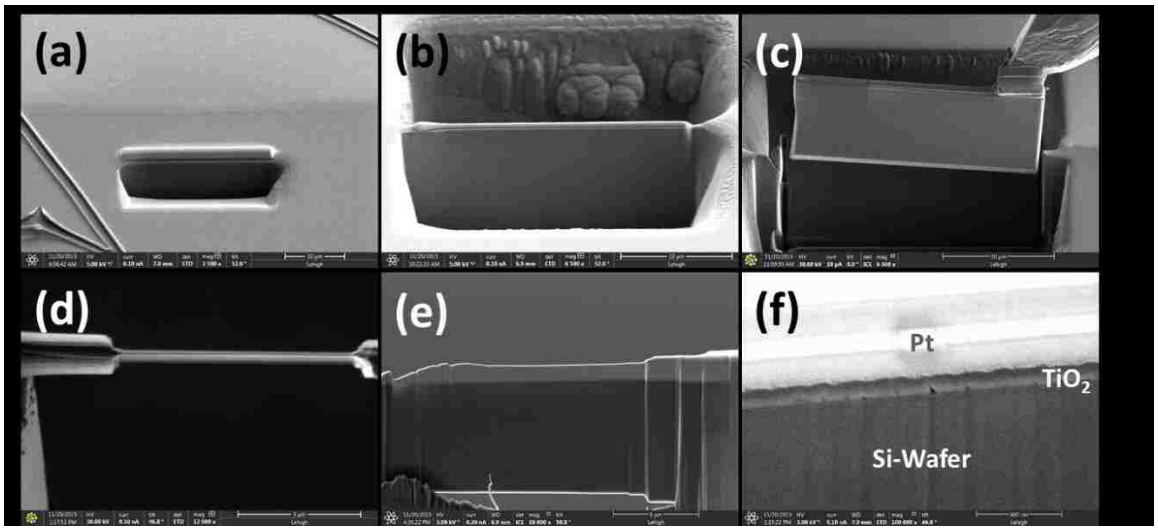

Figure 4-10. FIB lithography images during sample preparation. The sample consisted of a thin TiO_2 film prepared via deposition of a 20 µL aliquot of precursor solution at 1.2 cm/min and calcined for three hours at 800˚C. **(a)** preparation of coupon via ion milling; **(b)** the resulting coupon after milling; **(c)** *in situ* lift-out of the coupon; **(d) i**on milling process to thin the wafer; **(e)** the resulting coupon after lift out and milling; **(f)** a magnified image of the resulting coupon.

Thin Film ARM Imaging and EDS Mapping

Atomic resolution imaging was used to analyze the phase and elemental content of various grains in a thin titania film prepared via convective deposition of 20 µL of solution at a coating rate of 1.2 centimeters per minute and subsequently calcined at 800˚C for three hours (See **Figure 4-11a**). High resolution imaging depicts a layer of platinum nanoparticles positioned atop the titania film and underlying substrate. Each titania crystallite is coherently attached to both the substrate and neighboring titania crystallites resulting in a film with minimal pore structure. EDS line scans show the platinum layer is several hundred nanometers thick followed by a 40 nm thick titania layer and a 25 nm thick SiO_2 layer (See **Figure 4-11b**). Thickness of the silica layer corresponds well to previous measurements conducted via ellipsometry on uncoated silicon films (See **Figure 4-2**).

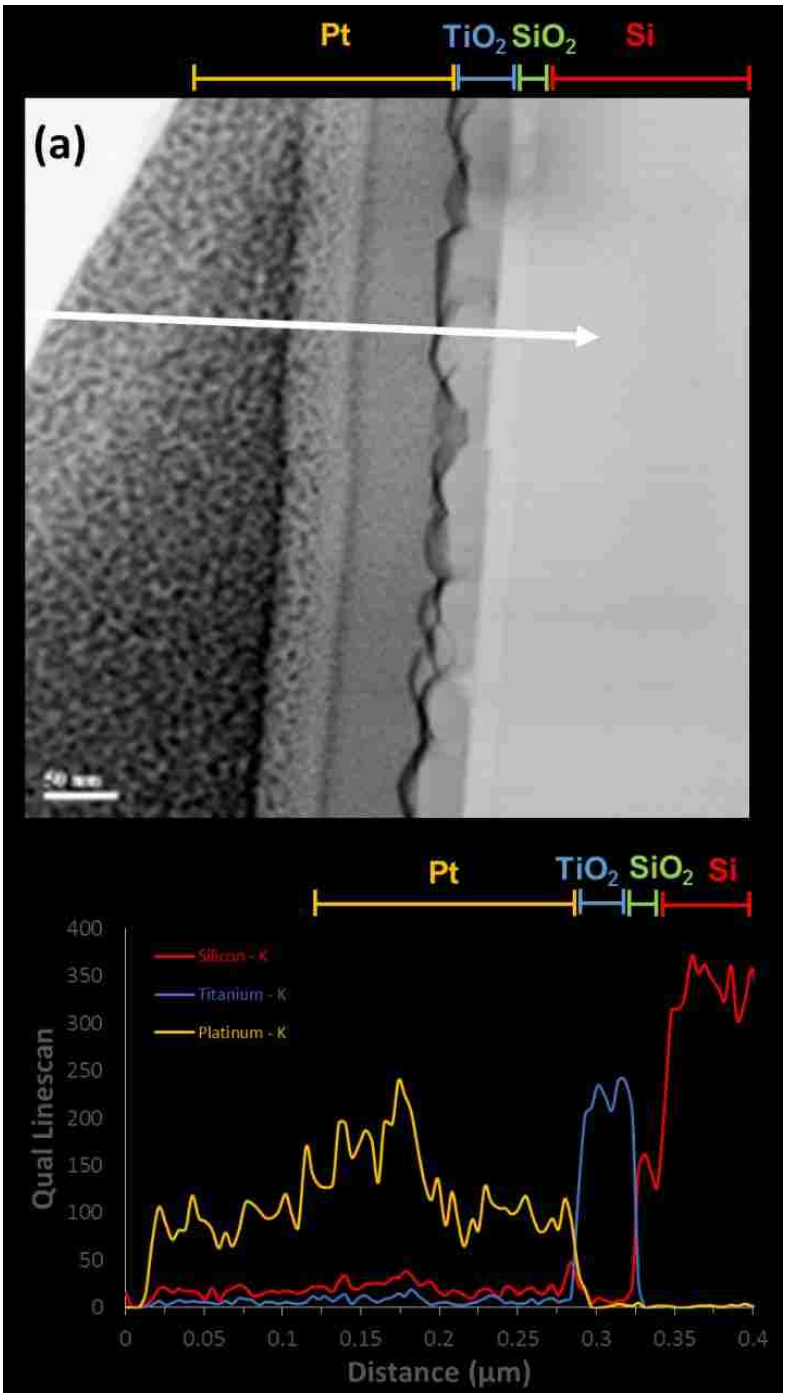

Figure 4-11. ARM characterization and EDS line scan of the thin titania film after FIB lithography: **(a)** representative profile image of the coupon; **(b)** an EDS line can of the corresponding ARM image. The film was prepared via convective deposition of 20 µL of solution at a coating rate of 1.2 centimeters per minute and subsequently calcined at 800˚C for three hours.

Energy dispersive x-ray spectroscopic mapping was used to assess elemental composition within the thin, single layer, TiO_2 film calcined at 800˚C (See **Figure 4-12**). EDS mapping detected a concentrated oxygen K-alpha signal along the TiO_2 and SiO_2 layers. Additionally, the oxygen signal overlaps areas of concentrated titanium and silicon K-alpha signals and matches the corresponding ARM image. This verifies that EDS mapping provides an accurate reflection of elemental composition in each layer. However, EDS mapping does show low concentrations of each element along the surface of the film; this K-alpha noise is likely an artifact of the FIB lithography process. During focused ion beam etching residual etched material can be redeposited along the surface of the film. This residual material appears to collect more readily along rough areas, such as in between the nanoporous platinum region of the film.

Detection of silicon K-alpha signal was largely absent within the TiO_2 portion of the film. Similarly minimal titanium K-alpha signal is detected within the SiO_2 layer. These findings suggest that homogenous elemental doping is absent within the TiO_2 crystallites and SiO_2 layer. It is probable however, that doping exists to some extent along the immediate interface of the TiO_2 and SiO_2 boundary. As mentioned previously, doping of silicon species within TiO_2 has been reported to inhibit the anatase to rutile transformation.[26] Thus, the combination of localized doping near the interface and coherency of titania crystallites with the substrate likely assists in anatase stabilization as shown with XRD characterization (See **Figure 4-6b**).

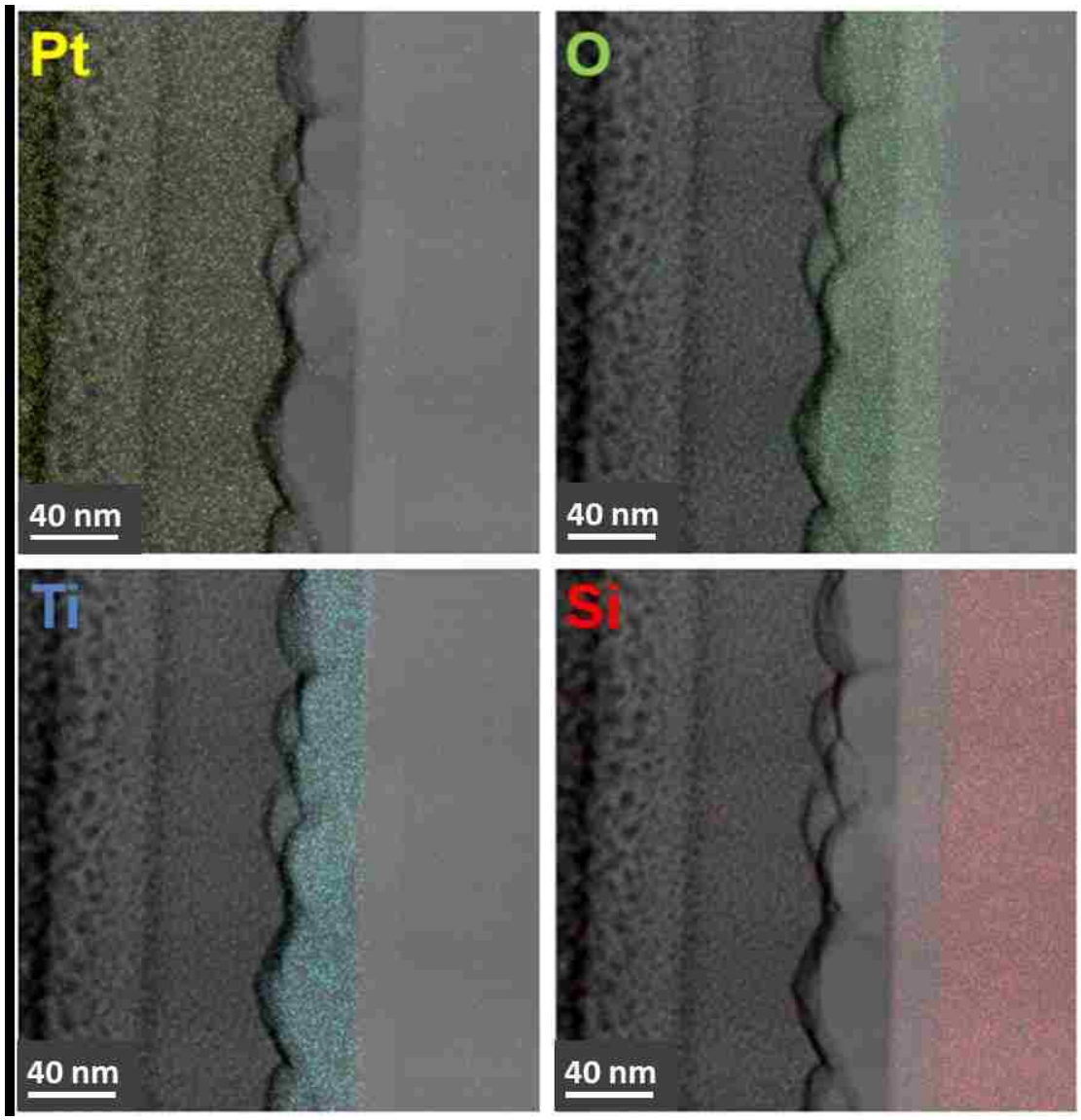

Figure 4-12. EDS maps of a titania film overlaid on the corresponding ARM image. The film was prepared via convective deposition of 20 µL of solution at a coating rate of 1.2 centimeters per minute and subsequently calcined at 800˚C for three hours.

Thick Film ARM Imaging and EDS Mapping

TEM and ARM imaging was conducted on the thick TiO_2 film prepared via multiple depositions of precursor solution and iterative calcination at 800˚C. A final calcination at 950˚C was performed to induce rutile development and access mechanistic transformation of the film (See **Figure 4-13**). A series of small coherent crystallites and large TiO_2 platelets lined the

surface of the substrate (See **Figure 4-14**). This variability in crystallite size was observed previously during SEM imaging of the films (See **Figure 4-8**). The TiO_2 layer was approximately 160+/-25nm thick and was successfully grown via the multi-deposition process. The SiO_2 layer was approximately 83+/-3nm thick nearly three times that observed in the thin TiO_2 film prepared with one deposition and calcination. Growth of the SiO_2 layer follows the general trend measured by ellipsometry on pure silicon films after cyclical calcination.

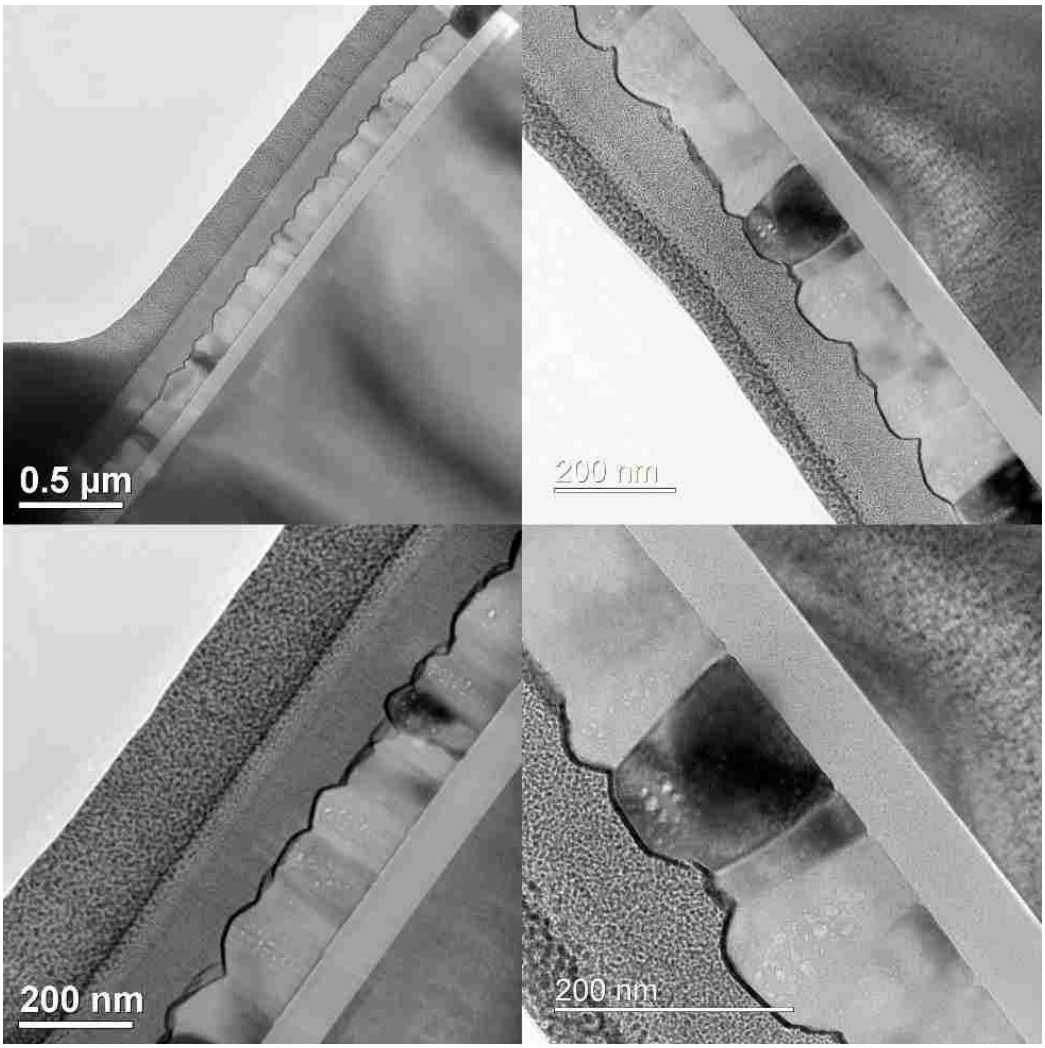

Figure 4-13. TEM images of small crystallites within the thick TiO_2 film. The sample was prepared via multiple convective depositions of 20 µL of solution at a coating rate of 1.2 centimeters per minute and intermittent calcination at 800˚C for three hours. A final calcination step was conducted at 950˚C.

Crystallites in the thick film are distinguishable from neighboring grains as they are each adhered to the substrate at a different orientation. This provides variety in grain coloration with darker grains diffracting more electrons than lighter grains. Crystallites appear to have developed in a perpendicular fashion relative to the substrate as the film is comprised of crystals which span from the TiO_2/SiO_2 interface to the surface of the film; and are no longer comprised of stacked crystallites as was observed after calcination at 800˚C (See **Figure 4-7b**). Thus, calcination at 950˚C facilitated sintering and coalescence of stacked crystallites. Pocked features are observed to run vertically down the center of the grains. These small air pockets were likely confined within the crystal during sintering and annealing of stacked crystallites within the film.

Large platelets rapidly appear after calcination above 800˚C as previously observed with SEM characterization (See **Figure 4-8**). These large plates extend several microns across the substrate and span from the surface of the film to the oxide interface (See **Figure 4-14**). Additionally, platelet growth corresponds to rutile development as characterized by XRD (See **Figure 4-7d**). The large grains appear to protrude into neighboring crystallites, suggesting grain growth is more rapid in the interior of the crystal as opposed to either the surface or the TiO_2/SiO_2 interface; a phenomenon likely accelerated when approaching the characteristic Tammann temperature of titania.

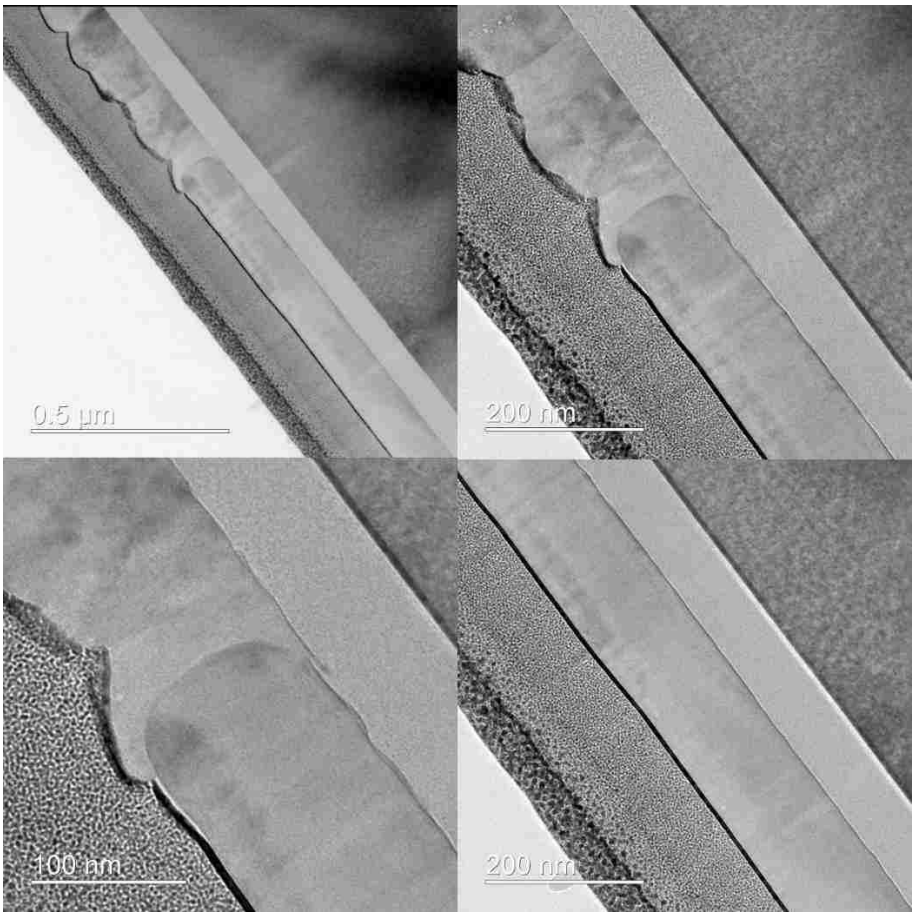

Figure 4-14. TEM images of a large crystallite within the thick TiO_2 film. The sample was prepared via multiple convective depositions of 20 µL of solution at a coating rate of 1.2 centimeters per minute and intermittent three hour calcinations at 800˚C. A final calcination step was conducted at 950˚C to induce phase change.

EDS mapping was performed on the thick TiO_2 film to assess elemental composition in each layer (See **Figure 4-15**). The oxygen K-alpha signal overlapped both the TiO_2 and SiO_2 regions of the sample, while the titanium and silicon K-alpha peaks were largely confined within the corresponding oxide layers. Homogeneous silicon doping does not appear to comprise a significant portion of the TiO_2 layer. However, the silicon K-alpha signal can be detected along the entire surface of the film. It is believed that a large portion of this signal is an artifact of the lithography process and primarily due to the presence of redeposited silicon. High temperature calcination of the thick film at 950˚C did not significantly promote silicon

doping versus that observed in the thinner film calcined at 800˚C. A common method used for the doping of photovoltaics (PV's) is the blanket doping technique. This method is performed by putting a dopant paste in contact with the PV via screen printing and rapidly heating and cooling at extreme rates in order to kinetically trap dopants within a material.[53] The slow heating rate (5˚C/min) and three hour dwell time utilized during the calcination process facilitated thermodynamic relaxation of both the TiO_2 and SiO_2 layers. This likely limited the extent of doping to the immediate vicinity of the TiO_2/SiO_2 interface.

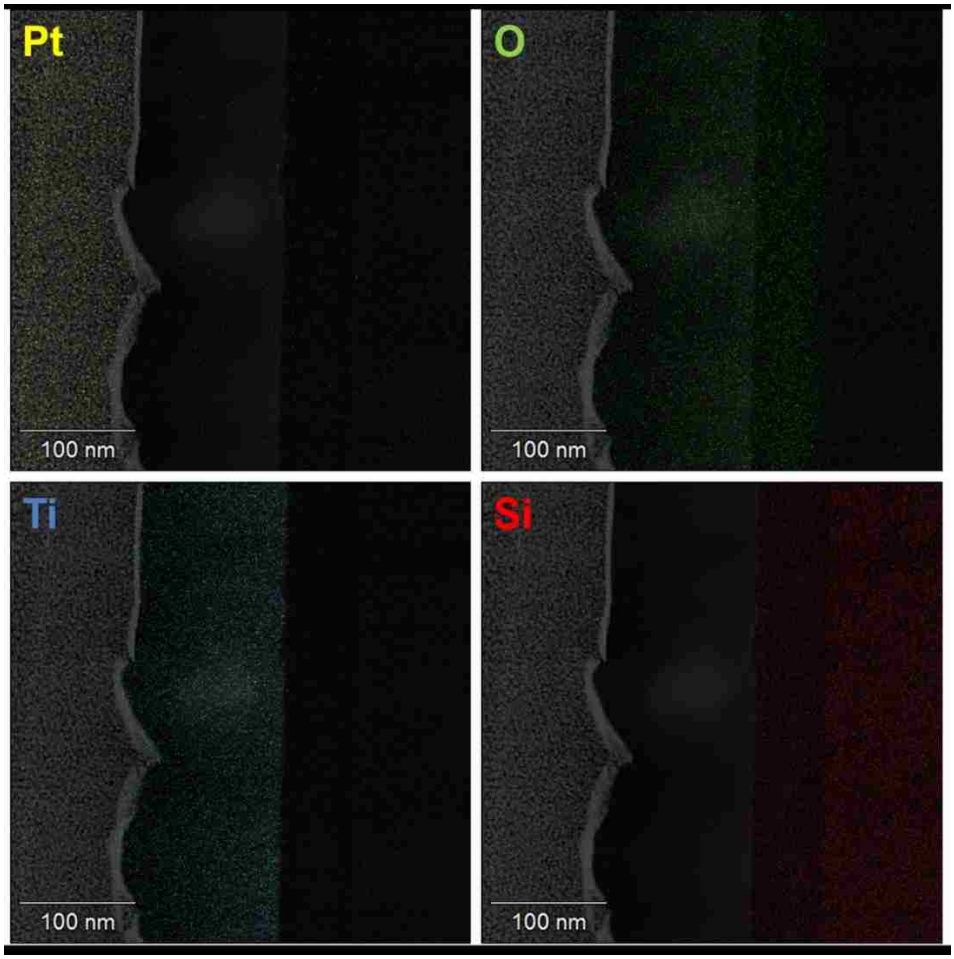

Figure 4-15. EDS maps of the thick TiO_2 film overlaid on the corresponding ARM image. The film was prepared via multiple convective depositions of 20 µL of solution at a coating rate of 1.2 centimeters per minute and intermittent three hour calcinations at 800˚C. A final calcination step at 950˚C was conducted to induce phase change.

Phase Reconstruction Discussion

Phase transformation is a reconstructive process requiring anatase titania crystals to break their current bond structure and reconfigure into the more stable rutile phase. This requires atoms within a crystal to gain enough energy to break their current bonds, become mobile, and reform new bonds. This process can occur either by surface driven atomic transport in which metastable crystallites feed growing rutile grains or by internal atomic reconfiguration. Powdered titania samples were observed to change phase at temperatures consistent with the characteristic Hüttig temperature while titania films undergo phase transformation at temperatures more consistent with the Tammann temperature. It is proposed that titania films provide a more coherent structure of crystallites and stabilizes the metastable phase at elevated temperatures. This particle-to-particle coherency provides more atomic cohesion and limits the degree of atomic surface mobility by reducing the number of surface atoms (See **Figure 4-16**). Finally, localized doping along the TiO_2/SiO_2 interface likely assists in stabilization of the anatase structure along the interface.

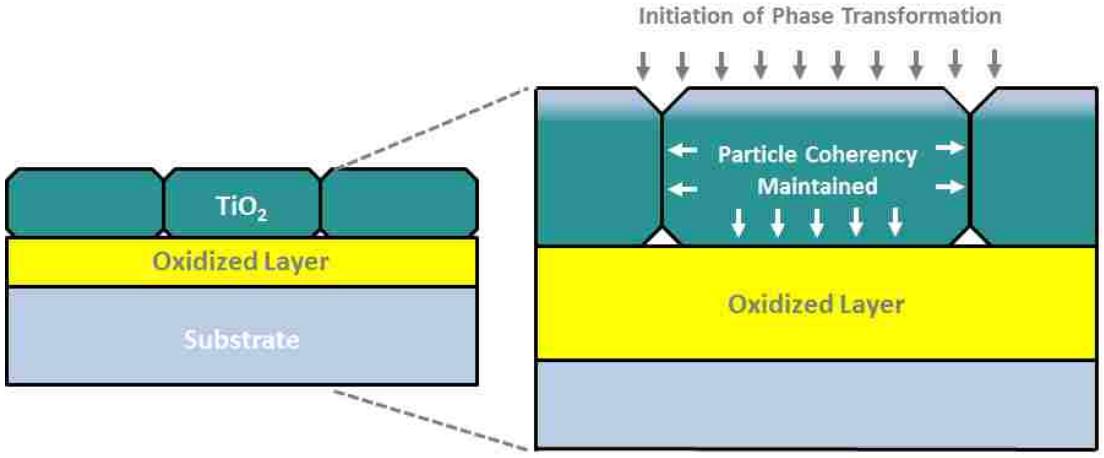

Figure 4-16. Schematic depicting particle to particle coherency as a mechanism of phase stabilization.

4.5 Conclusions

This work demonstrates a phenomenon which preserves the traditionally metastable anatase crystal structure of titania at elevated temperatures (T > 500˚C) along a TiO_2/SiO_2 interface. A SiO_2 layer was grown on the surface of a Si(100) wafer and subsequently coated with a TiO_2 film via convective deposition. Fast deposition rates (1.2 cm/min) provided uniform film consistency while slow coating rates (0.12 cm/min) were susceptible to crack and defect formation. XRD experiments demonstrate that TiO_2 films with large numbers of cracks and defects were more conducive to development of the rutile phase. SEM characterization revealed that the crystallites along these defects were larger in size, not coherently adhered to the substrate, and more susceptible to sintering. XRD further verified that TiO_2 films facilitated stabilization of the anatase phase of titania, while corresponding bulk-titania control powders rapidly converted to the more stable rutile phase. Phase transformation of the powdered samples occurs at temperatures consistent with the characteristic Hüttig temperature of titania ($TiO_2^{Hüttig}$ ~ 610˚C), while phase transformation of the films occurred at temperatures closer to the Tammann temperature of bulk titania ($TiO_2^{Tammann}$ ~ 920˚C)**.** It is proposed that the powdered TiO_2 samples facilitate more surface driven methods of atomic mobility and allow low temperature phase transformation as the powdered samples afford larger surface areas than the films. Rutile grain growth in the films accelerates when exceeding the Tammann temperature of the oxide as bulk-to-surface mobilization allows rapid lateral growth of rutile grains along the surface of the film. This is complemented by SEM and ARM characterization which demonstrates that anatase-to-rutile transformation corresponds to the development of large surface platelets after high temperature calcination 800-1000˚C. EDS mapping shows the TiO_2 layer of the film is not significantly doped with a large amount of

residual silicon. However, localized doping likely promotes anatase stabilization in the immediate vicinity of the TiO_2/SiO_2 interface. This interface allows the titania film to more fully coordinate along the substrate, while neighboring TiO_2 crystallites are coherently confined in a two-dimensional arrangement within the film. This reduced dimensionality acts to inhibit rutile grain propagation by limiting the number of neighboring crystallites versus that observed in bulk control powders; which, traditionally consist of three-dimensionally aggregated crystallites. The combination of these effects reduces the amount of exposed TiO_2 surface area and thus mitigates the rate of phase transformation due to atomic surface mobility. This method of film stabilization is thought to be a general phenomenon similar to that observed in supported oxide systems (See Chapter 3).

4.6 References

[1]O'Neill, Brandon J., David H. K. Jackson, Jechan Lee, Christian Canlas, Peter C. Stair, Christopher L. Marshall, Jeffrey W. Elam, Thomas F. Kuech, James A. Dumesic, and George W. Huber. "Catalyst Design with Atomic Layer Deposition." *ACS Catal. ACS Catalysis* 5.3 (2015): 1804-825.

[2]Jiang, Changyun, Man Yin Leung, Wei Ling Koh, and Yuning Li. "Influences of Deposition and Post-annealing Temperatures on Properties of TiO_2 Blocking Layer Prepared by Spray Pyrolysis for Solid-state Dye-sensitized Solar Cells." *Thin Solid Films* 519.22 (2011): 7850-854.

[3]Verbruggen, Sammy W., Shaoren Deng, Mert Kurttepeli, Daire J. Cott, Philippe M. Vereecken, Sara Bals, Johan A. Martens, Christophe Detavernier, and Silvia Lenaerts. "Photocatalytic Acetaldehyde Oxidation in Air Using Spacious TiO_2 Films Prepared by Atomic Layer Deposition on Supported Carbonaceous Sacrificial Templates." *Applied Catalysis B: Environmental* 160-161 (2014): 204-10.

[4]Vorotilov, K.a., E.v. Orlova, and V.i. Petrovsky. "Sol-gel TiO_2 Films on Silicon Substrates." *Thin Solid Films* 207.1-2 (1992): 180-84.

[5] Yan, Yongan, S. Ray Chaudhuri, and Arnab Sarkar. "Synthesis, Characterizations, and Optical Properties of Stacked Porous Thin Films Derived from Sol-Gel Process." *Journal of the American Ceramic Society J American Ceramic Society* 79.4 (1996): 1061-065.

[6] Yan, Yongan, S. Ray Chaudhuri, Din-Guo Chen, Barry Bolker, and Arnab Sarkar. "Microstructural Evolution of Titania Sol-Gel Thin Films." *MRS Proc. MRS Proceedings* 346 (1994): 973-978.

[7] Liu, Wei, Baoquan Zhang, Xiufeng Liu, and Liming Xu. "Thermal Stability of Silica-Zirconia Membranes." *Chinese Journal of Chemical Engineering* 14.1 (2006): 31-36.

[8] Phadke, Sarika, Judith D. Sorge, Sherwood Hachtmann, and Dunbar P. Birnie. "Broad Band Optical Characterization of Sol–gel TiO_2 Thin Film Microstructure Evolution with Temperature." *Thin Solid Films* 518.19 (2010): 5467-470.

[9] Gao, Liguo, Yawei Wang, Yang Yan, Qun Li, Ce Hao, and Tingli Ma. "Enhanced Photoactivities of TiO_2 Particles Induced by Bio-inspired Micro-nanoscale Substrate." *Journal of Colloid and Interface Science* 470 (2016): 10-13.

[10] Zainal, Zulkarnain, and Chong Yong Lee. "Properties and Photoelectrocatalytic Behaviour of Sol-Gel Derived TiO_2 Thin Films." *Journal of Sol-Gel Science and Technology* 37.1 (2006): 19-25.

[11] Shi, L.; Tin, K.; Wong, N. "Thermal stability of zirconia membranes." *Journal of Materials Science* 34 (1999): 3367-3374.

[12] Wachs, Israel E. "Recent Conceptual Advances in the Catalysis Science of Mixed Metal Oxide Catalytic Materials." *Catalysis Today* 100.1-2 (2005): 79-94.

[13]Takahashi, Yasutaka, Katsuhiro Niwa, Keisuke Kobayashi, and Michiyasu Matsuki. "Dip Coating of Zirconia and Mixed Zirconia Films." *Journal of the Ceramic Association, Japan* 95.1106 (1987): 942-48.

[14]Takahashi, Yasutaka, and Yoshihiro Matsuoka. "Dip-coating of TiO_2 Films Using a Sol Derived from Ti(O-i-Pr)4-diethanolamine-H_2O-*i*-PrOH System." *Journal of Materials Science* 23.6 (1988): 2259-266.

[15] Li, Xiao-Hang, Peifen Zhu, Guangyu Liu, Jing Zhang, Renbo Song, Yik-Khoon Ee, Pisist Kumnorkaew, James F. Gilchrist, and Nelson Tansu. "Light Extraction Efficiency Enhancement of III-Nitride Light-Emitting Diodes by Using 2-D Close-Packed TiO_2 Microsphere Arrays." *Journal of Display Technology* 9.5 (2013): 324-332.

[16] Kosacki, I.; Petrovsky, V.; Anderson, H. U. "Raman spectroscopy of nanocrystalline ceria and zirconia thin films." *Journal of the American Ceramic Society* 85 (2002): 2646-2650.

[17] Correa, Gabriela C., Bo Bao, and Nicholas C. Strandwitz. "Chemical Stability of Titania and Alumina Thin Films Formed by Atomic Layer Deposition." *ACS Appl. Mater. Interfaces ACS Applied Materials & Interfaces* 7.27 (2015): 14816-4821.

[18] Brinker, C.j., A.j. Hurd, P.r. Schunk, G.c. Frye, and C.s. Ashley. "Review of Sol-gel Thin Film Formation." *Journal of Non-Crystalline Solids* 147-148 (1992): 424-436.

[19] Brinker, C.j., D.m. Smith, R. Deshpande, P.m. Davis, S. Hietala, G.c. Frye, C.s. Ashley, and R.a. Assink. "Sol-gel Processing of Controlled Pore Oxides." *Catalysis Today* 14.2 (1992): 155-63.

[20] Davis, Pamela J., C. Jeffrey Brinker, and Douglas M. Smith. "Pore Structure Evolution in Silica Gel during Aging/drying I. Temporal and Thermal Aging." *Journal of Non-Crystalline Solids* 142 (1992): 189-96

[21]Davis, Pamela J., C. Jeffrey Brinker, Douglas M. Smith, and Roger A. Assink. "Pore Structure Evolution in Silica Gel during Aging/drying II. Effect of Pore Fluids." *Journal of Non-Crystalline Solids* 142 (1992): 197-207.

[22]Deshpande, Ravindra, Duen-Wu Hua, Douglas M. Smith, and C. Jeffrey Brinker. "Pore Structure Evolution in Silica Gel during Aging/drying. III. Effects of Surface Tension." *Journal of Non-Crystalline Solids* 144 (1992): 32-44.

[23] Davis, Pamela J., Ravindra Deshpande, Douglas M. Smith, C.jeffrey Brinker, and Roger A. Assink. "Pore Structure Evolution in Silica Gel during Aging/drying. IV. Varying Pore Fluid PH." *Journal of Non-Crystalline Solids* 167.3 (1994): 295-306.

[24] Yi, Guanghua, and Michael Sayer. "Sol-Gel Processing of Complex Oxide Films." *American Ceramic Society Bulletin* 70.7 (1991**)**: 1173-1177.

[25] Ertl, G., H. Knözinger, and J. Weitkamp. "Spreading and Wetting." *Preparation of Solid Catalysts*. Weinheim: Wiley-VCH, 1999. 501-26.

[26] Hanaor, Dorian A. H., and Charles C. Sorrell. “Review of the Anatase to Rutile Phase Transformation.” *Journal of Materials Science* 46 (2010): 855-874.

[27] Wachs, I. E., and C. J. Keturakis. "Monolayer Systems" *Comprehensive Inorganic Chemistry II: From Elements to Applications*. Ed. Jan Reedijk and Kenneth Poeppelmeier. Burlington: Elsevier, 2013. Chapter 7.06, 131-151.

[28] Wang, Chuan-Bao, Yeping Cai, and Israel E. Wachs. "Reaction-Induced Spreading of Metal Oxides onto Surfaces of Oxide Supports during Alcohol Oxidation: Phenomenon, Nature, and Mechanisms." *Langmuir* 15.4 (1999): 1223-1235.

[29]Takagi, Mieko. "Electron-Diffraction Study of Liquid-Solid Transition of Thin Metal Films." *Journal of the Physical Society of Japan J. Phys. Soc. Jpn.* 9.3 (1954): 359-63.

[30] Stevens, R. *Zirconia and Zirconia Ceramics*. Manchester, U.K.: Magnesium Elektron, 1986.

[31]Garvie, Ronald C. "The Occurrence of Metastable Tetragonal Zirconia as a Crystallite Size Effect." *The Journal of Physical Chemistry J. Phys. Chem.* 69.4 (1965): 1238-243.

[32]Garvie, R. C. "Stabilization of the Tetragonal Structure in Zirconia Microcrystals." *The Journal of Physical Chemistry J. Phys. Chem.* 82.2 (1978): 218-24.

[33] Garvie, R. C., and M. F. Goss. "Intrinsic Size Dependence of the Phase Transformation Temperature in Zirconia Microcrystals." *J Mater Sci Journal of Materials Science* 21.4 (1986): 1253-257.

[34] Garvie, R. C., R. H. Hannink, and R. T. Pascoe. "Ceramic Steel?" *Nature* 258.5537 (1975): 703-04.

[35] Kingery, W. D. "Boundary Stresses." *Introduction to Ceramics*. New York: John Wiley & Sons, 1960. 201-203.

[36] Harmer, M. P. "The Phase Behavior of Interfaces." *Science* 332.6026 (2011): 182-83.

[37] Li, Meijun, Zhaochi Feng, Pinliang Ying, Qin Xin, and Can Li. "Phase Transformation in the Surface Region of Zirconia and Doped Zirconia Detected by UV Raman Spectroscopy." *Phys. Chem. Chem. Phys. Physical Chemistry Chemical Physics*5.23 (2003): 5326-5332.

[38] Li, Can, and Meijun Li. "UV Raman Spectroscopic Study on the Phase Transformation of ZrO_2, Y_2O_3-ZrO_2 and SO_2^{-4}/ZrO_2." *J. Raman Spectrosc. Journal of Raman Spectroscopy* 33.5 (2002): 301-08.

[39] Li, Meijun, Zhaochi Feng, Guang Xiong, Pinliang Ying, Qin Xin, and Can Li. "Phase Transformation in the Surface Region of Zirconia Detected by UV Raman Spectroscopy." *The Journal of Physical Chemistry B J. Phys. Chem. B* 105.34 (2001): 8107-111.

[40] Kaul, A., O. Gorbenko, I. Graboy, M. Novojilov, A. Bosak, A. Kamenev, S. Antonov, I. Nikulin, A. Mikhaylov, and M. Kartavtzeva. "Epitaxial Stabilization in Thin Films of Oxides." *MRS Proc. MRS Proceedings* 755 (2002): 4026-043.

[41] Selvaraj, Ulagaraj, Alamanda V. Prasadarao, Sridhar Komarneni, and Rustum Roy. "Sol-Gel Fabrication of Epitaxial and Oriented TiO_2 Thin Films." *Journal of the American Ceramic Society* 75.5 **(1992**): 1167-1170.

[42] Legrand-Buscema, C., C. Malibert, and S. Bach. "Elaboration and Characterization of Thin Films of TiO_2 Prepared by Sol–gel Process." *Thin Solid Films* 418.2 (2002): 79-84.

[43] Kumnorkaew, Pisist, Yik-Khoon Ee, Nelson Tansu, and James F. Gilchrist. "Investigation of the Deposition of Microsphere Monolayers for Fabrication of Microlens Arrays." *Langmuir* 24.21 (2008): 12150-2157.

[44]Deal, B. E., and A. S. Grove. "General Relationship for the Thermal Oxidation of Silicon." *J. Appl. Phys. Journal of Applied Physics* 36.12 (1965): 3770.

[45]Bradley, D. C., R. C. Mehrotra, and D. P. Gaur. *Metal Alkoxides*. London: Academic, 1978.

[46]Bradley, Donald C. "Metal Alkoxides as Precursors for Electronic and Ceramic Materials." *Chemical Reviews Chem. Rev.* 89.6 (1989): 1317-322.

[47]Turova, Nataliya Ya. *The Chemistry of Metal Alkoxides*. Boston: Kluwer Academic, 2002.

[48] Basolo, Fred, and Ronald C. Johnson. *Coordination Chemistry; the Chemistry of Metal Complexes*. New York: W.A. Benjamin, 1964.

[49] Boettcher, Jane M., Midhun Joy, Kedar Joshi, Tanyakorn Muangnapoh, and James F. Gilchrist. "Spacing of Seeded and Spontaneous Streaks during Convective Deposition." *Langmuir* 31.40 (2015): 10935-0938.

[50] Cullity, B. D. "Diffraction I: The Direction of Diffracted Beams." *Elements of X-ray Diffraction*. Reading, MA: Addison-Wesley Pub., 1956. 96-102.

[51] Langford, J. I., and A. J. C. Wilson. "Scherrer after Sixty Years: A Survey and Some New Results in the Determination of Crystallite Size." *Journal of Applied Crystallography J Appl Crystallogr* 11.2 (1978): 102-13.

[52] Spurr, R. A., and Howard Myers. "Quantitative Analysis of Anatase-Rutile Mixtures with an X-Ray Diffractometer." *Analytical Chemistry Anal. Chem.* 29.5 (1957): 760-62.

[53] Hamm, Robert Wray., and Marianne Elizabeth. Hamm. "6.2 Doping of Si-Based Photovoltaic Cells." *Industrial Accelerators and Their Applications*. Hackensack, NJ: World Scientific Pub., 2012. 42-47.

Chapter 5. The Influence of Synthesis on the Stabilization of MO_x/ZrO_2^{Cryst} versus MO_x/ZrO_2^{Hyd} Catalysts

5.1 Abstract

A series of supported catalysts were prepared by means of traditional incipient wetness impregnation (IWI) procedures on commercial crystalline ZrO_2 supports for comparison with corresponding catalysts prepared via an unconventional IWI procedure on zirconium hydroxide ($Zr(OH)_x$). Catalysts utilized in this study include: MoO_3/ZrO_2, WO_3/ZrO_2, CeO_2/ZrO_2, and SiO_2/ZrO_2; additionally, each catalyst contained a 5wt% loading of the surface oxide. The catalysts were calcined at temperatures ranging from 500-1000˚C to disperse the surface component, crystallize the hydroxide, and to assess structural reconfiguration at elevated temperatures.

In order to assess structural stabilization and surface chemistry, the catalysts were characterized with thermogravimetric analysis (TGA), N_2 adsorption, X-ray diffraction (XRD), low energy ion scattering (LEIS), *in situ* Raman, *in situ* IR spectroscopy, and *in situ* IR spectroscopy during NH_3-desorption. The hydroxide based catalysts (i.e. MO_x/ZrO_2^{Hyd}) demonstrated stabilization of the metastable tetragonal phase of zirconia (t-ZrO_2), a significant promotion in BET surface area, and unique surface species in comparison to the corresponding catalysts prepared by traditional synthetic methods (i.e. MO_x/ZrO_2^{Cryst}).

in situ IR spectroscopy demonstrated a vibrational shift of ~20 cm^{-1} in the characteristic mono-oxo $O=WO_4$ and $O=MoO_4$ vibrations when supported on crystalline ZrO_2 supports (i.e. $O=WO_4$~1007 cm^{-1} and $O=MoO_4$~999 cm^{-1}) versus hydroxide supports (i.e. $O=WO_4^{New}$ ~990 cm^{-1} and $O=MoO_4^{New}$ ~982 cm^{-1}). This vibrational shift was also observed in the overtone region of

the corresponding IR spectra. *in situ* Raman spectroscopy revealed a similar vibrational shift of ~20 cm^{-1} in the characteristic mono-oxo $O=WO_4$ and $O=MoO_4$ vibrations on crystalline supports (i.e. $O=WO_4$~1008 cm^{-1} and $O=MoO_4$~1000 cm^{-1}) versus that observed on hydroxide supports (i.e. $O=WO_4^{New}$ ~999 cm^{-1} and $O=MoO_4^{New}$ ~985 cm^{-1}). These findings suggest a new series of distorted mono-oxo surface species are present on the MO_x/ZrO_2^{Hyd} catalysts.

It is hypothesized that the new surface sites are partially embedded within the outermost surface layer of the zirconia support and assist in both the structural stabilization of BET surface area and preservation of the underlying tetragonal crystal structure. Thus, this alternative synthetic approach to catalyst design facilitates the formation of enhanced supported catalysts which present unique distorted surface species; while simultaneously utilizing structural aspects of surface stabilization to promote surface area and preserve metastable crystal structures. The insight provided by this work should assist in the design and understanding of a series robust catalysts with increased catalytic performance in the area of acid catalysis.

5.2 Introduction

One of today's grand catalytic challenges is "the design and controlled synthesis of catalytic structures", as defined by the United States of America's Department of Energy (DOE).[1] Motivated by the constant pursuit for increasingly catalytically active materials, this chapter seeks to utilize the concepts of surface modification (as revealed in previous chapters) to produce stabilized materials with enhanced catalytically active surface chemistry. The mechanism of surface modification has been demonstrated to promote surface area and stabilize metastable oxide phases in previous chapters. We now extend the concept of surface

modification to examine the surface chemistry of modified supported catalysts for application as acid catalysis.

In this chapter, we examine the synthesis of zirconia supported catalysts (MO_x/ZrO_2) prepared from two different procedures; these procedures include: (1) the traditional incipient wetness impregnation (IWI) procedure performed on commercial crystalline ZrO_2 supports and (2) a non-conventional synthesis involving the IWI of amorphous commercial zirconium hydroxides ($Zr(OH)_X$). These synthetic procedures result in the formation of two distinct types of catalysts with unique surface chemistries. For notation purposes, we will denote the supported catalysts prepared with the crystalline ZrO_2 support by using a "Cryst" superscript (i.e. MO_x/ZrO_2^{Cryst}). Similarly, we will denote catalysts prepared from the zirconium hydroxide using a "Hyd" superscript (i.e. MO_x/ZrO_2^{Hyd}).

Before progressing further, we will now briefly highlight selected methods of synthesizing catalysts.

5.2.1 Overview of Selected Methods of Catalyst Preparation

It is important to note that only terminal surface species can participate in a catalytic reaction; thus, synthetic techniques must ensure that the catalytically active components are adequately dispersed on the surface of the catalyst. Selected techniques employed for the synthesis of supported and mixed catalytic oxides include IWI and co-precipitation; these two distinct synthetic techniques can be employed to synthesize a spectrum of oxide based materials (See **Figure 5-1**). On one end of the spectrum, bulk mixed oxides consist of homogeneously mixed "solid solutions" of elements. However, in this scenario, chemical species may become trapped in the crystalline lattice and remain catalytically inactive. At the other end of the spectrum, chemical species are separated into distinct phases and are thus

unable to interact for catalytic promotion. Materials in the center of the spectrum can be synthesized to exhibit synergistic chemical aspects between the surface of the catalyst and the underlying supporting phase.

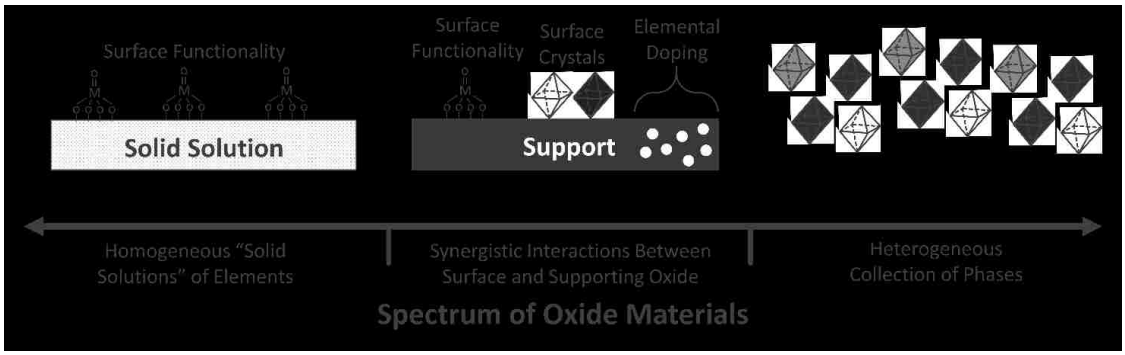

Figure 5-1. Spectrum of oxide materials.

Supported oxide catalysts are comprised of both a supported oxide phase and an underlying support phase.[2] They are traditionally prepared by the IWI of a crystalline oxide support with an oxide precursor solution.[3,4] IWI is then followed by calcination of the catalyst. Calcination facilitates dehydration of the catalyst, decomposes precursor ligands, and spreads the catalytically active surface component along the surface of the supporting oxide.[5,6] This introduces synergistic catalytic effects between the supported and supporting oxide.[7] Thus, IWI is an important synthetic technique for catalyst design as it allows direct modification of the surface of a catalyst.

Mixed catalytic oxides and bulk mixed catalytic oxides are typically prepared by means of the co-precipitation of multiple metal oxide precursors within solution.[8,9] Depending on the solution based processing conditions, co-precipitation based synthetic techniques allow the production of catalysts with either homogeneous or non-homogenous composition.[10] Variation of solution parameters during co-precipitation results in the formation of materials with elemental composition contained in either distinct component phases or within a single

"solid-solution".[11] Thus, co-precipitation techniques allow the production of catalysts with a spectrum of chemistries. However, co-precipitation techniques are more costly to manufacture in comparison to IWI methods, as they require substantial energy requirements for drying.[12] Furthermore, separation steps associated with removal of the solvent and precursor salts add to the cost of co-precipitated synthesis. Lastly, much of the elemental composition may become trapped within the internal lattice structure of the catalyst and not present on the surface of the catalyst.

Having discussed catalyst synthesis we now highlight two spectroscopic methods of characterization.

5.2.2 Dehydrated Catalyst Characterization via *in situ* Raman and IR Spectroscopy

All materials retain a physisorbed layer of water when in the presence of atmospheric moisture. This physisorbed layer of moisture coats the surface of a material and interacts with its surface chemistry. This can alter the surface of the catalyst and prevent accurate characterization of its terminal surface chemistry.[13] Thus, when studying the surface of a catalyst, one must study it under the environmental conditions most closely related to its use during reaction. This is best accomplished by either *in situ*[14] or *operando*[15] characterization of the catalyst after dehydration.

Operando spectroscopy refers to the characterization of a catalyst under realistic reaction conditions while simultaneously analyzing the catalytic activity and selectivity of the products.[16] *Operando* is Latin for "operating" or "working", while *in situ* means "in position" or "in place". Thus, *operando* applies to *in situ* catalyst characterization that is performed at or near the actual working conditions of the catalyst while concurrently analyzing its' products.

Surface probing spectroscopic techniques allow the characterization of the terminal surface functionality of a catalyst.[17] Alternative techniques such as X-ray diffraction (XRD) are bulk crystalline sensitive and detect the long range ordering of atoms;[18] not the terminal surface chemistry essential for catalysis. Raman spectroscopy selectively detects symmetric molecular vibrations while IR spectroscopy favors asymmetric vibrations.[19] The combination of *in situ* Raman and *in situ* IR spectroscopy can be used to provide complementary information about the surface and bulk characteristics of a dehydrated catalyst. These techniques can be utilized to differentiate between mono-oxo, dioxo, poly-oxo, and nanocrystals found on the surface of a supported oxide catalyst.

We now highlight common surface species found on supported oxides.

5.2.3 Common Terminal Surface Functionalities Observed on Supported Oxides

Metal ions with high oxidation states (i.e. oxidation states > M^{+4}) are able to exhibit high coordination numbers and terminate with mono-oxo or poly-oxo surface functionalities (i.e. M=O).[20] This is common for *d*-block transition metals with high valencies such as molybdenum, and tungsten. Transition metals with high oxidation states provide suitable surface candidates in supported oxide catalysts.[21] Conversely, metal ions with low oxidation states (i.e. oxidation states ≤ M^{+4}) present lower coordination numbers and normally terminate with hydroxyl (i.e. M-OH) and bridging surface functionalities (i.e. M-O-M). These materials offer suitable candidate supporting oxides (e.g. SiO_2, Al_2O_3, TiO_2, ZrO_2) and often exhibit both Lewis and Brønsted acidity.[22]

Depending on the loading of the surface oxide, different surface chemistries develop. At low loadings, small monomeric mono-oxo and dioxo species exist on the surface (See **Figure 5-2**). As the surface loading is increased, these monomeric species dimerize and polymerize

until the surface is coated with a monolayer of the surface oxide. At even higher loadings, the supported oxide begins to form surface crystals and nanoparticles along the surface of the support.[23] This diverse range of terminal surface species offers a wide range of catalytically active surface sites and are responsible for the effectiveness of supported oxide catalysts. Characterization of the catalyst with *in situ* Raman and IR spectroscopy can be utilized to determine if the surface species are mono-oxo, dioxo, or comprised in surface crystals.[24]

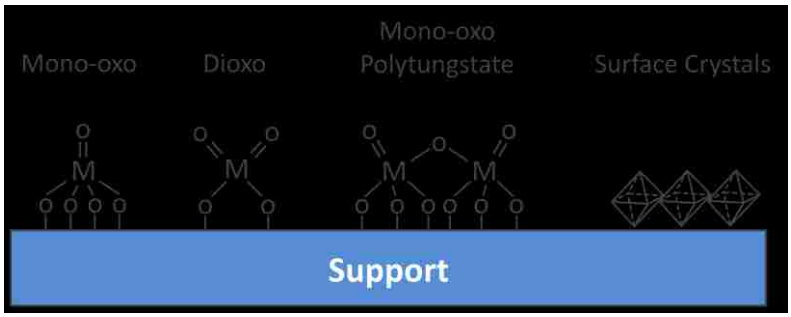

Figure 5-2. Generalized terminal surface species observed on supported oxides.

Having discussed the synthesis and characterization of catalysts we now highlight a recent discovery.

5.2.4 New Routes to Catalyst Synthesis

Recent research has revealed the presence of newly discovered, distorted mono-oxo $O{=}WO_4$ surface species during the synthesis of WO_3-TiO_2 and V_2O_5-WO_3/TiO_2 catalysts prepared from a non-conventional pH-mediated, co-precipitation procedure.[25,26] These materials exhibited enhanced catalytic activity for the selective catalytic reduction (SCR) of NO by NH_3 due to the presence of these newly discovered catalytic sites. These findings suggest that non-conventional co-precipitation techniques might be employed as a general synthetic approach for the formation of new catalytically active sites in similar catalytic materials.

The new sites were confirmed by the presence of two distinct mono-oxo $O{=}WO_4$ species during dehydrated characterization of the co-precipitated catalysts with *in situ* Raman

and IR spectroscopy. The co-precipitated WO_3-TiO_2 catalysts demonstrated both the traditional O=WO_4 site, distinguished by the symmetric vibration at ~1010-1016cm^{-1} (IR overtone at ~2017cm^{-1}) and a new symmetric vibration at ~983cm^{-1} (IR overtone at ~1992-2002cm^{-1}). This new vibration was indicative of a second O=WO_4 site which is believed to be semi-embedded within defects along the catalyst's surface.

The V_2O_5-WO_3/TiO_2 catalysts also demonstrated two similarly distinct mono-oxo sites for both the surface VO_4 and WO_4 species. The traditional O=WO_4 site found on crystalline TiO_2 supports is designated by a vibration at 1016cm^{-1}; with an IR overtone at 2020cm^{-1}. However, during characterization with *in situ* spectroscopy, the co-precipitated V_2O_5-WO_3/TiO_2 catalysts demonstrated two mono-oxo O=WO_4 sites designated by vibrations at 1013cm^{-1} and 984cm^{-1}; with IR overtones at 2017 cm^{-1} and 1992cm^{-1} respectively.

The traditional O=VO_3 site found on crystalline TiO_2 supports is designated by a vibration at 1037cm^{-1}; with an IR overtone at 2053cm^{-1}. However, during characterization with *in situ* spectroscopy, the co-precipitated V_2O_5-WO_3/TiO_2 catalysts demonstrated two mono-oxo O=VO_3 sites designated by a Raman vibration at 1034cm^{-1} and IR overtones at 2043cm^{-1} and 1960cm^{-1}. The shift observed in these peaks suggest the newly discovered sites reside in defects along the surface of the TiO_2 support, as opposed to oligomerized surface species.

The discovery of these new mono-oxo sites was subsequently correlated to enhanced catalytic performance during SCR reactions. These studies suggest non-conventional co-precipitation routes could be utilized to develop new catalytic materials. This could be achieved by employing the modified co-precipitation methods mentioned above or a similar approach such as the IWI of metal hydroxides.

We now extend the recent discoveries observed during the synthesis of non-conventionally prepared V_2O_5-WO_3/TiO_2 catalysts to prepare similar MO_x/ZrO_2 *catalysts for use as acid catalysis.*

5.2.5 Brief Review of Heterogeneous Acid Catalysis Involving MO_x/ZrO_2^{Hyd} Catalysts

Solid acid catalysts offer environmentally benign alternatives to homogeneous acid catalysts such as sulfuric and hydrofluoric acids. Today acid catalysts are widely used in industry with mixed oxides constituting a large fraction of these catalytic materials.[27] Alkylation and isomerization processes typically employ acid catalysts during processing (e.g. aluminosilicates, tungstated, sulfated, and phosphated mixed oxides).[28] Many of these catalysts have been termed "solid super acids" due to their low Hammett acidity function (H_o); which is a parameter used to measure the acidity of a solid material.[29] A material is deemed a super acid when its Hammett function is measured below $H_o < -11.9$.

Supported zirconia catalysts (MO_x/ZrO_2) have been widely studied for use in acid catalysis due to their unique Lewis and Brønsted acidity.[30,31] In particular, sulfated zirconia (SO_4/ZrO_2), tungstated zirconia (WO_3/ZrO_2), and molybdena supported zirconia (MoO_3/ZrO_2) have seen wide interest for acid-based catalytic reactions such as the skeletal isomerization of alkanes and hydrocarbon cracking.[32,33] However, these catalysts are reported to only be active when synthesized via non-conventional methods of synthesis.[34] The active MO_x/ZrO_2 acid catalysts are typically prepared via non-conventional synthesis procedures which are very similar to that utilized during production of the WO_3-TiO_2 SCR catalysts mentioned above. Thus, it remains likely that these acid catalysts incorporate unique surface species similar to those discovered on the WO_3-TiO_2 SCR catalysts.

The synthetic procedure used to prepare active MO_x/ZrO_2 catalysts for acid catalysis involves the non-conventional IWI of zirconium hydroxides ($Zr(OH)_x$) as opposed to the more

traditional IWI of crystalline oxides.[35] Zirconium hydroxides can either be obtained from a commercial supplier or prepared directly via the pH-mediated hydrolysis of zirconia precursors (e.g. $ZrOCl_2$, $Zr(NO_3)_4$ or $ZrO(NO_3)_2$) in solution to produce a zirconium precipitate for subsequent IWI.[36] After precipitation, the $Zr(OH)_x$ gel is then washed and dried to remove ionic species (e.g. Cl^-), resulting in an amorphous $Zr(OH)_x$ powder. A WO_3 precursor solution is then introduced to the $Zr(OH)_x$ matrix via IWI and the sample is calcined in air at high temperatures (~500-1000˚C).[37] The resulting MO_x/ZrO_2^{Hyd} catalyst has been reported to be more catalytically active than the traditionally synthesized MO_x/ZrO_2^{Cryst} catalysts.[34]

Various theories have been proposed for the active site of the WO_3/ZrO_2 catalysts including (1) polytungstate networks incorporating exposed zirconium atoms to facilitate Brønsted acidity;[38,39] (2) polymerized tungsten oxides;[40] and (3) distorted Zr-WO_3 nanoparticles (NPs).[41] One of the major difficulties in accurately characterizing the active site of these catalysts is the dynamic reconstruction that occurs during its synthesis from a $WO_3/Zr(OH)_x$ precursor to the final WO_3/ZrO_2^{Hyd} catalyst. Accurate characterization is further hindered by the various calcination ranges (~500-1000˚C) utilized to prepare the catalysts and by the lack of use of *in situ* dehydration techniques. As the catalyst is heated the surface species become mobile, polymerize, form surface nanocrystals, and even distorted Zr-WO_3 NPs,[42] as depicted in **Figure 5-2**. This is compounded by sintering of the support which increases the concentration of the surface phase (See **Figure 5-3**). Thus, further work should be conducted to better understand the catalytic reconfiguration of acidic catalysts during the synthesis of based MO_x/ZrO_2^{Hyd} catalysts from zirconium hydroxides.

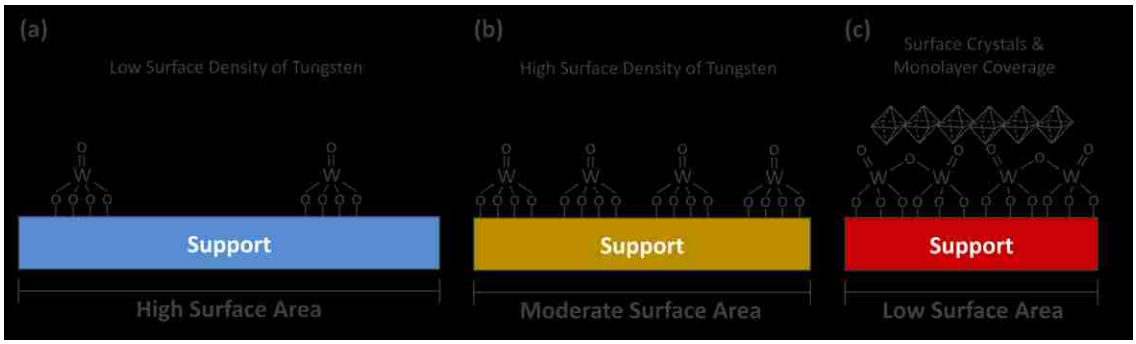

Figure 5-3. Schematic depicting the rise of polymeric surface species and NPs due to sintering of a catalyst after calcination at: **(a)** low temperatures; **(b)** elevated temperatures; **(c)** extreme temperatures.

5.2.6 Characterization of MO_x/ZrO_2^{Cryst} versus MO_x/ZrO_2^{Hyd} Catalysts

In this chapter we seek to better understand the general surface chemistry that develops during the catalytic synthesis of MO_x/ZrO_2^{Cryst} versus MO_x/ZrO_2^{Hyd} catalysts and their structural reconfiguration at elevated temperatures (500-1000°C). We employ a range of characterization techniques (N_2 adsorption, XRD, TGA, LEIS) to examine the structural changes that occur due to thermal reconfiguration of the catalyst. Additionally, we utilize *in situ* Raman and IR spectroscopy to monitor surface chemistry. These studies will provide general insight on the evolution of MO_x/ZrO_2^{Hyd} catalysts during synthesis, their surface chemistry, and high temperature reconfiguration.

5.3 Materials and Methods

5.3.1 Catalyst Synthesis

Commercial zirconium based materials including a crystalline zirconium dioxide (Degussa VP Zirkonoxid) and a zirconium hydroxide (MEL Chemicals, Product #XZO-631-01) were obtained for synthesis of the supported catalytic oxides. The as received crystalline ZrO_2 had a measured BET surface area of 64m^2/g and was comprised predominantly of the tetragonal ZrO_2 phase (t-ZrO_2 ~64vol.%). The commercial zirconium hydroxide was amorphous

with a measured BET surface area of 272m^2/g (See Chapter 3). Tetraethyl orthosilicate ($Si(OC_2H_5)_4$, 98%), ammonium metatungstate hydrate ($(NH_4)_6H_2W_{12}O_{40}\cdot xH_2O$, 99%), cerium(III) nitrate hexahydrate ($Ce(NO_3)_3\cdot 6H_2O$, 99%), and ammonium molybdate tetrahydrate ($(NH_4)_6Mo_7O_{24}\cdot 4H_2O$, 99%) were obtained from Sigma-Aldrich for deposition of the surface phase on the zirconium supports.

Supported catalysts were prepared by means of the traditional IWI technique on the crystalline ZrO_2 support and via a non-conventional IWI technique which utilized the $Zr(OH)_X$ support. The non-conventional IWI procedure resulted in formation of a mixed oxide similar to that which would be obtained during synthetic co-precipitation techniques. Prior to IWI, the support samples were dried at 120˚C under ambient conditions to desorb physisorbed surface moisture. The incipient wetness point of each powder was determined via incremental addition of solvent (i.e. water or ethanol). After determining the IW point of the powders, the support precursor was mixed with an appropriate amount of solvent for infiltration of the pore structure of the support. For SiO_2/ZrO_2 synthesis, the TEOS precursor was mixed in 200 proof ethanol within a glove box to avoid condensation of TEOS. All other catalyst precursors were dissolved in water under ambient conditions as they were water soluble and resistant to precursor condensation when in their native aqueous solution. Enough precursor was utilized in the IWI solutions to ensure the resulting catalysts would contain 5wt% of the supported phase (MO_X) after calcination.

After IWI, the samples were dried over night at room temperature and subsequently dried further at 120˚C to remove any remaining surface moisture. The samples were sieved through a size 40 mesh screen (0.42mm) to ensure particle size consistency during calcination. The samples were then calcined at 5˚C/min to a final temperature ranging from 500-1000˚C

with a three hour dwell time. After calcination the samples were allowed to cool within the furnace to ~120˚C and sealed in glass vials under desiccant for future characterization. This process facilitated the formation of MO_x/ZrO_2^{cryst} catalysts from the ZrO_2^{cryst} support and MO_x/ZrO_2^{Hyd} catalysts as prepared from the $Zr(OH)_x$ support.

5.3.2 Catalyst Characterization

Thermogravimetric Analysis (TGA)

A TA SDT Q600 instrument from TA Instruments was utilized for TGA analysis to assess weight loss and heat evolution of the catalysts during calcination. TGA analysis was conducted after synthesis and drying of the catalysts but prior to calcination. Approximately 10mg of the dried, uncalcined catalyst was loaded into the instrument at room temperature and ramped at 5˚C/minute to 1000˚C. The experiment was performed under dry flowing air with a flow rate of 100 mL/min. The air was filtered through a desiccant prior to addition to the sample chamber.

BET - Surface Area Measurement

A Micromeritics ASAP 2020 gas adsorption instrument was utilized to determine the BET (Brunauer-Emmett-Teller) surface area (S.A.) and pore structure of the catalysts via nitrogen (N_2) physisorption.[43] During each experiment, approximately 0.25g of catalyst was used for structural analysis. The samples were degassed at 250˚C for 6-12 hours. N_2 adsorption and desorption isotherms were then collected at the liquefied temperature of the adsorptive (Liquefied N_2 ~ -196˚C). Pore size distribution was determined using the BJH method (Barrett-Joyner-Halenda) to analyze the desorption portion of the resulting isotherms.[44] The Broekhoff-

De Boer correction was used to account for the chemical potential of adsorbed species by assuming a cylindrical pore structure.[45]

X-ray Diffraction (XRD)

XRD was used to assess the crystal phase composition of the catalysts. A Rigaku Miniflex II X-ray diffractometer with Cu K-alpha radiation (K_α=1.5418 Å)[46] was employed to scan the major peak regions of ZrO_2. This range included the characteristic t(101), m($11\bar{1}$), and m(111) peaks of ZrO_2 located in the domain between 25-35˚ 2-theta (2θ).[47] A scan rate of 0.5˚ 2θ per minute was used for data collection.

Low Energy Ion Scattering (LEIS)

A Qtac[100] HS-LEIS spectrometer equipped with a toroidal analyzer from ION-TOF was utilized for elemental analysis of the outermost surface layer of the 5wt% WO_3/ZrO_2 catalysts. HS-LEIS spectra was collected using a 3.0 KeV He^+ ion source to probe surface composition. Additionally, depth profiling experiments were performed via iterative HS-LEIS probe analysis, ion sputtering, and repeated HS-LEIS analysis. A total of eight cycles were performed during depth profiling, with each cycle utilizing a 1.0 keV Ar^+ ion source to sputter $1x10^{15}$ ions per cm^2. This facilitated removal of approximately one atomic surface layer (~0.2nm) per sputtering step.

in situ Raman Spectroscopy

in situ Raman spectroscopy was performed with a 532nm laser. A single stage Horiba-Jobin Yvon Laboratory Ram-HR Raman spectrometer was connected to an Olympus BX-30 confocal microscope for data collection. A Kaiser Super Notch filter with 900 groves/mm grating was also utilized. Laser excitation was generated with a Coherent Compass 315M-150 laser system utilizing a Nd-YAG double diode pumped laser with a 150mW output power and

10mW sample power. The data was collected by directing the scattered photons through a single monochromator focused on a UV-sensitive Horiba-Jobin Yvon CCD-3000V detector. The detector was cooled with liquid N_2 for analysis. Raman spectra was collected from 1100-100cm^{-1} with a ~2cm^{-1} spectral resolution.

During the dehydrated *in situ* Raman experiments, the sample was mounted in a Harrick environmental cell (model HVC-DRP-4) and dehydrated by flowing 10% O_2 in Ar at a rate of 30mL/min (Airgas supplied the 10% O_2 in Argon mixture). A Harrick ATC/Low Voltage temperature controller was utilized to heat the sample. The sample was heated at 10˚C/minute to 500˚C and dehydrated for one hour. The sample was then cooled to 120˚C and *in situ* Raman spectra was collected at 25-50˚C intervals. The effluent gas was neutralized with dilute aqueous H_2SO_4 contained in a glass bubbler and purged under a fume hood.

in situ IR Spectroscopy

in situ IR spectroscopy was utilized to determine surface chemistry of the catalysts under dehydrated conditions. A Thermo Nicolet 8700 FTIR spectrometer was utilized for data collection. The instrument incorporated a Harrick Praying Mantis attachment (model DRA-2) for cell mounting and data collection. A Harrick environmental cell (model HVC-DRP-4) was used for dehydration and incorporated an inlet port for adsorptive gas and an outlet port for effluent gas. All gas effluent was neutralized in a bubbler filled with dilute aqueous H_2SO_4 and purged through a fume hood. The environmental cell was mounted within the Praying Mantis during the dehydration experiment. The process gas cylinders were connected via Swagelok tubing to a parallel configuration of mass flow controllers (Brooks 5850E Series) and programmed by a Brooks Instrument set point controller (model 0254); additionally a Harrick

ATC/Low Voltage temperature controller was utilized to ensure proper environmental control within the reactor.

During the dehydrated *in situ* IR spectroscopy experiments, the catalysts were loaded into the environmental cell, sealed, and purged by flowing 10% O_2 in Ar at a rate of 30mL/min. After purging, the samples were heated at 10˚C/min to 500˚C and dehydrated for one hour under continuous 10% O_2/Ar flow. The catalysts were then cooled to 120˚C while collecting spectra at 25-50˚C intervals.

During the *in situ* IR NH_3-desorption experiments, the same IR spectrometer configuration was utilized as specified above. The samples were dehydrated following the procedure above using 10% O_2 in Ar with a flow rate of 30mL/min. However after dehydration, the gas was switched and the sample cell was purged with pure Ar for 30 minutes. Next, 2000 ppm NH_3 in He was introduced to the sample cell with a flow rate of 30mL/min for 30 minutes. The sample chamber was then purged with pure Ar once more to remove physisorbed NH_3 and excess NH_3 within the sample chamber. After Ar purging, the gas flow was once again switched to 10% O_2 in Ar with a flow rate of 30mL/min. The sample was then heated at 10˚C/minute to 500˚C and *in situ* IR spectra was collected at 25-50˚C intervals to assess NH_3 desorption.

5.4 Results and Discussion

5.4.1 Thermogravimetric Analysis

After IWI, the dried MO_x/ZrO_2^{Cryst} and MO_x/ZrO_2^{Hyd} catalyst precursors were calcined at temperatures ranging from 500-1000˚C in order to spread the surface phase along the support; and in the case of the $MO_x/Zr(OH)_x$ samples, promote crystallization of the underlying support

from $Zr(OH)_x$ (hydroxide) to ZrO_2 (crystalline oxide). This resulted in the formation of crystalline MO_x/ZrO_2^{cryst} and MO_x/ZrO_2^{Hyd} supported catalysts.

TGA was utilized to assess weight loss and exothermic heat evolution during calcination of the commercial ZrO_2 control samples, $Zr(OH)_x$ control samples, and the supported catalysts (See **Figure 5-4** and **Figure 5-5**). During TGA characterization, three general trends were observed; these include the endothermic desorption of physisorbed surface moisture at temperatures ranging from ambient conditions to ~450˚C, exothermic hydroxide crystallization at temperatures ranging from ~400-500˚C, and exothermic crystallite sintering at temperatures greater than 450˚C.

TGA analysis of the commercial crystalline ZrO_2 material demonstrated minimal weight loss (<5wt%) during calcination (See **Figure 5-4a**) and was indicative of the desorption of physisorbed surface water. A gradual exothermic heat evolution was observed at temperatures greater than 400˚C and is indicative of the sintering of crystallites. TGA of the commercial $Zr(OH)_x$ sample demonstrated large variations from that exhibited by the crystalline ZrO_2 material (See **Figure 5-4b**). The hydroxide experienced a substantial ~25% weight loss during calcination, which coincided with a large endothermic peak. This suggests a significant loss of physisorbed surface water and surface condensation of the hydroxide. A large exothermic crystallization peak was detected at ~447˚C as the sample crystallized from amorphous $Zr(OH)_x$ to crystalline ZrO_2^{Hyd}.

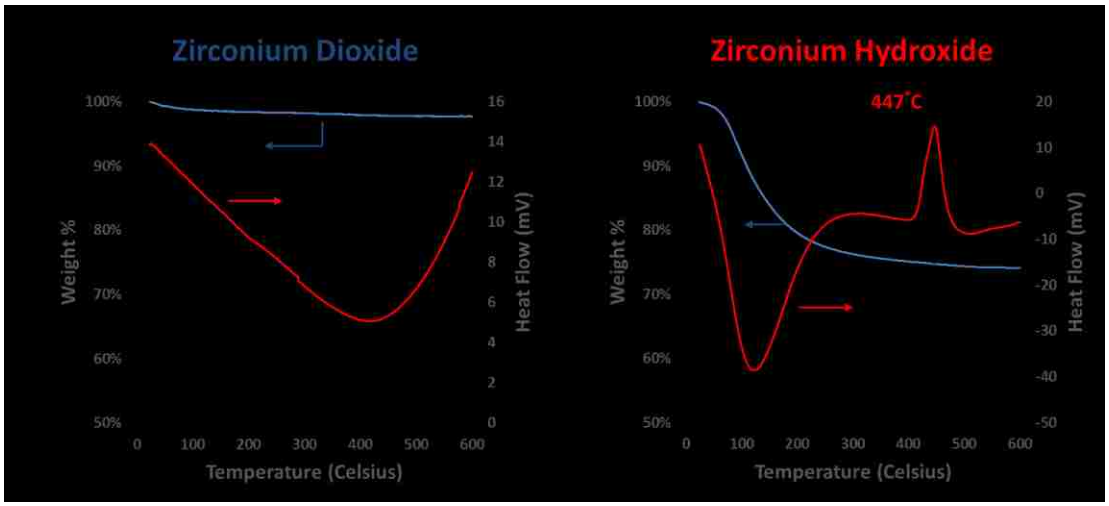

Figure 5-4. TGA of commercial **(a)** crystalline ZrO_2 and **(b)** amorphous $Zr(OH)_x$ samples after heating in dry air from ambient conditions to 600˚C.

The MO_x/ZrO_2^{Cryst} catalyst precursors exhibited similar thermogravimetric results to that provided by the ZrO_2^{Cryst} control sample. This included minimal weight loss during calcination (<5wt%), endothermic desorption of water, and gradual exothermic sintering (See **Figures 5-5a,c,e**). However, the $MO_x/Zr(OH)_x$ catalyst precursors exhibited substantially different thermogravimetric trends in comparison to the corresponding TGA of the $Zr(OH)_x$ control sample. Addition of a surface oxide (i.e. MoO_3, WO_3, and CeO_2) limited weight loss during calcination from ~25%, as observed in the $Zr(OH)_x$ control sample, to only ~5wt% in the supported samples. Additionally, the single crystallization peak presented by the $Zr(OH)_x$ control sample (T ~447˚C) became bimodal in structure during calcination of the $MO_x/Zr(OH)_x$ precursors (See **Figures 5-5b,d,f**). This suggests the surface oxide impedes crystallization of the hydroxide.

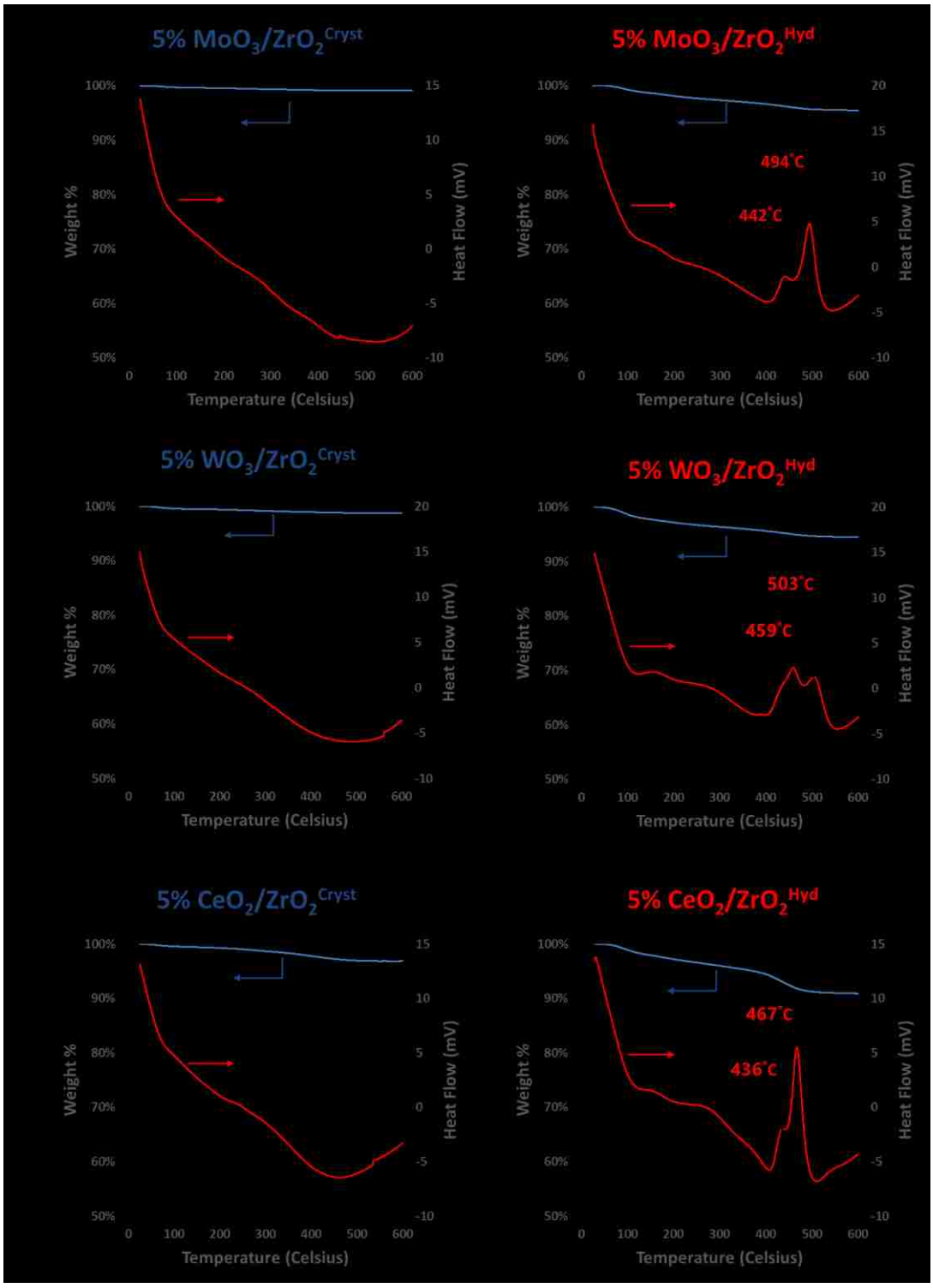

Figure 5-5. TGA of supported catalyst precursors during calcination in dry air from ambient conditions to 600˚C. Samples include: **(a)** 5% MoO_3/ZrO_2^{cryst}; **(b)** 5% MoO_3/ZrO_2^{Hyd}; **(c)** 5% WO_3/ZrO_2^{cryst}; **(d)** 5% WO_3/ZrO_2^{Hyd}; **(e)** 5% CeO_2/ZrO_2^{Cryst}; **(f)** 5% CeO_2/ZrO_2^{Hyd}.

5.4.2 BET Surface Area Analysis

Calcination of the commercial ZrO_2^{cryst} and $Zr(OH)_X$ materials resulted in traditional mechanisms of sintering when calcining at 500, 700, and 1000˚C (See **Figure 5-6**). The ZrO_2^{cryst} material demonstrated a loss of surface area ranging from ~64m^2/g after 500˚C calcination; to ~14m^2/g after 1000˚C calcination. Similarly the $Zr(OH)_X$ material demonstrated a reduction in surface area from ~272m^2/g (as received) to ~6m^2/g after calcination at 1000˚C.

The measured BET surface areas differed substantially between the MO_x/ZrO_2^{cryst} and MO_x/ZrO_2^{Hyd} catalysts. The MO_x/ZrO_2^{cryst} catalysts exhibited similar mechanisms of sintering as was observed in the commercial ZrO_2^{cryst} material (See **Figure 5-6a**). Conversely the supported MO_x/ZrO_2^{Hyd} catalysts exhibited significant promotions in surface area upon application of the surface oxide to the hydroxide support. The surface area of the MO_x/ZrO_2^{Hyd} catalysts were nearly double that of the commercial $Zr(OH)_X$ control at all temperatures analyzed. Thus, application of a surface oxide was shown to scaffold the amorphous $Zr(OH)_X$, limit sintering, and dramatically improve the BET surface area of the catalyst.

One notable exception to surface area promotion of the MO_X/ZrO_2^{Hyd} catalysts was the CeO_2/ZrO_2^{Hyd} based catalyst. This catalyst showed similar surface areas as that presented by the $Zr(OH)_x$ control. Additionally, CeO_2 was observed to be a large promoter of the t-ZrO_2 phase as characterized via XRD in **Figure 5-7b**. These are complementary results; CeO_2 is known to readily dope with ZrO_2 to form CeO_2-ZrO_2 solid solutions.[48] Thus, the CeO_2 deposited on the CeO_2/ZrO_2^{Hyd} catalysts via IWI rapidly dopes within the bulk crystal structure of the CeO_2/ZrO_2^{Hyd} catalyst. This phenomenon reduces ceria's capability to scaffold the surface area of the hydroxide but it dramatically increases it's stabilization of t-ZrO_2 phase. This concept of

bulk crystal stabilization has been used in high temperature applications such as the linings of furnaces and the stabilization of catalytic converters.[49]

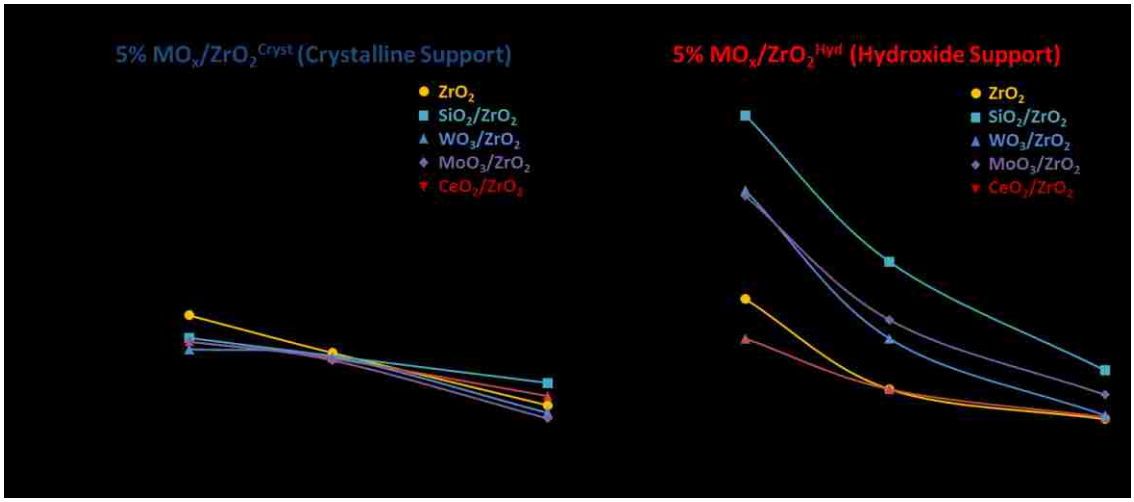

Figure 5-6. BET surface areas for **(a)** MO_x/ZrO_2^{cryst} samples and **(b)** MO_x/ZrO_2^{Hyd} as derived from N_2 adsorption isotherms of the supported catalysts after calcination at 5˚C/min to temperatures ranging from 500-1000˚C with three hour dwell times.

5.4.3 X-Ray Diffraction Characterization

Calcination of the commercial ZrO_2^{cryst} material demonstrated slight variations in crystal structure versus that observed during calcination of the MO_x/ZrO_2^{cryst} catalysts (See **Figure 5-7**). The commercial ZrO_2^{cryst} material was observed to transform from the tetragonal phase to the monoclinic phase as noted by a reduction in the t(101) peak and growth of the m($11\bar{1}$) and m(111) peaks (See **Figure 5-7a**). Conversely, the CeO_2/ZrO_2^{cryst} catalyst showed stabilization of the metastable t-ZrO_2 phase after calcination at 1000˚C (See **Figure 5-7b**). The WO_3/ZrO_2^{cryst} catalyst showed promotion of the m-ZrO_2 phase (See **Figure 5-7c**). The MoO_3/ZrO_2^{cryst} catalyst showed slight increases in the m-ZrO_2 phase after low temperature calcination (See **Figure 5-7d**). These findings demonstrate that addition of a surface oxide can either promote or hinder transformation of a metastable phase (i.e. m-ZrO_2) to a more stable phase (i.e. m-ZrO_2).

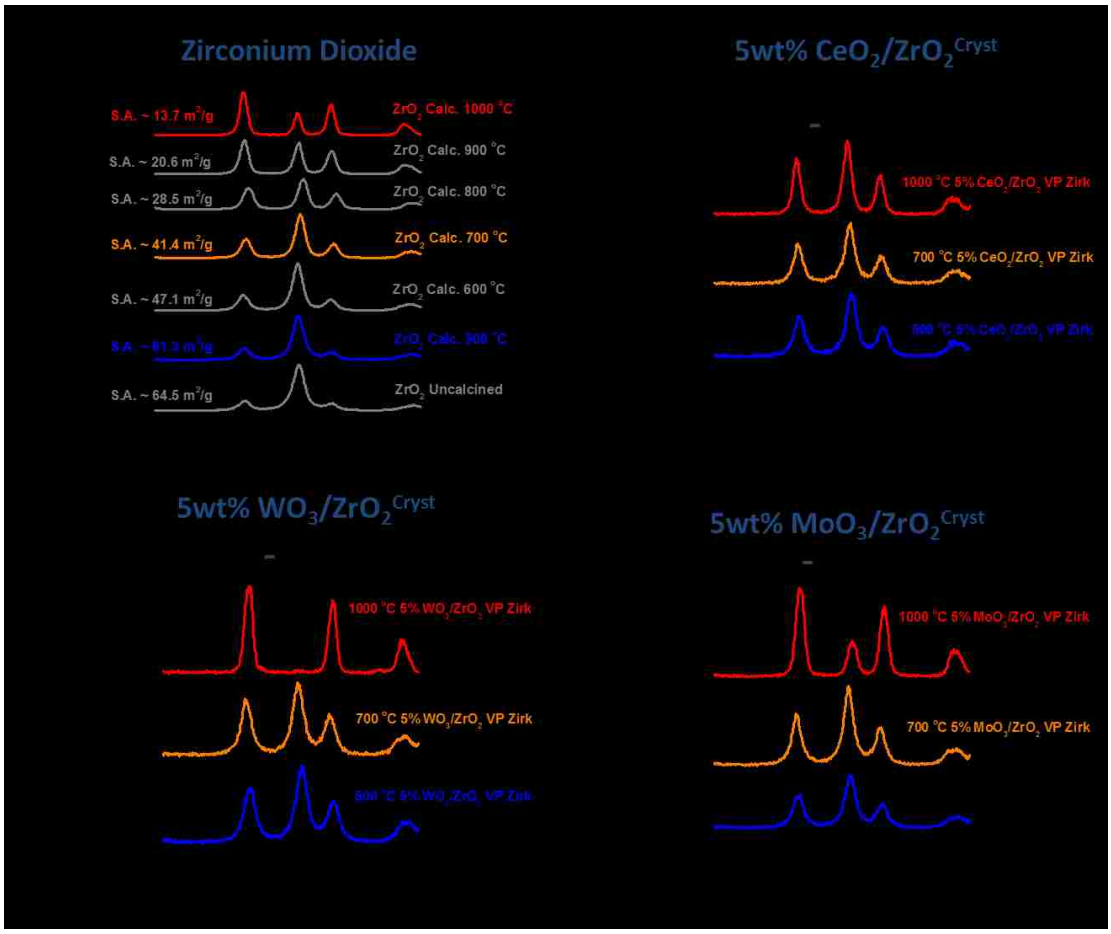

Figure 5-7. XRD of supported oxides prepared using the commercial crystalline ZrO_2 support after calcination at temperatures ranging from 500-1000˚C. Data includes: **(a)** XRD of commercial ZrO_2^{Cryst} samples; **(b)** XRD of 5wt% CeO_2/ZrO_2^{Cryst}; **(c)** XRD of 5wt% $WO_3/ZrO^{Cryst}{}_2$; **(d)** XRD of 5wt% MoO_3/ZrO_2^{Cryst}.

Calcination of the commercial $Zr(OH)_X$ demonstrated a dramatic variation in crystal structure versus that observed during calcination of the MO_x/ZrO_2^{Hyd} catalysts (See **Figure 5-8**). The commercial ZrO_2^{Hyd} material was observed to transform from an amorphous phase to the monoclinic phase as noted by growth of the m($11\bar{1}$) and m(111) peaks (See **Figure 5-8a**). Conversely, the CeO_2/ZrO_2^{Hyd} catalyst showed stabilization of the metastable t-ZrO_2 phase after calcination (See **Figure 5-8b**). The WO_3/ZrO_2^{Hyd} catalyst also showed direct promotion of the t-ZrO_2 phase (See **Figure 5-8c**). Lastly, the MoO_3/ZrO_2^{Hyd} catalyst also showed direct promotion of the t-ZrO_2 phase (See **Figure 5-8d**). These findings demonstrate that addition of a surface

oxide can be used to promote formation of the t-ZrO_2 phase from a $Zr(OH)_X$ based material. This concept was originally demonstrated during the preparation of SiO_2/ZrO_2^{Hyd} materials in Chapter 3.

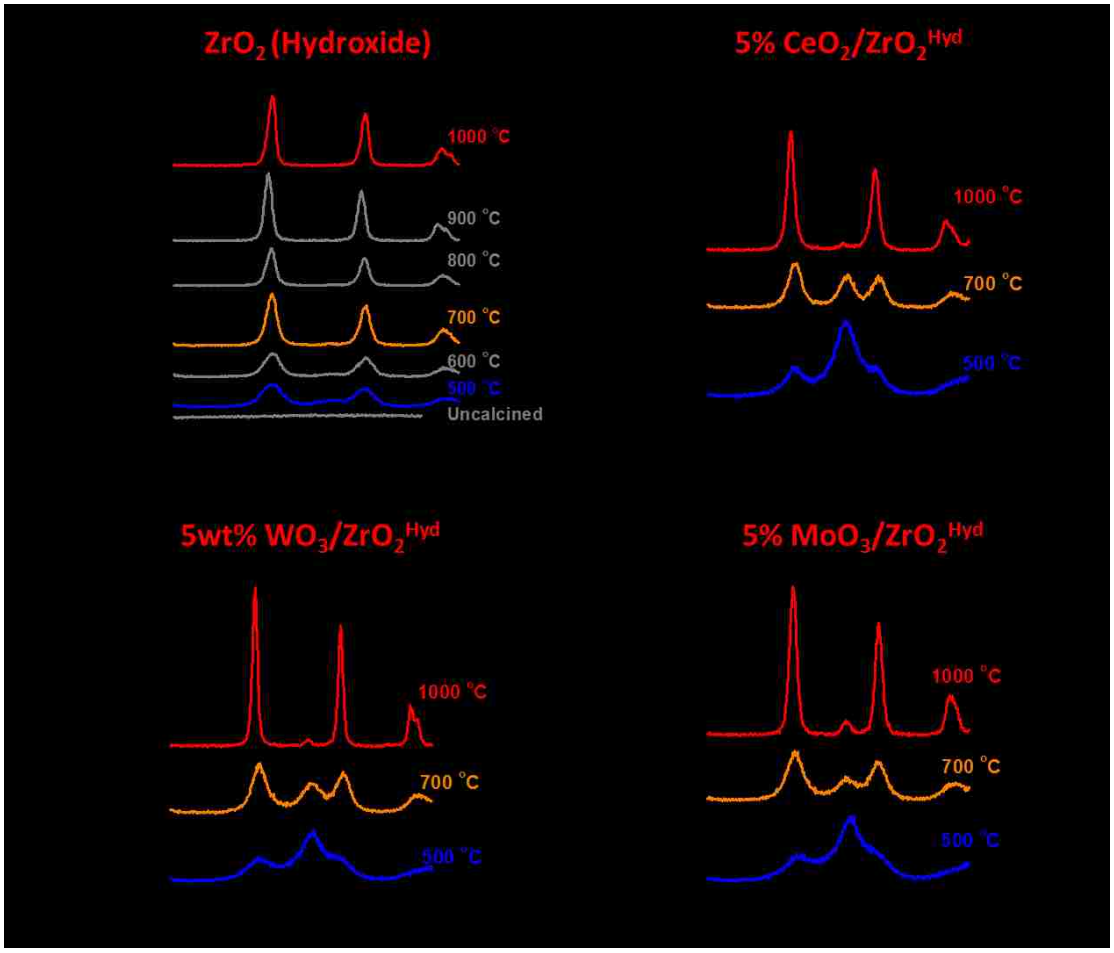

Figure 5-8. XRD of supported oxides prepared using the commercial hydroxide support after calcination at temperatures ranging from 500-1000˚C. Data includes: **(a)** XRD of commercial hydroxide based ZrO_2^{Hyd} samples; **(b)** XRD of 5wt% CeO_2/ZrO_2^{Hyd}; **(c)** XRD of 5wt% WO_3/ZrO_2^{Hyd}; **(d)** XRD of 5wt% MoO_3/ZrO_2^{Hyd}.

5.4.4 Complementary Analysis of Catalytic Reconstruction - TGA, N_2-ads, XRD, *in situ* Raman, and LEIS

in situ Raman spectroscopy was utilized to compare the surface chemistry of WO_3/ZrO_2 catalysts after calcination at 500, 700, and 1000˚C. General reconstructive trends are

demonstrated in the *in situ* Raman spectra provided in **Figure 5-9**. After calcination at low temperatures (i.e. 500˚C), the 5wt% WO_3/ZrO_2^{Cryst} catalyst was predominantly monoclinic in phase, exhibited a mono-oxo $O=WO_4$ peak (~1010cm^{-1}), and the presence of crystalline WO_X species were noticeably absent. However, after high temperature calcination (i.e. 1000˚C), crystalline WO_3 peaks were shown to develop along the surface of the catalyst (~715 and ~805cm^{-1}).[41] Characterization of the 5wt% WO_3/ZrO_2^{Hyd} catalyst showed the presence of the tetragonal phase of ZrO_2 after low temperature calcination (500˚C). This phase began converting to the m-ZrO_2 phase upon higher temperature calcination. This also corresponded with a loss of surface area and eventual development of the crystalline WO_3 peaks at ~715 and ~805cm^{-1} (See **Figure 5-9b**). These findings compliment the XRD characterization of the bulk crystal structure. Although not presented here, similar reconstructive phenomenon were obtained for the MoO_3/ZrO_2^{Hyd} catalyst versus the MoO_3/ZrO_2^{Cryst} catalyst.

LEIS experiments were performed to examine the elemental surface composition of the WO_3/ZrO_2 catalysts after high temperature calcination (See **Figure 5-10**). Calcination of both the WO_3/ZrO_2^{Cryst} and the WO_3/ZrO_2^{Hyd} catalysts demonstrated an enhancement in the tungsten content found along the surface of the catalysts. This was shown by an increase in the count ratio of the integrated W/Zr spectral peaks collected during LEIS depth profiling of the catalysts. This confirms that the tungsten content enriches upon calcination from 500˚C to 1000˚C. Surface enrichment should also occur in the MoO_3/ZrO_2 catalysts.

A Summary on the Characterization of Catalyst Reconstruction

The results presented in **Figures 5-5** through **Figure 5-10** demonstrate complementary characterization techniques employed to examine the catalytic reconstruction of MO_X/ZrO_2

based catalysts at elevated temperatures. Characterization of the reconstruction of WO_3/ZrO_2^{cryst} versus WO_3/ZrO_2^{Hyd} catalysts was specifically highlighted in this study. The reduction of BET surface area due to sintering at elevated temperatures caused surface enrichment of the tungsten species. This resulted in the development of surface WO_3 nanoparticles at ~1000˚C. This was a general phenomenon observed in both the WO_3/ZrO_2^{cryst} and WO_3/ZrO_2^{Hyd} based catalysts. Additionally, this concept has been observed previously in the literature for WO_3/Al_2O_3 Catalysts.[50] These findings demonstrate the dynamic reconstructive nature of the surface area, crystalline phase, and surface chemistry of a catalyst upon high temperature calcination (T>700˚C).

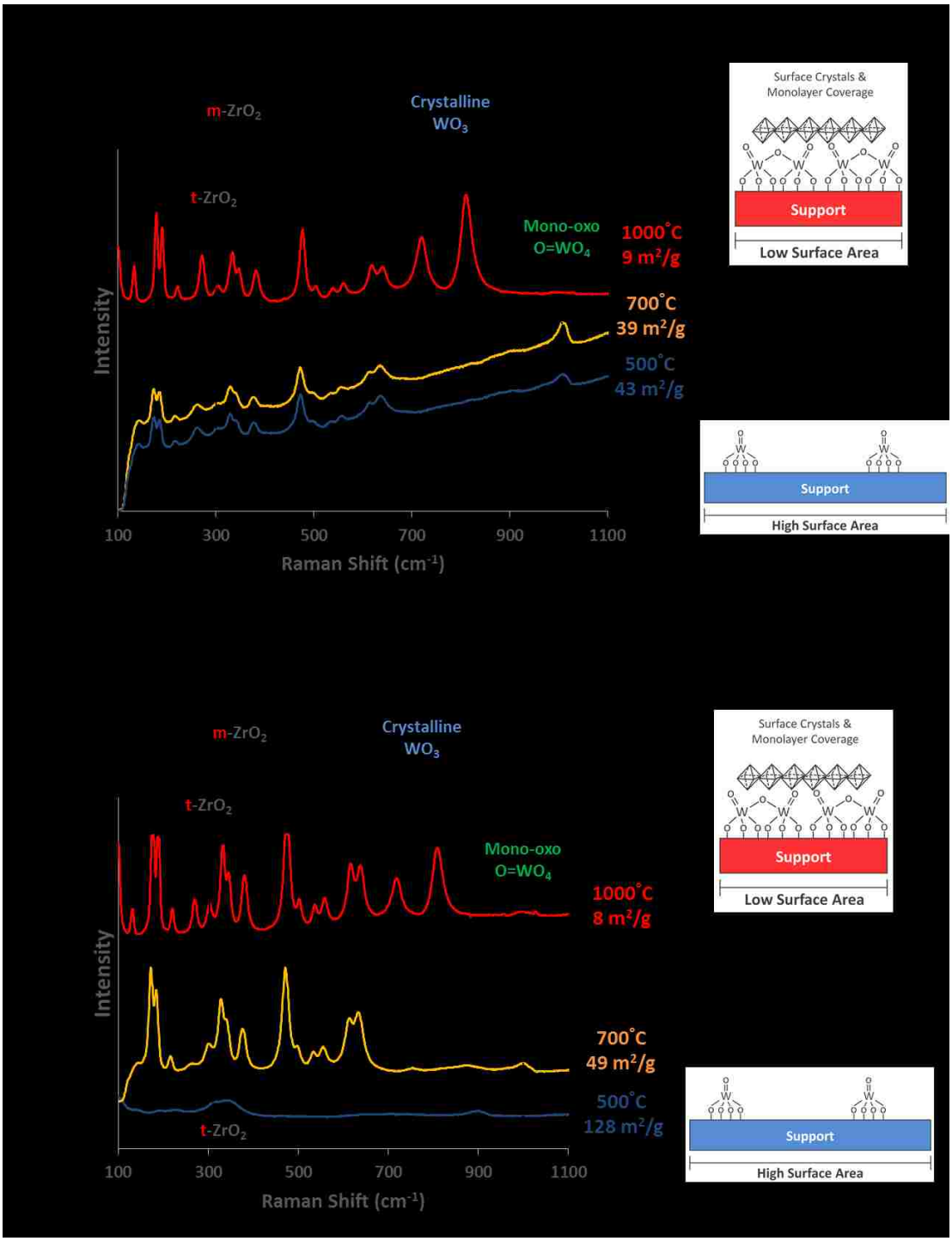

Figure 5-9. *In Situ* Raman characterization of dehydrated **(a)** 5wt% WO_3/ZrO_2^{Cryst} catalysts and **(b)** 5wt% WO_3/ZrO_2^{Hyd} catalysts after calcination at various temperatures. The samples were heated to 500˚C under flowing 10% O_2 in Ar for dehydration and subsequently cooled to 120˚C for collection of spectra.

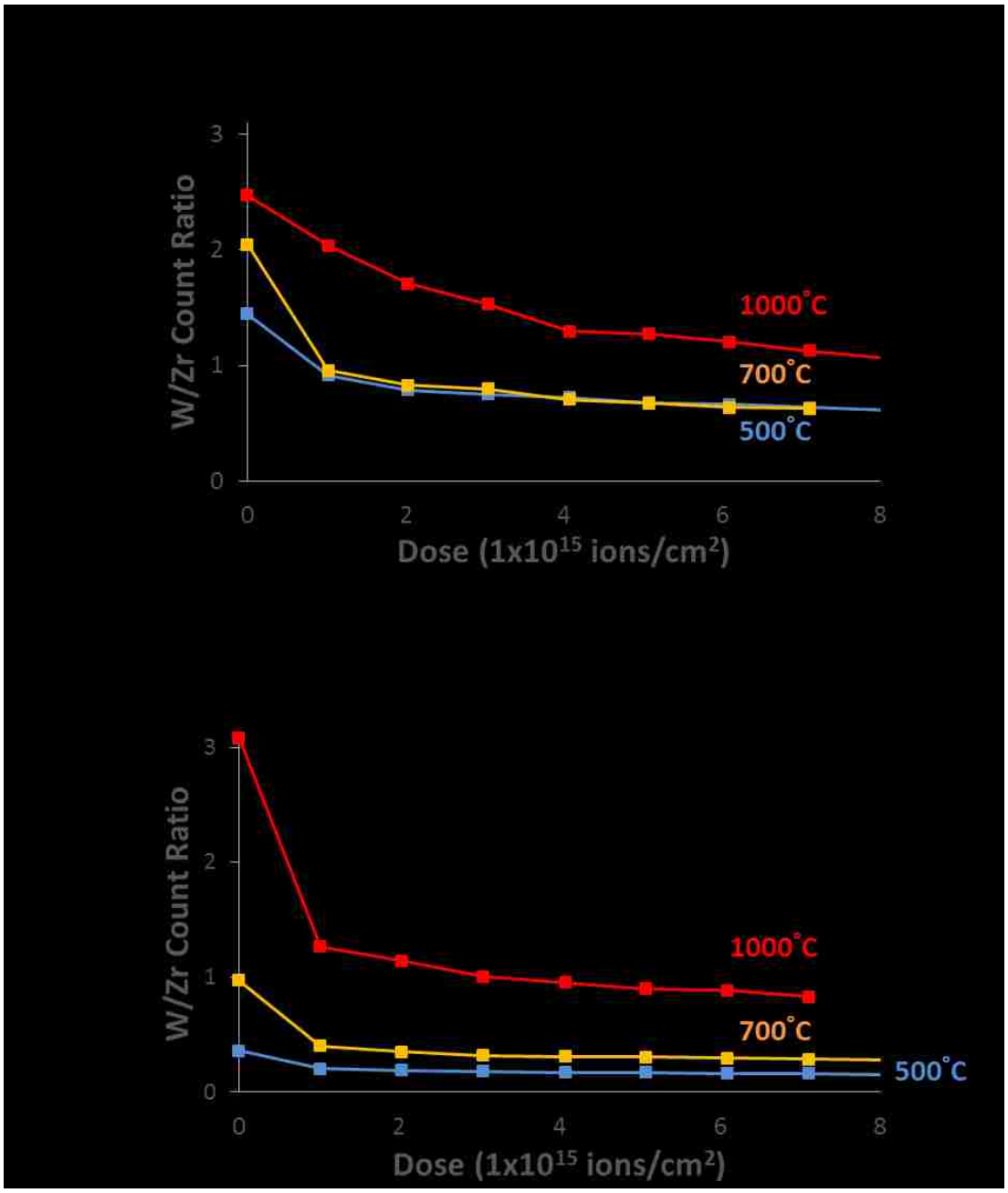

Figure 5-10. Integrated W/Zr count ratio collected during LEIS depth profiling of the **(a)** WO_3/ZrO_2^{Cryst} versus **(b)** WO_3/ZrO_2^{Hyd} catalysts after calcination at temperatures ranging from 500-1000˚C. *LEIS Experiments were performed by Dr. Henry S. Luftman.*

5.4.5 Characterization of the Surface Chemistry of Catalytic Oxides

in situ IR spectroscopy demonstrated unique surface mono-oxo $O=WO_4$ species in the WO_3/ZrO_2^{Hyd} versus WO_3/ZrO_2^{Cryst} catalysts (See **Figure 5-11a**). The traditional mono-oxo $O=WO_4$ vibration was observed to shift from ν(M=O)~1007cm^{-1} for the WO_3/ZrO_2^{Hyd} catalyst to ν(M=O)~990cm^{-1} for the WO_3/ZrO_2^{Cryst}. A similar shift was observed in the overtone region (See **Figure 5-11b**). Similarly, *in situ* IR spectroscopy demonstrated unique surface mono-oxo $O=MoO_4$ species in the MoO_3/ZrO_2^{Hyd} versus MoO_3/ZrO_2^{Cryst} catalysts (See **Figure 5-12a**). The mono-oxo $O=MoO_4$ vibration shifted from ν(M=O) ~999cm^{-1} for the MoO_3/ZrO_2^{Cryst} catalyst to ν(M=O)~982cm^{-1} for the MoO_3/ZrO_2^{Hyd} catalyst. This was also demonstrated by a similar shift in the overtone region (See **Figure 5-12b**).[51]

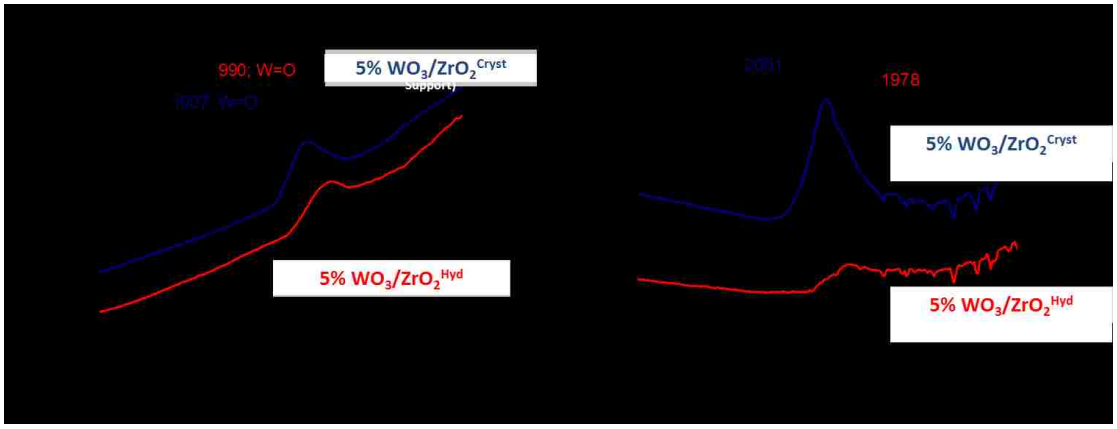

Figure 5-11. *in situ* IR spectra of dehydrated 5wt% WO_3/ZrO_2^{Cryst} versus WO_3/ZrO_2^{Hyd} catalysts prepared by calcination at 500˚C. Spectra examines the **(a)** mono-oxo region and the **(b)** overtone region.

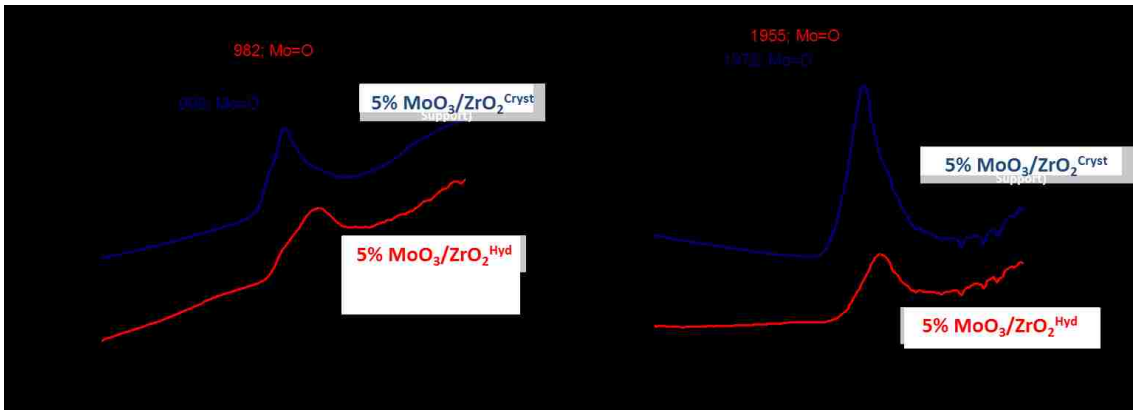

Figure 5-12. *in situ* IR spectra of dehydrated 5wt% MoO_3/ZrO_2^{Cryst} versus MoO_3/ZrO_2^{Hyd} catalysts prepared by calcination at 500˚C. Spectra examines the **(a)** mono-oxo region and the **(b)** overtone region. The samples were heated to 500˚C and cooled to 120˚C to collect the spectra.

in situ Raman characterization under dehydrated conditions provided complementary characterization of the two distinct mono-oxo species found on the 5wt% MO_X/ZrO_2^{Cryst} versus MO_X/ZrO_2^{Hyd} catalysts. The standard $O=WO_4$ vibration $\nu(M=O)$~1008cm^{-1} was observed for the 5wt% WO_3/ZrO_2^{Cryst} catalyst while the 5wt% WO_3/ZrO_2^{Hyd} catalyst presented a distorted vibration at ~999cm^{-1} (See **Figure 5-13a**). Similar results were obtained for the 5wt% MoO_3/ZrO_2catalysts. The standard $O=MoO_4$ vibration is $\nu(M=O)$~1000cm^{-1} but the observed vibration for the 5wt% MoO_3/ZrO_2^{Cryst} catalyst was $\nu(M=O)$~1000cm^{-1}. This value is a bit larger than the traditional value reported in the literature. Thus, this sample should be reanalyzed. However, the 5wt% MoO_3/ZrO_2^{Hyd} catalyst presented a distorted vibration at $\nu(M=O)$~985cm^{-1}, a shift of about 15cm^{-1} from the value reported in literature (See **Figure 5-13b**).[51]

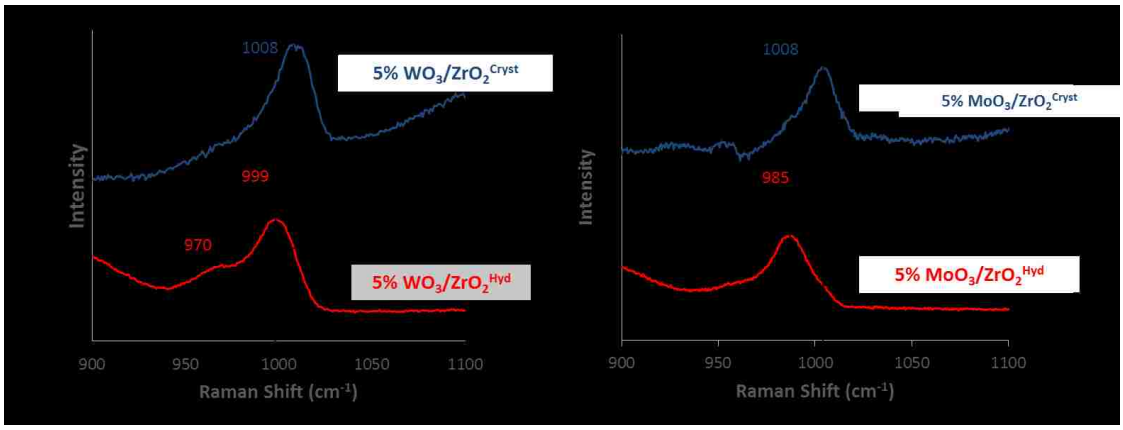

Figure 5-13. *in situ* Raman characterization of the surface $O=WO_4$ and $O=MoO_4$ species after dehydration. Data examines the **(a)** $O=WO_4$ vibrations on 5wt% WO_3/ZrO_2^{Cryst} versus WO_3/ZrO_2^{Hyd} catalysts; **(b)** $O=MoO_4$ vibrations on 5wt% MoO_3/ZrO_2^{Cryst} versus MoO_3/ZrO_2^{Hyd} catalysts. The catalysts were prepared via calcination at 500˚C. The catalysts were heated to 500˚C and cooled to 120˚C to collect the spectra under dehydrated conditions.

The results presented in **Figure 5-11**, **Figure 5-12**, and **Figure 5-13** suggest distorted surface mono-oxo species exist on the MO_X/ZrO_2^{Hyd} catalysts. This was shown by complementary *in situ* Raman and IR characterization of the catalysts under dehydrated conditions. It is hypothesized that the vibrational shift observed in the MO_X/ZrO_2^{Hyd} catalysts is a result of new mono-oxo species which are partially embedded within defects along the surface of the ZrO_2^{Hyd} support (See **Figure 5-14**). Additionally, these species may be partly responsible for structuring the t-ZrO_2 bulk crystalline phase and promoting increased BET surface area observed in the hydroxide based catalysts.

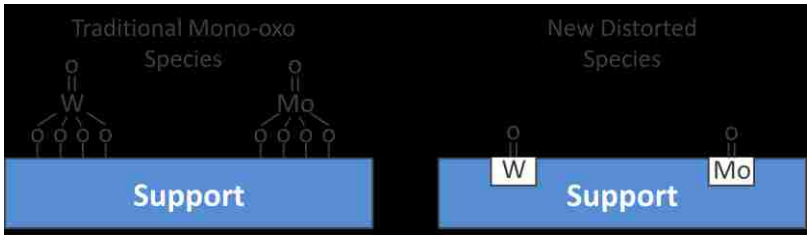

Figure 5-14. Graphic depicting the traditional mono-oxo $O=WO_4$ and $O=MoO_4$ terminal surface species and a possible interpretation of the distorted mono-oxo species which are hypothesized to reside within surface defects along the ZrO_2^{Hyd} support.

Characterization of surface acidity was performed to assess the acid sites present on the MO_X/ZrO_2^{Hyd} versus MO_X/ZrO_2^{Cryst} catalysts (See **Figure 5-15**). The MO_X/ZrO_2^{Hyd} catalyst shows a pronounced increase in the 3259cm^{-1} and 3347cm^{-1} vibrations versus the MO_X/ZrO_2^{Cryst} catalysts (See **Figure 5-15b,d**). These respective vibrations are characteristic of adsorbed ammonia (NH_3*) on Lewis sites.[25,26] Work is currently being conducted to quantify the relative amounts of NH_3 adsorption achieved by both types of catalysts. This is being conducted via integration of the characteristic NH_3* adsorption peaks and normalization with the BET surface area of the catalyst. This will provide insight into the acid-base nature of the distorted $O=MO_x$ sites versus the traditional mono-oxo sites.

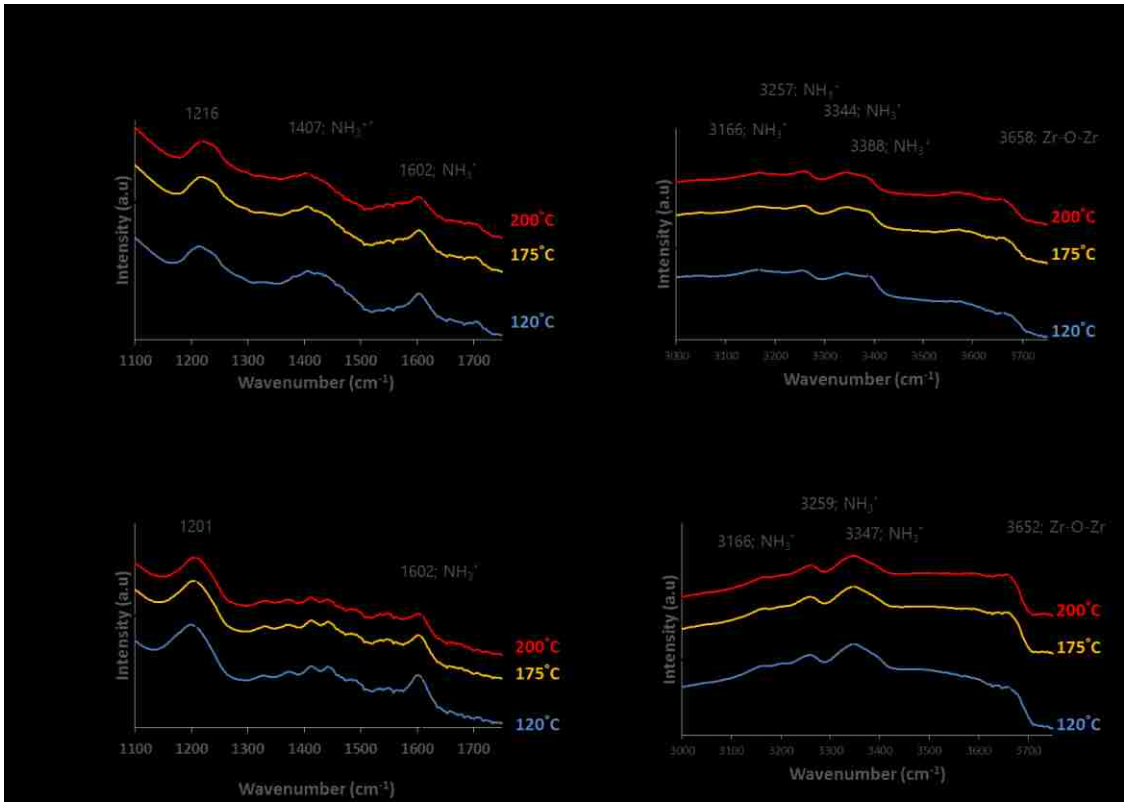

Figure 5-15. *in situ* IR spectroscopy during desorption of NH_3 on: **(a-b)** 5wt% MO_X/ ZrO_2^{Cryst} catalysts versus **(c-d)** 5wt% MO_X/ ZrO_2^{Hyd} catalysts. The catalysts were dehydrated prior to NH_3 adsorption.

Surface reconstruction of the MO_X/ZrO_2 catalysts was analyzed under dehydrated conditions with *in situ* IR spectroscopy (See **Figure 5-16**). The mono-oxo vibrations (~990-1010cm^{-1}) were observed to diminish in the WO_3/ZrO_2 samples prepared with high calcination temperatures (See **Figure 5-16a,b**). This corresponded with the rise of vibrations at higher wavenumbers (~1023cm^{-1}). This trend was also observed in the overtone region (See **Figure 5-16c,d**). This was a general trend that was observed in both the MO_X/ ZrO_2^{Hyd} and MO_X/ ZrO_2^{Cryst} catalysts. This vibrational shift corresponds to increasing poly-oxo content on the surface of the catalyst during high temperature reconstruction. As the catalyst sinters it loses surface area and the resulting WO_3 structures begin forming a monolayer, polymerizing, and forming surface crystals. This phenomenon is similar to that observed when approaching monolayer coverage of an oxide by increasing the surface loading through IWI.[51]

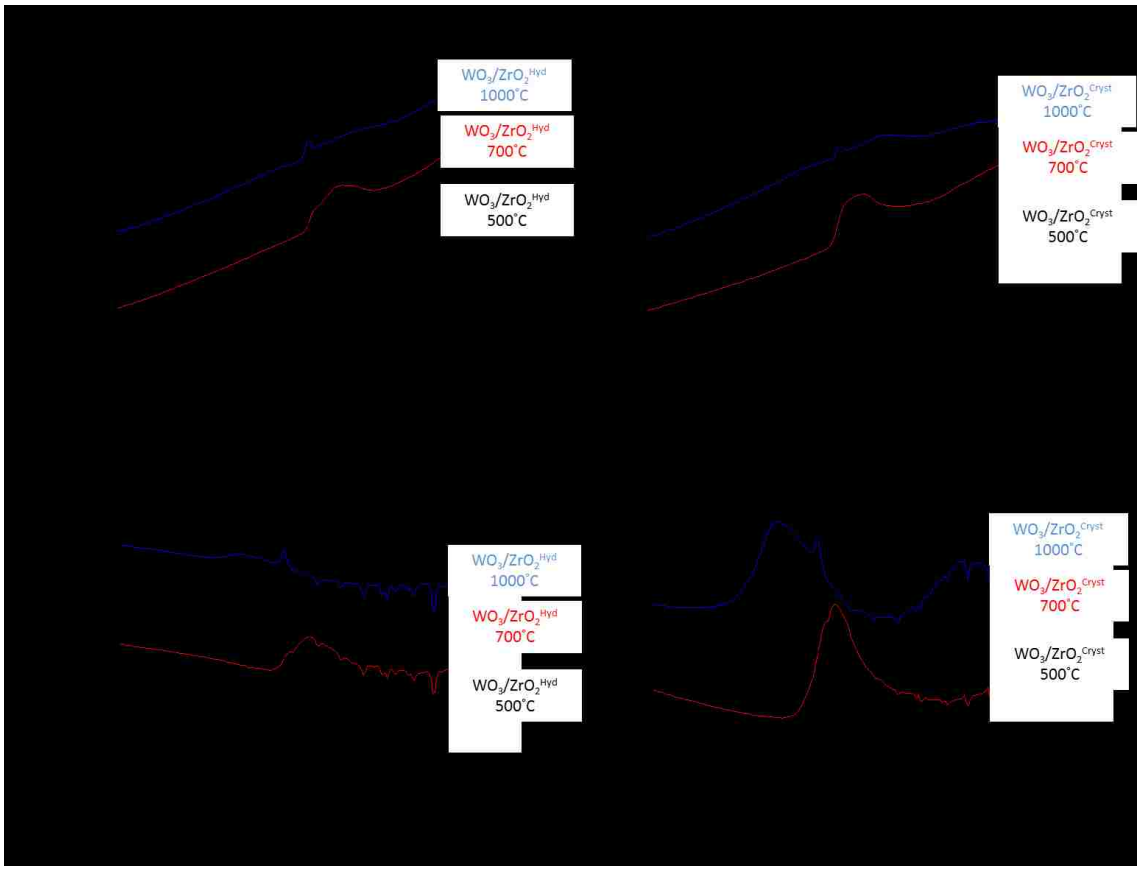

Figure 5-16. *in situ* IR characterization of dehydrated WO_3/ZrO_2 catalysts prepared with various calcination temperatures (500, 700, and 1000˚C) during synthesis.

5.5 Conclusions

This chapter demonstrated various aspects of catalyst stabilization, high temperature reconstruction, and unique surface chemistry. This was demonstrated with two synthetic approaches to catalyst preparation. A non-conventional synthetic technique was employed for the design of stabilized acid catalysts; this procedure involved the IWI of a commercial hydroxide (i.e. ZrO_2^{Hyd}) as opposed to a crystalline oxide support (i.e. ZrO_2^{Cryst}). This method of synthesis was demonstrated to stabilize the t-ZrO_2 phase and the BET surface area of the catalysts at elevated temperatures. Additionally, *in situ* Raman and IR characterization of the catalysts under dehydrated conditions shows the presence of unique distorted mono-oxo

$O=WO_4$ and $O=MoO_4$ species on the surface of the MO_X/ ZrO_2^{Hyd} catalysts. These surface species differ from the traditional mono-oxo species observed on the MO_X/ ZrO_2^{Cryst} catalysts. It is believed these unique terminal surface functionalities reside in defects along the surface of the ZrO_2^{Hyd} support and actively stabilize its BET surface area and the underlying tetragonal crystal structure. Lastly, various mechanisms of high temperature catalytic reconstruction were highlighted. As catalysts sinter, the surface layer reconfigures and forms oligomerized surface species, polymerized surface species, and nanoparticles.

5.6 References

[1] Bell, Alexis T., Bruce C. Gates, and Douglas Ray. "Grand Challenge 2: Design and Controlled Synthesis of Catalytic Structures." *Basic Research Needs: Catalysis for Energy: Report from the U.S. Department of Energy, Office of Basic Energy Sciences Workshop, August 6-8, 2007, in Bethesda, Maryland*. Washington, D.C.: Office of Basic Energy Sciences, U.S. Dept. of Energy, 2007. 22-37.

[2] Knözinger, Helmut, and Karl Kochloefl. "Heterogeneous Catalysis and Solid Catalysts." *Ullmann's Encyclopedia of Industrial Chemistry* (2003): 36-42.

[3] Marceau, Eric, Xavier Carrier, and Michel Che. "Chapter 4. Impregnation and Drying." *Synthesis of Solid Catalysts*. By Krijn Pieter De. Jong. Weinheim: Wiley-VCH, 2009. 59-82.

[4] Che, M., O. Clause, and Ch. Marcilly. "Chapter 4.1 Impregnation and Ion Exchange." *Preparation of Solid Catalysts*. By G. Ertl, H. Knözinger, and J. Weitkamp. Weinheim: Wiley-VCH, 1999. 315-40.

[5] Leyrer, J. "Spreading Behavior of Molybdenum Trioxide on Alumina and Silica: A Raman Microscopy Study." *Journal of Catalysis* 124.2 (1990): 349-56.

[6] Knözinger, H., and E. Taglauer. "Spreading and Wetting." *Preparation of Solid Catalysts*. Ed. G. Ertl, H. Knözinger, and J. Weitkamp. Weinheim: Wiley-VCH, 1999. 501-26.

[7] Wachs, Israel E. "Recent Conceptual Advances in the Catalysis Science of Mixed Metal Oxide Catalytic Materials." *Catalysis Today* 100.1-2 (2005): 79-94.

[8] Wachs, Israel E. "The Generality of Surface Vanadium Oxide Phases in Mixed Oxide Catalysts." *Applied Catalysis A: General* 391.1-2 (2011): 36-42.

[9] Wachs, Israel E., and Kamalakanta Routray. "Catalysis Science of Bulk Mixed Oxides." *ACS Catal. ACS Catalysis* 2.6 (2012): 1235-246.

[10] Schuth, F., and K. Unger. "3.4 Precipitation and Coprecipitation."*Preparation of Solid Catalysts*. By G. Ertl, H. Knözinger, and J. Weitkamp. Weinheim: Wiley-VCH, 1999. 60-84.

[11] Lok, Martin. "Chapter 7. Coprecipitation." *Synthesis of Solid Catalysts*. By Krijn Pieter De. Jong. Weinheim: Wiley-VCH, 2009. 135-51.

[12] Knözinger, Helmut, and Karl Kochloefl. "Heterogeneous Catalysis and Solid Catalysts." *Ullmann's Encyclopedia of Industrial Chemistry* (2003): 44-45.

[13] Wachs, I. E., and C. J. Keturakis. "Monolayer Systems" *Comprehensive Inorganic Chemistry II: From Elements to Applications*. Ed. Jan Reedijk and Kenneth Poeppelmeier. Burlington: Elsevier, 2013. Chapter 7.06, 131-51.

[14] Weckhuysen, Bert M. "In Situ Spectroscopy of Catalysts." *ChemInform* 36.23 (2005): 1-11.

[15]Weckhuysen, Bert M. "Snapshots of a Working Catalyst: Possibilities and Limitations of in Situ Spectroscopy in the Field of Heterogeneous Catalysis." *Chemical Communications Chem. Commun.* 2 (2002): 97-110.

[16] Bañares, Miguel A. "Operando Methodology: Combination of in Situ Spectroscopy and Simultaneous Activity Measurements under Catalytic Reaction Conditions." *Catalysis Today* 100.1-2 (2005): 71-77.

[17] Imelik, B., and Jacques C. Védrine. *Catalyst Characterization: Physical Techniques for Solid Materials*. New York: Plenum, 1994.

[18] Cullity, B. D. *Elements of X-ray Diffraction*. Reading, MA: Addison-Wesley Pub., 1956.

[19] Delgass, W. Nicholas. *Spectroscopy in Heterogeneous Catalysis*. New York: Academic, 1979.

[20] Wachs, Israel E. "Chapter 1. Molecular Structures of Surface Metal Oxide Species: Nature of Catalytic Active Sites in Mixed Metal Oxides." *Metal Oxides: Chemistry and Applications*. By J. L. G. Fierro. Boca Raton, FL: Taylor & Francis, 2006. 1-30.

[21] Wachs, Israel E. "Recent Conceptual Advances in the Catalysis Science of Mixed Metal Oxide Catalytic Materials." *Catalysis Today* 100.1-2 (2005): 79-94.

[22] Busca, G. "The Surface Acidity of Solid Oxides and Its Characterization by IR Spectroscopic Methods. An Attempt at Systematization." *Phys. Chem. Chem. Phys. Physical Chemistry Chemical Physics* 1.5 (1999): 723-36.

[23] Kim, T., A. Burrows, C. Kiely, and I. Wachs. "Molecular/electronic Structure–surface Acidity Relationships of Model-supported Tungsten Oxide Catalysts." *Journal of Catalysis* 246.2 (2007): 370-81.

[24] Busca, Guido. "Differentiation of Mono-oxo and Polyoxo and of Monomeric and Polymeric Vanadate, Molybdate and Tungstate Species in Metal Oxide Catalysts by IR and Raman Spectroscopy." *J. Raman Spectrosc. Journal of Raman Spectroscopy*33.5 (2002): 348-58.

[25] He, Yuanyuan, Michael E. Ford, Minghui Zhu, Qingcai Liu, Zili Wu, and Israel E. Wachs. "Selective Catalytic Reduction of NO by NH_3 with WO_3-TiO_2 Catalysts: Influence of Catalyst Synthesis Method." *Applied Catalysis B: Environmental* 188 (2016): 123-33.

[26] He, Yuanyuan, Michael E. Ford, Minghui Zhu, Qingcai Liu, Uma Tumuluri, Zili Wu, and Israel E. Wachs. "Influence of Catalyst Synthesis Method on Selective Catalytic Reduction (SCR) of NO by NH_3 with V_2O_5-WO_3/TiO_2 Catalysts." *Applied Catalysis B: Environmental* 193 (2016): 141-50.

[27] Tanabe, K. "Industrial Application of Solid Acid–base Catalysts." *Applied Catalysis A: General* 181.2 (1999): 399-434.

[28] Busca, Guido. "Acid Catalysts in Industrial Hydrocarbon Chemistry." *Chemical Reviews* 107.11 (2007): 5366-410.

[29] Tanabe, Kōzō. "Chapter 2. Determination of Acidic Properties on Solid Surfaces." *Solid Acids and Bases; Their Catalytic Properties*. Tokyo: Kodansha, 1970.

[30] Tanabe, Kozo. "Surface and Catalytic Properties of ZrO_2." *Materials Chemistry and Physics* 13.3-4 (1985): 347-64.

[31] Tanabe, Kōzō, and Hideshi Hattatori. "2.4 Solid Superacids." *Handbook of Heterogeneous Catalysis*. By G. Ertl, H. Knözinger, and J. Weitkamp. Weinheim: VCH, 1997. 404-12.

[32] Davis, Burtron H., Robert A. Keogh, and Ram Srinivasan. "Sulfated Zirconia as a Hydrocarbon Conversion Catalyst." *Catalysis Today* 20.2 (1994): 219-56.

[33] Yamaguchi, Tsutomu. "Application of ZrO_2 as a Catalyst and a Catalyst Support." *Catalysis Today* 20.2 (1994): 199-217.

[34] Hino, Makoto, and Kazushi Arata. "Synthesis of Solid Superacid of Tungsten Oxide Supported on Zirconia and Its Catalytic Action for Reactions of Butane and Pentane." *Journal of the Chemical Society, Chemical Communications J. Chem. Soc., Chem. Commun.* 18 (1988): 1259.

[35] Tanabe, Kōzō. "3.9 Superacids." *New Solid Acids and Bases: Their Catalytic Properties*. Tokyo: Kodansha, 1989. 199-211.

[36] Arata, Kazushi. "Chapter 17. Preparation of Super Acidic Metal Oxides and Their Catalytic Action." *Metal Oxide Catalysis*. By S. D. Jackson and J. S. J. Hargreaves. Weinheim: Wiley-VCH, 2009. 665-704.

[37] Corma, A. "Inorganic Solid Acids and Their Use in Acid-Catalyzed Hydrocarbon Reactions." *Chemical Reviews* 95.3 (1995): 559-614.

[38] Scheithauer, Markus, Robert K. Grasselli, and Helmut Knözinger. "Genesis and Structure of WO_X/ZrO_2 Solid Acid Catalysts."*Langmuir* 14.11 (1998): 3019-029.

[39] Barton, D. G., S. L. Soled, and E. Iglesia. "ChemInform Abstract: Solid Acid Catalysts Based on Supported Tungsten Oxides."*ChemInform* 29.48 (2010): 87-99.

[40] Barton, David G., Stuart L. Soled, George D. Meitzner, Gustavo A. Fuentes, and Enrique Iglesia. "Structural and Catalytic Characterization of Solid Acids Based on Zirconia Modified by Tungsten Oxide." *Journal of Catalysis* 181.1 (1999): 57-72.

[41] Rossmedgaarden, E., W. Knowles, T. Kim, M. Wong, W. Zhou, C. Kiely, and I. Wachs. "New Insights into the Nature of the Acidic Catalytic Active Sites Present in ZrO_2-supported Tungsten Oxide Catalysts." *Journal of Catalysis* 256.1 (2008): 108-25.

[42] Zhou, Wu, Elizabeth I. Ross-Medgaarden, William V. Knowles, Michael S. Wong, Israel E. Wachs, and Christopher J. Kiely. "Identification of Active Zr–WO_x Clusters on a ZrO_2 Support for Solid Acid Catalysts." *Nature Chemistry Nature Chem* 1.9 (2009): 722-28.

[43] Brunauer, Stephen, P. H. Emmett, and Edward Teller. "Adsorption of Gases in Multimolecular Layers." *J. Am. Chem. Soc. Journal of the American Chemical Society* 60.2 (1938): 309-19.

[44] Barrett, Elliott P., Leslie G. Joyner, and Paul P. Halenda. "The Determination of Pore Volume and Area Distributions in Porous Substances. I. Computations from Nitrogen Isotherms." *J. Am. Chem. Soc. Journal of the American Chemical Society* 73.1 (1951): 373-80.

[45] Webb, Paul, and Clyde Orr. *Analytical Methods in Fine Particle Technology*. Norcross, GA: Micromeritics Instrument, 1997.

[46] Bearden, J. A. "X-Ray Wavelengths." *Reviews of Modern Physics Rev. Mod. Phys.* 39.1 (1967): 78-124.

[47] Toraya, H., M. Yoshimura, and S. Somiya. "Calibration Curve for Quantitative Analysis of the Monclinic-tetragonal ZrO_2 System by X-ray Diffraction." *Journal of the American Ceramic Society* 67.6 (1984): C-119-121.

[48] Stevens, R. *Zirconia and Zirconia Ceramics*. Manchester, U.K.: Magnesium Elektron, 1986.

[49] Chorkendorff, I., and J.W Niemantsverdriet. "10.2.1.1 Catalytic Converter." *Concepts of Modern Catalysis and Kinetics*. 2nd ed. Weinheim: Wiley-VCH, 2007. 385-87.

[50] Chan, Shirley S., Israel E. Wachs, Lawrence L. Murrell, and Nick C. Dispenziere, Jr. "Laser Raman Characterization of Tungsten Oxide Supported on Alumina: Influence of Calcination Temperatures."*Journal of Catalysis* 92.1 (1985): 1-10.

[51] Wachs, Israel E. "Raman and IR Studies of Surface Metal Oxide Species on Oxide Supports: Supported Metal Oxide Catalysts."*Catalysis Today* 27.3-4 (1996): 437-55.

Chapter 6: Conclusions and Future Outlook

6.1 Summary

Metal oxides are utilized in a wide range of industrial applications including catalysts,[1] ceramics,[2] fuel-cells,[3] and adsorbents.[4] Their wide utilization is due in part to their unique crystal structure,[5] surface chemistry,[6] and material properties. Specifically, transition metal oxides found in the *d*-block of the periodic table offer a palette of chemical attributes necessary to meet the needs of many industrial applications.[7] However at elevated temperatures, mechanisms of material reconfiguration cause the surface of an oxide to become mobile, redeposit, and alter its structural configuration.[8,9] This leads to problems with material performance including deactivation, surface area loss, molecular transport limitations, and phase changes.[10] This thesis has examined various mechanisms of surface stabilization which can be utilized to synthesize catalysts and porous materials in order to minimize transport limitations, promote phase stabilization, prevent sintering, and produce unique surface chemistry.

6.2 Chapter Reviews and Future Research Opportunities

6.2.1 Synthesis of 3DOm Materials via Templating to Mitigate Transport Limitations

In chapter 2 we demonstrated how the application of a hard templating technique can be utilized to tune the surface area and pore size of a material. This concept can be used for the mitigation of internal transport limitations during catalytic processing and molecular separation. Three dimensionally ordered mesoporous (3DOm) materials including carbons, titanias, and zirconias were successfully templated with colloidal silica nanomolds. These materials demonstrated the ability to tune both surface area and pore size by varying the

diameter of the colloidal SiO_2 nanospheres. Additionally, the SiO_2 template was found to promote stabilization of metastable oxide phases (i.e. tetraongal ZrO_2 and anatase TiO_2). This was found to be a general interfacial phenomenon that could be achieved via various synthetic means including: the physical mixing of oxide powders, IWI of a supporting phase, and 3DOm templating.

These discoveries provide new areas for future research in the synthetic design of mesoporous materials. Many novel synthetic techniques are not stable at the elevated temperatures or pressures typical of most industrial scale operations. Thus, hard templating has shown the unique ability to both scaffold the pore structure of a material and simultaneously stabilize it. Future research should be conducted to assess the stability of these materials in adsorption and separation processes. Additionally, experiments should be conducted to demonstrate how 3DOm materials can be utilized to optimize transport limitations; as has already been shown with alternative templating techniques, such as the commercially available "riving" technique.[11,12] Lastly, simulation based research should be conducted to account for the spherical pore structure of similar 3DOm materials during N_2 physisorption. The traditional BJH method assumes cylindrical pores exist during calculation.[13] This introduces a slight error when utilizing the BJH method to measure pore size in materials with ordered spherical pores; yet it provides a new area for simulation based research.

6.2.2 Surface Stabilization of Metastable Oxide Powders

In chapter 3 we demonstrated how metastable oxide powders can be stabilized by incorporation of a supported SiO_2 surface layer. Stabilized 5-15wt% SiO_2/MO_x materials were prepared using commercial polymorphic oxide supports including Degussa P25-TiO_2 (~87vol% anatase), VP-ZrO_2 (~64vol% tetragonal), and a commercial zirconium hydroxide (amorphous

$Zr(OH)_x$ from MEL Chemicals). IWI with tetraethyl orthosilicate and subsequent calcination at temperatures ranging from 500-1000˚C demonstrated stabilization of the metastable supporting phase and provided a resistance to sintering. The $SiO_2/Zr(OH)_x$ sample demonstrated an enhanced resistance to syneresis and sintering upon application of the SiO_2 surface layer and resulted in a large promotion in BET surface area. Stabilization of the underlying supporting oxide finally broke down during prolonged periods of calcination at temperatures above the bulk characteristic Tammann temperature of the supporting oxide.

Future characterization techniques should be utilized to assess stabilization of these powdered SiO_2/MO_x materials. Ambient pressure x-ray photoelectron spectroscopy (APXPS) could be used to assess the oxidation state near the surface of the stabilized materials for comparison with the unstabilized oxide controls.[14] This could provide insight into composition and chemical state near the surface of the material (~2-5nm)[15] at ambient conditions. This would provide information about the interaction between the SiO_2 surface layer (SiO_2 layer~1.5nm thick) and the supporting oxide. Additionally, low energy ion scattering (LEIS) could be used to examine surface reconstruction after calcination at various temperatures. LEIS could also be used to probe elemental composition via depth profiling experiments. This would determine how the surface of the stabilized oxide changes with calcination and how the mechanism of stabilization ultimately breaks down. Finally, *in situ* transmission electron microscopy could be used to probe the mechanistic restructuring of stabilized versus unstabilized oxides. *in situ* TEM technologies allow heating of a sample up to 1000˚C,[16] this would provide an adequate temperature range necessary to assess surface reconstruction of the stabilized SiO_2/MO_x materials studied within this thesis.

6.2.3 Interfacial Stabilization of Metastable Oxide Films

In chapter 4 we demonstrated how the concept of interfacial stabilization could be employed to stabilize metastable oxide films. Anatase TiO_2 films ranging in thickness from ~20-200nm were prepared by the blade-driven convective deposition of a chelated TiO_2 precursor solution onto the surface of oxidized silicon (100) wafers. Subsequent calcination at elevated temperatures (500-1000˚C) facilitated crystallization of the TiO_2 film and stabilized the traditionally metastable anatase phase versus bulk TiO_2 control powders. Stabilization finally broke down when surpassing the Tammann temperature of titania ($TiO_2^{Tammann}$ ~920˚C).

Microscopy studies showed that films which maintained increased coherency to the underlying oxidized wafer promoted enhanced stabilization of the anatase phase; conversely, films which delaminated from the wafer exhibited slight conversion to the more stable rutile TiO_2 phase. Focused Ion Beam lithography was utilized to remove a portion of the wafer for profiled characterization of the interfacial a-TiO_2/SiO_2 layers. Atomic resolution microscopy and energy dispersive spectroscopic mapping revealed the interface responsible for anatase stabilization. EDS-mapping indicated that silicon doping was largely absent within the a-TiO_2 layer and not the primary mode of stabilization. These results demonstrate the ability of interfacial stabilization phenomenon to stabilize oxide crystals on the order of several hundred nanometers from the interface.

The thin film materials prepared in this thesis provide a model platform which can be utilized to study interfacial mechanisms of stabilization. Future work should be conducted to demonstrate this is a general phenomenon which can be employed for the stabilization of other metal oxide films (e.g. t-ZrO_2). Thicker films could be prepared to examine the length scale upon which interfacial stabilization can impart on larger metastable oxide crystals.

Further characterization with surface destructive mass spectrometry techniques could be utilized to accurately assess elemental silicon doping spanning the thickness of the film. Techniques such as inductively coupled plasma mass spectrometry (ICPMS), LEIS depth profiling, and secondary ion mass spectrometry (SIMS) could be utilized to determine elemental silicon composition at various length scales of the film.

6.2.4 Influence of Synthesis on the Stabilization of MO_x/ZrO_2^{Cryst} versus MO_x/ZrO_2^{Hyd} Catalysts

In chapter 5 we demonstrated how a non-conventional IWI procedure which utilizes commercial hydroxides ($Zr(OH)_x$) could be used to promote unique surface chemistry in supported oxide catalysts for applications in the area of acid catalysis.[17,18,19] Zirconium hydroxide ($Zr(OH)_x$) materials were utilized as precursors to crystalline ZrO_2 supports for the non-conventional production of MO_x/ZrO_2^{Hyd} catalysts; these catalysts were compared to more traditional MO_x/ZrO_2^{Cryst} catalysts, which were prepared via the conventional IWI procedure with commercial crystalline ZrO_2 supports. The structural configuration and high temperature reconfiguration of these materials were analyzed at temperatures ranging from 500-1000˚C. The MO_x/ZrO_2^{Hyd} catalysts demonstrated the ability to stabilize the metastable tetragonal phase of ZrO_2, scaffold the surface area of the catalyst, and induce distorted mono-oxo surface species. This was a general phenomenon observed with both WO_3/ZrO_2^{Hyd} and MoO_3/ZrO_2^{Hyd} catalysts. These findings are analogous to those observed in recent studies on similarly synthesized WO_3-TiO_2 and V_2O_5-WO_3/TiO_2 catalysts for the SCR of NO to NH_3.[20,21]

These catalysts should be investigated further by performing catalytic tests to determine the activity of the distorted mono-oxo sites. Acid catalysts such as WO_3/ZrO_2 and MoO_3/ZrO_2 are often studied for the skeletal isomerization of alkanes.[22,23] Reactions such as the isomerization of *n*-butane to *i*-butane or n-pentane to i-pentane[24] could provide a means

of testing the catalytic activity of the of MO_x/ZrO_2^{Hyd} versus MO_x/ZrO_2^{Cryst} catalysts. This would also provide a means of assessing the turnover frequency of the active sites on each catalyst. This research could directly correlate the distorted mono-oxo sites to the increased catalytic performance which is traditionally observed among acid catalysts. Additionally, density functional theory (DFT) could be utilized to simulate the molecular structure of the newly discovered sites.

6.3 Conclusion

We have demonstrated in this thesis how the addition of a surface oxide to a metastable supporting oxide can be utilized to stabilize the underlying crystal structure of the supporting oxide, promote its surface area, and generate unique surface chemistry. This was first observed during 3DOm templating utilized for the promotion of surface area and pore structure of various materials (See Chapter 2). It was then validated as a general phenomenon which could be utilized to stabilize model supported oxide powders (See Chapter 3) and thin films (See Chapter 4). We then demonstrated how the concept of surface stabilization can be employed for the promotion of surface area, stabilization of metastable crystal structures, and enhancement of surface chemistry during the synthesis of uniquely stabilized MO_x/ZrO_2^{Hyd} catalysts (See Chapter 5).

6.4 References

[1] Thomas, Charles La Mar. *Catalytic Processes and Proven Catalysts*. New York: Academic, 1970.

[2] Kingery, W. D. *Introduction to Ceramics*. New York: John Wiley & Sons, 1960.

[3] Stevens, R. *Zirconia and Zirconia Ceramics*. Manchester, U.K.: Magnesium Elektron, 1986.

[4] White, Laurence, and George Duffy. "Staff-Industry Collaborative Report Vapor-Phase Production of Colloidal Silica." *Ind. Eng. Chem. Industrial & Engineering Chemistry* 51.3 (1959): 232-38.

[5] Palache, Charles, Harry Berman, and Clifford Frondel. *Dana's System of Mineralogy: Vol. 1*. 7th ed. New York: Wiley & Sons, 1963.

[6] Wachs, I. E., and C. J. Keturakis. "Monolayer Systems" *Comprehensive Inorganic Chemistry II: From Elements to Applications*. Ed. Jan Reedijk and Kenneth Poeppelmeier. Burlington: Elsevier, 2013. Chapter 7.06, 131-51.

[7] Cotton, F. Albert. *Advanced Inorganic Chemistry*. 5th ed. New York: Wiley, 1999.

[8] Stevenson, Scott A. *Metal-support Interactions in Catalysis, Sintering, and Redispersion*. New York: Van Nostrand Reinhold, 1987.

[9] Knözinger, H., and E. Taglauer. "Spreading and Wetting." *Preparation of Solid Catalysts*. Ed. G. Ertl, H. Knözinger, and J. Weitkamp. Weinheim: Wiley-VCH, 1999. 501-26.

[10] Roberts, G. W. "Chapter 9. Heterogeneous Catalysis Revisited." *Chemical Reactions and Chemical Reactors*. Hoboken, NJ: John Wiley & Sons, 2009. 305-69.

[11]Li, Kunhao, Julia Valla, and Javier Garcia-Martinez. "Realizing the Commercial Potential of Hierarchical Zeolites: New Opportunities in Catalytic Cracking." *ChemCatChem* 6.1 (2013): 46-66.

[12] García-Martínez, Javier, Marvin Johnson, Julia Valla, Kunhao Li, and Jackie Y. Ying. "Mesostructured Zeolite Y—high Hydrothermal Stability and Superior FCC Catalytic Performance." *Catal. Sci. Technol. Catalysis Science & Technology* 2.5 (2012): 987-94.

[13] Barrett, Elliott P., Leslie G. Joyner, and Paul P. Halenda. "The Determination of Pore Volume and Area Distributions in Porous Substances. I. Computations from Nitrogen Isotherms." *J. Am. Chem. Soc. Journal of the American Chemical Society* 73.1 (1951): 373-80.

[14] Schnadt, Joachim, Jan Knudsen, Jesper N. Andersen, Hans Siegbahn, Annette Pietzsch, Franz Hennies, Niclas Johansson, Nils Mårtensson, Gunnar Öhrwall, Stephan Bahr, Sven Mähl, and Oliver Schaff. "The New Ambient-pressure X-ray Photoelectron Spectroscopy Instrument at MAX-lab." *J Synchrotron Radiat Journal of Synchrotron Radiation J Synchrotron Rad* 19.5 (2012): 701-04.

[15] Imelik, B., and Jacques C. Védrine. "Chapter 1. General Introduction." *Catalyst Characterization: Physical Techniques for Solid Materials*. New York: Plenum, 1994. 1-10.

[16] Ferreira, P.j., K. Mitsuishi, and E.a. Stach. "In Situ Transmission Electron Microscopy." *MRS Bull. MRS Bulletin* 33.02 (2008): 83-90.

[17] Tanabe, Kōzō. "3.9 Superacids." *New Solid Acids and Bases: Their Catalytic Properties*. Tokyo: Kodansha, 1989. 199-211.

[18] Arata, Kazushi. "Chapter 17. Preparation of Super Acidic Metal Oxides and Their Catalytic Action." *Metal Oxide Catalysis*. By S. D. Jackson and J. S. J. Hargreaves. Weinheim: Wiley-VCH, 2009. 665-704.

[19] Tanabe, Kōzō, and Hideshi Hattatori. "2.4 Solid Superacids." *Handbook of Heterogeneous Catalysis*. By G. Ertl, H. Knözinger, and J. Weitkamp. Weinheim: VCH, 1997. 404-12.

[20] He, Yuanyuan, Michael E. Ford, Minghui Zhu, Qingcai Liu, Zili Wu, and Israel E. Wachs. "Selective Catalytic Reduction of NO by NH_3 with WO_3-TiO_2 Catalysts: Influence of Catalyst Synthesis Method." *Applied Catalysis B: Environmental* 188 (2016): 123-33.

[21] He, Yuanyuan, Michael E. Ford, Minghui Zhu, Qingcai Liu, Uma Tumuluri, Zili Wu, and Israel E. Wachs. "Influence of Catalyst Synthesis Method on Selective Catalytic Reduction (SCR) of NO by NH_3 with V_2O_5-WO_3/TiO_2 Catalysts." *Applied Catalysis B: Environmental* 193 (2016): 141-50.

[22] Corma, A. "Inorganic Solid Acids and Their Use in Acid-Catalyzed Hydrocarbon Reactions." *Chemical Reviews* 95.3 (1995): 559-614.

[23] Busca, Guido. "Acid Catalysts in Industrial Hydrocarbon Chemistry." *Chemical Reviews* 107.11 (2007): 5366-410.

[24] Hino, Makoto, and Kazushi Arata. "Synthesis of Solid Superacid of Tungsten Oxide Supported on Zirconia and Its Catalytic Action for Reactions of Butane and Pentane." *Journal of the Chemical Society, Chemical Communications J. Chem. Soc., Chem. Commun.* 18 (1988): 1259.

Daniel Graham Gregory

111 Research Dr. Iacocca Hall, Department of Chemical and Biomolecular Engineering
Bethlehem, PA 18015

Phone: (302)-542-3182
Email: dgg310@lehigh.edu

SUMMARY

Ph.D. candidate with experience in the design, synthesis, characterization, and application of inorganic and organic materials with tunable properties for use as stable catalysts, adsorbents, and thin films.

Expertise & Specialties:

- Metal oxide synthesis
- Synthesis of colloidal nanoparticles
- Synthesis of porous carbons
- Material characterization
- Thin film preparation
- Polymer liquefaction
- Polymer microcapsule spraying
- High pressure tubing design/plumbing

EDUCATION and WORK EXPERIENCE

- Lehigh University, Bethlehem, PA — Sep. 2010-May 2016
  Ph.D. Candidate, Chemical Engineering
- University of Delaware, Newark, DE — Sep. 2005-May 2010
  B.S., Chemical Engineering; Minor, Chemistry
- University of Delaware, Newark, DE — Jun. 2009-May 2010
  Undergraduate Researcher
- State of Delaware Office of Drinking Water, Dover, DE — Summers 2005, 06, 07, 08, 10
  Environmental Control Tech II — Winters 07, 08, 09, 10

PUBLICATIONS and REPORTS

1. **Daniel Gregory**, Mark A. Snyder, "Stabilization of Metastable Oxides via Surface Modification," *in preparation* (2016).

2. Qianying Guo, **Daniel Gregory**, Won Cheol Yoo, Mark A. Snyder "Solvothermal synthesis of tunable three-dimensionally ordered mesoporous TiO_2 for enhanced photocatalysis of bulky molecules," *in preparation* (2016).

3. Israel E. Wachs, Christopher J. Keturakis, Soe Lwin, Yadan Tang, Minghui Zhu, Anisha Chakrabarti, Michael Ford, **Daniel Gregory**, Zhou Yang, and RongRong Hu, "A Decade of *Operando* Molecular Spectroscopy in Catalysis," *in preparation, to be submitted to Operando V Conference Proceedings* (2015).

4. **Daniel Gregory**, Mark A. Snyder, "Templated Growth of Three-Dimensionally Ordered Mesoporous (3DOm) Zirconia and the Influence of Template Confinement on Polymorphism," *EPI Graduate Research Progress Report* (GRPR) (2013).

RESEARCH EXPERIENCE

Stabilization of Metastable Oxides via Surface Modification

- Synthesized various oxides and supported oxides via incipient wetness, precipitation, thermo-physical spreading, and convective deposition for use as catalysts and thin films.
- Characterized porosity, morphology, and crystallinity of products via TEM, EDS, XRD, WAXS, and gas adsorption (N_2, Kr, Ar Adsorption).
- Realized methods of stabilizing the crystal structure, surface area, and pore size distribution of oxides via surface modification.
- Characterized thin films via SEM, Ellipsometry, Profilometry, and contact angle measurements.
- Demonstrated the versatility of oxide stabilization in thin films with potential applications for the semiconductor and photovoltaic industry.

Synthesis and Analysis of Porous Carbons for the Separation of Biomass Derived Products

- Synthesized pore size tunable carbons via liquid and gas infiltration of colloidal SiO_2 templates.
- Characterized carbon adsorbents via TEM, SEM, and gas adsorption (N_2 and Ar adsorption).
- Conducted performance testing of as made carbon adsorbents for the separation of biomass derived sugars via HPLC.

Templated Growth of Three-Dimensionally Ordered Mesoporous (3DOm) Oxides

- Synthesized pore size tunable oxides via liquid infiltration of colloidal SiO_2 templates.
- Characterized porous oxides via TEM, SEM, and gas adsorption.
- Realized appropriate synthetic techniques necessary for the templated growth of oxides.

Polymer Liquefaction Using Supercritical Solvation

- Conducted Polymer Liquefaction Using Supercritical Solvation (PLUSS) experiments to produce polymer micro-particles for new methods of pulmonary drug delivery.
- Designed a high pressure tubing apparatus for the expulsion of liquefied polymers.
- Manipulated liquefied polymer viscosity by altering the molecular weight of a polymer to control particle size and morphology.

- Demonstrated that polymers below the molecular weight of critical entanglement were conducive to forming particles with uniform size and shape necessary for micro-encapsulation.

Mapping of Ground Water Contaminants in the State of Delaware

- Collected ground water samples throughout the state of Delaware and preformed routine on-site chemical analysis of samples. Reviewed analytical laboratory data for contaminants.
- Worked in conjunction with the Delaware Cancer Consortium to produce maps correlating ground water aquafers, contaminant levels, and cancer Superfund locations.

SKILLS and EXPERTISE

Synthesis and characterization of particulate materials and thin films including: colloids, oxides, supported oxides, porous carbons, polymer micro-particles.

- Microscopy Characterization: TEM, SEM, Optical Microscopy
- X-ray Characterization: XRD, EDS
- Spectroscopy: *in situ* FT-IR, Raman, UV-Vis
- Particle Characterization: Gas Adsorption, TGA/DSC, DLS, Zeta-Potential
- Thin Film Preparation: Convective Deposition, Vapor Deposition
- Film Characterization: Ellipsometry, Profilometry, Contact Angle Measurements
- High Pressure Processing: Polymer Liquefaction/Spraying, High pressure tubing design

AWARDS

- 1st Place Poster in the Catalysis Club of Philadelphia's Fall Poster Competition 2016
- Chevron Scholars Award 2015
  The Chevron Scholars Award recognizes Lehigh Chemical Engineering graduate students for their contributions and accomplishments in the lab and classroom.
- William C. Gottshall Graduate Fellowship, Lehigh University, PA 2012
- Outstanding Senior Design Project: UDiesel May 2010
  Modeled a biodiesel production plant and performed an economic feasibility assessment for a University scale facility. Project concept was later adopted by the university (UDiesel).
- Outstanding Junior Lab Project May 2009
  Modeled and designed a new Alaskan Pipeline to meet increased oil production.

SELECTED CONFERENCE PRESENTATIONS

- Daniel Gregory, Michael Ford, Israel E. Wachs, Mark A. Snyder, "Stabilization of Metastable Oxides via Surface Modification," The Catalysis Club of Philadelphia's 2016 Annual Symposium, Newark, DE, May. 12, 2016.

- Daniel Gregory, Mark A. Snyder, "Stabilization of Metastable Oxides via Surface Modification," 2015 Materials Research Society (MRS) Fall Conference, Boston, MA, Dec. 4, 2015.

- Daniel Gregory, Mark A. Snyder, "Realization of Three Dimensionally Ordered Mesoporous Materials (3DOm) via Templating," 2015 Materials Research Society (MRS) Fall Conference, Boston, MA, Nov. 30, 2015.

- Daniel Gregory, Mark A. Snyder, "Stabilization of Metastable Oxides via Surface Modification," 2015 American Institute of Chemical Engineers (AIChE) Fall Conference, Salt Lake City, UT, Nov. 12, 2015.

- Daniel Gregory, Mark A. Snyder, "Stabilization of Porous, High Surface Area, Metastable Oxides at Elevated Temperatures," American Institute of Chemical Engineers (AIChE) Fall Conference, Salt Lake City, UT, Nov. 10, 2015.

SELECTED POSTER PRESENTATIONS

1. Daniel Gregory, Christopher J. Kiely, Israel E. Wachs, Mark A. Snyder, "Stabilization of Metastable Oxides via Surface Modification," 2015 Catalysis Club of Philadelphia's Annual Poster Competition, Newark, DE, Nov. 20, 2016. *1st Place Poster Award*

2. Daniel Gregory, Mark A. Snyder, "Stabilization of Metastable Oxides via Surface Modification," 2015 Catalysis Society of Metropolitan New York Annual Symposium, New Jersey Institute of Technology, Newark, NJ, Mar. 18, 2015. *Poster Presentation*

3. Daniel Gregory, Mark A. Snyder, "Stabilization of High Surface Area Metastable Oxides via Surface Modification," 2014 Northeast Corridor Zeolite Association Annual Meeting, University of Pennsylvania, Philadelphia, PA, Dec. 12, 2014. *Poster Presentation*

4. Daniel Gregory, Qianying Guo, Won Cheol Yoo, Mark A. Snyder, "Meso- and Hierarchically-Porous Materials for Biomass Processing," 2014 Catalysis Center for Energy Innovation Annual Meeting, University of Delaware, Newark, DE, April 6-7, 2014. *Poster Presentation*

5. Daniel Gregory, Mark A. Snyder, "Templated Growth of Three-Dimensionally Ordered Mesoporous (3DOm) Zirconia Materials as Tunable Catalysts for Biomass Conversion," 2013 Catalysis Society of Metropolitan New York Annual Symposium, Princeton University, Princeton, NJ, Mar. 20, 2013. *Poster Presentation*

6. Daniel Gregory, Mark A. Snyder, "Templated Growth of Three-Dimensionally Ordered Mesoporous (3DOm) Zirconia Materials as Tunable Catalysts for Biomass Conversion," 2012 Northeast Corridor Zeolite Association Annual Meeting, University of Pennsylvania, Philadelphia, PA, Dec. 14, 2012. *Poster Presentation*

7. Daniel Gregory, Mark A. Snyder, "Templated Growth of Three-Dimensionally Ordered Mesoporous (3DOm) Zirconia Materials as Tunable Catalysts for Biomass Conversion," 2012 AIChE Annual Meeting, Pittsburgh, Oct. 29-Nov. 2, 2012. *Poster Presentation*

8. Daniel Gregory, Mark A. Snyder, "Templated Growth of Three-Dimensionally Ordered Mesoporous (3DOm) Zirconia Materials as Tunable Catalysts for Biomass Conversion," 2012 Catalysis Center for Energy Innovation Annual Symposium, University of Delaware, Newark, DE, April 29-30, 2012. *Poster Presentation*

9. Daniel Gregory, Mark A. Snyder, Annual Review Meeting of the Emulsion Polymers Institute (EPI), Lehigh University, Bethlehem, PA, 2011-2014. *Poster Presentation*

CERTIFICATIONS

- Fundamentals of Engineering (FE) Oct. 2009
- Approved Sampler/Tester Jun. 2005
  State of Delaware Office of Drinking Water, Delaware Health and Social Services

RESEARCH AFFILIATIONS

- Materials Research Society (MRS)
- American Institute of Chemical Engineers (AIChE)
- Catalysis Society of Metropolitan New York (NYCS)
- Catalysis Club of Philadelphia (CCP)
- Lehigh University's Chemical Engineering Graduate Association (ChEGA)
- Lehigh University's Emulsion Polymers Institute (EPI)